METEOROLOGICAL OFFICE
131017
1 OCT 1987
LIBRARY

ADVANCED LECTURES 1987

SATELLITE METEOROLOGY

Permission to quote from this document must be obtained from the Principal, Meteorological Office College, Shinfield Park, Reading, Berkshire RG2 9AU.

ADVANCED LECTURES

SATELLITE METEOROLOGY

Lecture 1.

AN INTRODUCTION TO SATELLITE METEOROLOGY

by C G Collier

1. INTRODUCTION

The purpose of this series of lectures is to discuss ways in which satellite techniques can be applied to meteorology. The aim is to provide an appreciation of potential applications of satellite data, including their strengths and shortcomings.

The first meteorological observations were made from a satellite only 25 years ago, and satellites are the basic vehicle for space research being the major source of observations of the upper atmosphere. This series of lectures will concentrate on applications of satellite techniques to studies of the lower atmosphere, particular in operational meteorology. Useful review papers on satellite meteorology can be found in the list of references.

Before describing the satellite techniques it is necessary to consider the basic motivation for using observation platforms in space. Typical meteorological satellites orbit the earth at elevations of either 36000 km or about 850 km, and yet we expect them to give us useful quantitative information about surface features and about a region of the atmosphere (the troposphere) extending only 10 km from the surface of the earth. At first glance successful remote sensing from this altitude would appear to be a highly unlikely undertaking, so why try?

The imaging capability of meteorological satellites provides part of the justification. Cloud images provide invaluable diagnostic information which assists in the analysis of meteorological features. This benefit can be extended by the use of time lapse image sequences which transform our understanding of atmospheric processes. However, this information is not quantitative, and numerical forecast models need precise measurements of atmospheric parameters at frequent time intervals, for many levels and at close intervals over the surface of the earth. The spacing of the observations depends upon the nature of the model, but for operational meteorology the British National Space Centre Columbus/Space Station United Kingdom Utilisation Study 1985/86 suggested the observational requirement summerised in Table 1.

TABLE 1A

Parameters	Accuracies
Surface Pressure	2 mb
Surface Wind	1 m sec^{-1}
Wind profiles	3 m sec^{-1} (vector error) at all levels.
Temperature profiles	1° K at all levels
Humidity profiles	10% in relative humidity at all levels (but lower in regions of little climatological variance, such as the maritime atmospheric boundary layer).
Cloud	10% in fractional coverage, 0.5 km in cloud top height, 20% in water content.
Precipitation	50% instantaneously, but 10% for time-averaged values.

TABLE 1B

Requirements for different scales of forecasting

	GLOBAL	REGIONAL	LOCAL
Timescale of forecasting	Medium-range	Short-range	Very short-range
	2-14 days	12-48 hours	0-12 hours
Area of interest (in km radius around point for which forecast is required)	global	3000	1000
Horizontal resolution of model (km)	150	75	15 (5 for Nowcasting)
Frequency of coverage	12 hr	6 hr	1 hr (15 mins for Nowcasting)
Speed of delivery of products.	3 hr	2 hr	30 mins (5 mins for Nowcasting)

The global requirement could be met by an adequate network of about 5,000 conventional stations, preferably regularly distributed all over the globe, each measuring the pressure at the surface as well as the wind, temperature, and humidity at many levels, from the surface to 50 mb, 2 to 4 times each day. However ocean areas could not sustain such a network, and the cost of such a network would be of the order of $1010 per year. The UK financial contribution might be as low as 1% of the global programme cost, but this would still exceed the present total annual budget of the Meteorological Office by a substantial margin.

By contrast, the entire globe can be observed by a system of 7 meteorological satellites. A global programme to launch 2 new satellites each year and to operate the total system could cost less than 2×10^8 per year; excluding development costs, a UK financial contribution of even 10% to this global system would amount to a more realistic 25% of the present Meteorological Office budget.

Similar arguments can be advanced concerning the denser observational networks required for regional and local scale forecasting. Additional conventional stations will be needed to satisfy these observational requirements whereas the same global system of satellites could, if appropriately specified, also provide the increased density of observations without additional cost.

Therefore the satellites, although individually expensive, provide more observations per £ and hence the main motivation for our interest in quantitative uses of meteorological satellites is financial. They appear to offer cost effective solutions to the problem of acquisition of observational data with useful resolution and accuracy. It is the purpose of this series of lectures to demonstrate to what extent satellites are able to satisfy the general observational requirements.

2. Space vehicles

In designing a space vehicle one must take into account the lack of gravity in a free orbit, the high-vacuum conditions in which materials behave very differently from their behaviour at the earth's surface, and the presence of energetic particle radiation and micro-meteoritic dust.

The satellite vehicle, or bus, acts as a frame on which to mount the instruments monitoring the earth and its atmosphere, but must also provide the necessary power for the instruments, thermal control, aspect control, a data-handling system and communications. Power is normally supplied by solar cells, backed up by batteries to store energy when the satellite is on the night-time side of the earth.

Sensors and other electrical equipment will only operate under particular temperature ranges. Hence heat generated by electronic equipment, or absorbed from incident radiation, must be balanced by longwave radiation emission into space. Active control of the temperature can be achieved by varying the net longwave radiation via attitude control, or by the operation of shutters to increase or decrease the area of radiation surfaces pointing towards cold space.

Aspect control of a space vehicle is achieved by several different means dependent upon the overall design. Precise spin rates can be maintained by alteration of the mass distribution of the satellite and hence its moment of inertia. Alternatively inertial systems are used which torque with respect to the earth's magnetic field, and reaction jets may be activated. It is worth noting that the more stable the vehicle is, the longer will be its useful life. Atmospheric drag prevents orbits much below 300 km altitude from being used as the vehicle lifetime is considerably reduced. However, at higher obits this drag is very small and lifetimes of several years are achieved.

3. Satellite orbital dynamics

A satellite moving without friction in the gravitational field of a spherical planet has a trajectory which is either elliptical, parabolic or hyperbolic depending upon its starting velocity (Massey, 1964). For an earth-orbiting satellite an elliptical orbit, or the special case of a circular orbit, is required. For the elliptical orbit shown in Figure 1a, the distance r of the satellite from the centre of the earth is given by,

$$r = \frac{a\,(1-e^2)}{(1+e\cos\theta} \qquad 1.$$

where θ is the angle between between the satellite's present radius vector and that at perigee (the orbit's closest point to the Earth); a is the semi-major axis of the ellipse and ae is the displacement of the ellipse centre from the centre of the earth where e is the eccentricity of the ellipse.

The period T for the satellite to travel round the orbit is,

$$T = 2\pi\,(a^3/GM)^{\frac{1}{2}} \qquad 2.$$

where G is the gravitational constant, M is the mass of the earth, and GM = $3.98603 \times 10^{14}\ m^3\ s^{-2}$. For a circular orbit centred on the earth e = o, a = r and the horizontal speed of the satellite is,

$$V_o = (GM/a)^{\frac{1}{2}} \qquad 3.$$

In terms of the height h above the earth, Figure 1b, and the acceleration due to gravity at the earth's surface $g = GM/R^2$, where R = 6378 km is the earth's mean equatorial radius then,

$$V_o = R\left[g/(R+h)\right]^{\frac{1}{2}} \qquad 4.$$

The rocket on which a satellite space vehicle sits must be launched to obtain a trajectory such that the desired height h and its speed V result. If when the satellite reaches h its speed $V < V_o$ then the vehicle will fall into an elliptical orbit for which $a < (h+R)$. However, if $V > V_o$ the satellite will move out into a higher ellipse and $a > (h+R)$. If $V > 2V_o$ then the orbit becomes parabolic, the satellite has reached escape velocity, and it will not remain in orbit around the earth.

A geostationary orbit is achieved if the satellite orbits in the same direction as the earth with a period of one day. If the orbit is circular above the equator it becomes stationary relative to the earch and therefore always views the same area of the earth's surface. Taking T = 1 day = 86400 seconds then from equation 2. a = 42290 km, and therefore for a geostationary orbit h = a-R = 35910 km.

Lower orbits have much shorter periods. Satellites at altitudes between 500 and 2000 km are normally placed in nearby circular polar orbits such that they move over the poles with a period of around 1 or 2 hours. As the earth rotates under this orbit the satellite effectively scans from north to south over one side and south to north across the other side of the earth, several times each day, achieving much greater surface coverage than if it were in a non-polar orbit.

So far orbits have been discussed assuming spherical symmetry and zero drag. In practice this is not so, however the main deviation from a pure elliptical orbit is due to non-symmetrical gravity forces caused by the irregular figure and mass distribution of the earth. Solar and lunar

gravitation is not important, but the equatorial bulge of the earth is of major importance causing a slight change to the satellite period which results in the perigee of an elliptical orbit changing position with time. This precession causes the orbital plane, Figure 1c, to rotate. For a given orbit height, it is possible to select the inclination i to achieve a rate of change of the orbital plane of 0.986° per day which is equivalent to one rotation of the orbit plane per year, infact $i > 90°$. Hence the orbit can be fixed relative to the sun as the earth orbits it once per year; this is known as a sun-synchronous orbit. The satellite crosses the equator at the same local solar time on each pass throughout the year. Most polar-orbiting satellites are in sun-synchronous orbits. In prectice the inclination of a geostationary orbit will also change, and the more general term, geosynchronous orbit should really be used. The satellite will appear to move in the sky through a narrow "figure of 8" pattern, each day. King-Hele (1964) considers orbit dynamics in detail.

Satellite orbital height controls the radius of the contact circle for direct reception of data transmitted in real time from the satellite, and the width of the swath which can be observed by a satellite sensor. Both are improved by increasing the satellite height. However, whilst greater orbital height has its advantages there are practical difficulties. Satellites in orbit above 1100 km encounter a much increased flux of charged particles (which can degrade performance of solar cells and other materials). Increases in satellite height also require more sensitive instruments to maintain the same ground resolutions.

4. Satellite sensors

The sensors mounted on satellites to observe the atmosphere use electromagnetic radiation (e.m.r.) either passively, that is detect e.m.r. emitted from the earth's surface or from the atmosphere, or actively, that is by using e.m.r. generated in the sensor to probe the atmosphere and measure the surface

characteristics. Figure 2. shows the electromagnetic spectrum in which different wavelength bands are defined as follows,

L Band $\simeq$ 250 mm (1.2 GHZ) (1 GHZ = gigahertz = 10^9cps)

S Band $\simeq$ 100 mm (3 GHZ)

C Band $\simeq$ 50 mm (6 GHZ)

X Band $\simeq$ 30 mm (10 GHZ)

K Band $\simeq$ 10 mm (30 GHZ)

The parts of the spectrum which are currently used by remote-sensing sensors on satellites are also shown in Figure 2. To observe features of the land and sea using solar radiation, then wavelengths between 100 nm and 100 μm (nm = 10^{-9}m) must be used. However, radiation emissions from the sea are detected in the range 3 to 40 μm. Not all the parts of these ranges can be used as the atmosphere will not transmit e.m.r. at all wavelengths, as shown in Figure 3. This will be discussed further in section 5.

There are broadly two types of sensor, those sensors which scan and those which do not. The angle of view from which a signal is received by the sensor at any one instant is known as the instantaneous field of view (IFOV). The IFOV is not a precise demarcation between zero and total response, but is really some arbitrary threshold response value. By rotating the space vehicle the field of view can be extended to a large area. The spin-scan axis may be perpendicular to the earth's surface or parallel to the earth's equator. Geostationary satellites scan the earth's disk in this way within 25 minutes. Sensors are scanned both mechanically and electronically. In mechanical (whiskbroom) scanning, the field of view is changed by mechanical rotation of the sensor system or angular movement of the scan mirror either in the cross-track direction for the earth's surface or in a special direction for limb measurements. Electronic (pushbroom) scanning relies on the orbital motion of the sensor to sweep the area to be observed. Both types of scanning are shown in Figure 4.

Many telescopes used in satellite sensors make use of mirrors to form primary images. A mirror has the advantage over a lens of being absolutely free from colour aberrations, but has the disadvantage of suffering from spherical aberration. Hence parabolic or hyperbolic mirrors are generally employed. Later lectures in this series will consider in detail specific sensor designs.

5. Radiation

5.1 Wavelength and frequency

Radiation may be described by its wavelength (λ) or frequency (ν), which are related by:

$$C = \nu.\lambda \qquad 5.$$

where C is the velocity of light, 3×10^8 m sec^{-1}.

5.2 Emission: some definitions.

A 'black body' absorbs all radiation which falls upon it. In general a body absorbs only a fraction of incident radiation, known as the absorptivity, this is wavelength dependent. Similarly, the efficiency for emission is known as the emissivity. At a given wavelength:

Emissivity = Absorptivity (KIRCHHOFF'S LAW) 6.

Power emitted per unit area, steradian and wavenumber is known as radiance.

5.3 Emission from a blackbody

Flux (ie energy per unit area) per unit wavelength interval emitted by a blackbody at temperature T at wavelength λ is given by:

$$B(\lambda) = \frac{2\pi hc^2 \lambda^{-5}}{\exp(hc/k\lambda T)^{-1}} \qquad 7.$$

$B(\lambda)$ and its equivalent in frequency units, $B(\nu)$, are known as the Planck Function.

$B(\lambda)$ peaks at wavelength λm given by:

$$\lambda m.T = 0.29 \text{ deg. cm} \qquad \text{(WIEN'S LAW)} \qquad 8.$$

For the Sun: T = 6000 K: $\lambda m = 0.48$ micron

For the Earth T = 290 K; $\lambda m = 10$ micron

Total energy emitted by a blackbody:

$$= \int B(\lambda)\, d\lambda = \sigma T^4 \quad \sigma, \text{ STEFAN'S CONSTANT} \quad 9.$$

B is proportional to T at microwave and far infra-red wavelengths. Typical dependence of B on T for λ at or below λ m is shown in Figure 5.

5.4 Atmospheric absorption:

Atmospheric absorption in the infra-red is dominated by "absorption bands" of water, carbon dioxide, ozone etc. Studies of radiation within these bands enables the characteristics of the atmosphere to be determined; its temperature and the concentration of the absorber. However there are regions of the spectrum where absorption is low, providing the possibility for a satellite sensor to view the surface and to determine its temperature or other characteristics. Such spectral regions are called "windows". There is a particularly important window near the peak of the earth/atmosphere emission curve, around 11 microns, see Figure 3.

5.5 Sounding of the atmosphere

Values of radiance in bands of gases with a fixed concentration can be used to measure vertical temperature profiles. For gases with a variable concentration, measurements from satellites can be used to estimate the verical concentration profiles.

Consider an infinitely deep horizontally stratified atmosphere, each layer having a temperature T and containing a path length dZ of absorber in the vertical direction. Assuming local thermodynamic equilibrium then at a wavelength, λ , integrating over the region of the atmosphere, the total radiance at the top of the atmosphere from equation 9 is,

$$L(\lambda) = \int B(\lambda, T) d\tau(\lambda, P) \qquad 10.$$

Taking τ as the transmittance of the atmosphere, Z =-lnP, and P is the atmospheric pressure, equation 10 may be written,

$$L(\lambda) = \int B(\lambda, T) \frac{d\tau(\lambda, P)}{dZ} dZ \qquad 11.$$

Hence the radiance L is the weighted average of the blackbody intensity.

The weighting function is $d\tau/dz$, which is nearly independent of temperature, and represents the best region of the emitted radiation at a given wavelength and height. For different wavelengths the weighting function will peak at different altitudes. Temperature soundings may be constructed if a set of wavelength intervals can be chosen such that the corresponding radiances originate from substantially different levels in the atmosphere. Figure 6 shows the weighting functions currently used in the Meteorological Office retrieval system for processing data from the high resolution infrared spectrometer (HIRS).

Although operational meteorological sounders look straight down from the satellite to the earth's surface, an alternative approach is to look at the earth's limb. The weighting functions are very sharp for limb-scanning sensors and always peak at the highest pressure in the field of view. Hence good vertical resolution ($\sim$ 1 km) is obtained with a horizontal resolution of around 10 km. Somewhat poorer resolutions are available with vertical sounding, although it is not possible to make measurements lower than about 15 km altitude with limb sounding techniques, and therefore vertical sounding is necessary for tropospheric measurements.

6. Current operational meteorological satellite series

There are 3 types of low orbiting meteorological satellite in operation. These are:-

TIROS-N: the US civil satellites. The system comprises two satellites, currently NOAA-7 and NOAA-8. They provide image services and carry instruments for temperature sounding as well as for data collection and data platform location. Some of the products of the system are provided on the GTS.

DMSP: the US military satellites. These provide image and (less sophisticated) sounding data. Their real time transmissions are encrypted.

METEOR-2: the USSR series: image and sounding services, but lower quality infra-red imagery. No products are made available on the GTS.

Complete coverage of the extra-polar regions requires 5 geosynchronous satellites. The current position is:

GOES: the US satellites. At present only one satellite GOES-6 provides imagery.

GMS: the Japanese satellite. A US designed and launched satellite operating at 140°E.

METEOSAT: the ESA satellite. METEOSAT-1 has a fault, only the data collection system can be operated, and is maintained at 10°E. METEOSAT-2 has a complimentary fault, the data collection system cannot be used, but all other functions are operational and this satellite is maintained at 0° longitude.

INSAT: the Indian satellite located at 74°E.

There are therefore effectively 4 geosynchronous satellites presently in operation, although the INSAT satellite is primarily a communication system, regarded as a national resource rather than part of a global system. The World Weather Watch global observation satellite system is summarized in Figure 7, and more details of the individual satellites are given in Appendix A.

7. Operational satellite products

7.1 Qualitative products

Images from satellites can be used to locate features (cloud bands, fog patches, snow and ice cover) and to estimate the vigour of synoptic systems. Polar orbiting satellites transmit imagery in real time direct from the satellite. Given suitable reception and display facilities the forecaster can have access to image data over an area of radius about 2500 km. Such imagery is available 4 time per day, that is during daylight hours and at night from each of the 2 satellites. Reception of data from a geostationary

satellite provides more frequent pictures over a wider area. In either case images can be available within 10-20 minutes of the time of observation, the delay being associated with addition of geographical location information (for example grids or coastlines).

7.2 Quantitative products

Images, supplemented by observations of radiance in a range of spectral channels, particularly in absorption bands of carbon dioxide, are used to generate a range of quantitative products. Principle amongst these are:

Winds, derived from the motion of clouds as seen from the frequent images of geostationary satellites. Each satellite operator is providing about 1,000 winds per day within the latitude belt 50°N to 50°S.

Temperature profiles derived from radiances. NOAA produce and distribute about 8000 atmospheric profiles per day, on a 300 km spacing. The HERMES system also produces about 7000 atmospheric profiles per day at about a 100 km spacing, from the same satellites.

Other products now regularly available include sea surface temperatures, cloud and humidity information.

8. Conclusion

Satellites provide data which have operational applications. The following lectures will explain the sources of the data, the means by which products are generated and an indication of their quality. In this paper we have concentrated on aspects of current operational satellites. Within the next few years several improved and new satellites will be launched including Meteosat 2nd Generation and the ESA ERS-1 satellite which promise to have a major impact on the preparation of meteorological forecasts.

References

King-Hele, D. 1964 Theory of satellite orbits in an atmosphere, London Butterworth, 165 pp.

Massey, H. 1964 Space Physics, Cambridge University Press, London, 237 pp.

Further reading:-

Chen, H. S. 1985 Space Remote Sensing Systems. An introduction, Academic Press, London 257 pp.

Houghton, J. T., Taylor, F. W., and Rodgers, C. D. 1984 Remote Sounding of Atmospheres, Cambridge. University Press, London, 343 pp.

Robinson, I. S. 1985 Satellite Oceanography. An introduction for oceanographers and remote-sensing scientists, Ellis Harwood Ltd.,Chichester, 455 pp.

FIGURE 1

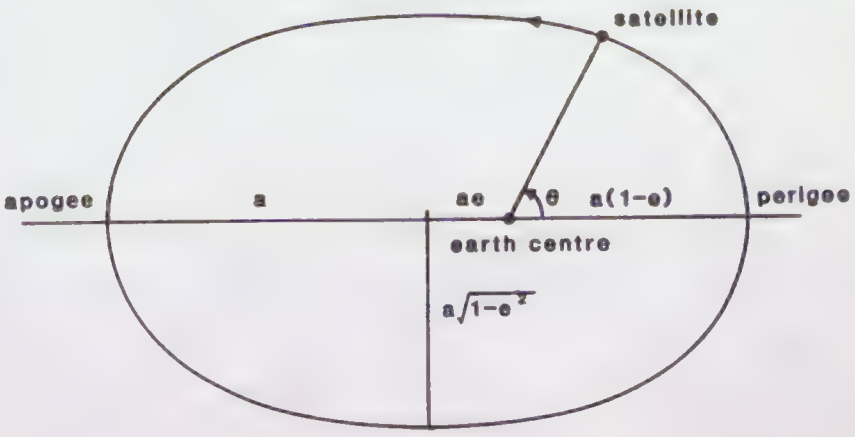

(a) Elements of a satellite elliptical orbit

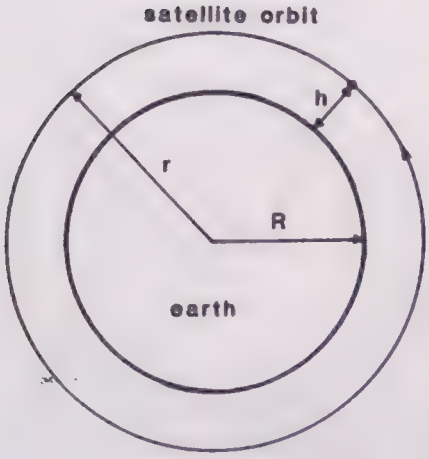

(b) Circular satellite orbit

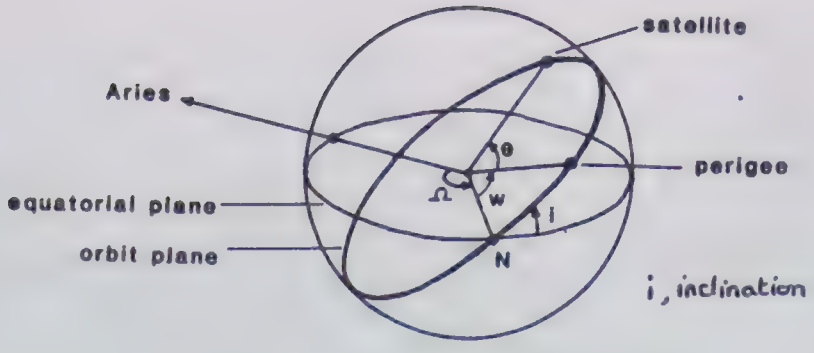

(c) Satellite orbital elements on the celestial shell

FIGURE 2

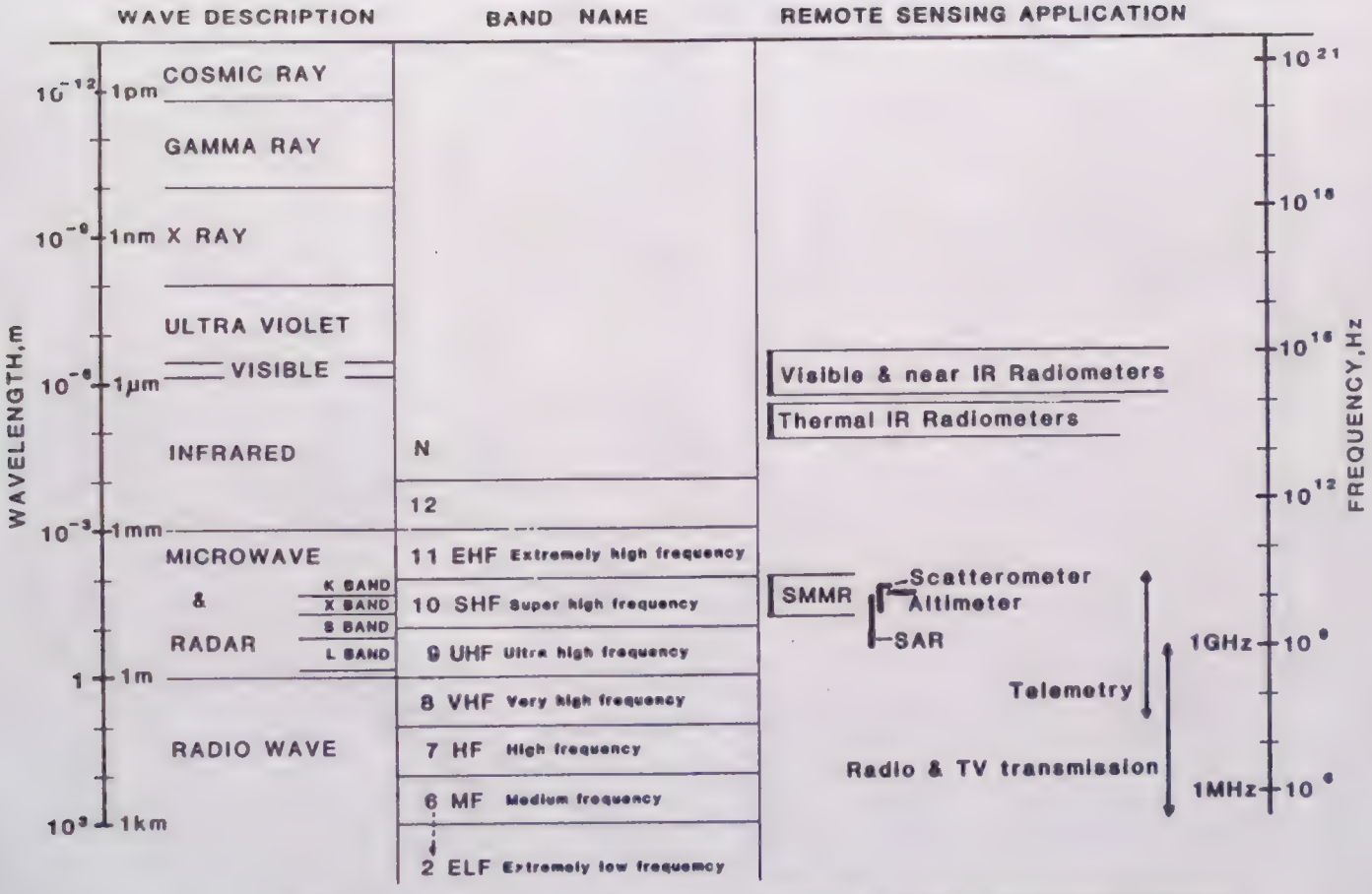

The electromagnetic spectrum, showing some band definitions and typical remote-sensing applications

FIGURE 3

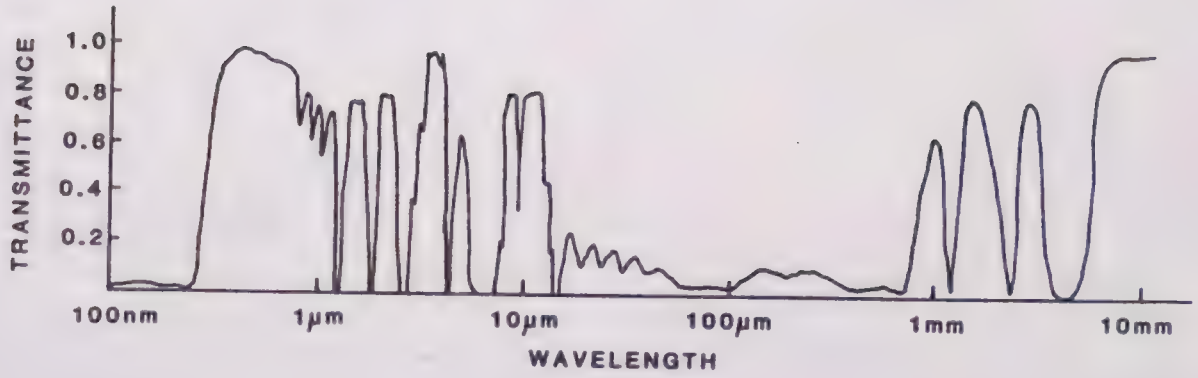

Approximate transmittance of electromagnetic waves through the atmosphere

FIGURE 4

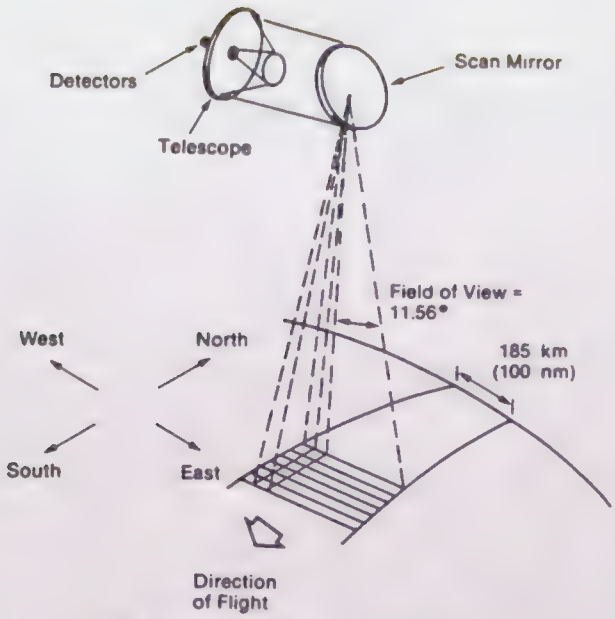

(a) Satellite whiskbroom scanning technique.

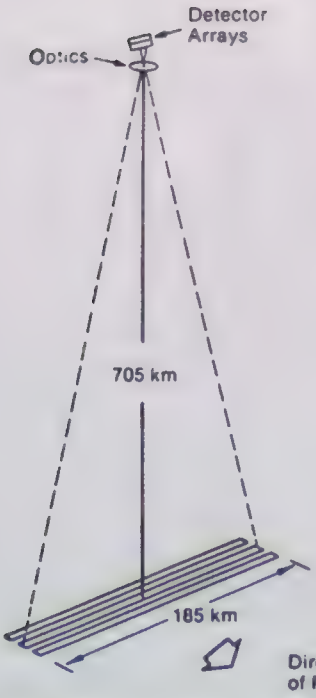

(b) Satellite pushbroom scanning technique.

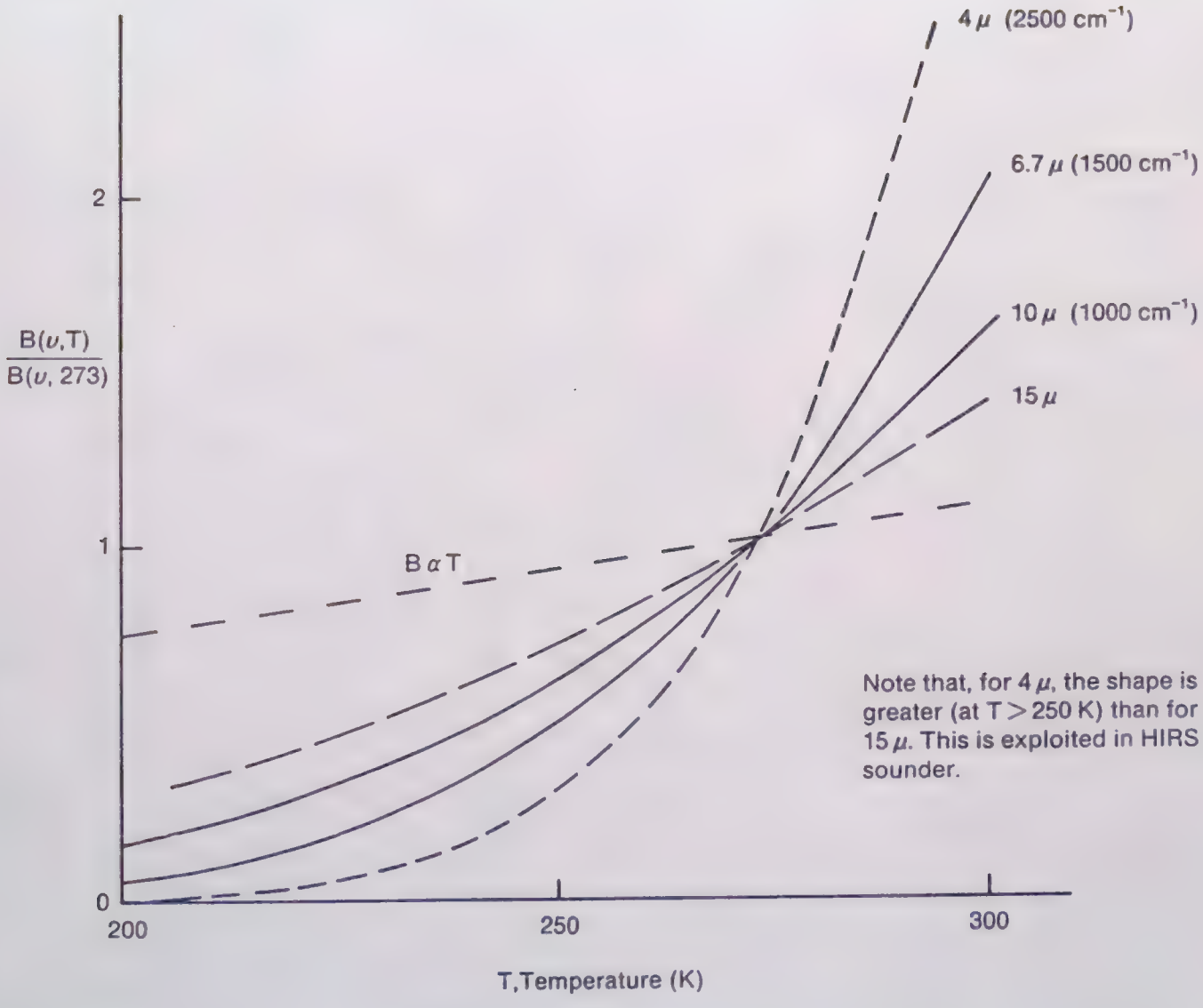

Figure 5 Temperature dependence of Planck function.

FIGURE 6

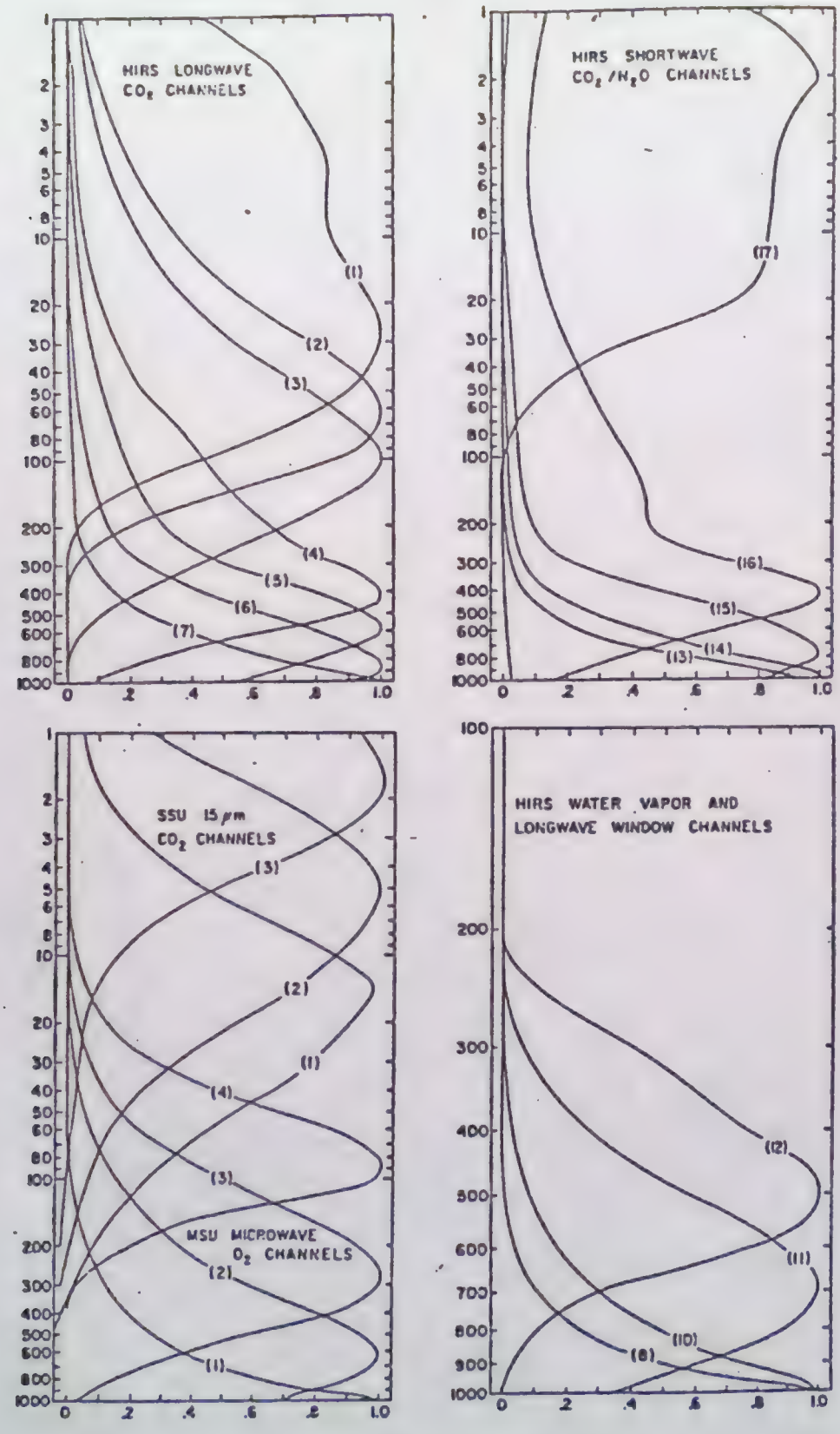

TOVS weighting functions (normalized).

FIGURE 7

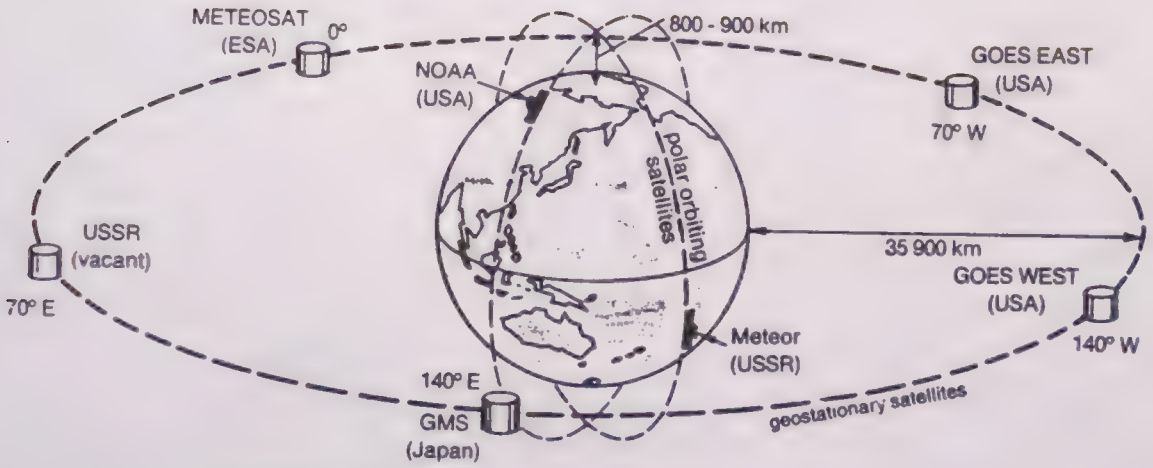

The World Weather Watch global observation satellite system.

2. RADIATIVE TRANSFER THEORY APPLIED TO SATELLITE MEASUREMENTS OF RADIATION

D R Pick Met O 19

2.1 INTRODUCTION

The radiative transfer theory applicable to the interpretation of radiation measurements made by satellite-borne instruments will be developed. The absorption, transmission and emission of monochromatic radiation by atmospheric paths containing absorbing gases will be considered and the corresponding radiative transfer equation derived. The application of this equation to satellite measurements will be presented with attention to the integration over sections of the electromagnetic spectrum required when considering a real (polychromatic) radiometer. The theory of absorption by single spectral lines will be given, and some approximations commonly used to simplify complex radiative transfer calculations will be discussed.

2.2 BASICS

2.2.1 Absorption, reflection and scattering

A beam incident on a plane opaque surface is mainly reflected back at an angle i (figure 2.1). A portion is also scattered about the reflected direction due to surface irregularities at angles different from i. A lambertian surface is when the energy is scattered uniformly within the hemisphere and is independent of i. The total energy reflected back is always less than the incident energy and can be frequency dependent. The difference between the incident energy and the total

energy reflected (specular plus scattered) is said to have been absorbed. The ratio of specular + reflected to the incident energy is called the albedo. If all the incident energy is absorbed, the surface is said to be black.

2.2.2 Emission, Planck's radiation equation

For a black body, Planck deduced that the spectral flux as a function of the temperature of the black body was given by :

$$B_\lambda = C_1 \cdot \lambda^{-5} \cdot (\exp(C_2/(\lambda.T))-1)^{-1} \quad \ldots 2.1$$

where C1 = 3.742×10^{-16} W m^2

C2 = 1.439×10^{-2} mK

λ = wavelength m

T = Temperature K

(Note B_λ is the energy over the hemisphere divide by π to give value per steradian)

Figure 2.2 illustrates the Planck function for two different temperatures 6000 K , the sun, and 270 K, the 'earth'. Note the areas have been normalised so that the energy flux is the same (i.e the sun is a long way away and subtends a small angle). The peak wavelength can be found from the Wein displacement expression:

$$\lambda_{max} \cdot T = 2.8978 \times 10^{-3} \text{ m K} \quad \ldots 2.2$$

The spectrum is divided up into regions shown in the following table

Table of spectral regions

name	range		usual units
	Hz		
Ultra violet	10^{15} - 2.10^{16}	.375-.0117μm	nm, μm
visible	~6.10^{14}	.75 - .375μm	nm, μm
infrared	~10^{11} -~10^{10}	1000 - .75μm	μm, cm^{-1}
mm) micro-	10^12 - 4^{10}	.1- 8 mm	mm, GHz
cm) wave	10^9 -4.10^{10}	30 - .8 cm	cm, GHz/MHz
radio	-10^9	- 30 cm	m/dm/km MHz,kHz

Since black bodies do not exist the expression given in 2.1 is scaled by a factor ε_λ, 'emissivity' , to cope with 'grey bodies'. ε_λ is always less than 1. The wavelength dependence of ε is crucial in determining thermal balance particularly when considering sunlight effects.

2.2.3 Kirchoff's law

Kirchoff's law states that the emissivity is equal to the absorptivity. (This can be shown on thermodynamic grounds e.g. Penner 1959).

2.2.4 Typical values

Aluminium has a reflectivity of ~0.95 almost independent of wavelength, and hence an emissivity of ~0.05. Gold has a reflectivity of ~ 0.9 in the blue end of the spectrum but up to 0.97 in the near I R. Hence it will heat up in sunlight. 'White paints' usually have an effective infrared emissivity

of ~ 0.9 with quite high scattering in the visible, i.e. an albedo of > ~ 0.5; hence objects painted white will tend to run cold in sunlight. Dielectrics have a more complicated behaviour. Figure 2.3 shows the reflective properties of sea water in the microwave region. Of note is the differing value with angle and with orientation of polarisation vector within the plane containing the normal, incident beam and reflected beam. An added complication is that the surface is disturbed by wind. Below ~ 7 m/s this causes random surface undulations over finite areas with associated scattering effects. Above 7 m/s the onset of foam is found, which is effectively black in the microwave region.

2.3 GASEOUS ABSORPTION

2.3.1 Vibrational and Rotational Spectra

The classic work is the set of three volumes by Herzberg (1945, 1950, 1966)

2.2.1.1 Diatomic Molecules. A diatomic molecule can be represented by a potential well diagram see figure 2.4. This diagram represents the bond energy as a function of the interatomic separation. A set of discrete almost equally spaced energy levels are allowed. Assume the atoms are at a separation of a' and stationary (figure 2.4). This is unstable and the atoms will tend to close together, converting potential energy into kinetic energy by accelerating towards b the potential energy minimum and overshooting to a. Hence the molecule vibrates between a and a'. Transitions are usually allowed between these different 'allowed' energy levels

through photon emission or absorption. If the excitation energy is near or less than kT (where k is the Boltzman's constant, T temperature K; at 290 K kT ≈ 200 cm^{-1}) photon-less collision induced transmissions can occur. De-excitation of vibrational energy into translational motion is called quenching. As a consequence of requiring an energy 'match' for vibrational energy transitions solar radiation which has a relatively high kT value tends to cause electronic level excitation or break up of the molecule (photo chemistry).

The rotation of the molecule is also quantized with a separation of the form J(J+1)B where J is the rotational quantum number and B is related to the moment of inertia of the molecule. Transitions of $\Delta J = 0$ (Q branch), +1 (P lines) and -1 (R branch) are allowed. The energy distribution among these allowed levels usually follows a Boltzman distribution given by $(2J+1)(\exp-(B.J.(J+1)/kT))$. An idealised band (e.g. NO) is shown in figure 2.5. The usual unit is cm^{-1} since differences in line positions are linearly related to energy.

The main atmospheric diatomic constituents (O_2 and N_2) do not have 'active' infrared systems, although they of course have quantised vibrational levels. This is because they do not have a dipole moment. However they do play a role in the heat exchange in the atmosphere through the quenching process mentioned above. Oxygen also has a microwave band at 50 - 60 GHz and a strong line at 118 GHz which are of importance for remote sensing if not for the heat balance of the atmosphere.

2.3.1.2 Triatomic Molecules. The triatomic molecules H_2O, CO_2 and O_3 dominate the gaseous component of the atmospheric

spectra in the thermal part of the spectrum. While the diatomic molecules have only one vibrational mode (along the axis joining the molecules) the triatomic molecules have three normal vibrational modes, which with combinations of transitions give a large number of bands. For CO_2 the bands at 4.3 μm (ν_3, no Q branch), and at 15 μm (ν_2, with Q branch) are the most important for sounding and atmospheric heat balance. The two H_2O bands at 2.7 μm and 6.3 μm (no Q branch) and ozone at 9.6μm are also important. The weak ozone band at 14 μm is an important contaminant of the 15 μm CO_2 band used for temperature sounding.

2.3.1.3 Quadratomic Molecules. Methane is the only molecule of significance for radiative transfer in the four atom class. Only two of its four normal vibration modes (and their combinations) are active.

2.3.2 Line Widths

So far the lines have been considered to be monochromatic, however there are several broadening effects.

2.3.2.1 Natural Width. The natural line shape is determined by the fact that the emission of a photon is a finite time process. Assuming no other sources of perturbation then Heisenberg's uncertainty principle can be used. The expression is $\Delta\tau.\Delta E = h/2\pi$ where $\Delta\tau$ is the life time of the energy state ~ 10^{-3}, ΔE the consequential energy uncertainty ~ 10^{-8} cm^{-1}, and h is Planck's constant). Other perturbing process collisions and random thermal motions swamp this width.

2.3.2.2 The Doppler Width. Molecules are moving around with a Maxwellian velocity distribution. The radial component of the motion (the 'radius' is the vector direction between the emitter and observer) causes a Doppler shift of the emitted radiation. Hence the emission consists of a series of naturally broadened lines, where each line is Doppler shifted in frequency. The number distribution as a function of frequency is Gaussian in shape and is directly related to the Gaussian distribution of velocities appropriate to the kinetic temperature of the emitting molecules. The line shape is given by (e.g Kondratoyev 1965):

$$k_\nu = S \cdot \exp-((\nu-\nu_o)^2/\alpha_D^2))/(\sqrt{\pi}.\alpha_D) \quad \ldots 2.3$$

and

$$\alpha_D = \nu_o/c.\sqrt{(2.k.T.\ln(2)/m)} \quad \ldots 2.4$$

where

S = Line strength

ν_o = line centre (unshifted)

α_D = ½ width of line between ½ absorption points

m = actual mass of the molecule

k = Boltzman's constant

T = Temperature

c = velocity of light

Putting numbers in for CO_2 at 270 K and for the 667 cm^{-1} (14.7 μm) gives $\alpha_D = 6.10^{-4}$ cm^{-1}.

2.3.2.3 Lorentz / pressure broadening. This line broadening is induced by the perturbation of the energy life time by

collisions. The effect is pressure dependent and is collision partner dependent, in that identical molecules or molecules with matching energy levels are more efficient in broadening than are none 'resonant' type collisions. The shape factor has the form:

$$k_\nu = S \cdot \alpha_L/(\pi((\nu-\nu_o)^2)+\alpha_L^2)) \quad \ldots 2.5$$

where

α_L = Lorentz line width and is linear in pressure

Typically $\alpha_L \simeq 0.1$ to 0.01 cm^{-1} at standard atmospheric pressure. Hence the line shape model is predominantly Doppler in the higher stratosphere and above and Lorentz in the lower atmosphere.

2.3.2.4 Voigt / composite line shape. Since the Doppler line shape falls off exponentially with $(\nu-\nu_o)^2$, while the Lorentz shape falls off more slowly, line centres in the stratosphere are dominated by Doppler broadening while the wings of the line are Lorentz. The Voigt line shape goes asymptotically to both Doppler and Lorentz for the different limits.

2.3.3 Transmission and Equivalent Width

The quantity usually measured is the transmission τ_ν given by $\exp(-k_\nu.a)$ where a is the absorber amount. The absorption $A_\nu = 1 - \tau_\nu$ is also used. The expression $W = \int_o^\infty(1-\tau_\nu)d\nu$ is called the equivalent width and is the 'width' of the equivalent rectangular line which is completely blacked out. It is a useful concept for estimating energy contributions since in general the Planck function is slowly varying over the main contributions to the integral. I.e the flux is given

by $W.B_{\bar{\nu}}(T)$. Also W as measured by a spectrometer is independent of the slit width. The variation of equivalent width with absorber amount is the curve of growth. For low absorber amounts the curve of growth is linear. This is the weak region and the absorber is partially transparent at all frequencies. In the weak region W is also independent of pressure. Further up the curve the dependence becomes proportional to $\sqrt{pa}$. This happens when parts of the spectrum become blackened out (opaque) and in these regions the absorption is of course independent of further increase in amount and it is the wing absorption only that is increasing. Similarly the wing absorption can be increased by increase in pressure. See figure 2.6.

2.3.4 Band Models and Curtis Godson approximation

Band models are used to reduce the computational load involved in doing repeated line by line calculations for slightly differing conditions, (e.g. atmospheric attenuation calculations relating satellite observations to temperature fields.) Figure 2.7 illustrates 'before' and 'after'. A model sometimes used is the Goody random model. This was derived (Goody 1964) assuming random line positions and strengths. It can be written in the form

$$\bar{\tau}_{\nu} = \exp-(a_1/a^2 + a_2/u)^{-\frac{1}{2}} \quad \ldots 2.6$$

where

$$a_1 = (\Sigma_i/\Delta\nu)^{-2} \quad \ldots 2.7$$

and $$a_2 = (2.\Sigma\sqrt{S_i\alpha_o}/\Delta\nu)^{-2} \quad \ldots 2.8$$

where

Σ is summation over the spectral interval

$\Delta\nu$ the spectral interval width

S_i the strength of the i th line

α_o the line width at pressure p_o

a is the absorber amount

$u = \int p/p_o.da$ over the path. (This is the Curtis Godson approximation for inhomogeneous paths.

The model has two asymptotic solutions. For 'a' small the first term dominates and $\bar{\tau} \equiv \exp - (\Sigma/\Delta\nu.a)$. Now W the equivalent width $= 1 - \Delta\nu.\bar{\tau}_\nu$ hence $W \equiv \Sigma S.a$ the linear case. Similarly it can be shown that for large 'a' then $W \equiv 2\Sigma\sqrt{S\alpha_o}(a.p/p_o)^{-\frac{1}{2}}$. This is the strong limit. The model fits reasonably well over ~ 10 cm^{-1} steps for CO_2, O_3, and H_2O, but experimental values of a_1 and a_2 do not always agree with the expected values of a_1 and a_2 derived from quantum mechanical calculations. In practice this approach has been over taken by the work of Mcmillin, Fleming and Hill (1976, 1977 and 1979) who tailored an interpolation technique matched to the needs of atmospheric sounding. Their starting point is complete line by line calculations for a set of 19 atmospheres at 1 cm^{-1} intervals.

2.4 LOCAL THERMODYNAMICAL EQUILIBRIUM

The concept of Local Thermodynamical Equilibrium (LTE) is used to relate the various energy distributions to a common Temperature. I.e. the distribution of kinetic energy within the molecular motions, the distribution among rotational states and the distribution among vibrational states have the same T factor in the exp(-E'/kT) term. This requires that the radiative life time is 'long' compared to non radiative

redistribution of energy through collision process (quenching). LTE generally holds up to 45 -50 km; above this altitude care has to be taken. The best example of the breakdown of LTE is with the 4.3 band of CO_2 under sunlight conditions (originally one of the stratospheric sounding channels on HIRS).

2.5 RADIATIVE TRANSFER

2.5.1 The radiative transfer equation

Consider the layer δz shown at height z in figure 2.8a. The gaseous absorption of this layer can be calculated as discussed above to give a monochromatic value of $k_\nu . \rho_z dz$ (k_ν is the sum of the contributions at ν for all lines e.g. 2.3 or 2.5 as appropriate and other absorbers/ continuum absorption effects; ρ_z dz is the absorber amount). Hence across this layer we have;

$$\delta I_\nu = - I_\nu \, k_\nu \rho_{xn} \, \delta z$$

$$\tau_{\nu . z \to \infty} = I_\nu(\infty)/I_\nu(z) = \exp(-\int_z^\infty k_\nu . \rho_z . dz) \quad \ldots 2.9$$

where

$\tau_{\nu . z \to \infty}$ is the transmission from z to 'space'

By Kirchoff's law this term is also the layer emissivity. This layer emission passes up through the atmosphere with a transmission given by 2.9 (see figure 2.8b). The emission reaching the top of the atmosphere in a solid angle $d\Omega$ can be written as:

$$dE_z = (d\Omega/\pi)(k_\nu . \rho_z . dz) B_\nu(T_z) \tau_{\nu . z \to \infty}$$

$$= B_\nu . (\delta\tau/\delta z) . dz . (d\Omega/\pi) \quad \ldots 2.10$$

This equation must be integrated from the surface to the top of the atmosphere to give the complete upward emitted energy

reaching space. There are two further complications. Emission from the surface at z=0 can reach space and if the ground is not black then an upward contribution can be obtained from reflected downward propogation of energy. This gives the complete expression:

$$R_\nu(\Theta) = R_\nu^{\uparrow}(\Theta) + \tau_o(\nu,\Theta).\left\{ \varepsilon(\nu,\Theta,s).B(\nu,T_s) + (1-\varepsilon(\nu,\Theta,s)).R_\nu^{\downarrow}(\Theta) \right\} \quad \ldots 2.11$$

$$R_\nu^{\uparrow}(\Theta) = \int_{z=0}^{\infty} B(\nu,T_z).\frac{\delta\tau^{\uparrow}(\nu,\Theta,z)}{\delta z}dz \quad \ldots 2.12$$

$$R_\nu^{\downarrow}(\Theta) = \int_{z=0}^{\infty} B(\nu,T_z).\frac{\delta\tau^{\downarrow}(\nu,\Theta,z)}{\delta z}dz \quad \ldots 2.13$$

where the terms are

$R_\nu(\Theta)$ Energy reaching a satellite radiometer at

ν frequency (GHz) and

Θ viewing angle

$R_\nu^{\uparrow}(\Theta)$ is the component due to upward atmospheric emission

$\tau_o(\nu,\Theta)$ is the transmission from the ground to space

$\varepsilon(\nu,\Theta,s)$ is the surface emissivity

$B(\nu,T_s)$ is the Planck function for

T_s the surface temperature

$R_\nu^{\downarrow}(\Theta)$ the downward atmospheric emission term

$B(\nu,T_z)$ the Planck function appropriate to level z

T_z the temperature at layer z

$\tau^{\uparrow}(\nu,\Theta,z)$ the transmission from layer z to space

$\tau^{\downarrow}(\nu,\Theta,z)$ the transmission from layer z to the surface

Measurements of $R_\nu(\Theta)$ can be made from above using radiometers mounted on spacecraft. How this is done and the rôle of the Meteorological Office are the topic of the third lecture and the mathematics behind inverting this equation to recover Tz and relative humidity profiles are covered in later lectures (4 and 5) in this series. Here a more qualitative description will be given.

2.5.2 Weighting function

The atmospheric temperature profile T_z appears in equation 2.11 through the term $B(\nu,T_z)$. Consider initially those regions for which $\tau_o(\nu,\Theta)$ is less than 10^{-3}, i.e. the surface term and the reflected term do not significantly contribute to

$R_\nu(\theta)$. The behaviour of τ and $\delta\tau/\delta z$ is illustrated in figure 2.9. This figure illustrates, in combination with equation 2.12, that in the case under consideration, only over a restricted range of heights does thermal emission contribute significantly to $R^{\uparrow}$ with a peak occurring at the $\tau = 0.5$. The function $\delta\tau/\delta z$ or $\delta\tau/\delta\ln(p)$ is usually referred to as the weighting function. In the near infrared spectral regions (e.g 3 - 6 μm) the rapid change of $B_\nu(T)$ with height makes a plot of $B(\nu,T_z).\delta\tau/\delta z$ more appropriate in deciding on the level contributions. Also illustrated is the height shift with change in k. Hence if a measurement is non-monochromatic (range of ν and therefore non constant k) then the weighting function is broader than the basic weighting function. The usual rule of thumb in allowable degradation is about 10 in width. If the initial constraint on τ_o is relaxed then the surface emission contributes and if τ_o can be corrected for/and or is small then we have a window channel and surface temperature can be measured. In the microwave region over the sea the value of ε is about 0.6 hence $R^{\downarrow}$ can contribute by reflection at the surface. This has the effect of sharpening the weighting function in the bottom layers of the atmosphere (though care is needed to correctly deal with the variation in surface emission with wind speed. The use of weighting function plots is primarily as a diagnostic tool through providing a visual indication of where in the atmosphere the energy is primarily coming from. Most retrieval theories use linear combination of channels in deriving temperature profiles. A plot of the linear combination of weighting function $\delta\tau/\delta z$ (modified by $B(\nu,T_z)$ if necessary) is a good

indicator that the coefficients relate to the layer or are relying on a possibly spurious statistical correlation with other layers when the coefficients were statistically derived.

2.6 SPECTRAL CHOICE

Figure 2.10 is an example of the spectrum of emission of the atmosphere as viewed from space in the infrared. Figure 2.11 is a plot of the atmospheric transmission from the surface separated into the different contributions due to the absorbing molecules. While figure 2.12 shows the microwave spectrum. Figure 2.10 well illustrates how the energy follows the 'temperature' profile with increasing absorption, e.g. from the surface in the window region at 800 cm^{-1} up the CO_2 P branch towards the Q branch at 667 cm^{-1}. The strongest absorption feature at the centre of the Q branch is monitoring in the upper stratosphere where the temperature has started to rise again. Spectral regions of this band can be selected by infrared filters and the prime infrared sounder HIRS is based on this approach. In the microwave spectrum, the region at 50 to 60 GHz is used for temperature sounding and there are feasibility studies on the use of the 118 Ghz Oxygen line for temperature sounding from Geostationary orbit. The more detailed aspects of instrument design and channel selection are covered in the next lecture.

2.7 REFERENCES

McMillin L.M, Fleming H.E., 1976 'Atmospheric transmittance of an absorbing gas. A computationally fast and accurate transmittance model for paths with constant mixing ratio, in

inhomogeneous atmospheres.' Applied Optics 15 pp 358-363.

Fleming H.E McMillin L 1977 'Atmospheric transmittance of an absorbing gas 2: A computationally fast and accurate transmittance model for slant paths at different zenith angles' Applied Optics 16 pp 1366-1370

McMillin L.M, Fleming H.E and Hill M.L 1979 'Atmospheric transmittance of an absorbing gas 3: A computationally fast and accurate transmittance model for gases with variable mixing ratios' Applied Optics 18 pp 1600-1606

2.8 BIBLIOGRAPHY

Goody R M 1964 'Atmospheric Radiation' Oxford Clarendon Press

Herzberg G 1945 'Molecular Spectra and Molecular Structure II IR and Raman' van Nostrand

Herzberg G 1950 'Molecular Spectra and Molecular Structure I Diatomic molecules' van Nostrand

Herzberg G 1966 'Molecular Spectra and Molecular Structure III Electronic Structure of Polyatomic Molecules.' van Nostrand.

Penner S S 1959 'Quantitative Molecular Spectroscopy and gas Emission' Pergamon Press.

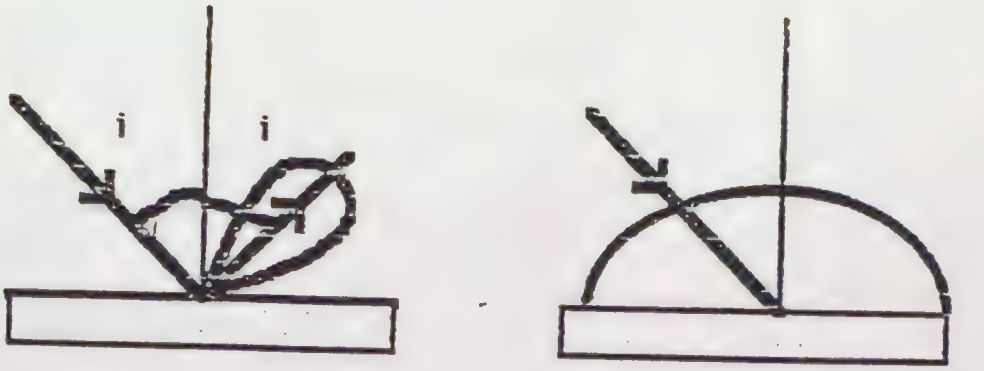

Figure 2.1 Reflection and scattering.

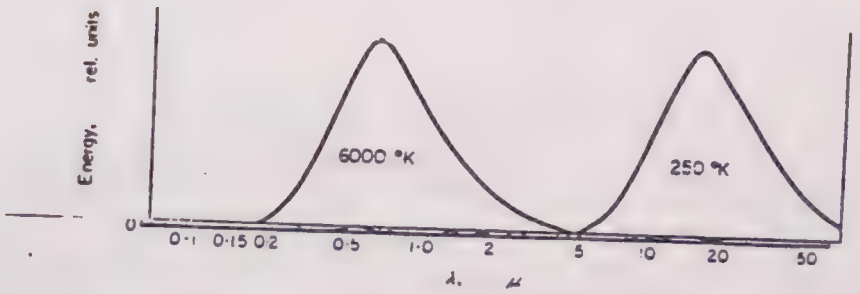

Figure 2.2 Illustrating the energy distribution for Black bodies at 6000K (the sun) and 250K(the thermal equilibrium temperature of the earth) (Note the areas under the curve are approximately equal to allow for the sun earth distance and the sun's effective diameter)

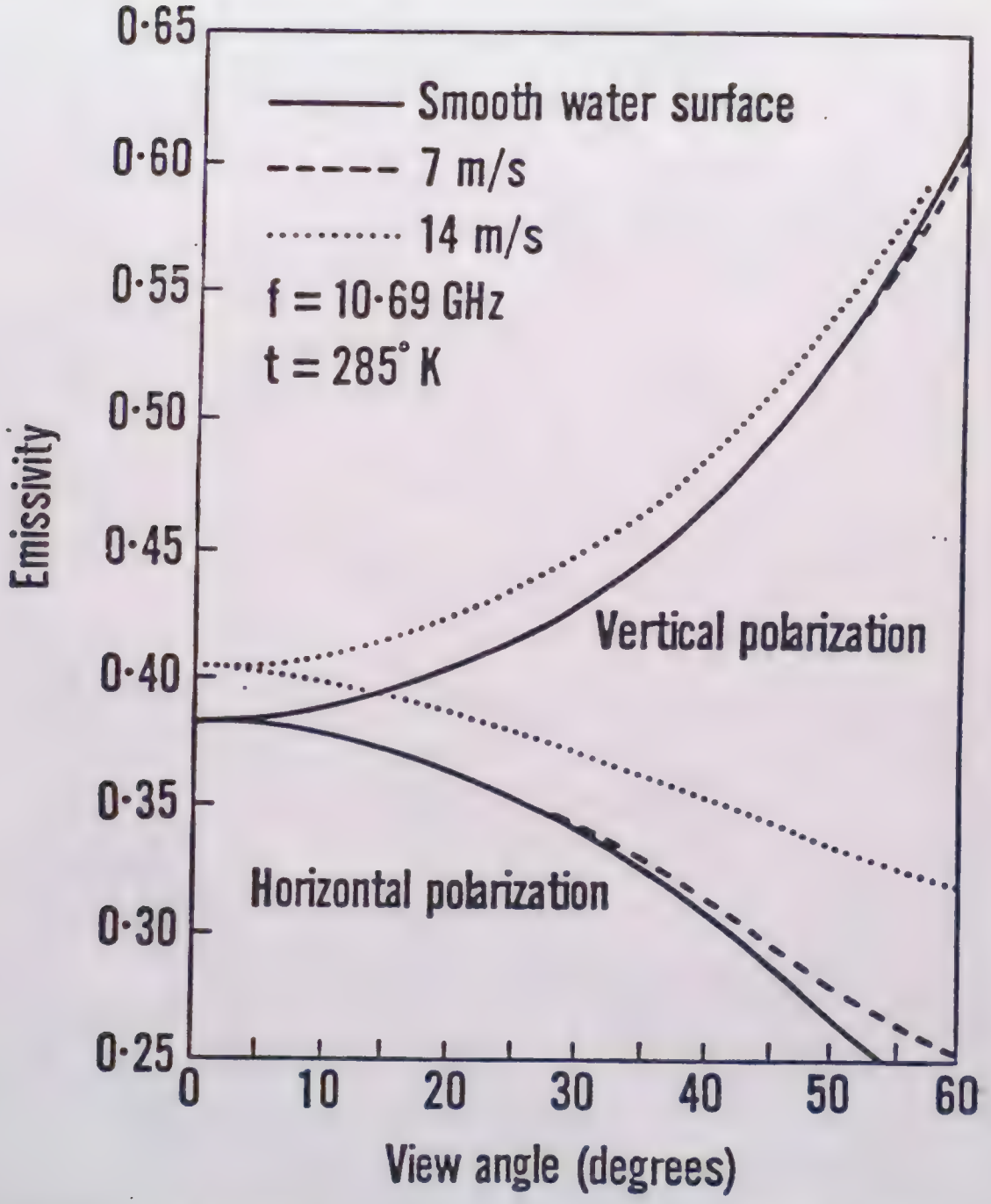

FIGURE 23 Emissivity as a function of view angle for a smooth water surface and for the ocean surface with 7- and 14-m/s wind speed.

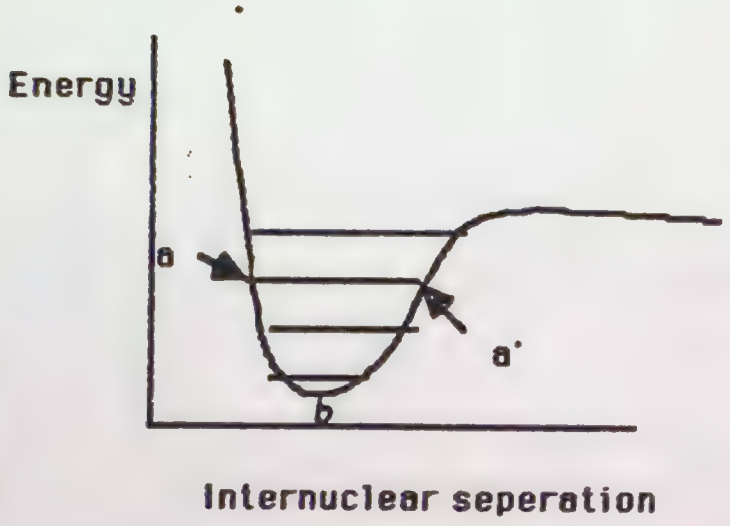

Figure 2.4 Potential Well diagram for a diatomic molecule

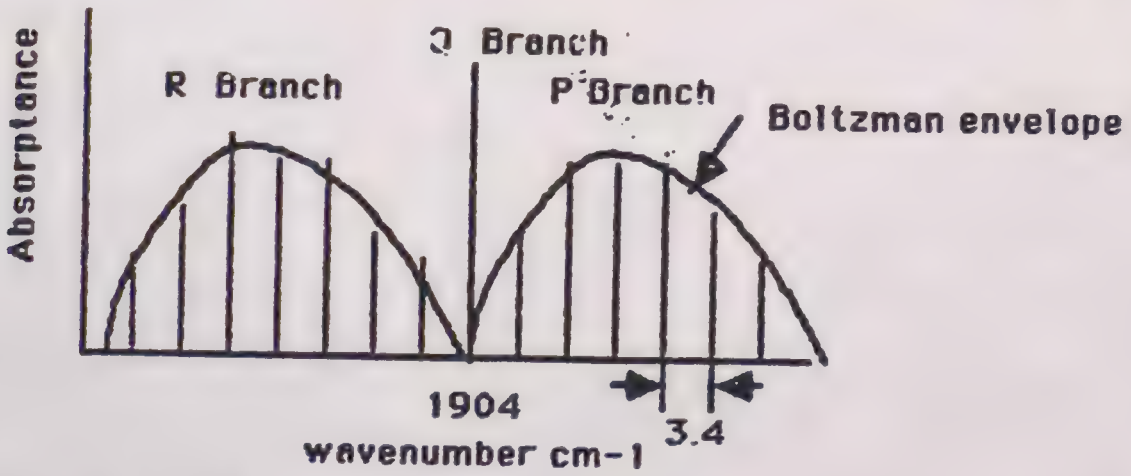

Figure 2.5 Example of the rotational energy distribution for NO

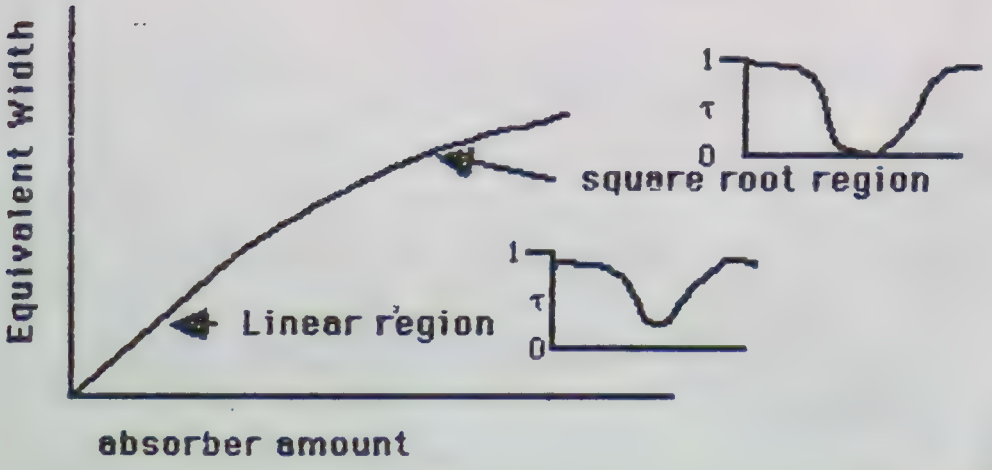

Figure 2.6 Curve of Growth showing linear and square root region

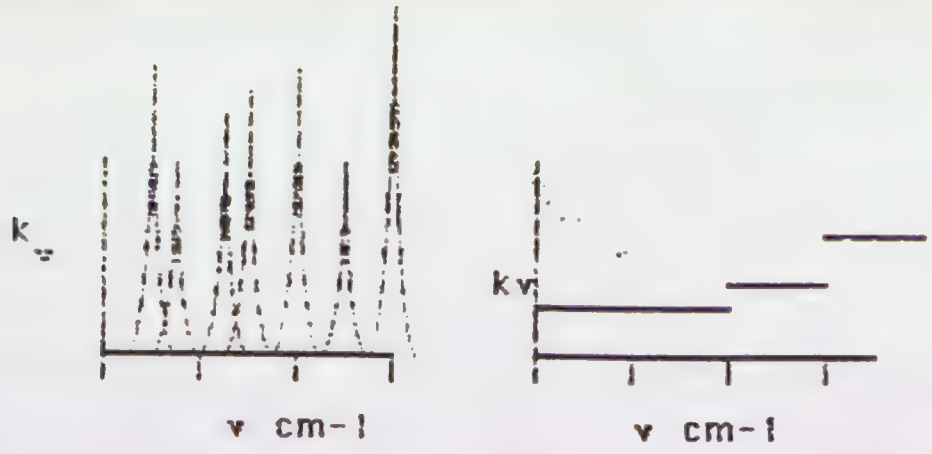

Figure 2.7 Illustrating the use of a band model

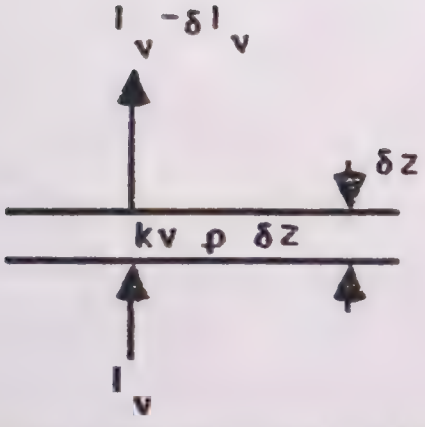

Figure 2.8a absorption by a layer

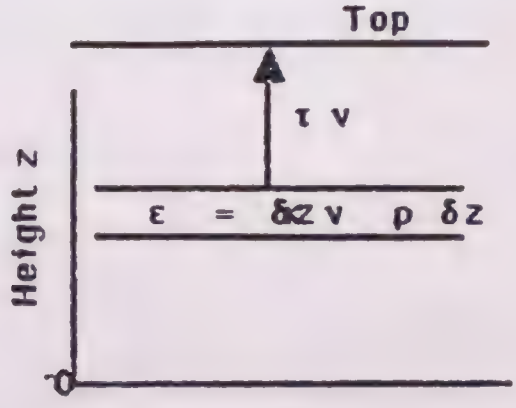

Figure 2.8b radiative transfer through a layer

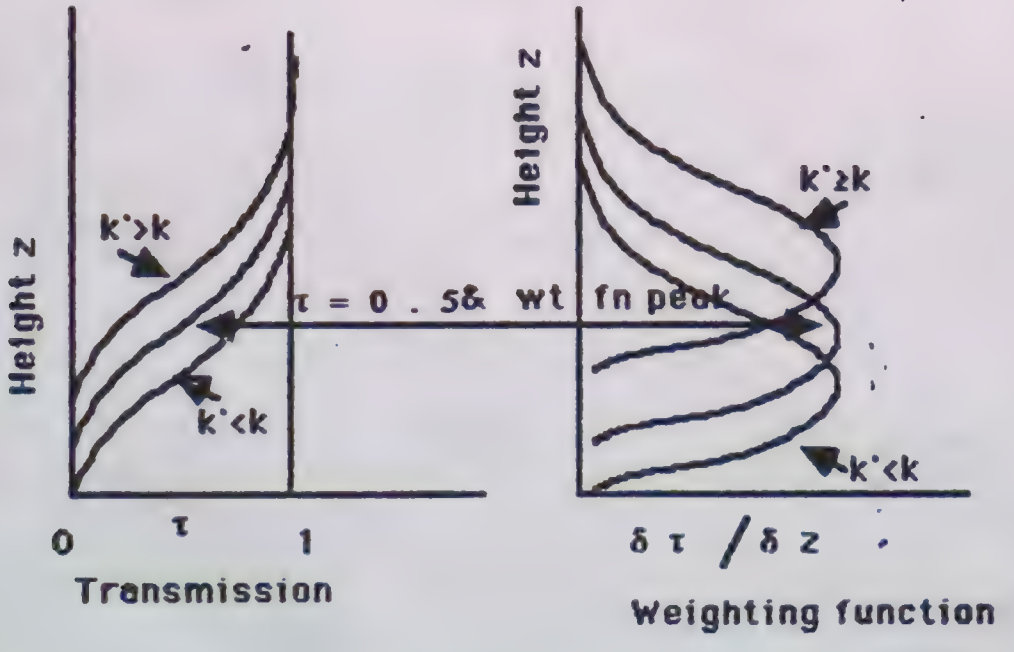

Figure 2.9 Sketches of transmission and weighting function with height in the atmosphere also shown is the dependence on k the absortion coefficient

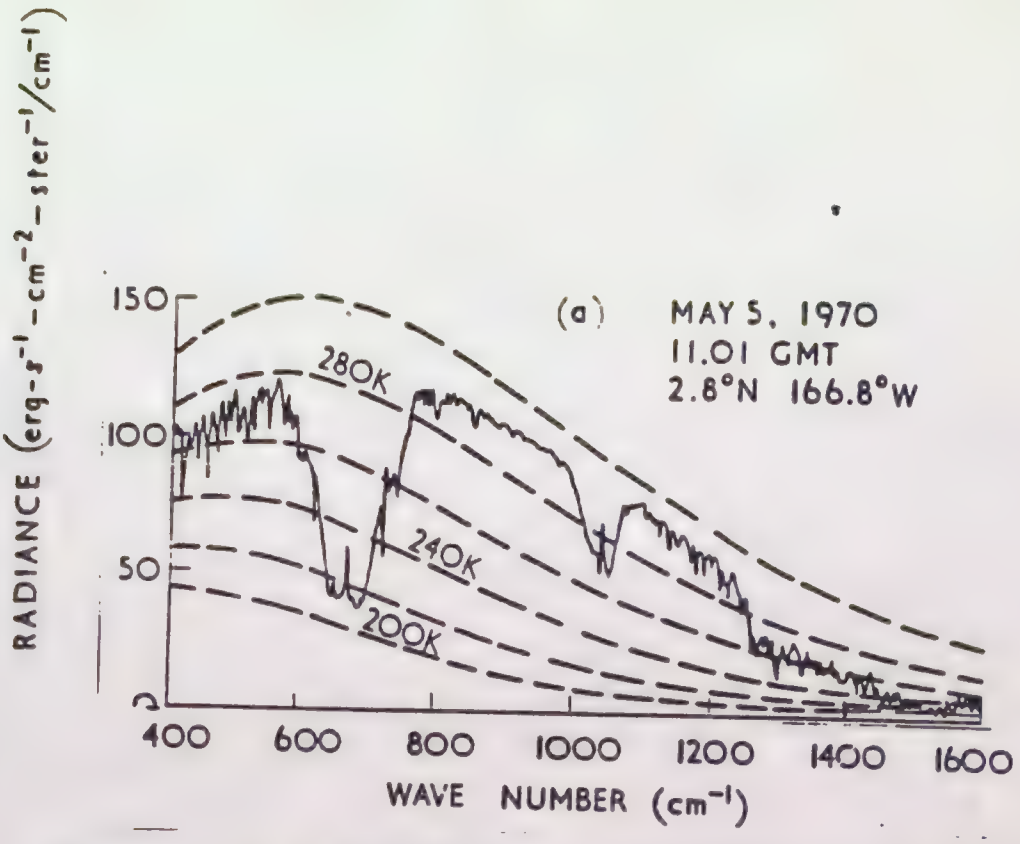

Figure 2.10 An example of an atmospheric spectrum as viewed from space (Hanel GSFC)

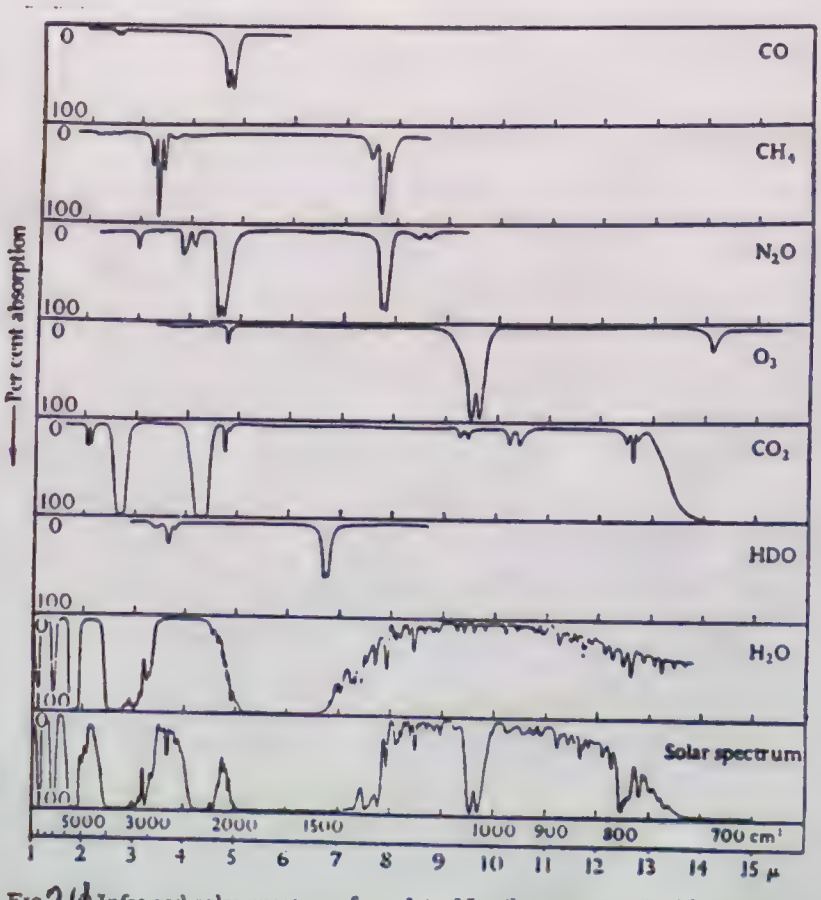

FIG 2.8 Infra-red solar spectrum from 1 to 15 μ (bottom curve) with positions and relative intensities of absorption bands due to known atmospheric constituents shown on the other curves (after J. H. Shaw).

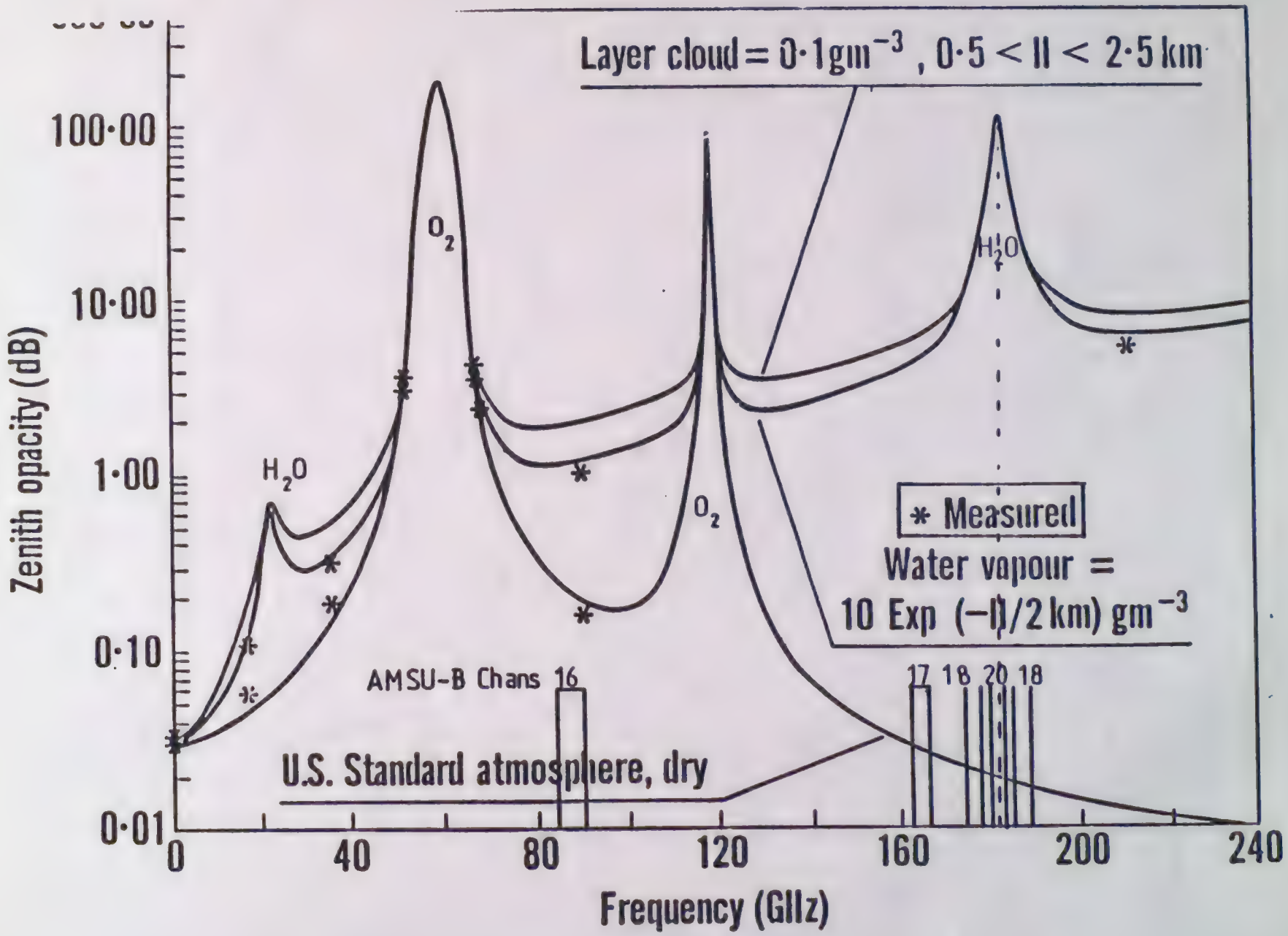

FIGURE 2.12 Calculated zenith opacity

MSSM/VG6
DO 3586

3. THE OFFICE'S CONTRIBUTION TO SATELLITE INSTRUMENTATION

D R Pick Met O 19

3.1 INTRODUCTION

The Satellite Meteorology Branch is directly involved in the design and provision of satellite instruments. The Stratospheric Sounding Unit (SSU) has been developed and tested. Eight units have been made and are being flown on the current TIROS-N series. Work on the next major instrument, the Advanced Microwave Sounding Unit -B (AMSU-B) is under way; this unit, which is expected to be operating in 1992, will primarily measure tropospheric water vapour. The Rutherford Appleton Laboratory (RAL) are developing a new instrument - The Along the Track Scanning Radiometer - to measure sea surface temperature with improved accuracy. This lecture will review some of the design aspects and scientific testing needed to ensure that the observations can be interpreted in terms of geophysical parameters.

3.2 BASICS

In lecture 2 the basic radiative transfer equation was derived and was written as:

$$R_\nu(\Theta) = R_\nu^{\uparrow}(\Theta) + \tau_o(\nu,\Theta).\left\{ \begin{array}{l} \varepsilon(\nu,\Theta,s).B(\nu,T_s) + \\ (1-\varepsilon(\nu,\Theta,s)).R_\nu^{\downarrow}(\Theta) \end{array} \right\} \quad \ldots 3.1$$

where the terms are

$R_\nu(\Theta)$	Energy reaching a satellite radiometer at
ν	frequency (GHz) and
Θ	viewing angle
$R_\nu^\uparrow(\Theta)$	is the component due to upward emission
$\tau_o(\nu,\Theta)$	is the transmission from the ground to space
$\varepsilon(\nu,\Theta,s)$	is the surface emissivity
$B(\nu,T_s)$	is the Planck function for
T_s	the surface temperature
$R_\nu^\downarrow(\Theta)$	the downward atmospheric emission term
$B(\nu,T_z)$	the Planck function appropriate to level z
T_z	the temperature at layer z
$\tau^\uparrow(\nu,\Theta,z)$	the transmission from layer z to space
$\tau^\downarrow(\nu,\Theta,z)$	the transmission from layer z to the surface

The following sections are concerned with the practical measurement of the radiation incident on a satellite radiometer, how the spectral response of such a radiometer is determined and how some of the spectroscopy included in equation 3.1 is experimentally verified. The discussion is illustrated by those instruments in which the Meteorological Office has an active role viz. the Stratospheric Sounding Unit (SSU), the Advanced Microwave Sounding Unit - B (AMSU-B) and the Along the Track Scanning Radiometer (ATSR).

3.2.1 Infrared Radiometry

The energy in the ith channel reaching a detector in a radiometer is given by:

$$R_i(\phi) = \int_\nu \tau_i(\nu) . \int_\phi \int G_i(\theta,\psi) . A_i . R_\nu(\theta,\psi) . d\nu . d\theta . d\psi \quad \ldots \quad 3.2$$

where $\tau_i(\nu)$ = the spectral response of the i th channel

$G_i(\phi,\psi)$ = the angular response of the viewing telescope about scan angle ϕ

A_i = the appropriate area for the input telescope

$R_\nu(\theta,\psi)$ = Equation 3.1 for the scan angle ϕ.

The spatial resolving power (or viewing pixel area) is given by $\int\int_\phi G_i(\theta,\psi).d\theta.d\psi=\Omega.(\text{Radiometer height})^2$. The product $A\Omega$ is a basic parameter for a radiometer since ideally $A\Omega$ is conserved during passage of radiation through an optical system. Loss due to optical aberrations and diffraction effects are usually included in the τ term. For a 'small' external field of view 3.2 can be simplified to give:

$$R_i(\phi) = A.\Omega_i.\int\tau_i(\nu).R_\nu(\phi).d\nu \quad \ldots 3.3$$

The trade-off loop logic can now be seen as follows:

Flow	Comment
Channel Purpose	Sounding, window etc
↓	
→ Choose spectral region	Infrared, microwave, visible
↓	
Choose detector type	e.g uncooled thermal, cooled photo-diode, heterodyne receiver etc.
↓	
Potential performance	≡ ΔR at detector, depends inter alia on sample measurement time
↓	
Pixel size required (Ω)	atmospheric structure
↓	
Practical telescope size (A)	space craft constraints
↓	
$\tau_i(\nu)$	defines weighting function width or transparency of window
↓	
no— Useful performance?	
↓	
Yes	
↓	
Next channel	

The potential channel performance is then usually given in

terms of NER (noise equivalent radiance at the input) or NET_T (noise equivalent temperature at the input for a scene brightness temperature of T). The A term has been scaled out. Typical NET performance requirements per pixel are in the range 0.1K for sea surface temperature mapping to < 1 K for atmospheric temperature sounding.

The absolute accuracy of the measurement of radiation is also required to a similar level (~¼K). Current radiometer design is such that this requirement can only be met by providing an inflight calibration system and such a system must encompass as much of the optical system as is economically possible. Such an inflight calibration system can consist of an 'ambient' target and space (SSU, AMSU-B) or two calibration targets at different temperatures (ATSR). Any inaccuracy in this calibration system or scan dependent errors are quantified by vacuum chamber tests before launch.

3.2.2 Microwave Radiometry

Microwave radiometers are subject to similar guidelines with two notable exceptions. The radiometer is usually constructed as a superheterodyne system with a power measurement being made using a diode on the shifted frequency. The other exception is that $A\Omega$ cannot be decoupled into a separate choice of A and Ω. This is because the external acceptance solid angle Ω is primarily determined by diffraction considerations of the radiation field of area A, since the wavelength of the radiation is comparable with the dimensions of A.

3.2.3 Spectroscopic Considerations

Besides $A\Omega$ the other important term is $\tau_i(\nu)$. The quantity $W_i = \int \tau_i(\nu).d\nu$ usually expressed in cm^{-1} is called the (spectral) equivalent width. The energy reaching the radiometer detecting system is linear in this term. However as discussed in lecture 2 an increase in W, while improving the signal to noise ratio or NET usually leads to an increase spread of the weighting function. This happens when such an increase causes an increase in the distribution of absorption coefficients accepted by the radiometer channel.

Current infrared systems used for temperature sounding eg HIRS on the TIROS-N series of weather satellites use narrow band (9-10 cm^{-1}) multilayer filters to define the spectral regions required. Such a filter contains many lines leading to broadening of the weighting function. State of the art filters can achieve ~3 cm^{-1} with $\tau \sim 0.6$ (c.f. 10 cm^{-1} $\tau \sim 0.9$) with a factor of 5 loss in NET. The SSU described below partially overcomes this problem by using a selective filtering technique. A dramatic improvement in spectral resolution in the infrared needs either a grating system or an interferometer system. Such a spectrometer has been proposed for the TIROS-N by Kaplan and Chahine and is called the Advanced Meteorological Temperature Sounder (AMTS). This spectrometer is however about 5-10 times bigger than HIRS and consumes all the available spacecraft power and is not likely to be flown in the next decade. A more practical interferometer system has been proposed for the geostationary satellite by W L Smith. This 'High resolution Interferometer

Sounder (HIS)' is undergoing aircraft trials. The spectral resolution in this cases is $<.7cm^{-1}$.

3.2.4 Spacecraft Environment and Constraints

The advanced TIROS-N satellite (ATN) shown in Figure 3.1 illustrates most of the salient features of a civilian weather satellite. Electrical power is obtained from the solar panel array (when illuminated by sunlight) through the use of silicon photocells. The efficiency of this conversion process is about 3% (i.e $0.03 \times 1.4\ kW/m^2 \sim 40W/m^2$). Rechargeable batteries are used to maintain spacecraft power availability as the solar generated power varies around the orbit.

Thermal control of the spacecraft requires that a thermal balance is achieved between the input radiation sources (earth thermal radiation ($\sim$=240K), earth albedo (scattered sunlight), varying solar radiation (mainly varying due to shadowing by the earth $0 - \sim 1.4\ kW/m^2$), internally generated heat (usually electrical) and radiative heat loss from the spacecraft surfaces. Basic control for ATN is achieved through the use of a combination of surface finishes and liberal use of multilayer thermal blanket. A serious problem with the use of such blankets is their propensity to exude large quantities of water vapour especially during the first weeks in orbit. This water vapour can condense onto optical components, particularly those components whose temperature has been deliberately cooled with respect to the surrounds, with a consequential degradation in radiometric performance.

Orbital variations in radiation loading is damped to some

extent by the thermal capacity of the satellite systems. Finer control to about 1K is achieved through the use of louvre systems. Locally much finer control to ~0.01K can be achieved by electrical thermostating arrangements. Hence for example a space borne precision radiometer is designed to survive ± 40°C and to operate at 20°C with an orbital variation of about 1-2K (over 100 mins) with particularly sensitive areas controlled to ~0.01K if required. This is a more stable environment than obtained in an average laboratory and the thermal requirement is less stringent than for example a military specification.

Satellite orientation is actively controlled through servo controlled gyroscopes. Coarser control is achieved by dumping momentum through gas discharge via suitably sited nozzles.

3.2.5 Resources Needed to Design and Build a Flight Radiometer

The design and build of a radiometer for space use involves scientists and engineers with a variety of backgrounds as well as an intensive test and calibration programme. To put this activity into prospective for the SSU the resources required were:

Development model and 4 flight models employed 80 man years of effort at the contractors, cost ~£3.5m (83 prices) and involved 20 my of effort at the Met Office in monitoring the contractor, developing the science, field trials, providing the in-house calibration facility and scientifically testing the 5 SSU's.

A further 4 flight models cost £1.7m (83 prices).

3.3 THE STRATOSPHERIC SOUNDING UNIT

The Stratospheric Sounding Unit (SSU) was built by Marconi Space Defence systems for the Meteorological Office. Some 9 of these units have been built and tested. 7 have been successfully flown on the ATN spacecraft. The SSU is a self calibrating infrared radiometer sounding the temperature structure of the stratosphere through making absolute radiometric measurements of emission by atmospheric carbon dioxide in the 15μm band.

3.3.1 Spectroscopic Selection

The problem mentioned above of restricting the range of absorption values while still accepting a sufficiently wide spectral range to provide acceptable radiometric performance is solved in the SSU by using a selective chopping technique. Figure 3.2 outlines the SSU optical system. Signal modulation is provided by changing the amount of carbon dioxide in the transmission cell A shown in this figure. The effect on the radiation passing through the system is illustrated in figure 3.3 for the top channel 27. Curves A and B of figure 3.3b indicate the range of transmission values for the cell for a single carbon dioxide line in the ν_2 band at 15 μm. Cycling between these values causes selective modulation with a spectral frequency dependence given by curve C. I.e. only spectral regions from 1.10^{-3} to 6.10^{-3} cm^{-1} from the line centre are modulated for lines of this strength. The broad filter also shown in figure 3.2 limits the spectral response to lines in the 15 μm band over some 60 cm^{-1}. The equivalent width of this channel is ~0.4 cm^{-1}. Increasing the amount of

carbon dioxide gas in the cell moves the effective spectral modulation curve 'c' (figure 3.3b) away from the line centre and hence lowers the weighting function in the atmosphere.

Figure 3.4 shows the weighting functions achieved for the SSU. Curve 1 is the top channel achieved by a 3 cm^{-1} filter in HIRS using the same band of CO_2. Of note is the much better height resolution of the SSU when compared to that which can be achieved by the simple filter technique used in HIRS. However the selective chopping technique is not 'perfect'. Curve 24 in figure 3.4 illustrates the near monochromatic weighting function achieved by the Microwave Sounding Unit (MSU) on ATN. In the 1990's an Advanced Microwave Sounding Unit (AMSU) which among others will have channels with weighting functions within the range of the SSU will replace the SSU as the stratospheric sounder on the ATN spacecraft.

3.3.2 Spectroscopic Verification

In lecture 2 mention was made of the Curtis Godson approximation. This approximation allows the direct measurement of weighting functions in the laboratory using an uniform pressure path provided that for such a path and for the equivalent varying pressure path in the atmosphere the quantities $\int du$ and $\int p.du$ are matched. For CO_2 an approximate fit can be found for laboratory paths of ~10 m and a CO_2/N_2 mixing ratio of about 0.3.

Figure 3.5 outlines the system installed in a Met O 19 laboratory to make such measurements. In addition to such laboratory measurements a direct measurement of atmospheric

transmission has been made. For this measurement a high pressure cell (peak of weighting function at 15 mbar) was mounted at the output of a balloon borne sun seeker and was used to make direct measurements of solar intensity as a function of height from the ground to a balloon float altitude of 4 mbars.

Both the balloon borne experiment and the laboratory measurements demonstrated the need for small empirical corrections to the line by line theory used to calculate the atmospheric weighting function.

Account must also be taken of a weak ozone band at 14 μm. Measurements were made with ozone in the weighting function rig transmission cell. These ozone transmission measurements demonstrated that a small correction (~0.15K) is needed only in the radiance measured by channel 25 (the lowest SSU weighting function). The variation of this correction (~0.05K) with variation in atmospheric ozone is ignored for the SSU. The correction needed by a filter radiometer is much larger e.g. for HIRS the worst channel has 1 to 2 K offset where the size depends on the ozone column amount.

3.3.3 Radiometric assessment

Also shown in figure 3.5 is the 'earth' target used to verify the SSU inflight calibration. The target fills the whole scan angle of the SSU and hence tends to be rather bulky. Even from this sketch the salient features in the design of precision calibration target can be seen. The SSU views the corrugations shown on the base of the target. These

corrugations improve the blackness of a plane painted surface from ~0.95 to ~0.99 and the baffling arrangement further enhances this emissivity to ~0.998 as well as reducing the temperature gradients within the paint. Helium gas, thermostatically controlled, is vigorously pumped round the target and its baffle to minimise temperature gradients to less than 0.2K within a field of view and <~0.5K across all fields of view.

3.4 ADVANCED MICROWAVE SOUNDING UNIT-B (AMSU-B)

The next major instrument development for the ATN spacecraft is the enhancement of the present 4 channel Microwave Sounding Unit by replacement with a 20 channel Advanced Microwave sounding Unit (AMSU). Such a radiometer will have significant impact on satellite based atmospheric temperature and humidity retrievals. This is mainly through providing soundings under cloudy conditions, since the current infrared system can only provide retrievals in clear areas or in gaps between clouds and cannot probe active frontal systems. Humidity profiles near the sea surface and quantitative precipitation mapping are also some of the new products expected from AMSU. Retrievals of humidity will be discussed in lecture 4.

The channels are listed in table 3.1 and figure 3.6 shows the calculated weighting functions for the AMSU sounding channels. AMSU has been divided into two sections AMSU-A the first 15 channels and AMSU-B the channels 16 to 20. The Met Office is involved in the processes leading to the provision of the AMSU-B units.

3.4.2 Spectroscopy of AMSU-B

The AMSU channels are located in the microwave region 20 - 190 GHz. Figure 3.7 shows this part of the spectrum. There are 5 main features apparent. Features 1, 4 and 5 are isolated water vapour lines, 2 is a band of some 50 oxygen lines while 3 is an isolated oxygen line at 118 GHz (potentially a frequency that can be used for microwave temperature sounding from a geostationary satellite). AMSU-B has a channel in the window region between features 2 and 3. Here the main contribution under cloud free conditions is due to the wing effects of water vapour and a continuum term. A channel at 157 GHz and 3 channels straddling the single line at 183 GHz at differing locations down the line.

A field trial programme is already under way to experimentally test the spectroscopy of AMSU-B. Dr T Wilheit of NASA GSFC has built a down-viewing radiometer with channels similar to AMSU-B (except for the 157 GHz channel). Several flights with his radiometer mounted on an aircraft have been made. On the most recent flight the Met Office provided in situ measurements by dropping sondes in a joint exercise between Gander and 6°N. The results indicate that there is good agreement between theoretical brightness temperature calculations based on the drop sonde profile date and measured brightness temperature calculations based on the drop sonde profile data and measured brightness temperature for the channels near the strong water line but poor agreement ~10-15K difference in the window channel region at 90 GHz.

The aircraft experiment is being upgraded by the addition of

channels at 157 GHz (to simulate AMSU-B) and upward viewing channels. This will enable the Met Office to use it's Hercules to investigate the spectroscopy of the window channels in more detail through separating out the terms in equation 3.1.

The aircraft spectroscopy programme is also being supplemented by laboratory measurements. Measurements are being made at AMSU-B frequencies of the microwave properties of water in it's three phases: vapour - attenuation in a large untuned cavity with an effective path of ~ 500m; liquid - dielectric constant / reflection measurements in a small untuned cavity; ice - dielectric constant / absorption in a similar untuned cavity.

3.4.3 Radiometric Aspects

Precision radiometric calibration of a microwave radiometer present some challenging technical problems. The main problems are the lack of 'black' paint, the large field of view of AMSU-B, presence of side-lobes to this field of view and the possibility of resonant scattering (induced by standing waves set up in the calibration target cavities because of the wavelengths involved are comparable with the structuring used to enhance the basic absorption properties of a calibration target). A design consisting of a shaped metal plate coated with a suitable microwave absorber was evolved from contracts with Heriot watt University (Peckham and Suttie) and Bath University (Cronin). As AMSU-B is a heterodyne receiving system it responds to a given orientation of the polarisation vector. Because channels 16, 17 and 18

have a surface contribution and the sea reflectivity / emissivity is polarisation sensitive all AMSU-B channels have been arranged to have the same polarisation orientation sensitivity. Hence it is only necessary to make the target highly non-reflecting in one polarisation direction. In addition, any machined surfaces will behave as specular reflectors in the mm wave region (surface roughness << wavelength).

Consequently, if radiation incident on the target dielectric coating undergoes a number of reflections close to the Brewster angle for a dielectric then a high degree of attenuation will be obtained in one polarisation direction. The target, therefore, consists of a series of grooves inclined close to the Brewster angle of the microwave absorber chosen. Such a design is shown in Figure 3.8.

A similar design will be used for the external calibration targets used to verify overall system performance.

3.4.4 The AMSU-B Receiver

The AMSU-B microwave receiver is a hybrid between a conventional heterodyne receiver system and an optical receiver. The heterodyne technique is basically a frequency down converter where-by the signals received at e.g 89-91 GHz are mixed with a locally generated 90 GHz signal to move the signal frequency to the range 0-1 GHz (note frequency folding occurs!). This intermediate frequency (IF) is amplified and rectified to give the desired measurement. (Conventional radio receivers also work in this way.) Figure 3.9 shows in

practice how the 5 channels in AMSU-B have been configured. Note the quasi-optical approach. The 'quasi' qualification is because normal geometric optics design criterion do not apply when the wavelength is only an order of magnitude different from the component dimensions, and diffraction considerations are important.

Most of the elements shown in figure 3.9 exist and will be assembled into a bread board system later this year.

3.5 THE ALONG THE TRACK SCANNING RADIOMETER (ATSR)

ATSR is a sensitive infrared radiometer designed to measure sea surface temperature with an accuracy of better than ± 0.5K. This 4 channel radiometer is being designed by RAL and will fly on ERS-1 (ESA Remote-sensing Satellite number 1), with a tentative launch date of 1991. The spectral frequencies for ATSR have been chosen to be identical to those of the four channel AVHRR currently providing the operational sea surface temperature observation from the ATN spacecraft. However ATSR is expected to improve on AVHRR by viewing the same area of the earth's surface at two angles, which gives a direct measurement of the 'atmospheric correction' to be applied to the surface radiance.

Figure 3.10 shows an outline of the instrument. This will be the first civilian instrument with detectors cooled by a Stirling engine cooler. This cooler has been developed by Oxford University Engineering Department. The cooler arrangement uses the same type of pressure 'modulation' mechanics as the SSU (beefed up for the higher pressures

involved). A prototype model has been built with a heat dumping capability of ~0.5W at 75K (compared to passive coolers of 10 - 50 mW at ~100K).

The Meteorological Office's contribution to this instrument is through providing the detail design and fabrication of the focal plane assembly. The high performance required by ATSR has lead to the design shown in figure 3.11. The ultimate performance of cooled detectors is achieved when the background radiation is reduced to a low level to avoid the statistical fluctuation of the quanta from the background being the main noise source. To achieve this the entrance aperture, beam dividers (dichroic mirrors), optical filters and detectors together with some active preamplifier components need to be cooled to 80K. An engineering model has been constructed and a flight model is being assembled.

The Meteorological Office's Research Flight (MRF) is also involved in mounting an experiment on their Hercules aircraft. this experiment is designed to experimentally verify the dual angle approach of compensating for atmospheric absorption and emission effects on the sea temperature measurements.

3.6 SUMMARY

The table below lists the Met Office's involvement in space borne instrument hardware.

Space Hardware provided by the Met Office.

Unit	involvement	s/c	launch	data
SSU	all aspects	ATN	78-90	Stratospheric thickness maps 150 km resolution
AMSU-B	all aspects	ATN	92-	Maps at 15 km resolution of water vapour profiles, cloud liquid water and precipitation
ATSR	focal plane assembly design and build	ERS-1	91	sea surface temp ~2 km resolution

3.7 REFERENCES

H H Aumann and M T Chahine 1976 'Infrared multidetector spectrometer for remote sensing of temperature profiles in the presence of clouds' Applied Optics 15P p2091-2094

D L Croom 1982 'Workshop on next generation operational satellite meteorological sounding systems' RAL 2-5 Nov 1982

D E Miller, J L Brownscombe, C P Carruthers, D R Pick and K H Stewart 1980 'Operational temperature sounding of the stratosphere' Phil Trans R Soc Lond A296 p 65-71

D R Pick 1986 'The operational sounding of the lower atmosphere from satellites using millimetre waves' 16th European Microwave Conference Dublin Sept 1986.

W L Smith et al 1983 'HIS a satellite instrument to observe temperature and moisture profiles with high resolution' Amer met Soc 5th Conf Atmos Radiat Oct 31- 4 Nov 1983 p1-9

D H Staelin 1981 'Passive microwave remote sensing for meteorology' IEEE Digest Int Geosci remote Sensing Symp June 8-10 1981 p 158-162

D Tinkler, D R Pick, S Stringer and C G Woods 1985 'The design of the focal plane assembly for the along the track scanning radiometer' SPIE Cannes 1985

Table 3.1A

AMSU-B Channel Characteristics

Ch No. Designation	Center Frequency (GHz)	No. of Pass Bands	Maximum Bandwidth (MHz)	Center Frequency Stability (MHz)	Temperature Sensitivity (K) Goal	Temperature Sensitivity (K) Req'd	Absolute Calibration Accuracy (K)	Inter-channel calibration accuracy (K)	Beam Width (degree)	Prime Polarization
16	89.0	1	6000*	50	0.60	1.0	1.0	.5	1.1	V
17	157.0	1	4000*	50	0.60	1.00	1.0	.5	1.1	V
18	183.31±1.00	2	1000	30	0.60	1.00	1.0	.5	1.1	V
19	183.31±3.00	2	2000	30	0.60	1.0	1.0	.5	1.1	V
20	183.31±7.00	2	4000	30	0.60	1.20	1.0	.5	1.1	V

* These bandwidths are double sided maximum because of spacecraft transmitters at 1.5 - 1.7 GHz. In practice the IF response will be limited to 0.5 - 1.5 GHz.

Table 3.1B AMSU-A Channel Characteristics (as of 5 Oct 1982)

Ch No. Designation	Center Frequency (GHz)	No. of Pass Bands	Maximum Bandwidth (MHz)	Center Frequency Stability (MHz)	Temperature Sensitivity (K)		Absolute Calibration Accuracy (K)	Beam Width (degree)	Prime Polarization
					Goal	Req'd			
1	23.800	1	270	20	0.20	0.50	2.0	3.3	V
2	31.400	1	200	20	0.20	0.50	2.0	3.3	V
3	50.300	1	200	50	0.30	0.40	1.5	3.3	V
4	52.800	1	400	5	-	0.25	1.5	3.3	V
5	53.330	1	400	5	-	0.25	1.5	3.3	V
6	54.400	1	400	10	-	0.25	1.5	3.3	-
7	54.940	1	400	10	-	0.25	1.5	3.3	-
8	55.500	1	400	20	-	0.25	1.5	3.3	
9	57,290.334 MHz $= f_{10}$	1	330	0.5	-	0.25	1.5	3.3	-
10	$f_{10} \pm 217$ MHz	2	78	0.5	-	0.35	1.5	3.3	-
11	$f_{10} + 322.2 \pm 48$ MHz	4	36	0.5	-	0.35	1.5	3.3	-
12	$f_{10} + 322.2 \pm 22$ MHz	4	16	0.5	-	0.50	1.5	3.3	-
13	$f_{10} + 322.2 \pm 10$ MHz	4	8	0.5	-	0.80	1.5	3.3	-
14	$f_{10} + 322.2 \pm 4.5$ MHz	4	3	0.5	-	1.30	1.5	3.3	-
15	89.0	1	6000	50	0.60	1.00	2.0	3.3	V

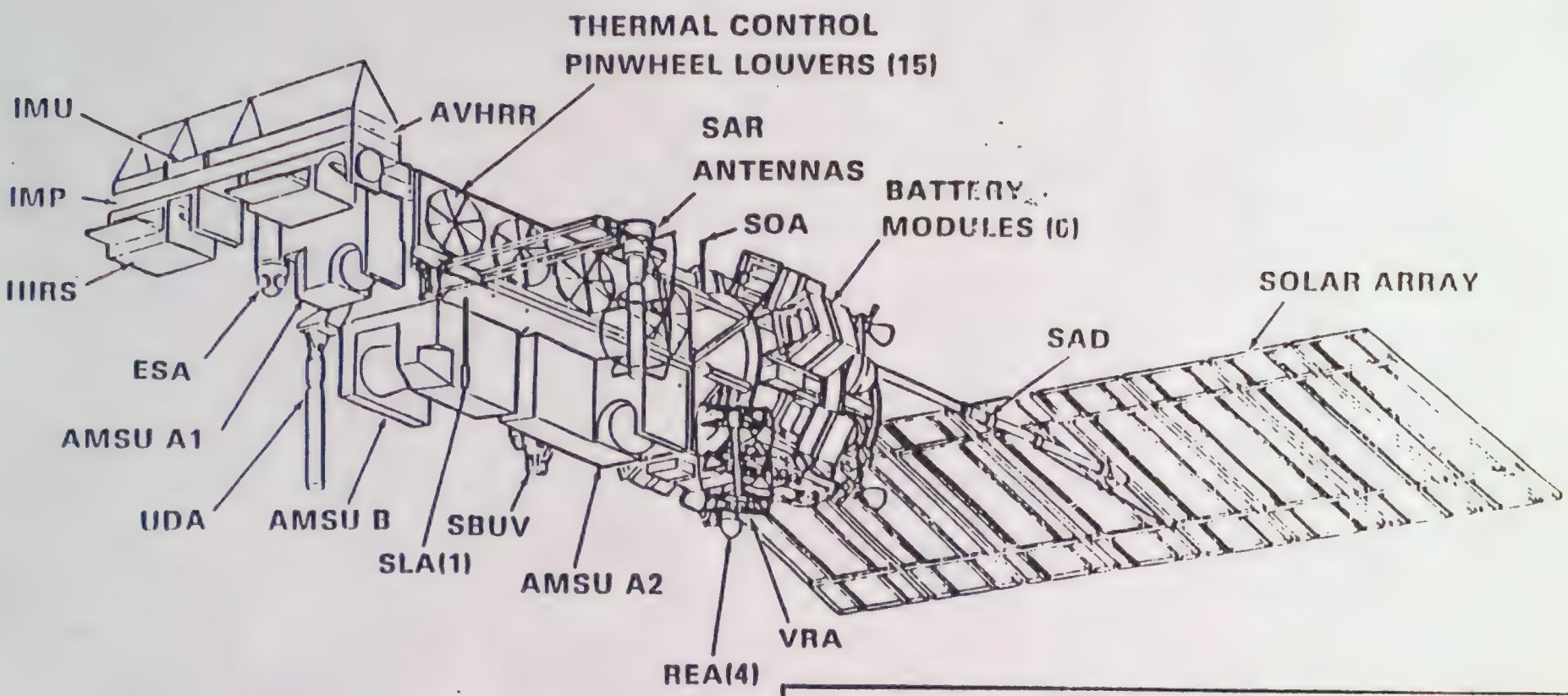

LEGEND	
AMSU	ADVANCED MICROWAVE SOUNDING UNIT
AVHRR	ADVANCED VERY HIGH RESOLUTION RADIOMETER
ESA	EARTH SENSOR ASSEMBLY
HIRS	HIGH-RESOLUTION INFRARED SOUNDER
IMP	INSTRUMENT MOUNTING PLATFORM
IMU	INERTIAL MEASUREMENT UNIT
REA	REACTION ENGINE ASSEMBLY
SAD	SOLAR ARRAY DRIVE
SAR	SEARCH AND RESCUE
SBUV	SOLAR BACKSCATTER ULTRAVIOLET SOUNDING SPECTRAL RADIOMETER
SLA	SEARCH AND RESCUE TRANSMITTING ANTENNA (L BAND)
UDA	ULTRA-HIGH-FREQUENCY DATA COLLECTION SYSTEM ANTENNA
VRA	VERY-HIGH-FREQUENCY REALTIME ANTENNA

Figure 3.1 The TIROS N Spacecraft configuration

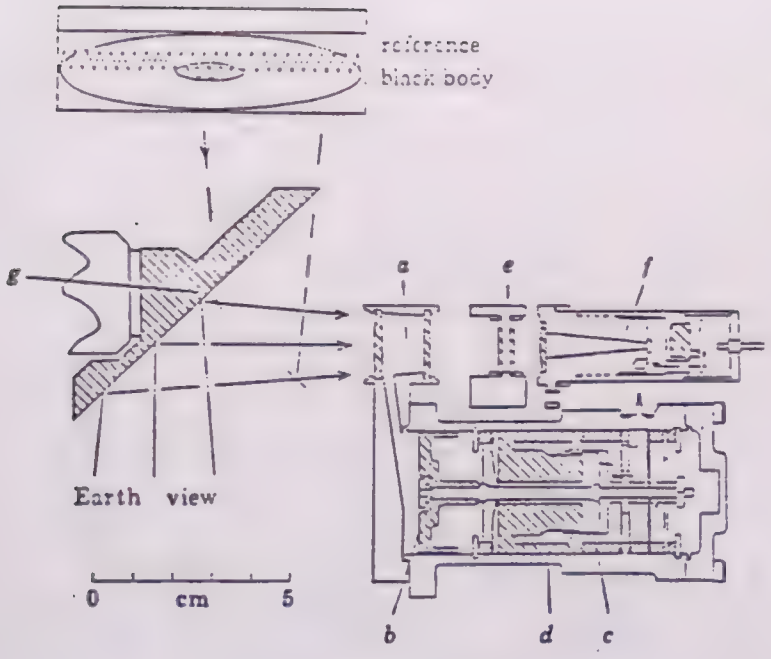

Figure 3.2 The Optical system and pressure modulator of a stratospheric sounding unit. a, Absorption cell; b, piston; c, drive coil; d, magnet; e, interference filter; f, detector; g, scan mirror. Another two optical channels share the scan mirror.

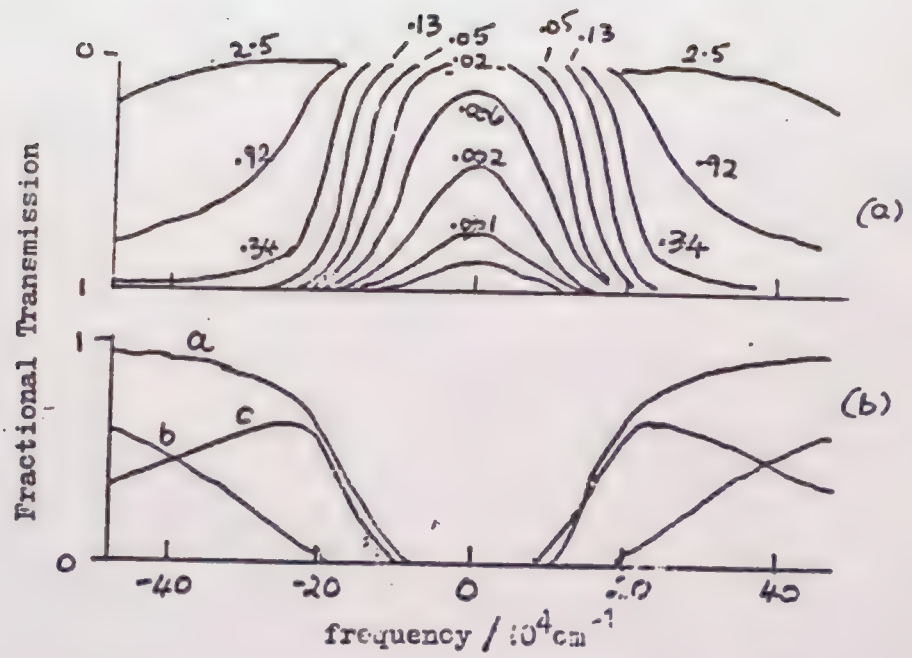

Figure 3.3 Illustrating the technique of pressure modulation applied to a single line (strength 2 cm^{-1} $(atm\ cm)^{-1}$ ν_2 CO_2)

a) Transmission plotted against frequency for various vertical atmospheric paths from level of pressure p in millibars to the top of the atmosphere for a single line.

b) Transmission of a pressure modulator cell 1 cm long for the same line as a). Cell pressure is 5 millibars for curve a, 14 millibars for curve b and difference curve c.

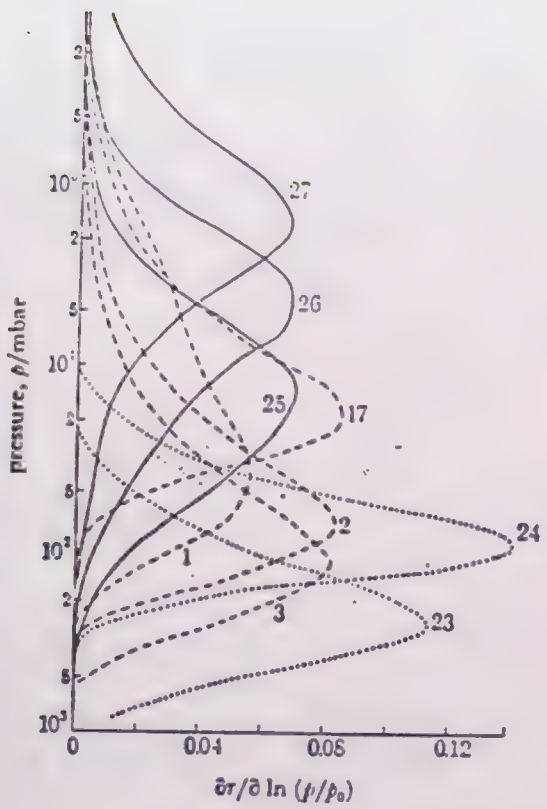

Figure 3.4 Weighting functions for those channels used in stratospheric analysis. The labels indicate the channel designations within the Tiros operational vertical sounder. The associated instruments are :___ SSU, ... MSU, ---- HIRS.

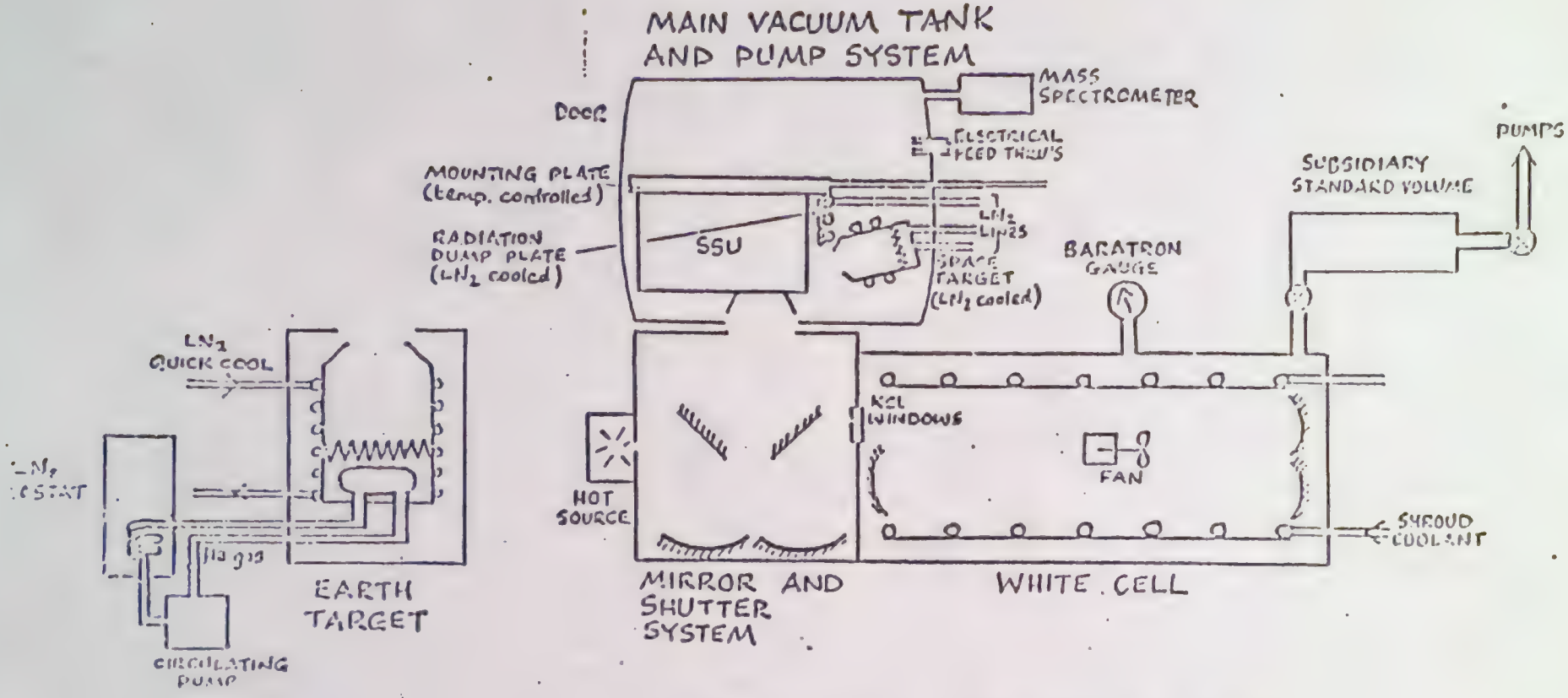

Figure 3.5 The SSU Calibration facility.

The main vacuum tank and pumping system can be moved from the weighting function rig to the earth target. the area around the tank door is enclosed in a clean room with a filtered air supply.

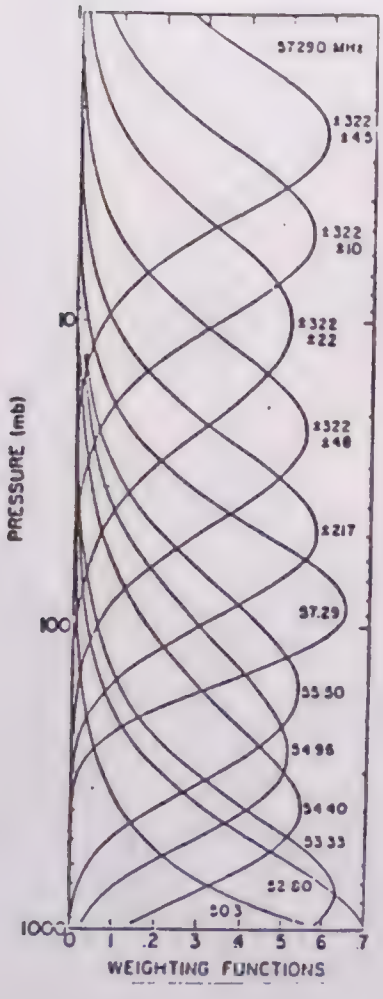

Figure 3.6a Temperature weighting functions AMSU channels 4 - 15.

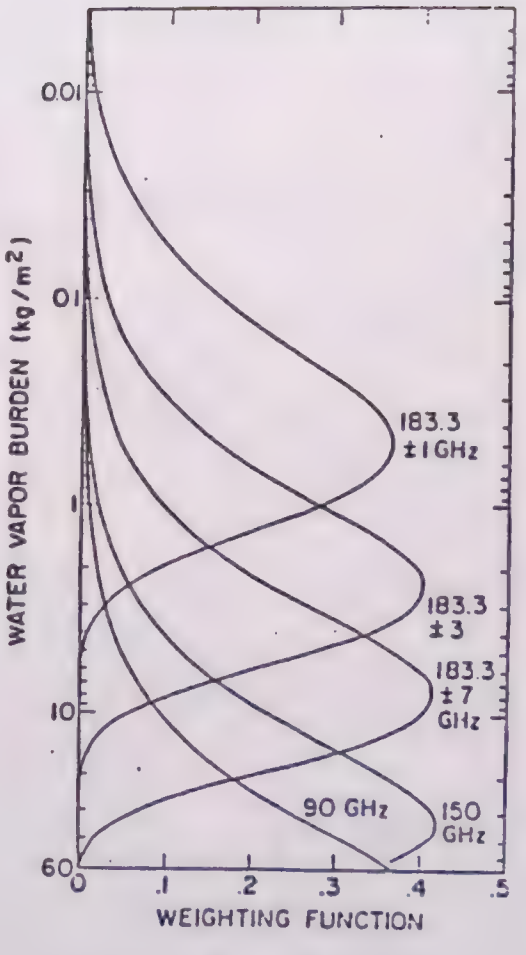

Figure 3.6b Water vapour burden weighting functions AMSU-B chans 16 - 20.

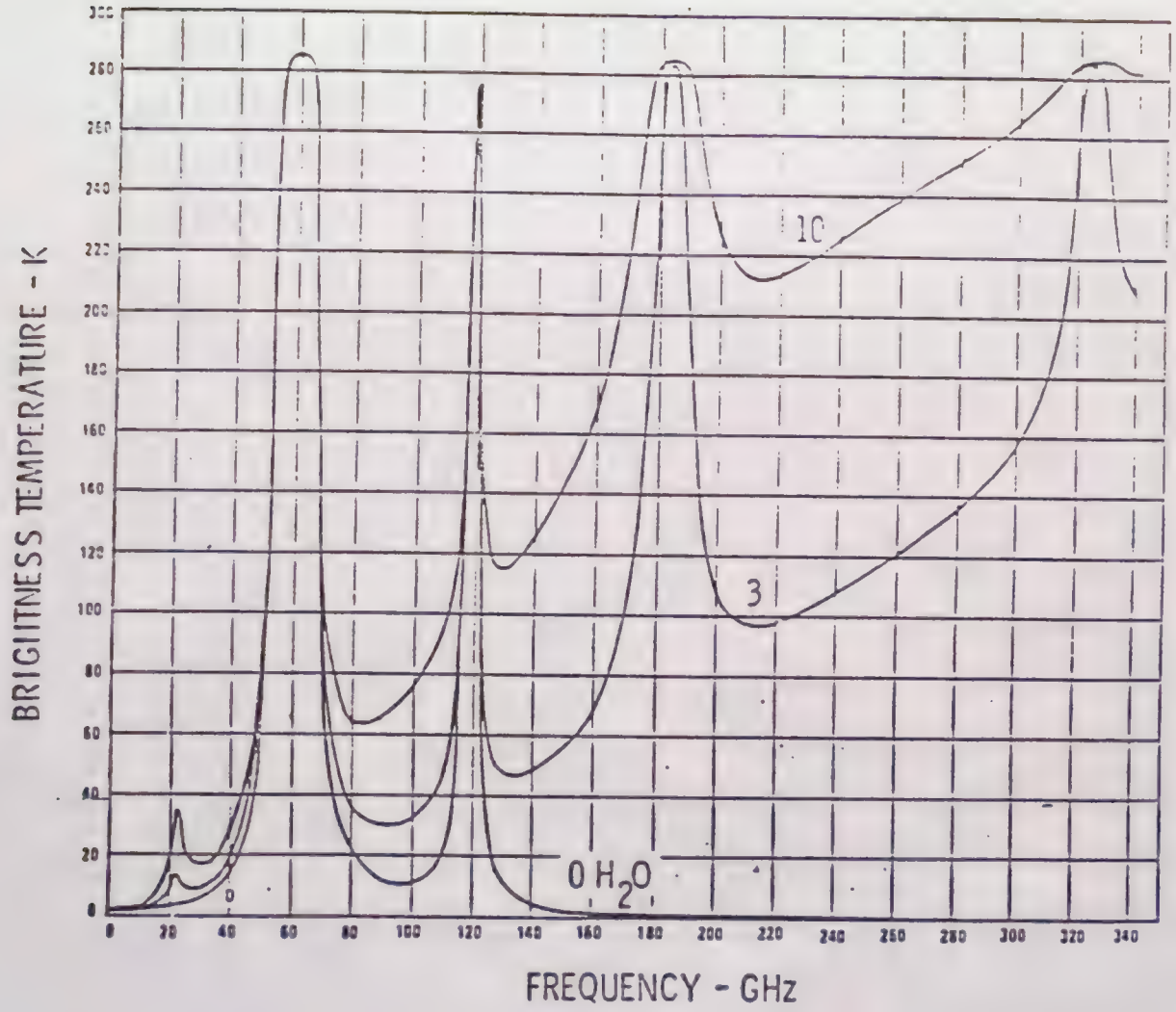

Figure 3.7 Zenith brightness for 0.3 and 10 gm^{-3} surface water vapour (2 km scale height) added to the US standard Atmosphere.

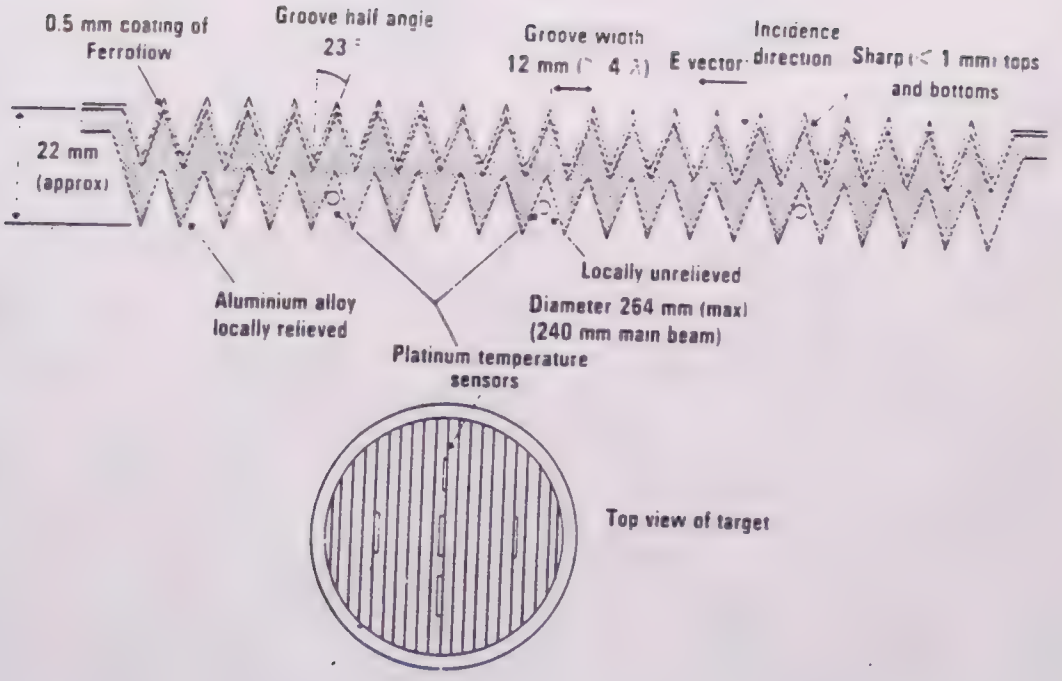

Figure 3.8 Outline design of the AMSU-B calibration target.

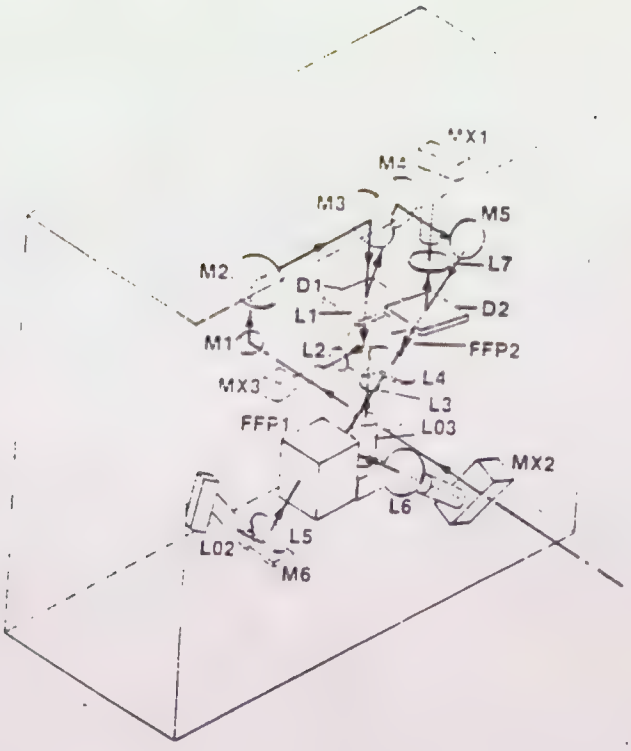

Figure 3.9 Schematic diagram of the AMSU-B quasi-optics

Key to figure

D1 Dichroic beamsplitter reflects 90 and 157 Ghz channels
D2 Dichroic beamsplitter reflects 90 Ghz channel

FFP1 Folded Fabry Perot channel 17 157 GHz
FFP2 Folded Fabry Perot channels 18, 19 and 20
(Combines local oscillator (transmitted) with earth signal (reflected))

L Lens

LO2 Local Oscillator 2 157 GHz channel
LO3 Local Oscillator 3 183 GHz channels

M Mirror

Mx1 Channel 16 90 GHz mixer
Mx2 Channel 17 157 GHz mixer
Mx3 Channels 18, 19 and 20 mixer

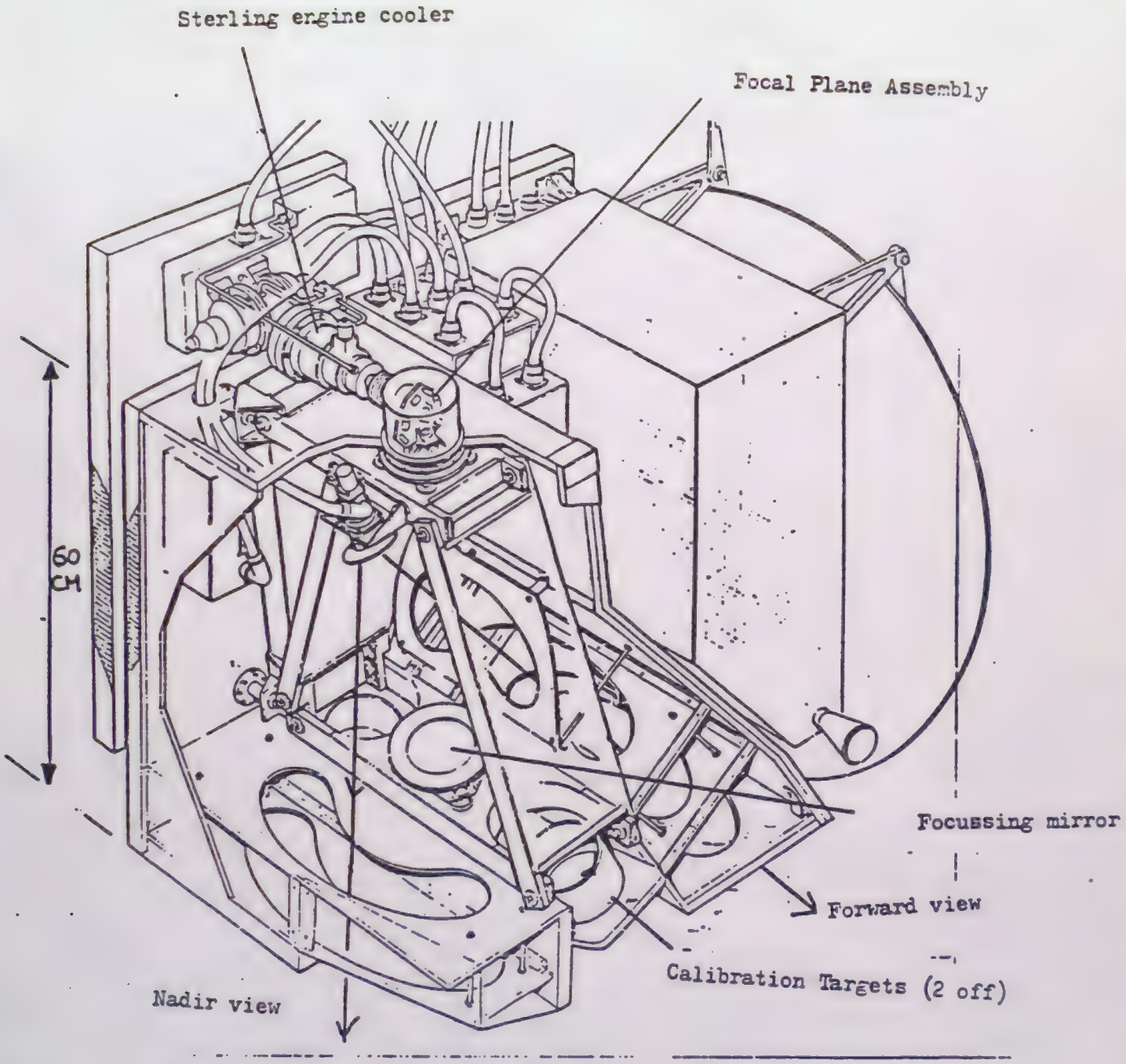

Figure 3.10 Outline design of the Along the track scanning radiometer

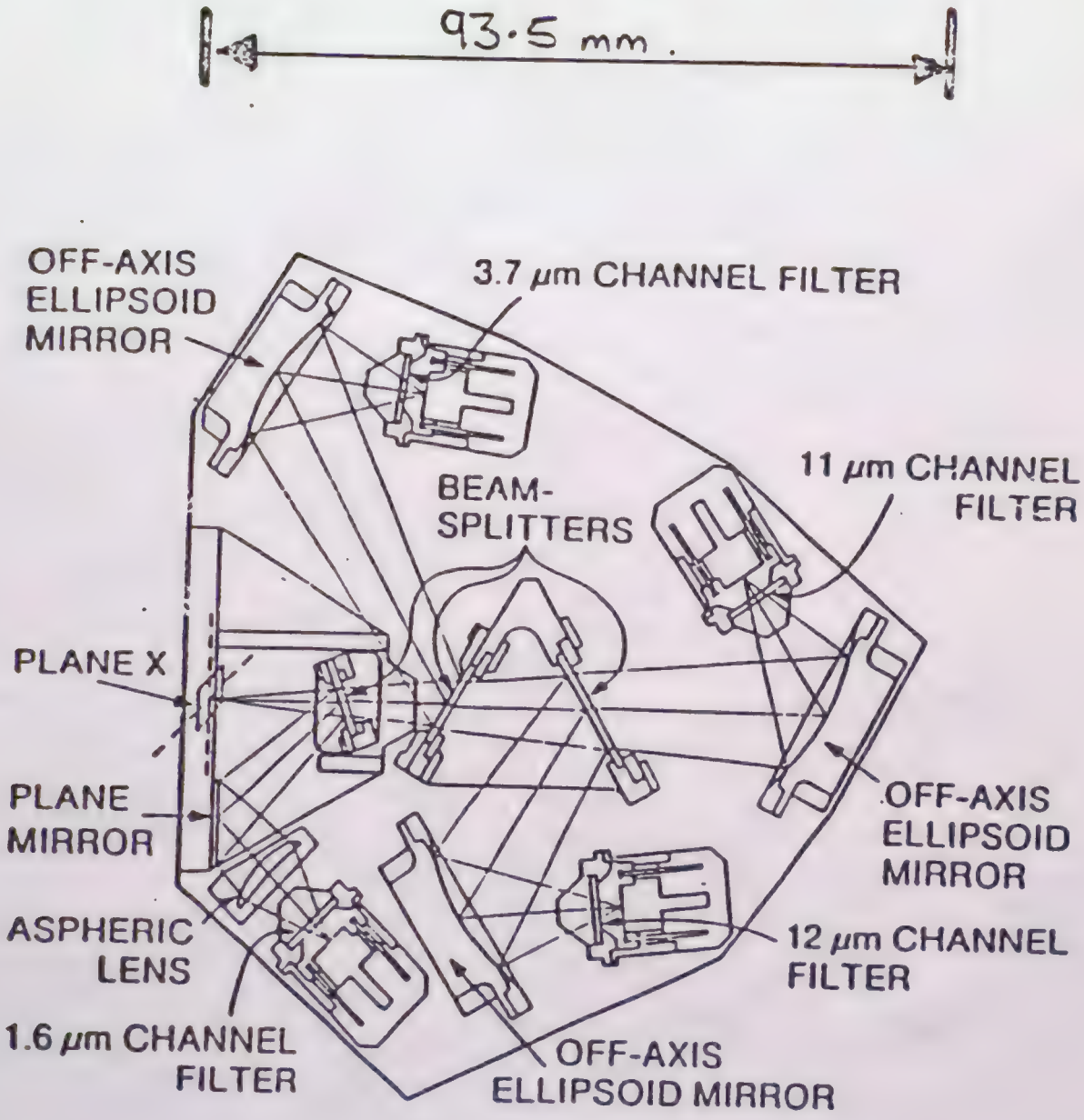

Figure 3.11a Optical layout for the ATSR focal plane assembly.

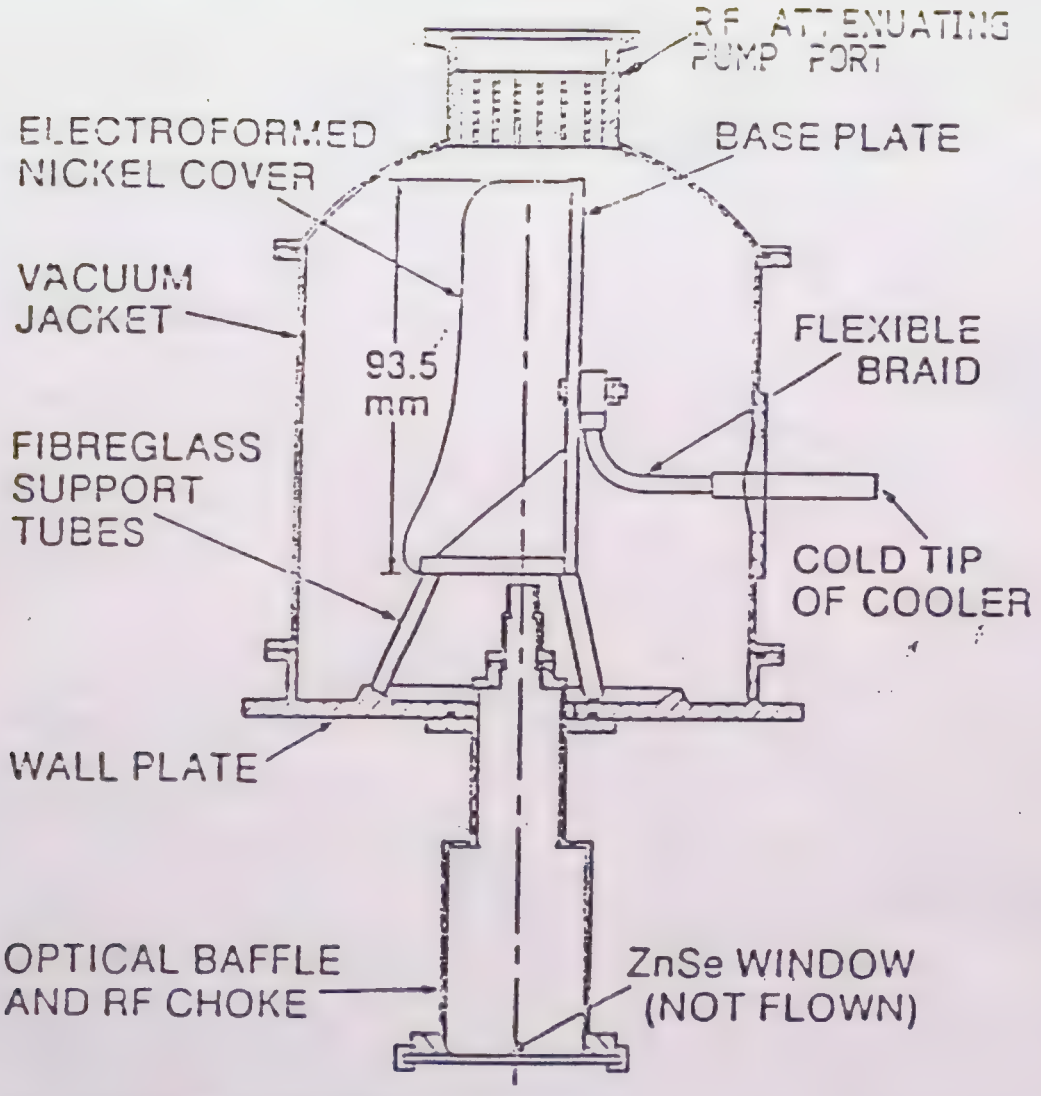

Figure 3.11b Mounting arrangement for the ATSR focal plane assembly.

ADVANCED LECTURES - SATELLITE METEOROLOGY - 1987

LECTURE 4: THE RETRIEVAL OF ATMOSPHERIC TEMPERATURE AND HUMIDITY FROM SATELLITE MEASUREMENTS OF RADIATION

by J.R.Eyre and P.D.Watts

1. Introduction

We have seen in lecture 2 that the intensity of radiation emitted from the top of the atmosphere varies with wavelength and is a function of the temperature and composition structure. Atmospheric sounding instruments measure radiation over a number of spectral intervals or 'channels' at wavelengths chosen such that most of the radiation detected has been emitted by the atmosphere itself. Measurements of emission from gases of known concentration such as carbon dioxide and oxygen can be used to retrieve atmospheric temperature. Alternatively, if the temperature structure is known, information on the variable concentration profiles of constituents such as water vapour can be deduced from measurements at the wavelengths of the appropriate absorption bands. The channels used by the present TIROS Operational Vertical Sounder (TOVS) instruments on the TIROS-N satellite series are given in table 1 and typical weighting functions for them are shown in figure 1.

The theory presented in lecture 2 allows us to calculate the emitted radiance given the state of the atmosphere (and underlying surface). In interpreting satellite measurements we are faced with the *inverse problem*, i.e. given the measured radiances, we have to estimate the atmospheric state. For sounding systems using infra-red measurements, the retrieval problem is usually divided into 2 major stages:

(a) allowing for the effects on the radiances of cloud,

(b) using the cloud-free or 'cloud-cleared' radiances to deduce the temperature and humidity profiles.

In this lecture we shall consider the theoretical aspects of (b). Lecture 5 will discuss both (a) and (b) in the context of one practical retrieval scheme.

There is an extensive literature on the theory of inverse problems in general and temperature retrieval in particular. An excellent discussion of the problem and

literature review is given by Rodgers (1976). Hayden (1979) and Twomey (1977) also give useful introductions to the subject.

2. Temperature retrieval: characteristics of the inverse problem

Using the theory developed in lecture 2, we can express the radiance measured by the i^{th} channel of a satellite-borne radiometer as:

$$R_i = (I_o)_i \bar{\tau}_i(z_o) + \int_{z_o}^{\infty} B_i(z) K_i(z) dz \qquad 2.1$$

Here we have chosen scale height, $z = -ln(pressure)$, as the vertical co-ordinate (with z_o as the surface value), and we have used mean quantities averaged over the spectral response of the radiometer channel: $\bar{\tau}_i(z)$ is the mean transmittance from z to space for the i^{th} channel, and $K_i(z)$ is the corresponding weighting function $(= d\bar{\tau}_i(z)/dz)$. $B_i(z)$ is a Planck function slightly modified so as to represent the mean Planck function for the spectral response of the channel, and $(I_o)_i$ is the surface radiance evaluated in a similar manner. The approximations involved in the representation of this polychromatic problem by an equation in the form of the monochromatic problem usually produce negligible error.

For numerical solution of the problem it is more convenient to replace the integral equation by a vector formulation:

$$R_i = \mathbf{K_i}.\mathbf{B} \qquad 2.2$$

Here we have expressed the atmosphere's vertical temperature profile at a finite number of pressure levels and represented it by the corresponding Planck function vector, **B**. $\mathbf{K_i}$ is the weighting function vector, the elements of which represent the layers centred on the levels at which **B** is expressed. **B** and $\mathbf{K_i}$ are vectors of length, J, the number of levels. The surface term has been absorbed as the first element of each vector. J must be sufficiently large for accurate approximation of an integral by a vector equation.

Equation 2.2 refers only to one channel. For a radiometer with I channels we can write,

$$\mathbf{R} = \mathbf{K}.\mathbf{B} \qquad 2.3$$

where **R** is a vector of length I,

B is a vector of length J,

and $\mathbf{K}$ is a matrix, $J \times I$, containing the discrete weighting functions for all channels.

An important property of equation 2.3 (for the temperature sounding problem) is its degree of linearity. $\mathbf{B}$ is related in a known way to the unknown variable, i.e.the temperature profile, whilst $\mathbf{K}$ is only weakly dependent on temperature. This allows us to use linear inverse theory successfully. The linearity of the problem is usually improved further by expressing the radiances and Planck functions as deviations from mean values:

$$\mathbf{r} = \mathbf{R} - \bar{\mathbf{R}} \quad and \quad \mathbf{b} = \mathbf{B} - \bar{\mathbf{B}}$$

$$\Rightarrow \mathbf{r} = \mathbf{K}.\mathbf{b} \qquad 2.4$$

One further problem which must be tackled in practice concerns the nature of the function $\mathbf{b}$. Unless all channels are very close in wavenumber, we have a set of significantly different functions and we cannot solve for a single vector $\mathbf{b}$. There are several approaches to this problem. The one usually adopted for TOVS, which has temperature sounding channels in 3 widely separated spectral regions (the $15\mu m$ CO_2 band, the $4.3\mu m$ CO_2 band and the 50-60 GHz O_2 band), is to convert radiances to equivalent black body temperatures (often called 'brightness temperatures') and to derive the atmospheric temperature profile rather than the Planck function profile. Using 1^{st} order Taylor expansions we can write,

$$r_i = \frac{dR_i}{dT_{B_i}} t_{B_i} \quad and \quad b_j = \frac{dB_j}{dT_j} t_j, \qquad 2.5$$

where T_{B_i} is the brightness temperature of the i^{th} channel,

t_{B_i} is its deviation from the mean,

T_j is the temperature at the j^{th} pressure level,

and t_j is its deviation from the mean.

We can now re-write equation 2.4 as

$$\mathbf{t_B} = \mathbf{K'}.\mathbf{t} \qquad 2.6$$

where $K'_{ij} = K_{ij}(\frac{dB_j}{dT_j})$ / $(\frac{dR_i}{dT_{B_i}})$. This formulation is not quite as linear as equation 2.4 because of the nature of $\mathbf{K'}$, but it yields an expression in which there is a single unknown vector, $\mathbf{t}$, independent of the radiometer.

The fundamental difficulties of the retrieval problem can be seen by examining equation 2.4 or 2.6; we have I measurements of radiance and we wish to obtain a profile at J atmospheric levels. Usually $J > I$, giving an under-constrained problem and an infinite number of solutions t which satisfy the measurements $\mathbf{t_B}$. Referring back to equation 2.1 we see that we are really attempting to obtain the temperature profile, a continuous function of height, from a finite number of measurements. Our task is to find, from the infinite number of solutions, an acceptable solution and, if possible, the most probable solution. This involves constraining the solution using some a priori information which is equivalent to adding more equations to the problem so that we have at least as many equations as unknowns.

One obvious way of constraining the solution is to reduce the number of levels at which t is specified or to express t as a linear combination of a small number of pre-selected functions so that $J \leq I$. Neither of these simple approaches tends to work well in practice (see Rodgers, 1976). Briefly, problems arise in the mathematics of the inversion procedure. We are seeking a predictive equation of the form,

$$\mathbf{t} = \mathbf{D}.\mathbf{t_B} \qquad 2.7$$

The matrices D obtained by the simple methods suggested above tend to have elements which oscillate from large positive to large negative values. Consequently any small errors in t are amplified into unacceptably large errors in t. This instability arises because the weighting functions overlap significantly and we do not have I independent observations. Since t will always contain a contribution from instrumental noise, successful inversion methods must overcome this kind of instability.

3. Practical inversion methods for temperature retrieval

Numerous schemes have been devised for retrieving temperature profiles from satellite sounding data. In this section we examine 2 types of approach in common use.

3.1 Minimum variance method (regression)

This method recognises that there is insufficient information in the measured brightness temperatures, $\mathbf{t_B}$, for us to retrieve the exact, true temperature profile, $\mathbf{t}$. It does not attempt to find $\mathbf{t}$ but seeks an estimate profile, $\hat{\mathbf{t}}$, using a linear predictive equation,

$$\hat{\mathbf{t}} = \mathbf{D}.\mathbf{t_B} \qquad 3.1$$

$\mathbf{D}$ is a predictive matrix calculated such that the variance of $\hat{\mathbf{t}}$ from $\mathbf{t}$ is a minimum when averaged over a large number of profiles, M, i.e.

$$\Sigma_{m=1}^{M}(\mathbf{t_m} - \hat{\mathbf{t}}_\mathbf{m})^T.(\mathbf{t_m} - \hat{\mathbf{t}}_\mathbf{m}) \qquad 3.2$$

is minimised with respect to all elements of $\mathbf{D}$. (^{T} denotes matrix transpose.)

This procedure leads to the well-known multiple linear regression relation:

$$\mathbf{D} = (\mathbf{t}.\mathbf{t_B^T}).[\mathbf{t_B}.\mathbf{t_B^T}]^{-1} \qquad 3.3$$

where $\mathbf{t}$ is a matrix of dimension $M \times J$ containing M profiles specified at J levels,

$\mathbf{t_B}$ is a matrix of dimension $M \times I$ containing the corresponding M brightness temperature vectors for J channels,

and $[...]^{-1}$ denotes a matrix inverse.

$(\mathbf{t_B}.\mathbf{t_B^T})/M$ is the brightness temperature covariance matrix and $(\mathbf{t}.\mathbf{t_B^T})/M$ the covariance of temperature profile with brightness temperature. Thus there is a strong constraint on the inversion which enters the problem through the covariance matrices representing the statistical properties of atmospheric profile variations and the related statistics for the radiances measured at the satellite.

The minimum variance solution is discussed by Rodgers (1976) and shown to be identical to the 'maximum probability' solution for sets of profiles with Gaussian statistics.

In practice there are several possible ways of generating the predictive matrix, $\mathbf{D}$:

(a) We may neglect all considerations of the physics involved and collect a large set of measured brightness temperatures, $\mathbf{t_B}$, collocated with a set of radiosonde

profiles, $\mathbf{t}$, and hence derive $\mathbf{D}$. This is the basis of the method currently used by NOAA/NESDIS for the operational scheme which generates global soundings. The same coefficients are also used at present by Met.O.19 for routine generation of high-resolution regional retrievals (see lecture 5). The method was first developed in the simple form given here (Smith et al., 1970) but has been refined to use the coefficients of the eigenvectors of the temperature profile and brightness temperature covariance matrices rather than the vectors themselves (Smith and Woolf, 1976; Smith et al., 1979). This makes the inversion less sensitive to noise in the measurements.

(b) From equation 2.6 we can write a measured brightness temperature vector as

$$\mathbf{t_B} = \mathbf{K'}.\mathbf{t} + \epsilon \qquad 3.4$$

where ϵ represents random measurement error. Substituting equation 3.4 into equation 3.3, we obtain

$$\mathbf{D} = \{\mathbf{t}.(\mathbf{K'}.\mathbf{t} + \epsilon)^T\}.[(\mathbf{K'}.\mathbf{t} + \epsilon).(\mathbf{K'}.\mathbf{t} + \epsilon)^T]^{-1}$$

$$= \{\mathbf{S_t}.\mathbf{K'^T}\}.[\mathbf{K'}.\mathbf{S_t}.\mathbf{K'^T} + \mathbf{S_\epsilon}]^{-1} \qquad 3.5$$

where $\mathbf{S_t}$ and $\mathbf{S_\epsilon}$ are the covariance matrices of $\mathbf{t}$ and ϵ respectively, and ϵ is assumed to be uncorrelated with $\mathbf{t}$.

(c) Method (b) can only be applied satisfactorily if the problem is sufficiently linear for one set of weighting functions $\mathbf{K'}$ to be applied to all profiles. Because $\mathbf{K'}$ is in practice weakly dependent on temperature, it is preferable to apply an accurate radiative transfer model to each profile $\mathbf{t}$ and generate theoretically the corresponding brightness temperature vector, $\mathbf{t_B}$. Thus we obtain a set of profiles $\mathbf{t}$ and their corresponding synthetic brightness temperatures $\mathbf{t_B}$, from which $\mathbf{D}$ may be found as in method (a).

The advantage of method (c) over method (a) is that we can select carefully from a historical radiosonde data-base a set of profiles representative of the statistical behaviour of the atmosphere. Also the synthetic radiances do not have contributions from collocation errors as they do in method (a).

Methods (a), (b) and (c) all imply some first guess profile, namely $\bar{\mathbf{T}}$ and the corresponding $\bar{\mathbf{T}}_\mathbf{B}$, about which the minimum variance estimate is made. $\bar{\mathbf{T}}$ and $\mathbf{S_t}$ are the *a priori* information and its error covariance needed to constrain the solution. The importance of this information can be seen by examining the form of the error in the retrieved temperature profile. If $\mathbf{T_t}$ is the 'true' atmospheric profile then from 3.1 and 3.4 the retrieval is;

$$\hat{\mathbf{T}} - \bar{\mathbf{T}} = \mathbf{D}.\mathbf{K}'.(\mathbf{T}_t - \bar{\mathbf{T}}) + \mathbf{D}.\epsilon \qquad 3.6$$

And the error in the retrieval;

$$\hat{\mathbf{T}} - \mathbf{T}_t = (\mathbf{D}.\mathbf{K}' - \mathbf{I}).(\mathbf{T}_t - \bar{\mathbf{T}}) + \mathbf{D}.\epsilon \qquad 3.7$$

We know that the variance of this error is minimised with a $\mathbf{D}$ given by 3.3 and that attempting to remove the first term on the RHS by letting $\mathbf{D}.\mathbf{K}' \rightarrow \mathbf{I}$ (i.e. towards an 'exact' solution) causes large amplification of the measurement errors by way of the second term. Therefore our only hope is to reduce the term $\mathbf{T}_t - \bar{\mathbf{T}}$ as far as possible, i.e. our *a priori* information must be the best available.

(d) Probably the best estimate of the atmospheric state, at least in an operational sense, is a numerical weather prediction (NWP) model forecast for the time of the sounding data. (There may be exceptions e.g for a quickly changing parameter like surface temperature the satellite data itself provides the best estimate). Given, then, $\bar{\mathbf{T}}$ from a forecast and $\mathbf{T}_{\mathbf{B}_o}$ calculated from it we can proceed as in (b) to obtain;

$$\mathbf{D} = \{\mathbf{S}_c.\mathbf{K}'^{\mathbf{T}}\}.[\mathbf{K}'.\mathbf{S}_c.\mathbf{K}'^{\mathbf{T}} + \mathbf{S}_\epsilon]^{-1} \qquad 3.8$$

Where $\mathbf{S}_c$ is the error covariance of the forecast profile. If, as is usually the case, the retrieval is to be assimilated in the forecast model, care must be taken to account for the model information already used. It is sufficient to calculate and supply the retrieval error covariance for this purpose (see Lorenc).

Method (a) is a purely statistical approach, whereas methods (b) and (c) and (d) are mixed physical-statistical techniques. (a),(b) and (c) have the advantage that they are computationally fast (since the $\mathbf{D}$ matrices may be pre-computed) and take advantage of existing knowledge about atmospheric statistics. On the other hand, the profiles from which the statistics are derived must be chosen with care; inappropriate statistics lead to poor results as discussed above. For example, statistics based on tropical profiles will give large errors when used to retrieve profiles typical of higher latitudes. Similarly, seasonal dependence of statistics must be carefully considered. Another problem with the regression approach concerns the nature of the retrieved profile. The statistical data-base (particularly in mid-latitudes) will generally contain profiles of distinct and widely differing shape. In representing these profiles by a single covariance matrix, we usually lose the sense of these different shapes, and the retrieved profiles, whilst being optimum in the minimum variance sense, will tend to have shapes which are smoother than those which actually exist in the atmosphere.

3.2 Physical methods

Several 'direct', 'empirical' or 'physical' methods, which do not use atmospheric statistics are to be found in the literature. The iterative relaxation method, introduced by Chahine (1968) and reformulated by Smith (1970), is an example. In Smith's method the brightness temperatures $\mathbf{T_{B_o}}$, corresponding to a first-guess profile $\mathbf{T_o}$, are calculated using a radiative transfer model. Then the profile at the j^{th} level is adjusted according to the difference between the measured brightness temperatures $\mathbf{T_{B_m}}$ and the calculated brightness temperatures $\mathbf{T_{B_o}}$ using the weighting function values at the j^{th} level as relative weights:

$$(T_1)_j = (T_o)_j + \frac{\Sigma_{i=1}^{I} K'_{ij}\{(T_{B_m})_i - (T_{B_o})_i\}}{\Sigma_{i=1}^{I} K'_{ij}} \qquad 3.9$$

From $\mathbf{T_1}$ the equivalent brightness temperatures are computed and the process repeated. The iteration proceeds to a solution $\mathbf{T_n}$ at the n^{th} step, when the difference between measured and calculated brightness temperatures meets some criterion (related to instrument noise).

The a priori constraints in this method are not obvious but are effectively introduced in equation 3.6 through the implicit assumption that the temperature profile change at each step must be a linear combination of the weighting functions. In common with similar direct methods, a solution is obtained which may not be the most probable solution in the statistical sense. Also it is found that the solution is often sensitive to the first-guess profile, $\mathbf{T_o}$, particularly with respect to the shape of the profile. For example, with retrievals from data of current operational instruments, the tropopause height assumed in the first guess will tend to be altered little by the iterative procedure. A good first guess from a forecast model will yield a good solution, but in this case care must be taken to account correctly for retrieval errors correlated with those of the forecast model.

The strength of physical methods lies in their ability to include the physics of the radiative transfer problem directly. Non-linearities can be treated explicitly, even those caused by clouds, as are problems caused by the effects of high terrain or variable surface emissivity, which are difficult to handle in a regression scheme. These advantages are obtained at the expense of computation time, since radiative transfer calculations are required as part of the retrieval algorithm. This is not true of regression schemes (see figure 2).

A draw-back common to both physical and physical-statistical schemes is that they involve theoretical calculations of radiance, and hence they propagate errors in our knowledge of the spectroscopy into the solution. This problem can be tackled fundamentally by research to improve our understanding of the molecular spectroscopy involved in the calculations of transmittance. In the short term it can be treated reasonably well by making empirical corrections to the transmittance models to minimise differences between measured radiances and those calculated theoretically from collocated radiosonde data.

To summarise, it can be seen that statistical and physical methods have different strengths and weaknesses. It would appear therefore that the best results ought to be obtained using a combined approach which seeks to use all the available information – the radiance measurements and our knowledge of both the physics of the problem and the statistical behaviour of the atmosphere.

4. Humidity retrieval

By comparison with the temperature retrieval problem, humidity retrieval has received little attention. This reflects not only the relative importance of the two parameters in numerical forecasting but also the additional difficulties which arise in the case of humidity retrieval. Also errors in the temperature retrieval tend to propagate into the humidity retrieval and so it is sensible to give priority to the former.

The global operational retrieval scheme currently used by NOAA/NESDIS and Met.O.19's present system take a rather simplistic approach to the problem of humidity retrieval. By analogy with the linear regression scheme used for temperature retrieval (section 3.1(a) above), they use a regression of measured brightness temperatures against collocated humidity mixing ratio profiles and obtain a predictive matrix $\mathbf{D}'$ to be used in the retrieval as follows:

$$\hat{\mathbf{c}} = \mathbf{D}'.\mathbf{t_B} \qquad 4.1$$

where $\hat{\mathbf{c}}$ is a vector representing the minimum variance estimate of the water vapour mixing ratio profile (or rather its deviation from a mean profile).

It is accepted that there is a theoretical weakness in this approach. In using a linear regression retrieval we imply that the forward problem can be expressed as a linear equation, i.e. by analogy with equation 2.1 we are assuming an expression for the radiance measured by a water vapour sounding channel of the form,

$$R_i = (I_o)_i \bar{\tau}_i(z_o) + \int_{z_o}^{\infty} c(z)G(z)dz, \qquad 4.2$$

where c(z) is the humidity profile (in terms of mixing ratio or any other suitable humidity parameter) and G(z) is a weighting function which is only weakly dependent on c(z).

In fact it is not possible to derive such a formulation. This is because c(z) enters the radiative transfer equation through the monochromatic transmittance:

$$\tau_\nu(z) = exp\{-\int_z^{\infty} k_\nu(z')\rho(z')c(z')dz'\}, \qquad 4.3$$

where $k_\nu(z)$, $c(z)$ and $\rho(z)$ are the profiles of absorption coefficient, mixing ratio and atmospheric density respectively. The weighting functions are consequently strongly dependent on the unknown variable, c(z). The effect of increasing the humidity in the atmosphere is to decrease the transmittance from any level to space. Since the 'temperature weighting function' has the form $K(z) = d\tau(z)/dz$, the peak of this function will rise as the humidity increases, and so the layer from which we measure the radiation is a function of the variable profile we wish to measure. Consequently we have a very non-linear problem and it is perhaps surprising that retrievals based on equation 4.1 are as acceptable as they prove to be. Nevertheless we can argue on theoretical grounds that by treating the problem as a non-linear one, we should be able to improve significantly on the linear approach represented by equation 4.1. Several algorithms have been developed for humidity profile retrieval. An extensive bibliography on the subject has been compiled by Rosenberg et al. (1983).

The non-linear nature of the problem suggests that a physical retrieval will have advantages over a linear, statistical method. An example of the physical approach is given by Smith and Woolf (1981), who develop an algorithm of the form of equation 3.6 to solve iteratively for u_j, the water vapour overburden above pressure level j. u_j is related to the mixing ratio profile as follows:

$$u_j = \int_{z_j}^{\infty} c(z)\rho(z)dz = \int_{p_j}^{0} -c(p)dp/g, \qquad 4.4$$

and so, if required, c(p) can be found by differentiation of the u profile.

A different approach, which provides a theoretical basis for the use of atmospheric statistics in a linear manner, has been developed by Rosenkranz et al. (1982). Returning to equation 2.1, we can integrate the atmospheric term over any convenient vertical co-ordinate. Noting that the usual co-ordinate, pressure, can be thought of as 'mass overburden', for humidity retrieval we can change from pressure to water vapour overburden and thus obtain a term,

$$\int B\{T(u)\}K(u)du \qquad 4.5$$

For a water vapour sounding channel the transmittance to space, $\tau(u)$, from a level above which there is a given water vapour overburden, u, is fairly constant and is only a weak function of temperature. Since $K(u) = d\tau(u)/du$, it also is only weakly temperature-dependent, and so we have a temperature retrieval problem with the same properties as that discussed in section 2. The only difference is that we are using water vapour sounding channels to estimate the temperature profile, T(u), at levels of constant u. Hence, if we also have T(p), from a retrieval based on temperature sounding channels, we may combine the two to find u(p) as illustrated in figure 3. As explained above, the mixing ratio profile may be found in principle

by differentiation of the u(p) profile. In practice it is found more satisfactory to use a regression relation to derive c(p) from u(p).

A fundamental problem with humidity retrieval concerns the sensitivity of satellite measurements to low level water vapour. If the surface emissivity is high, as for microwave measurements over land or infra-red measurements over land and sea, there is usually little difference between the brightness temperature of the surface and the temperature of the lower layers of the atmosphere. Consequently, if we consider the effects of increasing the humidity in the lower layers on the radiation emanating from the top of these layers, the extra emission from the increased water vapour is almost exactly compensated by increased absorption of upwelling radiation from below. This means that the satellite measurements are relatively insensitive to humidity of layers close in temperature to the surface. This problem is perhaps the major limitation on the accuracy and utility of current humidity retrievals, particularly when we note that most of the water vapour in an atmospheric column is in the lower layers. It is ameliorated in the case of microwave measurements over the sea, where the surface emissivity is sufficiently low for there to be a large contrast between surface brightness temperature and atmospheric temperature in the lower layers. One of the primary products of the future Advanced Microwave Sounding Unit-B (AMSU-B) will be humidity profiles (see lecture 3).

The discussion so far has concentrated on the retrieval of humidity profiles. To obtain a profile we need multi-channel information; from a single humidity sounding channel of a radiometer it is only possible to retrieve one piece of information, such as the mean humidity of the layer from which the radiation is coming. This approach has been used to derive mean layer relative humidity from Meteosat water vapour ($6.5\mu m$) channel data (Meteosat System Guide, 1981; Eyre, 1980) and for the 3 humidity sounding channels of the GOES VISSR Atmospheric Sounder (VAS) used independently for 3 atmospheric layers (Smith and Zhou, 1982). It is advisable to retrieve relative humidity rather than other humidity parameters because it is the least sensitive to errors in the assumed temperature profile.

Also of interest is the total precipitable water of the atmosphere. This can be obtained most accurately using 'window' channels which are principally surface-sensing channels and have a relatively small contribution from atmospheric emission. However the atmospheric component of the radiation they measure is often closely related to the total water vapour in the column. Using brightness temperatures in 2 or more window channels with different absorption characteristics, we can set up regression relations to retrieve both surface temperature (lecture 8) and total water content (see, for example, Chesters et al., 1982).

REFERENCES

CHAHINE M.T. *J.Opt.Soc.Amer., 58, 1634-1637 (1968).* Determination of the temperature of an atmosphere from its outgoing radiance.

CHESTERS D., UCCELLINI L.W., ROBINSON W. *NASA Technical Memorandum, TM 83951 (1982).* Low-level water vapour fields from VISSR Atmospheric Sounder (VAS) split window channels at 11 and 12 microns.

EYRE J.R. *Proc.IAMAP Symp., Hamburg, August 1981 (ESA SP-165, 63-66, June 1981).* Direct use of Meteosat water vapour channel radiances to improve the humidity analysis in a forecast model.

HAYDEN C.M. *WMO Technical Note No. 166 (1979).* Quantitative meteorological products from satellites. Chapter 1: Remote soundings of temperature and moisture.

LORENC A.C. *MET O 11 Working Paper No.77* On the use of HERMES observations in data assimilation for Numerical Weather prediction.

Meteosat System Guide *ESA publication (ESOC/MDMD) (1980).*

RODGERS C.D. *Rev.Geophys.Sp.Phys., 14, 609-624 (1976).* Retrieval of atmospheric temperature and composition from remote measurements of thermal radiation.

ROSENBERG A., HUTTER E.C., HORAN J.J. *Nav.Env.Pred.Rsch.Fac. Contract Report CR 83-01(b) (1983).* Satellite moisture retrieval techniques. Volume 2: Atmospheric sounding bibliography.

ROSENKRANZ P.W., KOMICHAK M.J., STAELIN D.H. *J.Appl.Meteor., 21, 1364-1370 (1982).* A method for estimation of atmospheric water vapour profiles by microwave radiometry.

SMITH W.L. *Appl.Opt., 9, 1993-1999 (1970).* Iterative solution of the radiative transfer equation for the temperature and absorbing gas profile of an atmosphere.

SMITH W.L., WOOLF H.M. *J.Atmos.Sci., 33, 1127-1140 (1976).* The use of eigenvectors of statistical covariance matrices for interpreting satellite sounding radiometer observations.

SMITH W.L., WOOLF H.M. *Proc.4th Conf. on Atmospheric Radiation, 13-17, Toronto, June 1981.* Algorithms used to retrieve surface-skin temperature and vertical temperature and moisture profiles from VISSR Atmospheric Sounder (VAS) radiance observations.

SMITH W.L, WOOLF H.M, HAYDEN C.M, WARK D.Q., MCMILLIN L.M *Bull.Amer.Meteor.Soc., 60, 1177-1187 (1979).* The TIROS-N operational vertical sounder.

SMITH W.L., WOOLF H.M., JACOB W.J. *Mon.Wea.Rev., 98, 582-603 (1970).* A regression method for obtaining real time temperature and geopotential height profiles from satellite spectrometer measurements and its application to NIMBUS-3 SIRS observations.

SMITH W.L., ZHOU F.X. *Appl.Opt., 21, 924-928 (1982).* Rapid extraction of layer relative humidity, geopotential thickness and atmospheric stability from satellite sounding radiometer data.

TWOMEY S. *Elsevier Co. (1977).* Introduction to the mathematics of inversion in remote sensing and indirect measurements.

HIRS Channel number	Channel central wavenumber	Central wavelength (μm)	Principal absorbing constituents	Level of peak energy contribution	Purpose of the radiance observation
1	668	15.00	CO_2	30 mb	*Temperature sounding.* The 15-μm band channels provide better sensitivity to the temperature of relatively cold regions of the atmosphere than can be achieved with the 4.3-μm band channels. Radiances in Channels 5, 6, and 7 are also used to calculate the heights and amounts of cloud within the HIRS field of view.
2	679	14.70	CO_2	60 mb	
3	691	14.50	CO_2	100 mb	
4	704	14.20	CO_2	400 mb	
5	716	14.00	CO_2	600 mb	
6	732	13.70	CO_2/H_2O	800 mb	
7	748	13.40	CO_2/H_2O	900 mb	
8	898	11.10	Window	Surface	*Surface temperature* and cloud detection.
9	1 028	9.70	O_3	25 mb	*Total ozone* concentration.
10	1 217	8.30	H_2O	900 mb	*Water vapor sounding.* Provides water vapor corrections for CO_2 and window channels. The 6.7-μm channel is also used to detect thin cirrus cloud.
11	1 364	7.30	H_2O	700 mb	
12	1 484	6.70	H_2O	500 mb	
13	2 190	4.57	N_2O	1 000 mb	*Temperature sounding.* The 4.3-μm band channels provide better sensitivity to the temperature of relatively warm regions of the atmosphere than can be achieved with the 15-μm band channels. Also, the short-wavelength radiances are less sensitive to clouds than those for the 15-μm region.
14	2 213	4.52	N_2O	950 mb	
15	2 240	4.46	CO_2/N_2O	700 mb	
16	2 276	4.40	CO_2/N_2O	400 mb	
17	2 361	4.24	CO_2	5 mb	
18	2 512	4.00	Window	Surface	*Surface temperature.* Much less sensitive to clouds and H_2O than the 11-μm window. Used with 11-μm channel to detect cloud contamination and derive surface temperature under partly cloudy sky conditions. Simultaneous 3.7- and 4.0-μm data enable reflected solar contribution to be eliminated from observations.
19	2 671	3.70	Window	Surface	
20	14 367	0.70	Window	Cloud	*Cloud detection.* Used during the day with 4.0- and 11-μm window channels to define clear fields of view.

MSU	Frequency (GHz)	Principal absorbing constituents	Level of peak energy contribution	Purpose of the radiance observation
1	50.31	Window	Surface	*Surface emissivity* and *cloud attenuation* determination.
2	53.73	O_2	700 mb	*Temperature sounding.* The microwave channels probe through clouds and can be used to alleviate the influence of clouds on the 4.3- and 15-μm sounding channels.
3	54.96	O_2	300 mb	
4	57.95	O_2	90 mb	

SSU	Wavelength (μm)	Principal absorbing constituents	Level of peak energy contribution	Purpose of the radiance observation
1	15.0	CO_2	15.0 mb	*Temperature sounding.* Using CO_2 gas cells and pressure modulation, the SSU observes thermal emissions from the stratosphere.
2	15.0	CO_2	4.0 mb	
3	15.0	CO_2	1.5 mb	

Table 1.

Characteristics of TIROS Operational Vertical Sounder (TOVS) channels

from Smith et al., 1979

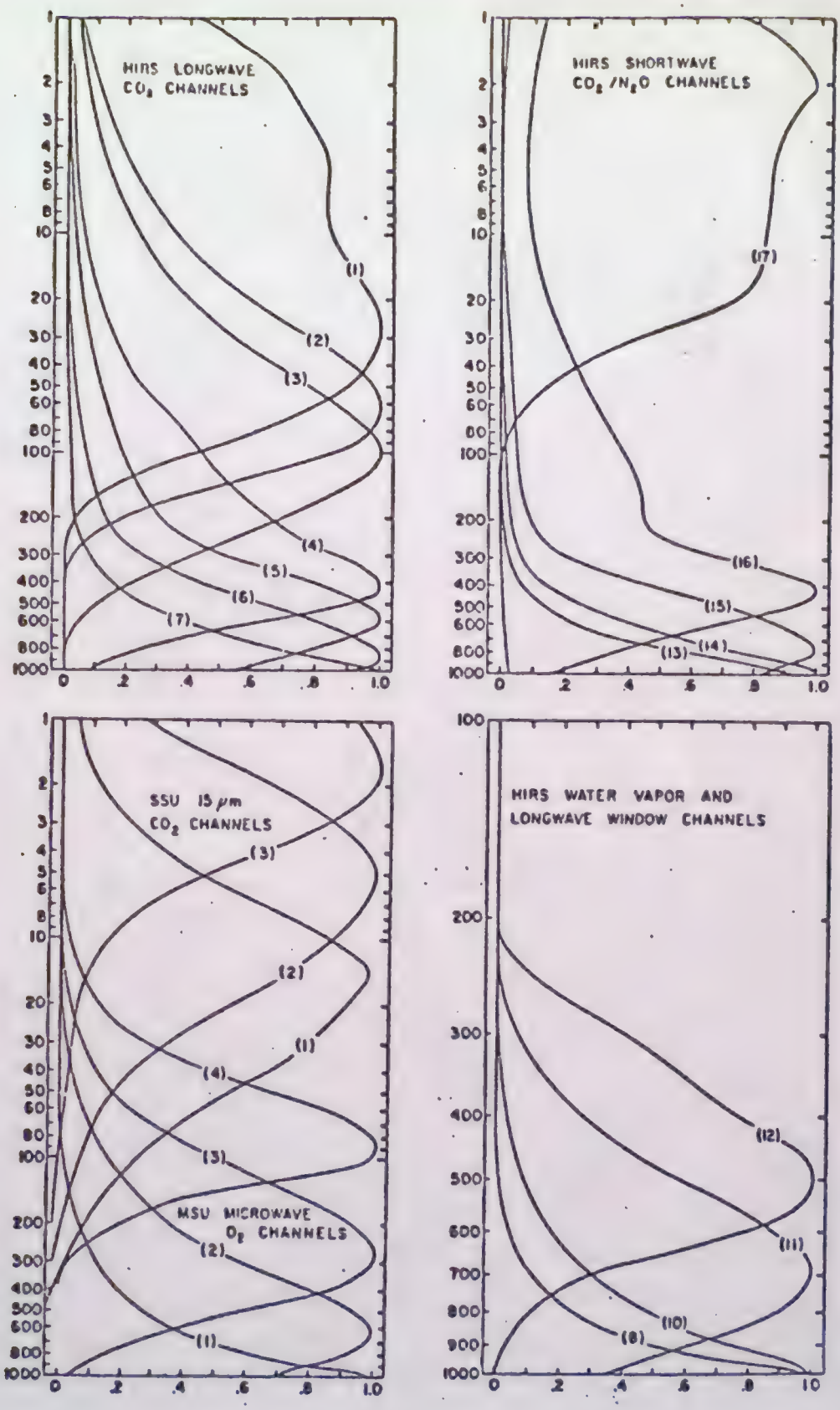

Figure 1

TOVS weighting functions

from Smith et al., 1979

FIGURE 2. SCHEMATIC REPRESENTATION OF REGRESSION AND PHYSICAL RETRIEVALS

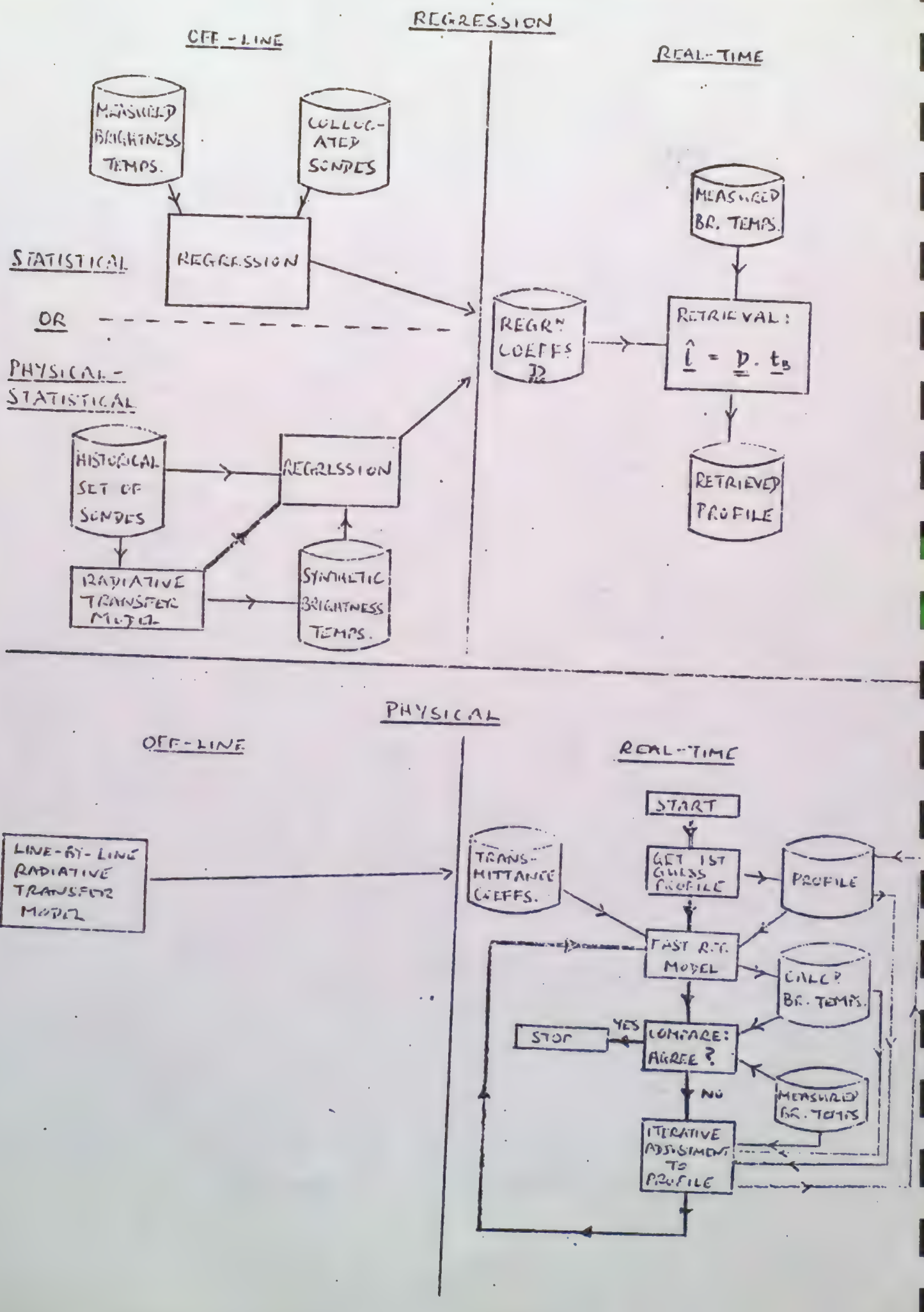

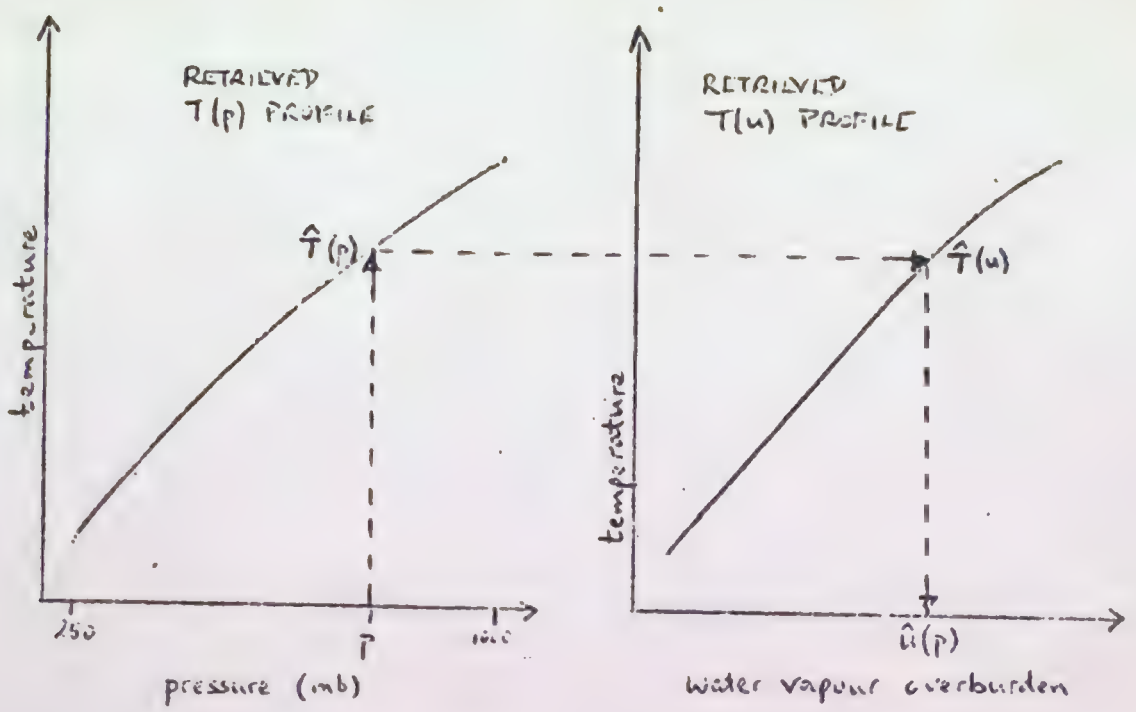

FIGURE 3. ILLUSTRATING THE RETRIEVAL OF WATER VAPOUR OVERBURDEN PROFILE USING THE METHOD OF ROSENKRANZ ET AL. (1982).

ADVANCED LECTURES - SATELLITE METEOROLOGY - 1987

LECTURE 5: THE HERMES LOCAL-AREA SOUNDING SYSTEM: AN EXAMPLE OF A PRACTICAL RETRIEVAL SCHEME

by J.R.Eyre (Updated by R.J.Allam)

1. Introduction

In 1983 a system was established in Met O 19 to process routinely data received locally from the TIROS Operational Vertical Sounder (TOVS) instruments on the TIROS-N series of polar-orbiting satellites. The system, known as HERMES (High-resolution Evaluation of Radiances from MEteorological Satellites), has two functions: processing TOVS data for use in operational forecasting, and research and development on satellite data interpretation techniques. In this lecture we shall consider details of the retrieval scheme currently used for TOVS data processing and the areas of potential future improvement. A description of the system in its development phase is given by Eyre and Jerrett (1982) and some case study results are presented in Jerrett et al. (1982).

2. Scientific overview

2.1 The radiometers

Operational atmospheric sounding is currently performed by the TOVS instruments described by Schwalb (1978) and Werbowetzki (1981). Briefly, each satellite carries 3 sounding radiometers collectively known as TOVS:

- The High-resolution Radiation Sounder (HIRS), which has 19 infra-red channels (and one visible channel) for measuring temperature in the troposphere and lower stratosphere, and for sounding tropospheric humidity.
- The Microwave Sounding Unit (MSU), which has 4 channels at frequencies around 55 GHz for measuring tropospheric and lower stratospheric temperature. It has inferior horizontal and vertical resolution to HIRS, but its measurements are affected relatively little by the presence of cloud.
- The Stratospheric Sounding Unit (SSU), which has 3 infra-red channels around 15 μm wavelength and uses a pressure modulation technique for sensing radiation from the middle and upper stratosphere (see Miller et al., 1980).

The details of the channels of these instruments are given in table 1. Considerable use has been made of SSU data for global stratospheric analysis. However, the retrieval scheme described here is intended to produce high-resolution tropospheric retrievals on a regional scale. Consequently it does not make use of SSU data (although it could be extended to do so).

Each instrument scans the Earth from left to right covering a swath below the satellite as illustrated in figure 1. (The scan

pattern of SSU is similar to that of MSU but covers a swath of reduced width, i.e. about 1500 km.) The horizontal resolution of the products obtained from each instrument cannot exceed that imposed by the separation of adjacent fields-of-view. This is on average about 40 km for HIRS and about 170 km for MSU.

2.2 The data processing scheme

The scheme used is similar in most respects to the global operational system used by NOAA/NESDIS, Washington D.C., to generate the soundings which are distributed internationally as SATEM messages (see Smith et al., 1979). The major difference concerns the horizontal resolution of the retrieved products: NESDIS derive products from "boxes" of 7 x 9 HIRS soundings with a spacing of about 300 km, whereas the HERMES scheme seeks to exploit more fully the resolution of the original data.

The retrieval scheme in current use was obtained from the NOAA/NESDIS Development Laboratory at the Co-operative Institute for Meteorological Satellite Studies, Madison, Wisconsin, and the scientific content of the scheme has been modified only slightly. The major elements of the data processing are presented below:

(i) "Decommutation"

The first stage in the processing chain "catches" the data broadcast by the satellite in real-time and received at the RAE site in Lasham, Hampshire. It unpacks the raw data stream, checks the gross structure of the data and strips out HIRS and MSU measurements.

(ii) Calibration

The raw data are in the form of digital counts and must be converted into physical units. This is done using the

calibration information in the data stream, as described in section 3.

(iii) Earth-location

The latitude and longitude of each sounding are calculated using knowledge of the satellite's orbital characteristics and the instruments' scanning geometries. The TBUS messages received daily from the USA over the GTS update the parameters of the satellite's orbit. This information acts as input data to an orbital prediction model which is used to calculate the sub-satellite point for any time up to a few days ahead with an accuracy sufficient for TOVS data location. Simple geometry allows the latitude and longitude of the sounding to be derived given the sub-satellite point, the inclination of the orbit, the satellite altitude and the scan angle of the instrument relative to the satellite.

(iv) "Pre-processing"

The next step consists of a series of small corrections to the measured brightness temperatures to put them into a form suitable for the inversion process. These include:

- correcting the HIRS brightness temperatures for scan angle, i.e. converting values at the angle of measurement to values which would have been measured if the instrument had been viewing vertically,
- correcting the HIRS window channels (numbers 8, 18 and 19) for the effects of atmospheric water vapour,
- correcting MSU brightness temperatures for scan angle,
- correcting MSU values for surface emissivity effects, i.e. correcting measured values to those which would have

been measured if the surface were black,

- o correcting MSU for the angular dependence of its antenna gain to obtain the values which would have been measured if the instrument had an infinitely narrow angular response,

- o interpolating MSU brightness temperatures to HIRS sounding locations.

The scan angle and other corrections are performed using regressions against other channels as explained in section 4. For MSU, the corrections for the 3 physical effects are combined into one regression-based correction.

(v) Cloud-clearing

This step treats the problem of cloud-contamination of infra-red radiances. The variables required at the end of this stage are, for each channel, the brightness temperature that would be measured from the profile if no cloud had been present, (the "clear-column radiance"), together with an estimate of the error in this value. Essentially, the method classifies the pre-processed brightness temperatures roughly according to their degree of cloud-contamination.

- o If the HIRS radiances are identified as cloud-free, a low error is attributed.

- o If the HIRS radiances are identified as cloud-contaminated and are amenable to cloud-clearing then the clear-column radiances are estimated as described in section 5.

- If the cloud-contamination is such that clear HIRS radiances cannot be accurately estimated, the clear-column HIRS brightness temperatures are estimated from MSU data using multiple linear regression.

Having obtained estimates of the brightness temperatures and their expected errors for all channels at every HIRS spot, these estimates are improved by combining data from surrounding spots. These data are weighted by their errors; a "clear" profile will be given more weight than an "MSU" profile. Actually, the combination process is achieved by moving a filter through the data, first forwards, and then backwards. The details are in Eyre and Watts (1987). The end result is a complete field of brightness temperatures with optimal error characteristics.

(vi) Inversion

As explained in lecture 4, the inversion is performed using a multiple linear regression relation which estimates vectors of temperature, $\underline{t}$, and humidity mixing ratio, $\underline{c}$, (expressed at standard pressure levels) from the vector of pre-processed, cloud-free (or cloud-cleared) brightness temperatures, $\underline{t}_B$:

$$\hat{\underline{t}} = \underline{\underline{D}} \cdot \underline{t}_B \qquad \cdots 2.1$$

$$\hat{\underline{c}} = \underline{\underline{D}}' \cdot \underline{t}_B \qquad \cdots 2.2$$

where all vectors are expressed as differences from mean vectors.

The predictive matrices $\underline{\underline{D}}$ and $\underline{\underline{D}}'$ (and the corresponding mean vectors) used to be obtained from a large set of collocated radiance measurements and radiosonde profiles by multiple linear regression on the eigenvector coefficients of the

appropriate covariance matrices (Smith and Woolf, 1976). The regression coefficients were updated every week by NOAA/NESDIS using collocations collected during the previous 2 weeks.

This use of global statistics, which are derived mainly from continental radio-sonde stations and are not characteristic of our air-mass climatology, was suspected of producing unnecessary error. Thus, the scheme was replaced in July 1985 by one that uses a carefully selected historical set of radiosonde profiles from the European / N. Atlantic area. The HIRS and MSU brightness temperatures corresponding to each radio-sonde profile can be calculated using a radiative transfer model. The set of real radio-sonde temperatures and synthetic brightness temperatures was processed as before using multiple linear regression on eigenvectors to give the predictive matrices. This scheme avoids any errors arising from the poor collocation of the radio-sonde and the satellite profile, but does rely upon an accurate radiative model.

For temperature retrieval both HIRS and MSU brightness temperatures are used in the vector, $\underline{t}_B$. At present HIRS channels 1-16 and MSU channels 2-4 are employed. HIRS channels 17-19 are subject to contamination by solar radiation and are difficult to use during the day-time. MSU channel 1 is a window channel and its interpretation is complicated by uncertainties in surface emissivity. It is therefore applied indirectly to correct other MSU channels for minor surface emissivity effects but is not itself used in the inversion. The mixing ratio retrieval uses the HIRS channels sensitive to humidity as well as those use for

temperature sounding. In this way information on the temperature profile, which is necessary for accurate humidity retrieval, enters the solution indirectly.

(vii) Derived quantities and additional processing

A number of additional checks and computations are performed following the inversion. The most notable are as follows:

- Mixing ratios are converted to dew points.
- The estimated profiles are integrated to provide quantities representing layer mean values, i.e. geopotential thickness and layer precipitable water, for layers between standard pressure levels.
- Using each retrieval as a processing centre, the local gradient of the thickness field is computed from a group of neighbouring soundings. This gradient is then expressed as a geostrophic thermal wind. These values do not contain any information which is not present in the thicknesses, but they are found helpful in visualising the fields when expressed in chart form and may prove useful as inputs to numerical analyses (see section 6).

Figure 2 gives an example of a plotted chart obtained from derived products and shows the 1000-500 mb thickness values and associated thermal winds retrieved from 3 consecutive passes of NOAA-10 data. Figure 3 gives an example of a retrieved vertical profile together with a collocated radiosonde ascent.

3. Calibration of HIRS and MSU

For HIRS, calibration measurements are made every 40 scan lines and occupy 3 scan lines (for which no earth-view data are available). During this period the instrument views an internal black-body target, the temperature of which is monitored. This gives a warm reference point. A cold reference point is obtained by viewing space, which acts as a black body at about 3 K, essentially a zero radiance target. Since the radiometer is designed to give an output linearly related to the incoming radiance, it can be calibrated as shown in figure 4.

The calibrated radiance for each channel is converted to an equivalent black body temperature ("brightness temperature") using a relation containing the inverse Planck function:

$$T_B = a + b\left\{\frac{c_2 \nu_0}{\ln\left[\frac{c_1 \nu_0^3}{R} + 1\right]}\right\} \quad \ldots 3.1$$

where $c_1 = 1.1911 \times 10^{-8}$ W.m^{-2}.sr^{-1}.(cm^{-1})$^{-1}$,

$c_2 = 1.4388$ K.(cm^{-1})$^{-1}$

ν_0 is the central wavenumber of the channel,

and R is the calibrated radiance.

a and b are known as "band correction coefficients". They allow for the fact that the radiometer channel is not monochromatic and are determined numerically using the spectral response of the radiometer channel (see Lauritson et al., 1979). For a narrow band radiometer such as HIRS $a \ll T_B$ and $b \approx 1$.

For MSU, the calibration sequence takes place at the end of each scan line and so no earth view data are lost. Again a 2-point calibration is provided from warm and cold reference sources. However, for MSU channel frequencies and typical earth-view temperatures, the measured radiances are in the Rayleigh-Jeans

tail of the Planck function, where radiance is proportional to brightness temperature. Therefore the data may be calibrated into brightness temperatures directly.

4. Limb correction

This term is used to describe the process whereby a brightness temperature measured at a non-zero nadir angle is corrected to provide an estimate of the value which would have been measured if the instrument had viewed the same volume of atmosphere vertically. The physical effect which necessitates this correction is illustrated in figure 5. As the angle of view moves away from the vertical, the path length of the radiation through the atmosphere increases. Therefore the transmittances from all levels to space decrease and the peak of the weighting function rises (see lecture 2). If the channel senses radiation from an atmospheric layer in which there is a temperature lapse rate, then the measured radiance will change; for tropospheric channels it will tend to decrease.

It would, of course, be possible to remove the need for a limb correction by using a temperature retrieval algorithm with a different set of regression coefficients for each scan angle, or by using a physical retrieval method in which radiances are applied at their angle of measurement. However, because we have chosen to perform a regression retrieval in which one set of coefficients (appropriate to a zero scan angle) is used, we must convert all brightness temperatures to this form.

Adequately accurate limb corrections are possible because the weighting function of the nadir view for one channel will, in general, peak at a level intermediate between the weighting

function peaks of 2 channels at the angle of measurement. Thus, for a given angle, θ, we may express the difference between the brightness temperature at nadir and at the angle of measurement as a linear combination of the measured brightness temperatures in a number of channels:

$$(T_B)_i^{\theta=0} - (T_B)_i^{\theta} = a_{oi}^{\theta} + \sum_{j=1}^{J} a_{ji}^{\theta} (T_B)_j^{\theta} \quad \cdots 4.1$$

The coefficients, a_{ji}^{θ} are found by multiple linear regression on synthetic brightness temperatures computed for a representative set of profiles.

5. Cloud-clearing

Infra-red radiances are affected markedly by the presence of clouds, since most are almost opaque in this wavelength region. Consequently the algorithms used in the retrieval of tropospheric temperature must be able to detect clouds which have a significant effect on the radiances and, if possible, make allowances for these effects. This is usually done by correcting the measured radiances to obtain "clear-column" values, i.e. the radiances which would be measured from the same temperature and humidity profiles in the absence of cloud. In most retrieval schemes the inversion process converts clear-column radiances to atmospheric parameters and so a preliminary cloud-clearing step is required.

A review of cloud-clearing methods is given by Eyre (1983). Many of the algorithms developed, including the one used in this retrieval scheme, are variants of the adjacent field-of-view or N* method first proposed by Smith (1968). In this approach, the measured radiances, R_1 and R_2, in two adjacent fields-of-view (hereafter referred to as "spots") of a radiometer channel can,

under certain conditions, be expressed as follows:

$$\left.\begin{aligned} R_1 &= N_1 R_{cloudy} + (1-N_1) R_{clear} \\ R_2 &= N_2 R_{cloudy} + (1-N_2) R_{clear} \end{aligned}\right\} \quad \cdots 5.1$$

where R_{clear} and R_{cloudy} are the radiances appropriate to clear and completely overcast conditions respectively, and N_1 and N_2 are the effective fractional cloud coverages in spots 1 and 2. In deriving these equations the following assumptions have been made:

- o that the atmospheric profile and surface characteristics in the two spots are the same,
- o that only one layer of cloud is present,
- o that the cloud top has the same height (and temperature) in both spots.

If the fractional cloud coverages in the two spots are different ($N_1 \neq N_2$), then equations 5.1 may be solved simultaneously to give the clear radiance:

$$R_{clear} = \frac{R_1 - N^* R_2}{1 - N^*} \qquad \cdots\cdots 5.2$$

where $N^* = N_1/N_2$. Alternatively,

$$N^* = \frac{R_{clear} - R_1}{R_{clear} - R_2} \qquad \cdots\cdots 5.3$$

and so N* can be found if we have an estimate of the clear radiance in one channel. The requirement for this additional piece of information leads to different practical formulations of the N* method suited to the type of data available and the products required, as explained below. Since N* is channel-independent, it can be used in equation 5.2 to find the clear radiance in all other channels. The method is illustrated in figure 6. For infra-red radiometers with moderately high

horizontal resolution (e.g. HIRS, with a field-of-view spacing of about 40 km), the inherent assumptions are true sufficiently often for the method to be useful. Various quality controls are applied to trap those cases for which the cloud field does not conform with the assumptions made.

The variant of this method used by NOAA/NESDIS for global retrievals is described by McMillin and Dean (1982). It has been developed specifically to meet the requirements for global, low-resolution retrievals on a scale of about 300 km. The Met O 19 system uses a variant more suited to regional and mesoscale applications, in which clear radiances are required at higher horizontal resolution.

The additional piece of information required for the solution of equation 5.3 is obtained from the measured value of MSU channel 2 which acts as a "pseudo-HIRS" channel. This approach is successful because the weighting functions of HIRS and MSU overlap, and the brightness temperature in MSU channel 2 can be predicted quite accurately from a linear combination of cloud-free HIRS brightness temperatures:

$$T_{MSU-2} \simeq b_0 + \sum_i b_i T_{HIRS-i} \quad \ldots . 5.4$$

The coefficients, b_i, are also calculated by regression on collocated measurements and are updated weekly by NOAA/NESDIS (although this is probably unnecessary). From equations 5.3 and 5.4, and assuming a linear relation between radiance and brightness temperature, we can obtain an expression for N*:

$$N^* = \frac{T_{MSU-2} - b_0 - \sum_i b_i T_{1i}}{T_{MSU-2} - b_0 - \sum_i b_i T_{2i}} \quad \ldots 5.5$$

where T_{1i} and T_{2i} are the measured HIRS brightness temperatures in channel i for spots 1 and 2 respectively, and T_{MSU-2} is the

measured brightness temperature in MSU channel 2 interpolated to the central HIRS spot. (The assumption of linearity between radiance and brightness temperature is an approximation which can lead to large errors in certain cases. This aspect of the cloud-clearing could be improved and is currently under review.) In the present implementation of the N* method, N* is calculated separately for the HIRS longwave tropospheric channels (4-12) and the shortwave tropospheric channels (13-16) in an attempt to allow for an instrument effect which may cause small differences in field-of-view location for the two sets of channels. For each pair of spots, the processing is only allowed to continue for values of N* less than 0.75. If N* is greater than 0.75, the error amplification is considered too large; physically, the spots are too similar for the N* technique to apply.

From all the sets (up to 8) of successfully cloud-cleared HIRS radiances generated from 8 N* calculations, plus the set of "clear" radiances (i.e. the measured radiances treated as cloud-free), the set is chosen which leads to the best agreement between N* values calculated separately for HIRS long-wave and short-wave channels.

6. Error characteristics

The accuracy of satellite retrievals is difficult to assess; as with many other observing systems, we are faced with the problem of "what is truth?". A widely-used method of assessing accuracy is the study of statistics of differences between retrievals and collocated radiosonde profiles. Such statistics will include the retrieval errors but will also contain contributions from radiosonde errors (which include the effects of both discrepancies from the true profile along the radiosonde ascent

path and also the degree to which this profile is representative of the surrounding volume of atmosphere) and collocation errors caused by the separation in space and time between the satellite sounding and the radiosonde ascent. Although retrieval-radiosonde collocation statistics are very useful, they should not be treated simply as measurements of retrieval error.

Figure 7 shows typical statistics from the HERMES retrieval system. The bias and standard deviation profiles for retrieval-radiosonde differences are shown. These are based on all collocations obtained from NOAA-7 retrievals during October 1983, with collocation criteria of ±3 hours time separation and 150 km horizontal separation. If the set of profiles in the collocations and the set from which the regression coefficients have been generated are large and both are representative of the same population, then the biases in these statistics should be very small. The biases found, about 1 degree at some pressure levels, are to be expected here, where collocations for a limited period and limited area may not be representative of a zonal set. The standard deviations, while they are larger than the equivalent values for retrieval errors alone, exhibit some of the expected characteristics of the retrieval error profile. They have a minimum in the mid-troposphere, with higher values near the surface and at the tropopause. The lower tropospheric values reflect problems associated with residual cloud contamination and various surface effects. Low level inversions will also tend to cause retrieval problems. The tropopause values reflect both the lack of information in the radiances from this part of the profile and also the tendency of the regression coefficients to "smooth out" features of this type.

It is possible to assess theoretically the accuracy which should be attained by studying the residual error in the regression between a set of profiles and corresponding calculated brightness temperatures, using realistic values for the "noise" in the cloud-cleared brightness temperatures. A theoretical error curve, obtain in this way from 400 profiles chosen to be representative of September conditions for the European and N. Atlantic areas, is also shown in figure 7. This represents the attainable limit for this combination of instruments with this retrieval scheme.

The errors in humidity retrievals are more difficult to study because of increased problems with radiosonde errors and the horizontal scales of humidity field fluctuations. Statistics from the HERMES system are currently showing standard deviations in dew point differences of about 6-7 degrees between retrievals and sondes. There are indications that retrieval errors are the major contributors below 800 mb, but that radiosonde errors (and failures to be representative of the surrounding atmospheric volume) are more important in the mid-troposphere, although this has not yet been clearly demonstrated.

A further aspect of the error characteristics which should be taken into account when using the data in numerical analysis concerns the spatial correlation of retrieval errors. Radiance measurements from channels with broad, overlapping weighting functions will lead to errors which are correlated in the vertical. Also the strong association between retrieval errors and profile shape will often lead to similar errors in adjacent profiles where the true atmospheric profiles are similar. This horizontal correlation of error can be put to good use, because it assist accurate computation of the gradient (i.e. geostrophic

thermal wind) in the retrieved field, which may itself be a useful analysis parameter.

Another method of estimating the errors in the retrieved profiles is to compare them against model analyses for the same time. Unfortunately, this introduces an element of circularity, since satellite soundings obtained previously contribute to the analysed fields. There are also problems of using fields appropriate to an asynoptic pass time, and in interpolating in space from a mesh of grid points to HIRS spot. Some work has been done in Met O 19, (Allam and Maine 1984), to compare retrieved 1000-500 mbar thicknesses with model analyses. Linear interpolation from fields of model data available at six-hour intervals was used to provide the comparison. The assumption made here was that the model analyses provide the best consistent information about the structure of the atmosphere!

Figure 8 shows a summary of the qualitative bias patterns found in the study. An analogous technique could be used to obtain the same type of quantitative statistics as those currently derived for collocated radio-sondes. Comparisons with the fine-mesh model's background field have started by using the Operational Product Data Base.

7. Future improvements

The retrieval scheme described above has been implemented with the intention of its output being used in operational forecasting, because the products are considered to have reached a level of accuracy at which they are potentially useful, particularly in data sparse regions. However, it is recognised that there is considerable scope for improvement in several

aspects of the retrieval process.

A number of minor improvements are planned in the calibration and limb-correction algorithms, the treatment of sea-ice, the mapping of MSU data to HIRS locations and others. In addition, more fundamental changes to the retrieval process will be tested. Better results might be expected if the cloud-clearing preceded the limb-correction. Another avenue of investigation with potential for improving the cloud-clearing concerns the use of Advanced Very High Resolution Radiometer (AVHRR) data. From this imagery, it is possible to extract information on the cloud field and surface temperature which should be of considerable value in the derivation of clear radiances. Successful developments in these areas are expected to improve the quality of retrievals in the lower troposphere.

A major change in the retrieval scheme is currently being tested. The motivation for this change comes from considerations of the final use of the soundings, that is, as input to a numerical model. The current method of producing profiles of temperature and assimilating them into the model as if they were poor-quality radio-sonde data can degrade the analysis. This occurs principally because the retrieved profiles contain information dependent upon the first-guess used in the inversion. The problem is particularly acute when a climatological first-guess profile is used; this is likely to differ markedly in shape from the true atmospheric profile. Data assimilation should recognise this dependence and compensate for it. Effectively, it is the difference between the retrieval and its first-guess that contains new information from the measured radiances, and which the model should attempt to assimilate.

The forecast first-guess method defines a vector of quantities that have a significant effect upon the TOVS radiances. These would include surface pressure and surface microwave emissivity as well as the more obvious temperature and humidity profiles. A vector of these quantities derived from an appropriate forecast would be needed for each vector of measured radiances. The retrieved vector would be computed using the vector equation:-

$$\hat{\underset{\sim}{x}} = \underset{\sim}{x}_1 + \underset{\sim}{C} \cdot \underset{\sim}{K}^T \cdot \left(\underset{\sim}{K} \cdot \underset{\sim}{C} \cdot \underset{\sim}{K}^T + \underset{\sim}{E} \right)^{-1} \cdot \left(\underset{\sim}{y}_m - \underset{\sim}{y}\{\underset{\sim}{x}_1\} \right) \quad \cdots 7.1$$

where,

$\underset{\sim}{x}_1$ is the first guess for the profile vector obtained from the forecast model,

$\underset{\sim}{C}$ is the covariance of the first guess error,

$\underset{\sim}{y}_m$ is the vector of measured (pre-processed and cloud-cleared) brightness temperatures,

$\underset{\sim}{E}$ is the error covariance of $\underset{\sim}{y}_m$,

$\underset{\sim}{y}(\underset{\sim}{x}_1)$ is the brightness temperature vector calculated from the first guess,

$\underset{\sim}{K}$ is a matrix containing the partial derivatives of the elements of $\underset{\sim}{y}$ with respect to the elements of $\underset{\sim}{x}$ (ideally estimated at $\underset{\sim}{x} = \underset{\sim}{x}_1$).

The rather complicated form of this equation can be explained using a scalar analogy. Consider the combination of two estimates of the same variable 'x' that have different expected error variance:

x_1 with error variance σ_1^2

x_2 with error variance σ_2^2

The best combined estimate of 'x' (that is the one with minimum

variance and, for normally distributed errors, the maximum probability) is given by;

$$\hat{x} = \frac{x_1/\sigma_1^2 + x_2/\sigma_2^2}{1/\sigma_1^2 + 1/\sigma_2^2} \qquad \ldots\ldots 7.2$$

This can be rearranged to give:-

$$\hat{x} = x_1 + \frac{\sigma_1^2 (x_2 - x_1)}{\sigma_1^2 + \sigma_2^2} \qquad \ldots\ldots 7.3$$

In the case of our inversion, we measure a vector of radiances and determine temperatures. In the scalar analogue, assume that the second measurement is actually made of a variable 'y' related to 'x' through the relation;

$$y = kx + c$$

where 'k' and 'c' are assumed constant and known.

Thus:-

$$x_2 = (y_2 - c) / k$$

with $\sigma_2^2 = \sigma_y^2 / k^2$

Substitution into equation 7.3 gives:-

$$\hat{x} = x_1 + \sigma_1^2 . \left(\sigma_1^2 + \sigma_y^2/k^2\right)^{-1} . \left(\frac{y_2 - c}{k} - x_1\right) \qquad \ldots\ldots 7.4$$

$$= x_1 + \sigma_1^2 k \left(k\sigma_1^2 k + \sigma_y^2\right)^{-1} . \left(y_2 - \{kx_1 + c\}\right) \qquad \ldots\ldots 7.5$$

or

$$\hat{x} = x_1 + \sigma_1^2 k \left(k\sigma_1^2 k + \sigma_y^2\right)^{-1} . \left(y_2 - y\{x_1\}\right) \qquad \ldots\ldots 7.6$$

where $y(x_1) = k.x_1 + c$, the value of 'y' corresponding to the first-guess value 'x_1'.

The vector generalisation of this relation is:-

$$\hat{\underset{\sim}{x}} - \underset{\sim}{x}_1 = \underset{\sim}{C} \cdot \underset{\sim}{K}^T \cdot \left(\underset{\sim}{K} \cdot \underset{\sim}{C} \cdot \underset{\sim}{K}^T + \underset{\sim}{E} \right)^{-1} \cdot \left(\underset{\sim}{y}_2 - \underset{\sim}{y}\{\underset{\sim}{x}_1\} \right) \quad \cdots 7.7$$

where,

$\underset{\sim}{C}$ and $\underset{\sim}{E}$ are the error covariances of the first guess vector $\underset{\sim}{x}_1$ and measurement vector $\underset{\sim}{y}(\underset{\sim}{x})$ respectively,

$\underset{\sim}{K}$ contains partial derivatives of the elements of $\underset{\sim}{y}$ with respect to those of $\underset{\sim}{x}$.

^{T} denotes a matrix transpose.

Note that:

→ $\underset{\sim}{K} \cdot \underset{\sim}{C} \cdot \underset{\sim}{K}^T$ maps temperature errors to radiance errors, $\underset{\sim}{E}$,

→ $\underset{\sim}{C} \cdot \underset{\sim}{K}^T \cdot$"$\underset{\sim}{E}^{-1}$" maps radiance to temperature.

See Eyre (1987) for a fuller discussion.

Clearly, these quantities have to be specified. '$\underset{\sim}{K}$' can be computed using a radiative transfer model.

'$\underset{\sim}{x}_1$' can be obtained from the fine-mesh model. To date, appropriate fields at six-hourly intervals have been extracted and values pertaining to the time of the satellite pass computed by linear interpolation. An option would be to use a more accurate interpolation scheme, such as a cubic spline method. Spatial interpolation is performed using a bilinear method in latitude and longitude.

The covariance of the first-guess error, '$\underset{\sim}{C}$', has been estimated by comparing 12-hour forecasts and analyses for the same time. Both the standard deviations and their inter-level correlations of the differences at each level have been computed. Since the analysis and forecast errors are likely to be correlated, these results will under-estimate the true forecast errors. In fact,

work using comparisons between radio-sonde data and forecasts indicates that the estimate is a factor of 1.4 too small.

'$\underset{\sim}{y}$' is a vector of TOVS brightness temperatures with corrections made for the presence of cloud in the field of view. The corresponding error covariance matrix, '$\underset{\sim}{C}$'. This has been assumed to be diagonal; the correlation between errors at different levels is assumed to be zero. The magnitude of the diagonal elements have been set (rather arbitrarily) to be between the radiometric noise and the standard deviations of the differences between measured brightness temperatures and those calculated using collocated radio-sonde temperature profiles.

REFERENCES

Allam R.J., Maine D.
Met O 19 Working Paper No 2 (1984)
(Available in Met O 19 only)
Note on the comparison of asynoptic HERMES thicknesses with fine-mesh analyses at synoptic hours.

Eyre J.R.
Met O 19 Branch Memorandum 72 (1983).
Towards an optimal approach to cloud-clearing for satellite temperature sounding.

Eyre J.R.
Met O 19 Working Paper 11 (1985).
(Available in Met O 19 only)
A theoretical assessment of a TOVS inversion scheme which uses forecast first-guess information.

Eyre J.R., Jerrett D.
Weather, 37, 314-322 (1982).
Local-area atmospheric sounding from satellites.

Eyre J.R., Watts P.D.
Submitted to QJ Royal Met Soc
A sequential estimation approach to cloud-clearing for satellite temperature sounding.

Jerrett D., Eyre J.R., McCallum E.
Proc.Annual Tech.Conf.Remote Sensing Society (Liverpool, Dec. 1982), pp. 230-237 (1983).
High resolution soundings of temperature in the European / N. Atlantic area.

Lauritson L., Nelson G.J., Porto F.W.
NOAA Technical Memorandum NESS 107 (1979).
Data extraction and calibration of TIROS-N/NOAA radiometers.

McMillin L.M., Dean C.
J.Appl.Meteor., 12,1005-1014 (1982).
Evaluation of a new operational technique for producing clear radiances.

Miller D.E., Brownscombe J.L., Carruthers G.P., Pick D.R., Stewart K.H.
Phil.Trans.R.Soc.Lond., A296, 65-71 (1980).
Operational temperature sounding of the stratosphere.

Schwalb A.
NOAA Technical Memorandum NESS 95 (1978).
The TIROS-N/NOAA A-G satellite series.

Smith W.L.
Mon.Wea.Rev., 96, 387-396 (1968).
An improved method for calculating tropospheric temperature and moisture profiles from satellite radiometer measurements.

Smith W.L., Woolf H.M.
J.Atmos.Sci., 33, 1127-1140 (1976).
The use of eigenvectors of statistical covariances matrices for interpreting satellite sounding radiometer observations.

Smith W.L., Woolf H.M., Hayden C.M., Wark D.Q., McMillin L.M.
Bull.Amer.Meteor.Soc., 60, 1177-1187 (1979).
The TIROS-N operational vertical sounder.

Werbowetzki A.
NOAA Technical Report NESS 83 (1981).
Atmospheric sounding user's guide.

HIRS Channel number	Channel central wavenumber	Central wavelength (μm)	Principal absorbing constituents	Level of peak energy contribution	Purpose of the radiance observation
1	668	15.00	CO_2	30 mb	*Temperature sounding.* The 15-μm band channels provide better sensitivity to the temperature of relatively cold regions of the atmosphere than can be achieved with the 4.3-μm band channels. Radiances in Channels 5, 6, and 7 are also used to calculate the heights and amounts of cloud within the HIRS field of view.
2	679	14.70	CO_2	60 mb	
3	691	14.50	CO_2	100 mb	
4	704	14.20	CO_2	400 mb	
5	716	14.00	CO_2	600 mb	
6	732	13.70	CO_2/H_2O	800 mb	
7	748	13.40	CO_2/H_2O	900 mb	
8	898	11.10	Window	Surface	*Surface temperature* and cloud detection.
9	1 028	9.70	O_3	25 mb	*Total ozone* concentration.
10	1 217	8.30	H_2O	900 mb	*Water vapor sounding.* Provides water vapor corrections for CO_2 and window channels. The 6.7-μm channel is also used to detect thin cirrus cloud.
11	1 364	7.30	H_2O	700 mb	
12	1 484	6.70	H_2O	500 mb	
13	2 190	4.57	N_2O	1 000 mb	*Temperature sounding.* The 4.3-μm band channels provide better sensitivity to the temperature of relatively warm regions of the atmosphere than can be achieved with the 15-μm band channels. Also, the short-wavelength radiances are less sensitive to clouds than those for the 15-μm region.
14	2 213	4.52	N_2O	950 mb	
15	2 240	4.46	CO_2/N_2O	700 mb	
16	2 276	4.40	CO_2/N_2O	400 mb	
17	2 361	4.24	CO_2	5 mb	
18	2 512	4.00	Window	Surface	*Surface temperature.* Much less sensitive to clouds and H_2O than the 11-μm window. Used with 11-μm channel to detect cloud contamination and derive surface temperature under partly cloudy sky conditions. Simultaneous 3.7- and 4.0-μm data enable reflected solar contribution to be eliminated from observations.
19	2 671	3.70	Window	Surface	
20	14 367	0.70	Window	Cloud	*Cloud detection.* Used during the day with 4.0- and 11-μm window channels to define clear fields of view.

MSU	Frequency (GHz)	Principal absorbing constituents	Level of peak energy contribution	Purpose of the radiance observation
1	50.31	Window	Surface	*Surface emissivity* and *cloud attenuation* determination.
2	53.73	O_2	700 mb	*Temperature sounding.* The microwave channels probe through clouds and can be used to alleviate the influence of clouds on the 4.3- and 15-μm sounding channels.
3	54.96	O_2	300 mb	
4	57.95	O_2	90 mb	

SSU	Wavelength (μm)	Principal absorbing constituents	Level of peak energy contribution	Purpose of the radiance observation
1	15.0	CO_2	15.0 mb	*Temperature sounding.* Using CO_2 gas cells and pressure modulation, the SSU observes thermal emissions from the stratosphere.
2	15.0	CO_2	4.0 mb	
3	15.0	CO_2	1.5 mb	

Table 1.

Characteristics of TIROS Operational Vertical Sounder (TOVS) channels

From Smith et al., 1979

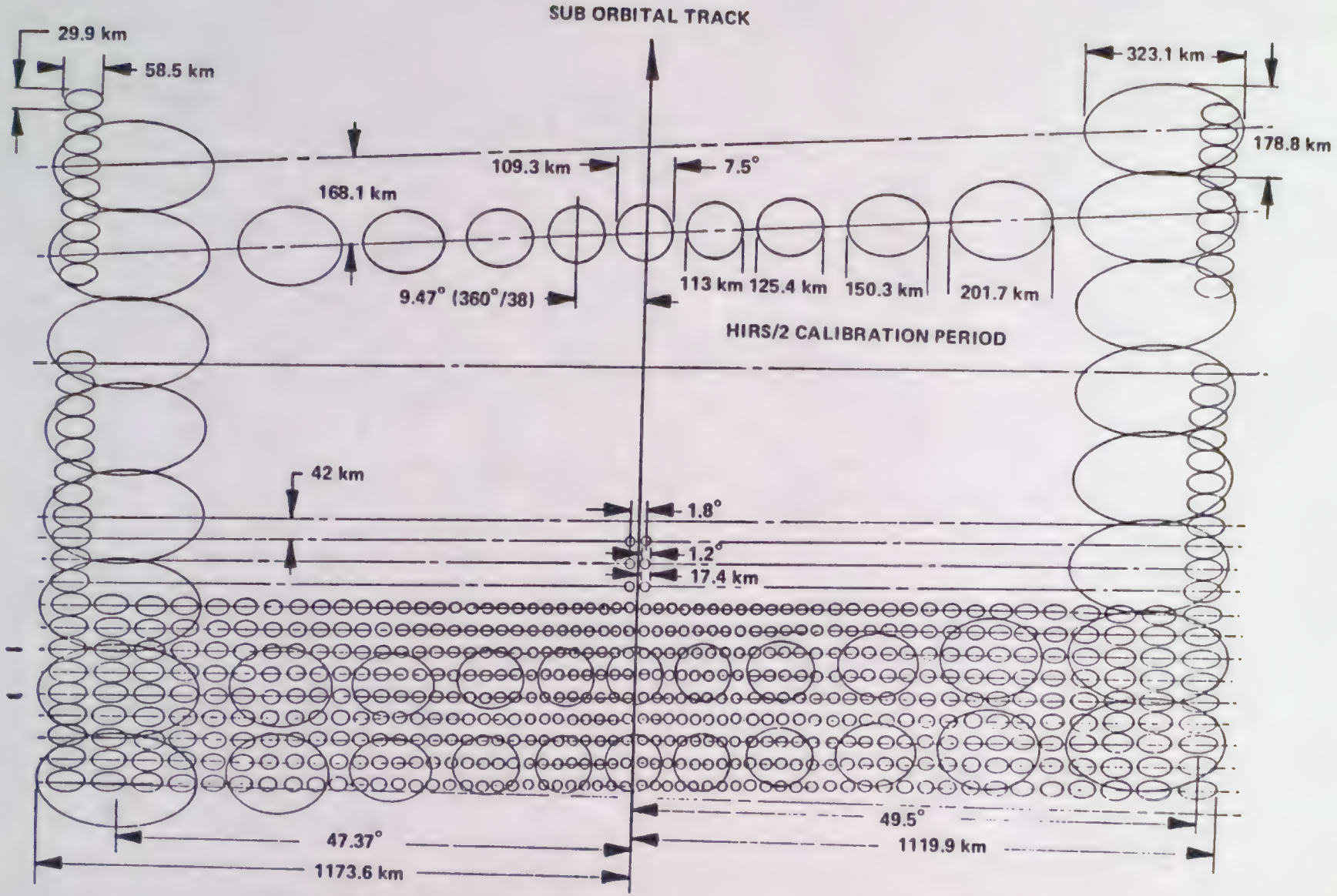

Figure 1 .--TIROS Operational Vertical Sounder HIRS/2 and MSU scan patterns projected on earth

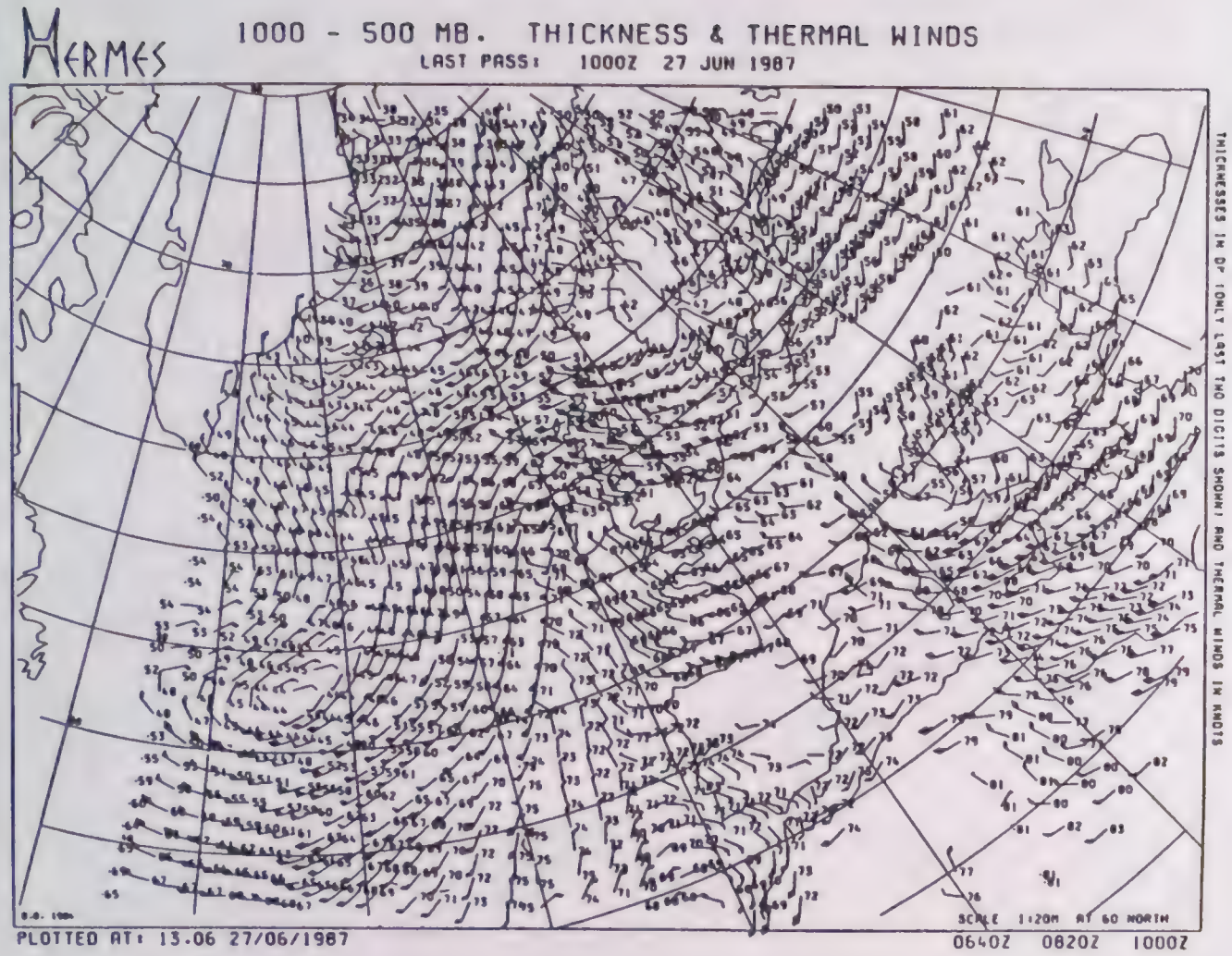
HERMES
1000 - 500 MB. THICKNESS & THERMAL WINDS
LAST PASS: 1000Z 27 JUN 1987
THICKNESSES IN DP (ONLY LAST TWO DIGITS SHOWN) AND THERMAL WINDS IN KNOTS
SCALE 1:20M AT 60 NORTH
PLOTTED AT: 13.06 27/06/1987
0640Z 0820Z 1000Z

Figure 2

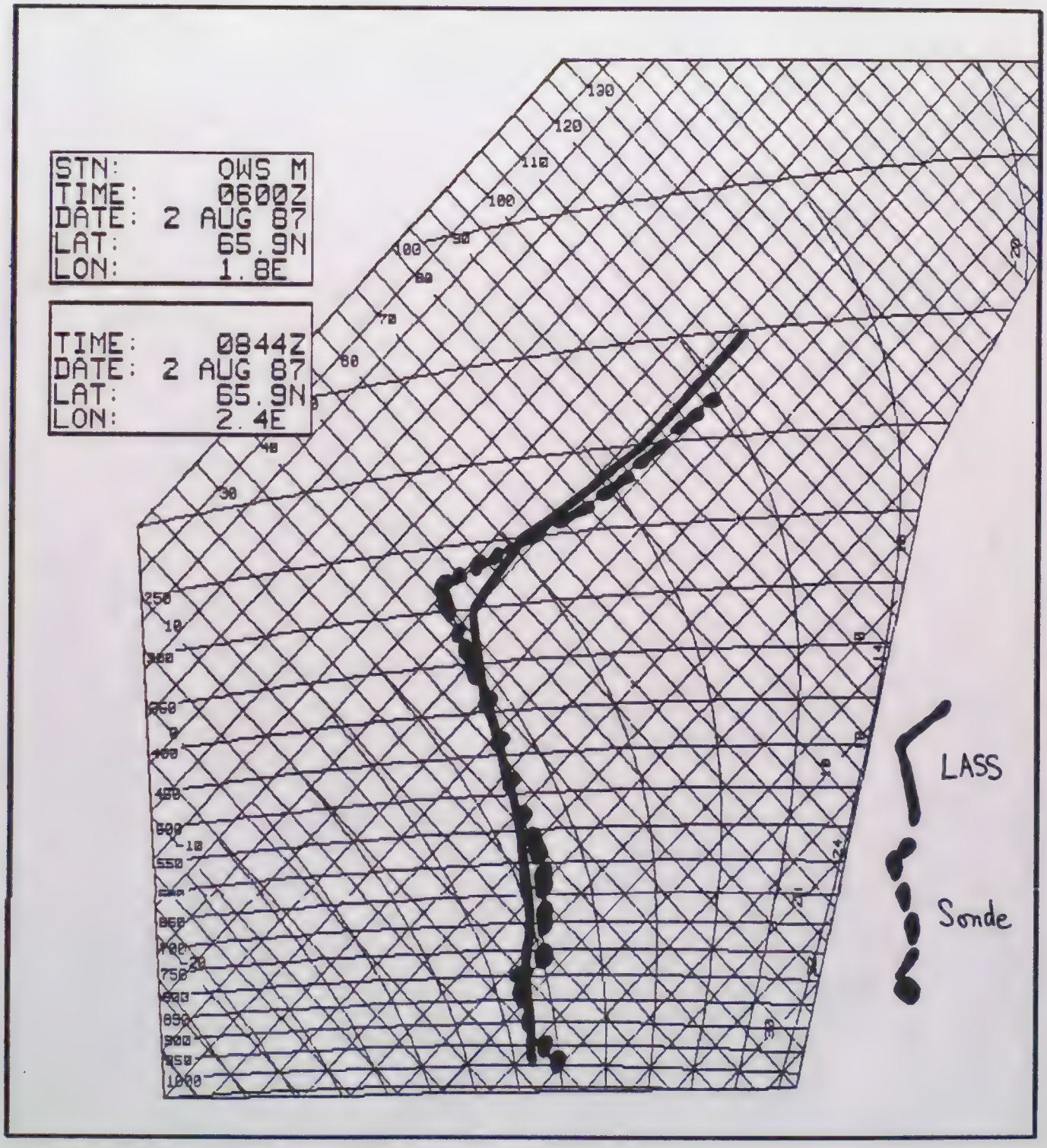
STN: QWS M
TIME: 0600Z
DATE: 2 AUG 87
LAT: 65.9N
LON: 1.8E
TIME: 0844Z
DATE: 2 AUG 87
LAT: 65.9N
LON: 2.4E
LASS
Sonde

Figure 3

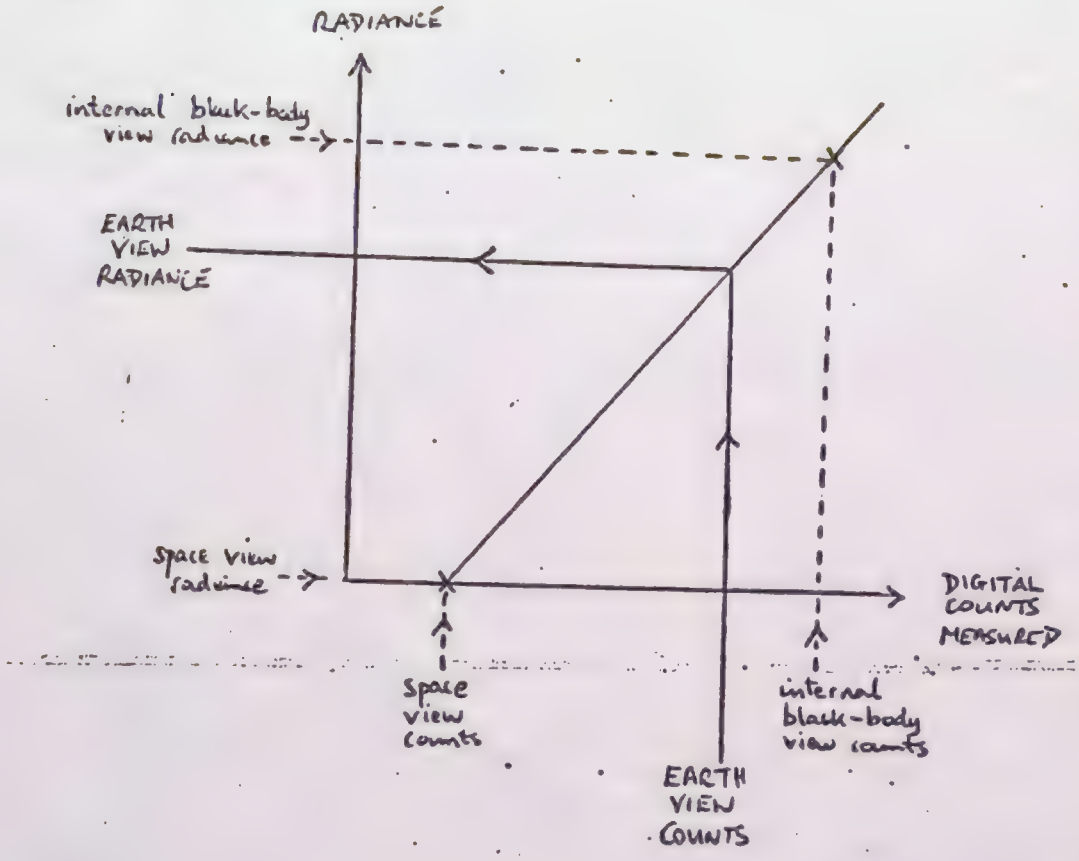

FIGURE 4.

Illustrating the 2-point calibration process for a linear radiometer.

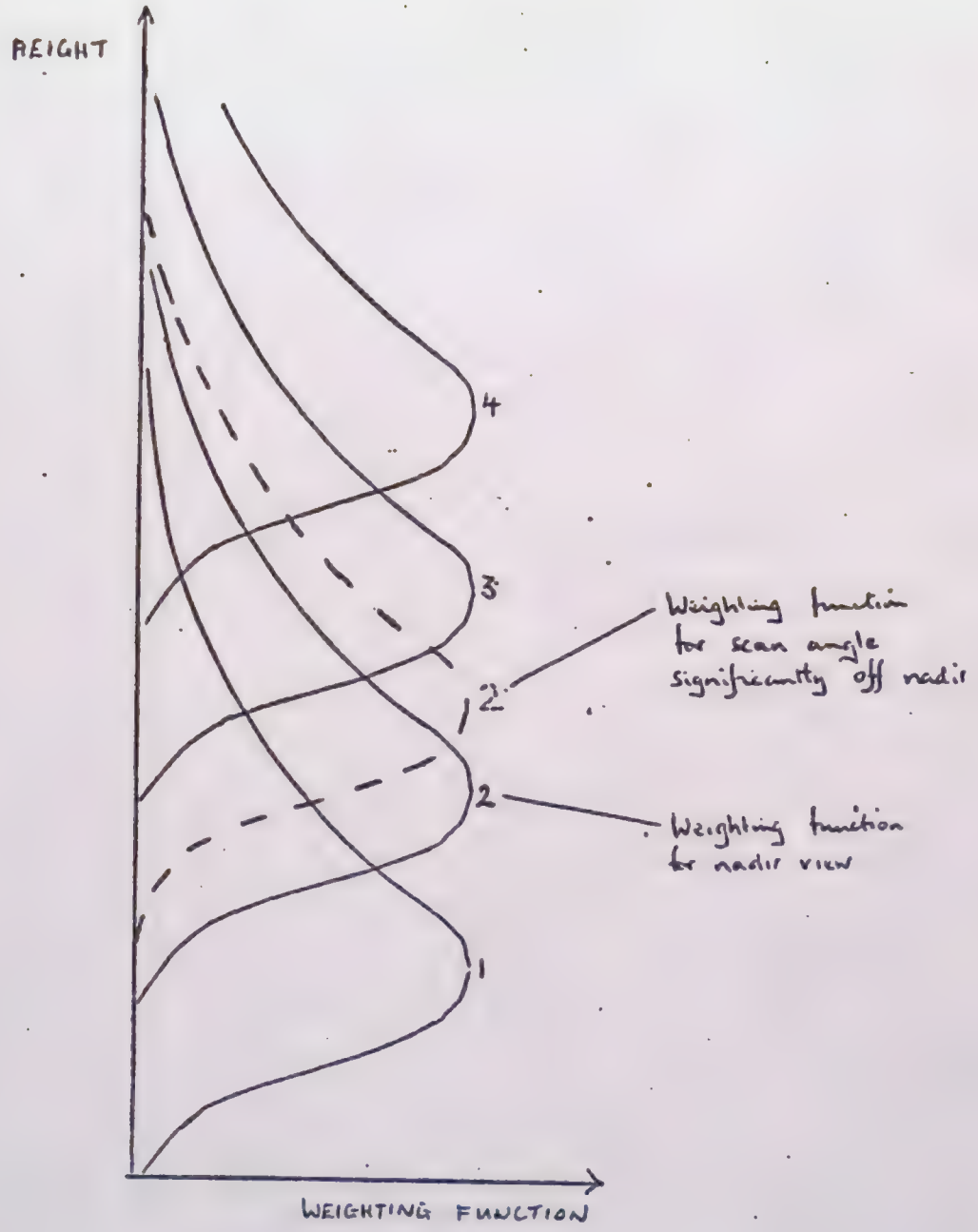

FIGURE 5.

Illustrating schematically a group of weighting functions for nadir viewing and the effect of scanning off nadir on one of these functions.

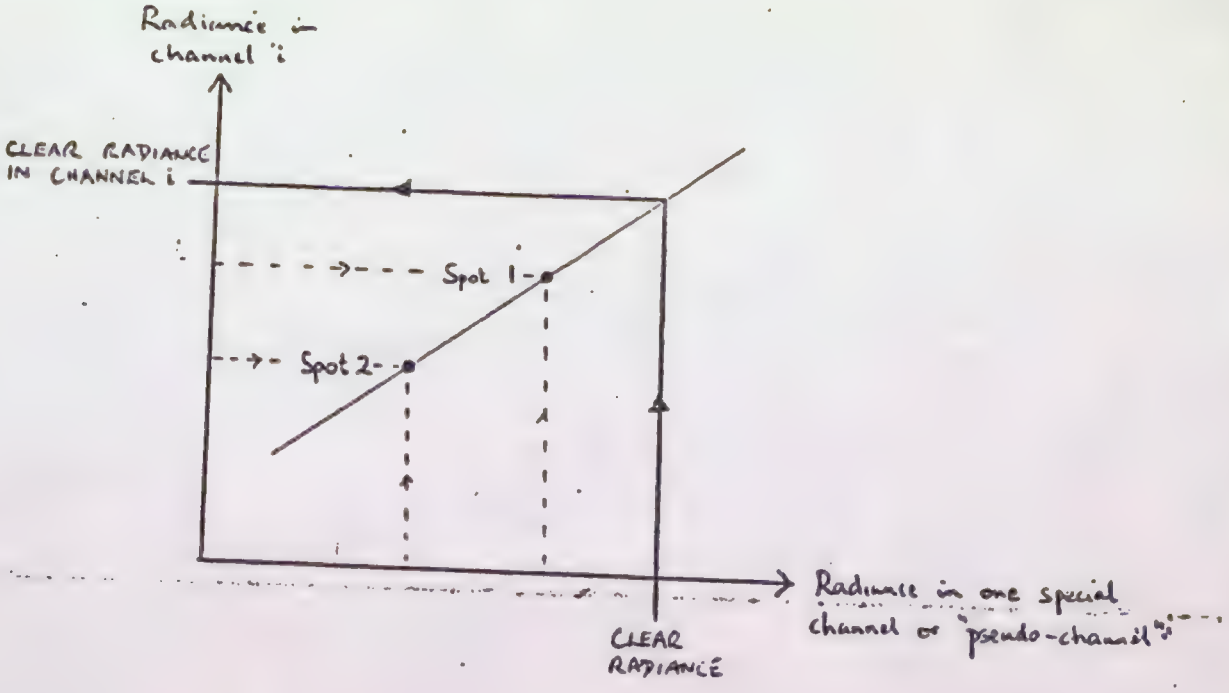

FIGURE 6(a). A graphical representation of the N* cloud-clearing method

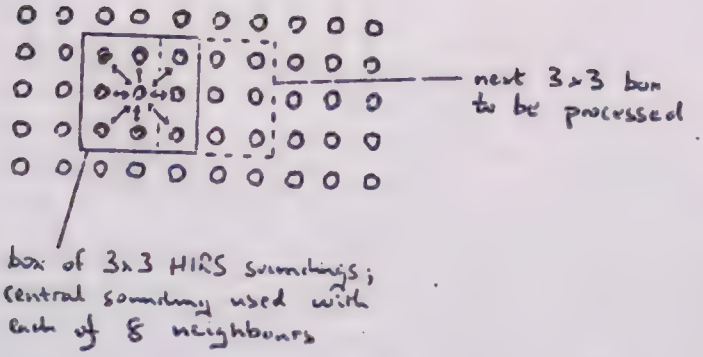

FIGURE 6(b). Illustrating the method of cloud-clearing using 3x3 boxes of HIRS soundings.

FIGURE 7

RETRIEVAL-RADIOSONDE TEMPERATURE DIFFERENCES

NOAA-7 OCTOBER 1983

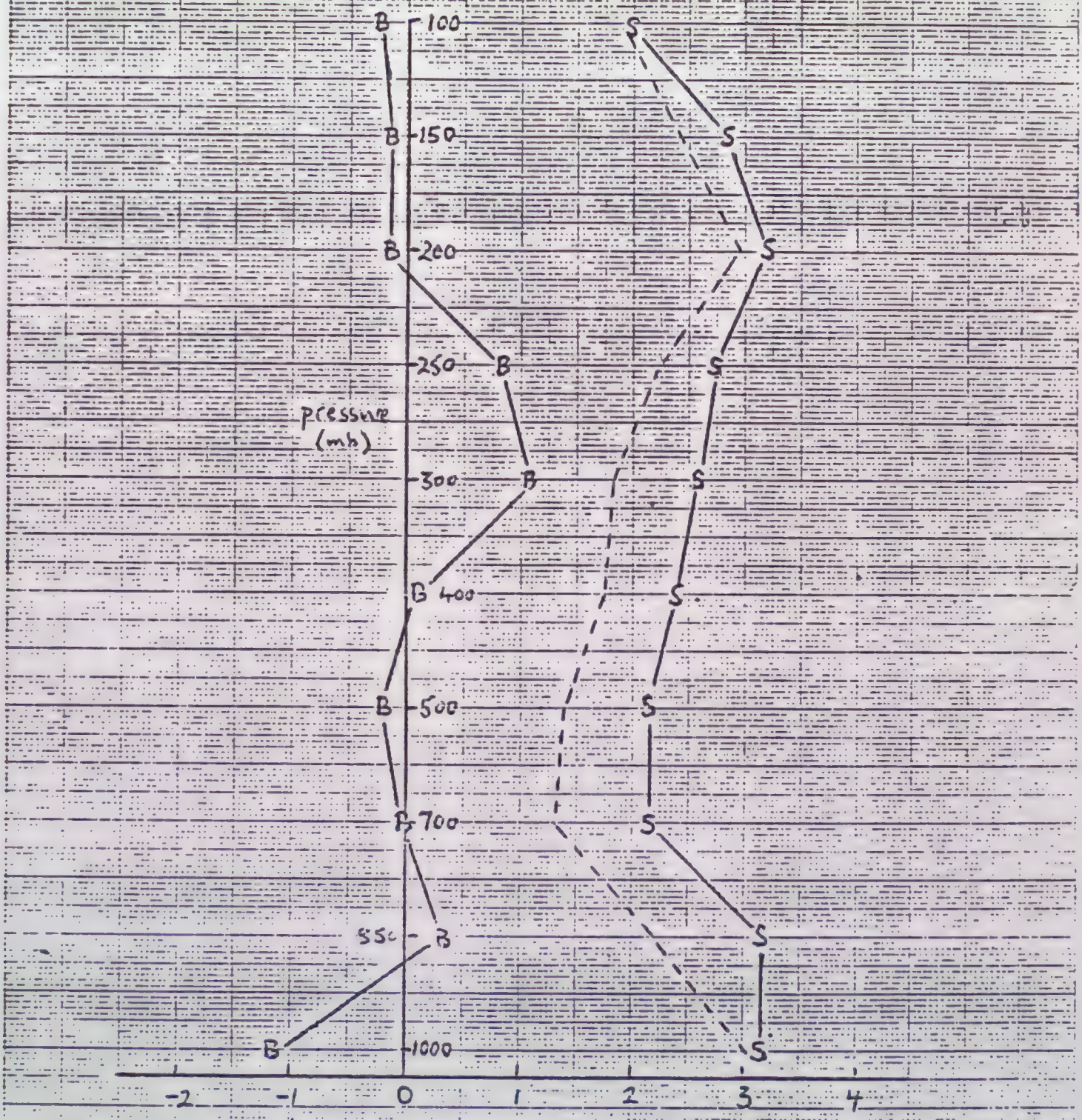

RETRIEVAL-RADIOSONDE DIFFERENCE STATISTICS { B = BIAS; S = STANDARD DEVIATION

THEORETICAL RETRIEVAL ERRORS (REGRESSION RESIDUAL ERRORS) :

Figure 8 — Schematic thermal patterns showing biases at both centre and edges of swath.

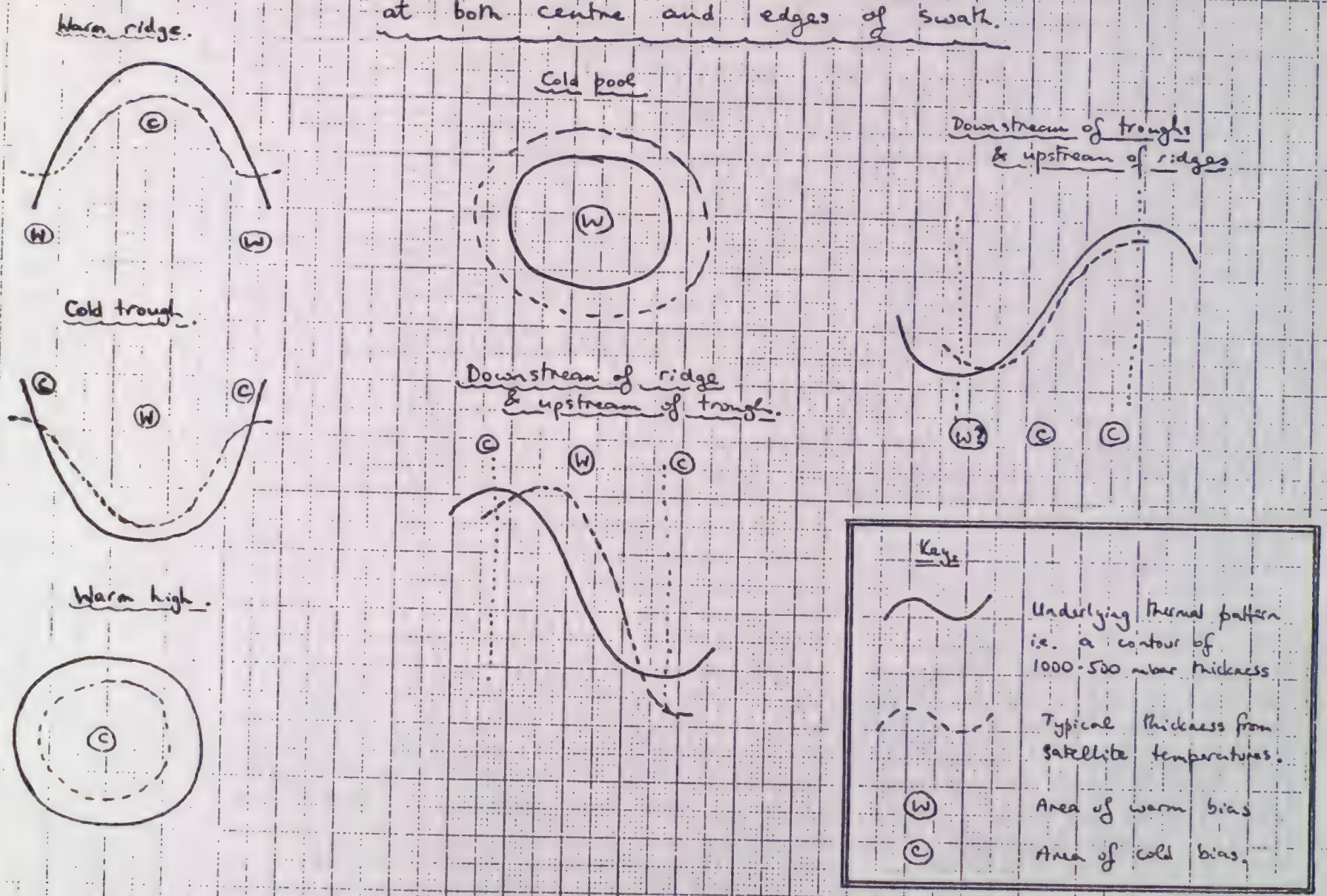

ADVANCED LECTURES - SATELLITE METEOROLOGY - 1987

LECTURE 6: QUANTITATIVE USES OF IMAGERY DATA

R.J.Allam

1. Introduction

The combination of eye and brain has evolved in man and other animals to process images quickly and effectively. Whilst this probably arose through increasing the ability to survive, man has retained his faculty for extracting information from images in real time. Non-literate societies used pictures in stained glass and in paint to convey complex religious and political messages. Even (or especially?) in today's literate society, the effectiveness of persuasion or education through the use of pictures is well recognised. Some examples would include the easily recognised political symbolism of flags and banners, the explosive growth in the video industry, the use of pictograms to convey information to users of roads and airports, and the use of symbols in the presentation of weather forecasts. All of these examples rely upon the near-instantaneous extraction of features of interest from a complex, continuous, two-dimensional field of information.

The meteorological community has exploited the ease with which information can be extracted from diagrams and pictures through its widespread use of charts and other graphical material. This lecture will try to examine how meteorological images are created, look at some of the problems encountered in doing so, discuss the advantages of quantitative images and demonstrate some of the applications. Sources of images useful in meteorology include passive imaging sensors, suface-based radars and active space-borne instruments. The examples used in the lecture will concentrate on the former but the techniques are usually more generally applicable. The annex gives additional information on two meteorological systems.

2. ...imagery data...

2.1 Background

The main difference between radiance data considered so far in this series of lectures and satellite images is one of presentation. The wavelengths of the imaging channels of the Advanced Very-High Resolution Radiometer (AVHRR) are similar in some respects to those of the instrument used for sounding (HIRS). The detection and use of the radiances are conceptually the same for both instruments, but the applications are usually, but not necessarily, different. Indeed, one of the recent trends in the use of imagery data is its exploitation in numerical models. In some designs of instrument, "sounding" and "imagery" channels are not distinguished: it is the application that determines the title.

However, it is usual to use the sounding data in numerical models and hence they are treated as point values. Conceptually, images are considered to be continuous two-dimensional distributions of brightness. It is this continuity that the brain seems so adept at handling. In practice, images are arrangements of closely spaced picture elements ("pixels"), each with a particular brightness. When viewed at a suitable distance, they are indistinguishable from continuous functions.

There are limits to both the amount and the quality of information that can be extracted from such a field. It is useful to consider an architypal passive remote-sensing system to see where these limits arise. It is assumed that the surface and atmosphere together reflect, or emit, or both, electro-magnetic radiation towards the system.

Essentially, our system will consist of some optics to collect the radiation, a detector to determine how much there is, some telecommunications equipment to encode this quantity and to transmit it to the ground, some more equipment to receive the information and decode it into something useful and a device upon which to display the information. At each stage, potentially useful information about a scene being viewed is "lost". Essentially, this arises as a consequence of a series of digitisation processes that transform the continuous scene. These include resolutions in space, wavelength and radiometric product.

2.2 Spatial Resolution

The continuous nature of the scene is divided into a number of discrete picture elements or pixels that are governed by the size of the optics, the integration time of the detectors and possibly by subsequent sampling. The size of object that can be resolved

in the displayed image depends upon the size of these pixels.

Due to the effects of diffraction by elements of the optical system, the focussed image of a distant point object in the scene has a characteristic angular distribution known as a "point-spread function" (PSF), or "Airy pattern". See figure 1a. Two distant point objects that are displaced within the field-of-view are considered separable (ie the Rayleigh criterion) if the angle between the maxima of their PSFs is greater than λ/D, where "λ" is the wavelength of the radiation and "D" is the diameter of the beam. See figure 1b.

However, if these two PSFs are close enough to be focussed onto the same detector, they cannot be resolved. In the case of most remote sensing systems, it is the effective displacement of adjacent detectors that limits the spatial resolution. (Slater 1980, appendix 1). Only if they are close together, as in figure 1c, the two objects can be resolved. A general method of determining the resolution of the optical system is by computing or measuring its modulation transfer function or MTF. The "modulation" of a sinusoidal function is the ratio of half its peak-to-peak amplitude to its mean value. The MTF is derived by evaluation the ratio of the output to input modulations as a function of the wavelength (or spatial frequency) of the sinusoid. (Slater 1980, appendix 1).

In practice, many space-borne systems use the motion of the satellite to extend the image along its track, and moving mirrors to build up the picture across the track. In such systems, the focussed image of the viewed objects is scanned across a detector. The output from the detector (see below) is integrated over short periods of time to achieve the separation of objects. The value obtained for each integration is a complicated

convolution of the point-spread functions of every object within the scene with the spatial response of the detector and the time of each integration.

An alternative to the scanning by moving mirrors is the use of linear arrays of detectors. With no moving parts they are much more reliable than mirrors, but introduce problems in the inter-calibration of the different detectors. These two methods are known in the jargon as "whisk-broom" and "push-broom" respectively. See figure 2.

2.3 Radiometric resolution

The instantaneous scene is focussed by the optics on to a detector which responds to the irradiance upon it. The response can either be through a direct effect on the electronic energy levels within the detector ("quantum detection"), or through the radiation being absorbed, warming the detector and changing some characteristic of it, such as resistance ("thermal detectors"). Voltages due to a number of extraneous sources are also detected, including those due to:

- the thermal motion of electrons within the detector ("Johnson" noise),
- surface irregularities and electrical contacts ("1/f" noise),
- the quantal nature of electrical currents ("shot" noise).

To increase the signal to noise ratio (SNR), the system can be provided with large collecting optics, cooled detectors and long detector integration times. The combination of signal and noise voltages (an analogue signal) is integrated in time to produce a digital value. The sequence of integrated values corresponding to each line of the scene has then to be encoded and transmitted

to the ground. A useful summary of techniques to do this is given by Baylis (1987). Having received the data, decoded and processed them into useful products (see below), the images can be displayed on a suitable device. Usually, this involves representing each pixel value as a suitable colour on a monitor or shade of grey on a facsimile recorder.

2.4 Display resolution

Thus, the continuous observed scene has been transformed to discrete pixels on a monitor. The discrete nature of the image is only disturbing when the resolutions of the image and the display device are grossly mismatched. The pixels on a typical monitor are separated by approximately 0.3mm. Each pixel itself comprises three dots of different coloured phosphors. At a reasonable viewing distance of 75cm, the eye can only resolve the pixels if they have high contrast. [Note that the resolution of the eye, about 0.2mrad, is limited by the separation of the photo-sensitive cells in the retina.]

The last part of our system involves the interpretive skills of the forecaster, who uses the images to obtain information about weather systems. The elements of these skills are continually being developed, in the Office by groups in Met O 15 and 19. Useful sources include Marshall (1982) and Brimacombe (1981).

3. ...quantitative...

3.1 Calibration

So far, the quantitative aspects of images have not been important. The eye and brain exploit the relative contrasts within scenes at various spatial frequencies, to identify positions and types of many weather phemomena. This use of contrasts allows us to see over an enormous range of

illuminations, (actually a dynamic range of 10^5; cf a factor of 16 in the area of the pupil, see Sabins (1978)), and also in colour (Brou and others (1986)).

A problem arises if the forecaster wishes to know, for example, the temperature of an object in the image. To obtain this information, the image has to be calibrated; each pixel value has to be associated with a temperature. This requirement has huge implications on the technology of the system. A frequently used method of relating the digital counts obtained to temperature is to allow the radiometer to look at objects with known or measured temperatures and to compare the counts obtained with those due to an object at an unknown temperature. Where possible, the same optical system should be used for observations of both the scene and the calibrating objects. For the AVHRR, (see annex), two "objects" are used, the zero (almost!) radiance of space, and a temperature patch (at T ≈ 288K) inside the instrument. A linear relationship between radiance and digital counts derived from the fixed points is used. See figure 3. A small non-linear correction is also applied.

3.2 Digitisation

The digitisation of the range of counts (and hence radiance) provides a number of discrete values separated by constant radiance. The temperature differences corresponding to these steps in radiance define the quanta of temperature in the final image. Due to the non-linearity of the black-body function with temperature, the size of these steps depends upon temperature. AVHRR data are digitised using 10 bits, thereby providing 1024 different values. For the thermal infra-red channels, the temperature step at 300K is about 0.1K, but is 0.3K at 220K.

Other systems are digitised using different numbers of bits. The infra-red images for Meteosat use 8 bits, but the visible and water-vapour channels have only 6 significant bits. Interestingly, tests performed in Met O 19 have demonstrated that a monochrome satellite image can be displayed without serious degradation using the equivalent of only five bits.

3.3 Data amounts

The quantitative applications of images require the transmission, storage and processing of large amounts of data, in near real-time. The data from AVHRR provide a useful example. Data are broadcast directly from the TIROS-N satellite and can be received at suitable ground-stations, but only while the satellite is within about 3000km of the station. For each pass of about 15 minutes, the data volume received is about 120Mbyte. Each satellite delivers six such passes every day. The TIROS-N system consists of two satellites. Thus, the daily volume of data from AVHRR is about 1.5Gbyte, the equivalent of 2½ 3380 disks on Cosmos. As remote sensing systems go, AVHRR is very modest! For example, the data rate from the Thematic Mapper on Landsat is 125 times greater than that for AVHRR.

3.4 Remapping

The requirements for the rapid processing of large amounts of data are best met by using digital computers. In an operational system, the most intensive computational task is to change the projection in which the image is displayed. This is necessary partly because of the distortions arising from viewing the curved earth using a scanning mirror, and partly because of the need to use images in conjunction with other meteorological data on standard chart backgrounds. A key element in the process of re-mapping the image as seen from space, ("space-view"), to fit

the required projection, is knowing the position on the earth of each pixel, ("navigation"). This is achieved by knowing the orbital characteristics of the satellite (supplied by the satellite operator), the precise time at which each line of the image was recorded, and the geometry of the scan.

In practice, the re-mapping is done as follows. The position within the space-view scene is located that corresponds to the centre of each pixel in the final reprojected image, using the orbital data and the geometry of the final projection. The values of the pixels at and in the locality of this point are used to compute a new value. Effectively, this is a weighted average of the near-by values and is assigned to the pixel in the final image. See figure 4.

Many sophisticated methods have been studied to perform this weighted average. (See Shlien 1979). Most are not applicable to near real-time applications due to the large amount of computing effort required. However, the increasing availability of parallel processing architecture is expected to change this position.

4. ...uses...

4.1 Background

Images in meteorology are of use in three main areas:

- in subjective analyses of the structure of the atmosphere and the surface,

- to provide quantitative information to models and forecasters,
- in providing short-period forecasts.

Different regions of the electro-magnetic spectrum can be used to extract information about weather systems. Figure 5 shows this spectrum. A channel receiving radiation in the infra-red can provide information about the temperature of objects within the scene. Channels responding to visible light give information about the reflectance of objects. Combinations of two or more channels permit most types of object in the scene to be characterised by their multi-channel signatures.

A simple example is the observation that warm, bright objects in a day-time scene correspond to low clouds or fog. See figure 6. The techniques of classifying objects from their multi-spectral signatures are well-developed, particularly using earth resource sensors such as Landsat's Thematic Mapper. An introduction to the subject is given by Mulder (1987) and a meteorological example by Liljas (1987). A more complete treatment is Pairman and Kittler (1986).

4.2 AVHRR data

A scheme developed in the Meteorological Office, (see Saunders (1986)), will be used to extract information about clouds and the surface for use in the mesoscale numerical weather prediction model. The scheme applies a succession of tests to each pixel within a scene in attempts to identify cloud. The first is a threshold test in the infra-red; essentially, any pixels colder than a specified temperature are deemed to contain cloud.

The second looks at the local variance of temperatures within an image. High values indicate either mixtures of clear and cloudy pixels or those containing clouds at different levels. Small values at low temperatures indicate fully cloudy pixels.

The brightness temperatures of an object in different channels depend upon the variations with wavelength in the emissivity of the object and in the attenuation of radiation by the atmosphere. It turns out that for thin clouds, temperatures in AVHRR channels 3 (3.7μm) are warmer than those in channel 4 (11μm) (see figure 7a). The converse is true for thick low cloud, this being the basis of the fog detection scheme described by Eyre and others(1984). (See figure 7b). The difference between AVHRR channels 4 and 5 (11μm and 12μm) is sensitive to the thickness of cloud and to the water vapour content of the atmosphere. A threshold applied to this difference facilitates the detection of thin cirrus.

During the day, reflected solar radiation, adjusted to eliminate the effects of variations of solar elevation, can also be used. A threshold test separates bright cloud from dark surfaces. A fourth test uses the ratio of the radiance of the near infra-red channel 2 (0.9μm) to that of the visible channel 1 (0.6μm). This ratio has a value;

- close to unity for clouds,
- about 0.5 for water, due to the enhanced back-scattering by aerosols at short wavelengths,

- about 1.5 for land, and particularly growing vegetation, due to the high reflectance of leafy structures in the near infra-red.

Having detected the location of the pixels uncontaminated by cloud using these methods, it is possible to determine some surface parameters. Of these, the most important is surface temperature. A single measurement of the surface brightness temperature within the 11μm CO_2 window would provide the physical temperature if the window region were not affected by the presence of water vapour, and if the surface emissivity were unity. In fact, absorption by water vapour (probably by pairs of molecules called "dimers") decreases the amount of radiation measured, resulting in an under-estimate of the surface temperature. However, it os possible to use the measurements in two (or more) infra-red channels to improve the estimate through the use of an empirical relationship of the form:

$$T_{surface} = T_4 + \alpha(T_4 - T_5) + \beta$$

Here, T_4 and T_5 are the brightness temperatures measured in channels 4 and 5 respectively. The physical reasoning behind this arises from the different amount of absorption by water vapour in channels 4 and 5. The values of the coefficients α and β can be computed either through comparing satellite measurements with sea surface temperatures obtainerd by collocated buoys, or by the use of accurate radiative transfer models. Details of the use of such algorithms can be found in McMillin and Crosby (1984) and Saunders and others (1982). Their use is usually confined to sea-surface temperatures; land surfaces have highly variable emissivities that change the validity of the simple formula.

Saunders and Kriebel (1987) shows how cloud parameters can be extracted using extensions to ths series of tests outlined previously. These include cloud-top temperatures, fractional cloud cover and optical thickness. It should be stressed that such products can only be derived from data-streams that contain precise calibration data.

In the spirit of section 2.1, these data can only be considered as images when they are displayed on a suitable device. Although the purpose of deriving them was as input variables for the mesoscale model, much useful information can be gained through viewing them.

5. Conclusion

We noted that the main characteristic of images was not their source or their resolution, but their presentation. We have also noted, but not explained, the comparative ease with which forecasters can extract useful information from satellite images. Quantitative products from images can be formed as long as the data streams are sufficiently precise and are supported by accurate calibration data. These can still be interpreted as images, and useful information extracted.

Many observation systems, both extant and planned, provide information suitable for display as images. Examples include ground-based precipitation radar, microwave imagers, space-borne radars and high resolution sounders. The problems of the reception, processing, archiving and the optimal use of such data will continue to provide major challenges to meteorologists.

ANNEX

Available and planned meteorological satellite systems

TIROS-N

TIROS-N is the generic name for the NOAA series of polar orbiting satellites that have been flown since 1978. These have an orbital period of about 100 minutes and are sun-synchronous. This means that the phase of the orbit remains the same relative to the sun. This ensures that the angle between the meridian containing the sub-satellite point and that containing the sun is constant.

The main imaging instrument is the five channel Advanced Very-High Resolution Radiometer (AVHRR). This observes at five different visible and infra-red wavelengths, although some versions were flown with only four. These channels are located in regions of the spectrum where the atmosphere absorption is low and hence the satellite views the surface or intervening clouds.

Two of the channels, namely 1 and 2, measure reflected solar radiation in the visible and "near infra-red" parts of the spectrum. Objects can often be characterized by their reflectances. For example, clouds reflect much of the solar radiation incident upon them and therefore appear bright. The sea surface is usually a poor reflector and therefore appears dark.

The other three channels observe the earth in the thermal infra-red part of the spectrum. Here, the radiation emitted is characterized by the temperature of the emitting object. Thus, the images formed from the infra-red channels can be interpreted in terms of the temperatures of objects within them. Cold objects such as high clouds are distinct from warm objects such as the surface of tropical oceans. A commonly-used convention for monochromatic images is to display the cold parts of the image as light shades and the warm ones as dark shades. This ensures that the images from visible and infra-red channels have broadly the same appearance with high clouds being bright and the sea being dark in both.

The AVHRR uses the satellite's own forward motion in the north-south direction to produce the different lines of the image. The instrument has a rotating mirror that scans the earth normally to the direction of the motion of the satellite, thereby recording each line of data. The rotation speed of the mirror is designed to produce each successive line next to the previous one, thereby producing a continuous picture. Below the satellite, the spatial resolution of the instrument is about 1.1 km. The ground-track speed of the satellite is 6.6 km/s and the mirror rotates six times every second.

A key element in the effective use of AVHRR is the provision of calibration data for the thermal infra-red channels. During each scan of the mirror, in addition to viewing the earth, the instrument measures both the temperature of space and of a black-body target. The physical temperature of this target is monitored by four platinum resistance thermometers. Measurements of the output of the channels when viewing the targets can be used to determine the temperature of objects seen when observing the earth.

AVHRR data are transmitted directly to users in two different forms. The first, High Resolution Picture Transmission (HRPT), transmits the observations of the radiance of individual pixels as numbers ranging between zero and 1023. All five spectral channels are transmitted for each pixel along with calibration data to facilitate the detailed interpretation of these values. The HRPT data-stream is transmitted at 665 kbit/s.

The second form, Automatic Picture Transmission (APT), is derived from the AVHRR data. The numerical data for two specified channels are processed on-board the satellite as follows. Firstly, only every third line of data is selected. Secondly, averages of neighbouring pixels are taken to reduce further the data volume. The number of AVHRR pixels that contributes to each APT "pixel" varies across the swath between 1 and 4 so that the distortion due to the curvature of the earth is reduced. The spatial resolution of the final product is about 4 km. An analogue signal is formed from these reduced data by modulating the amplitude of a 2400 Hz carrier. After filtering to remove high frequencies, this signal then modulates the frequency of a VHF radio signal for transmission. Some calibration data are also sent to enable image brightnesses to be related to temperature.

As well as being broadcast in real-time, the imagery data are also stored at reduced, 4 km, resolution on tape recorders on-board the satellite. These data are transmitted to three NOAA groundstations. They are then sent to Washington and stored permanently as Global Area Coverage (GAC) data for use in research. Selected imagery is also re-broadcast in analogue format by the GOES satellites so that low resolution, global satellite imagery is available to anyone capable of receiving the GOES-Wefax broadcasts.

Satellites carrying AVHRR in its current form are planned for use until about 1990. Three further polar-orbiting spacecraft will be launched to cover the period until 1995. The AVHRR on these satellites will have one additional channel for use in discriminating cloud and ice during the day. However, since it will share the data transmission facilities with an existing channel, no changes to reception hardware will be needed. The additional channel will yield new and unique products for forecasting.

Beyond 1995, it is hoped that new instruments of the same type as AVHRR will be produced for use on-board polar platforms as part of the international space station concept. Since both the number of channels will be increased and the spatial resolution improved, a considerable enhancement of processing equipment will be needed to process the data.

Meteosat

The Meteosat system is the European contribution to the World Weather Watch of the World Meteorological Organisation, forming part of what should be a global network of geostationary satellites. Images were received from Meteosat-1 between November, 1977 and its failure, two years later. Since August 1981, images have been received from Meteosat-2. A re-furbished prototype satellite, P2, will be launched in early 1988 to bridge the gap before the first of the operational series becomes available in late 1988.

Meteosat is placed in an orbit above the equator and at an altitude of 36000 km. This ensures that its orbital period is exactly the same as the time that it takes for the earth to rotate. It therefore remains above a fixed point, actually the Greenwich meridian, on the equator.

The main imaging instrument is a radiometer that views the earth in three spectral intervals. One responds to reflected solar radiation at visible wavelengths. A second channel measures emitted radiation in the thermal infra-red. The third channel receives radiation from an infra-red part of the spectrum for which the emission is governed largely by the presence of water vapour. This channel is able to provide information on the distribution of water vapour in the upper troposphere and is useful for delineating the positions of jet-streams.

The imager employs the rotational motion of the satellite to provide the lines from east to west. A stepping mechanism provides the scanning from south to north. The infra-red window and water vapour channels give images of 2500 lines of 2500 pixels each. The spatial resolution at the sub-satellite point is 5 km by 5 km, but at 50°N is about 5 km by 8 km. The spatial resolution of the visible channel is 5 km when the water vapour channels is being used, but 2.5 km when it is not. A second visible detector is used to provide this increased resolution.

Each scan from south to north takes 25 minutes, and images are available every half-hour. In-flight calibration of the infra-red detector is provided by viewing a cold reference point and a black-body at measurable temperature. However, since this procedure does not use the same optical assembly as the instrument when viewing the earth, the calibration is of limited use. In practice, absolute calibration has to be done using views of space, the earth and the moon.

One of the important features of the whole system is that processed products are disseminated using the satellite itself as a relay. In this process, raw data are transmitted to an acquisition station. These data are processed at the European Space Operations Centre (ESOC) in Darmstadt, FRG. During this processing, a number of defects in the raw image data, including registration errors of the different sensors, are corrected. The image is located precisely in terms of earth coordinates. This is necessitated by changes in the raw image due to small deviations in the satellites's orbit.

These enhanced images are broadcast to users using the satellite as a relay in two main forms. The first uses a digital transmission known as "High Resolution" (HR) or Primary Data Users Station (PDUS) format and requires, in general, a rather complicated and expensive system incorporating a small computer. This product is intended for users who need to process the image data further. Images covering two main areas of the earth are broadcast; the "A" format covers the full earth disc and is available every hour; the "B" format covers Europe, North Africa and much of the northern Atlantic Ocean and is available every half-hour.

The second form of the data is as a continuous analogue signal called "Wefax" or Secondary Data Users Station (SDUS) format which can be received on much simpler equipment. These data are intended for users who wish to display the imagery but do not need to perform significant local processing. Three main formats are broadcast; "C" format for visible images which cover most of the land areas within the view of the satellite in twenty-four sections; "D" and "E" formats for infra-red and water vapour respectively covering the full earth disc in nine sections. Those covering Europe are transmitted every half-hour. The remaining areas are transmitted at least twice each day. Each image has lines of latitude and longitude together with coastlines embedded within it.

Three operational versions of Meteosat are being built for launch between 1988 and 1991, which should provide useful data until about 1995. There will be no significant difference between these operational versions of Meteosat and that used at present.

Studies are well advanced to examine the requirement for the next generation of geostationary satellites for Europe. These would be expected to be needed from about 1995. It seems likely that the spatial resolution will be improved to 4 km for data from the full Earth disk, and 2 km for European and northern Atlantic data and also that the number of channels transmitted will be increased to about six. Also, the temporal resolution for the 2 km data will be 15 minutes. All these factors would result in dramatic increases in the amount of data to be processed. Assuming that six global images and twenty "European sectors" were broadcast every hour, the daily data volume will be about 4000 Mbyte, a factor of 6 higher than the current value.

Bibliography

Baylis, P.E. (1987)
Data reception, Archiving and Distribution
Remote Sensing Applications in Meteorology and Climatology
(ed Vaughan R.A.)
Proceedings of the NATO Advanced Study Institute on Remote Sensing Applications in Meteorology and Climatology, Dundee August 17-September 6, 1986

Brimacombe, C.A. (1981)
Atlas of Meteosat Imagery
ESA SP-1030

Brou, P., Sciascia, T.R., Linden, L. and Lettvin, J.Y. (1986)
The colors of things
Scientific American Vol 255, no 3, pp 80-87

Eyre J.R., Brownscombe J.L. and Allam R.J. (1984)
Detection of fog at night using Advanced Very-High Resolution Radiometer (AVHRR) imagery.
Meteorological Magazine, Vol 113, no 266

Liljas, E. (1987)
Multispectral classification of cloud, fog and haze.
Remote Sensing Applications in Meteorology and Climatology
(ed Vaughan R.A.)
Proceedings of the NATO Advanced Study Institute on Remote Sensing Applications in Meteorology and Climatology, Dundee August 17-September 6, 1986

Marshall, Capt T.A.
Weather Satellite Picture Interpretation
DNOM memo no 1/82

McMillin L.M. and Crosby D.S. (1984)
Theory and validation of the multiple window sea surface temperature technique
JGR Vol 89, no C3, pp 3655-3661

Mulder, N.J. (1987)
Image Processing, Pattern Recognition and Artificial Intelligence
Remote Sensing Applications in Meteorology and Climatology
(ed Vaughan R.A.)
Proceedings of the NATO Advanced Study Institute on Remote Sensing Applications in Meteorology and Climatology, Dundee August 17-September 6, 1986

Pairman D. and Kittler J. (1986)
Clustering algorithms for use with images of clouds
International Journal of Remote Sensing 1986, Vol 7, no 7, pp 855-866

Sabins, F.F (1987)
Remote Sensing: Principles and interpretation 2nd edition
W.H.Freeman and Co

Saunders R.W. (1986)
An automated scheme for the removal of cloud contamination from AVHRR radiances over western Europe.
International Journal of Remote Sensing 1986, Vol 7, no 7,

pp 867-886

Saunders R.W. and Kriebel K.T. (1987)
An improved method for detecting clear sky and cloudy radiances from AVHRR data
Submitted to International Journal of Remote Sensing

Saunders R.W., Ward N.R., England C.F. and Hunt G.E. (1982)
Satellite observations of sea surface temperature around the British Isles
Bulletin of the Ameican Meteorological Society, vol 63, no 3

Schlien, S. (1979)
Geometric correction, registration and resampling of Landsat imagery.
Canadian Journal of Remote Sensing, vol 5, no 1, pp 74-89

Slater, P.N. (1980)
Remote Sensing: optics and optical systems
Addison-Wesley

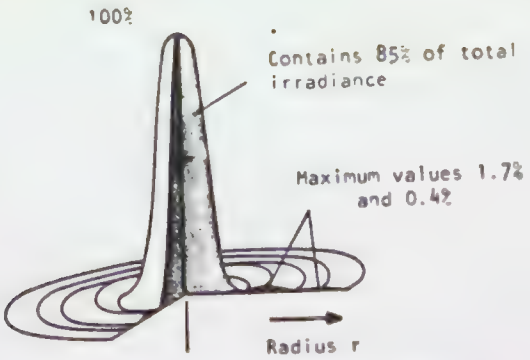

Figure 1a

The irradiance profile of the Airy diffraction pattern.

The distribution of irradiance in the Airy pattern is expressed as

$$E = \left[\frac{2J_1(z)}{z}\right]^2,$$

where $J_1(z)$ is a Bessel function of order 1.

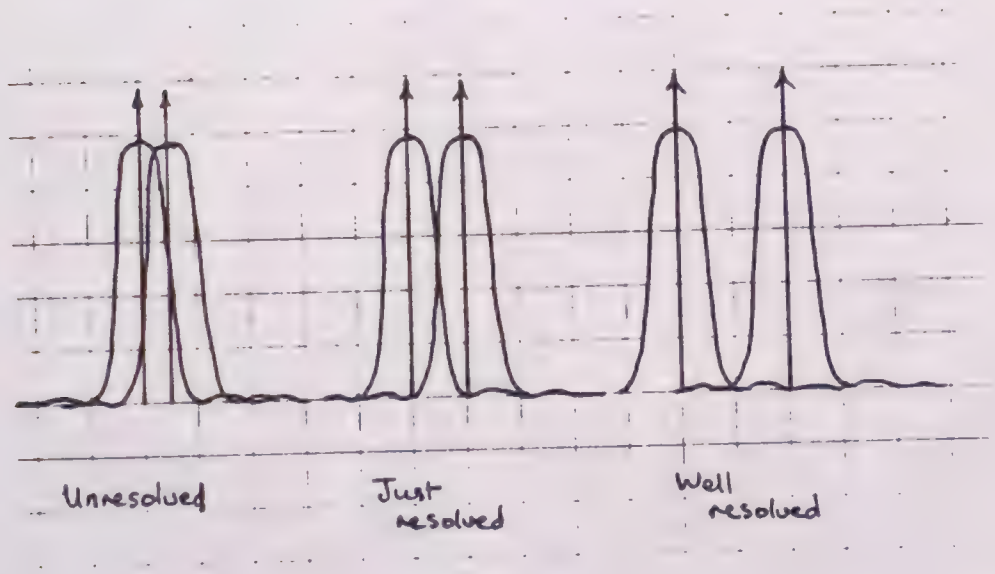

Figure 1b

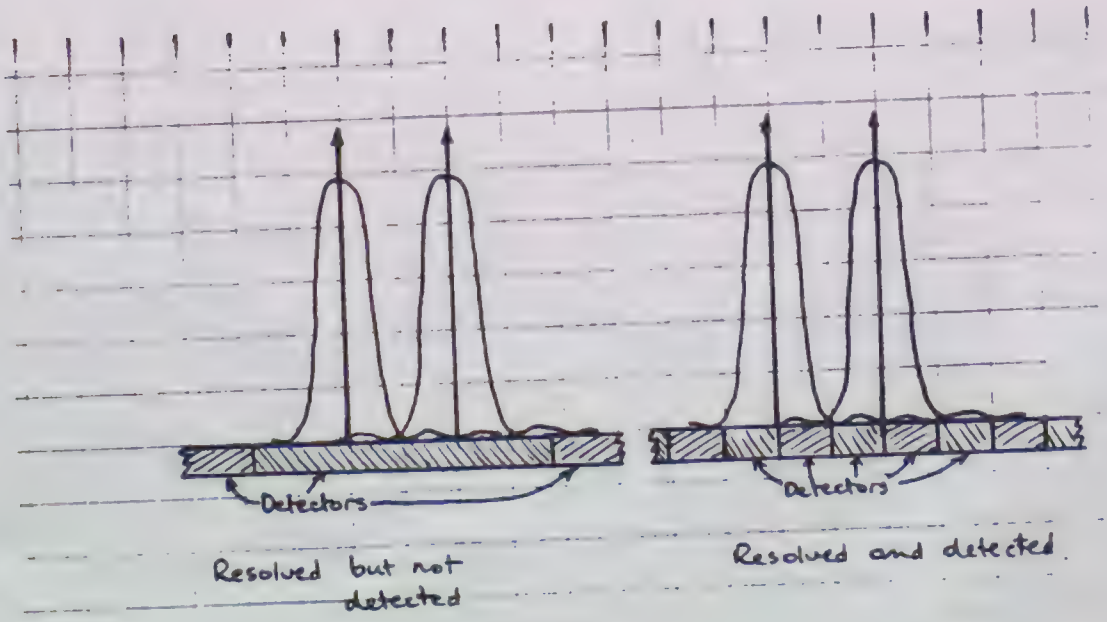

Figure 1c

Figure 2

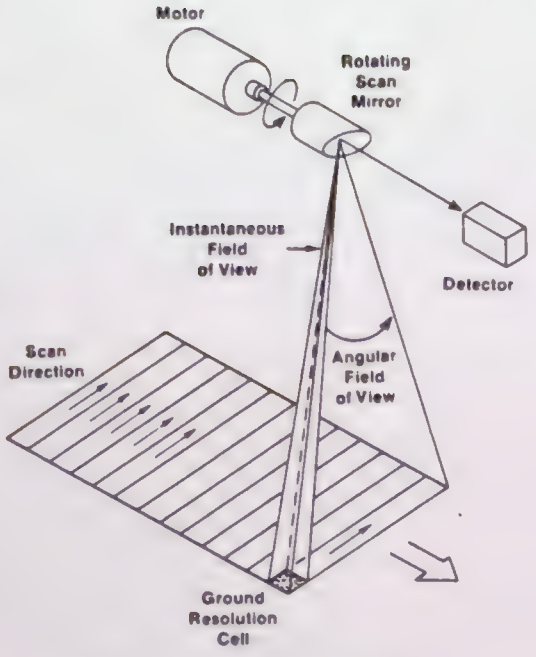

CROSS-TRACK SCANNER.

"Whisk-broom"

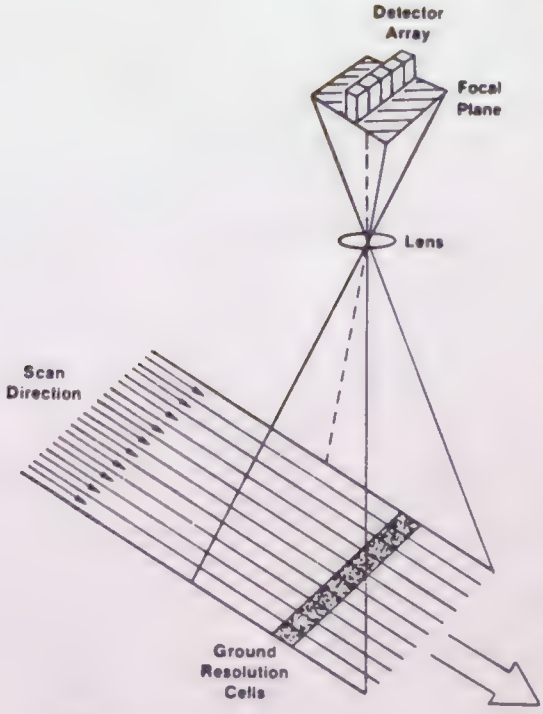

ALONG-TRACK SCANNER.

"Push-broom"

Figure 3

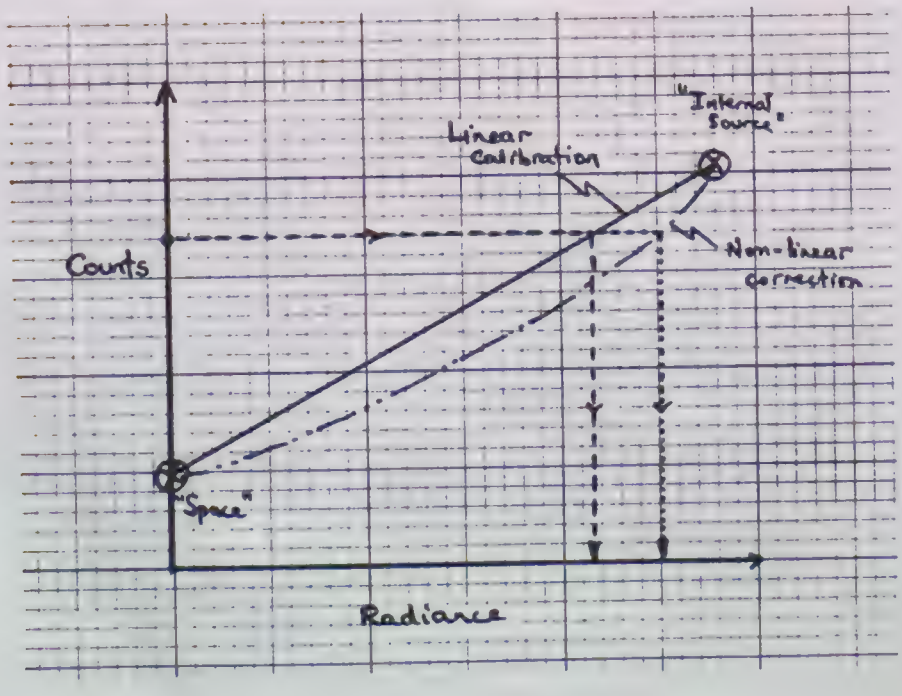

Figure 4

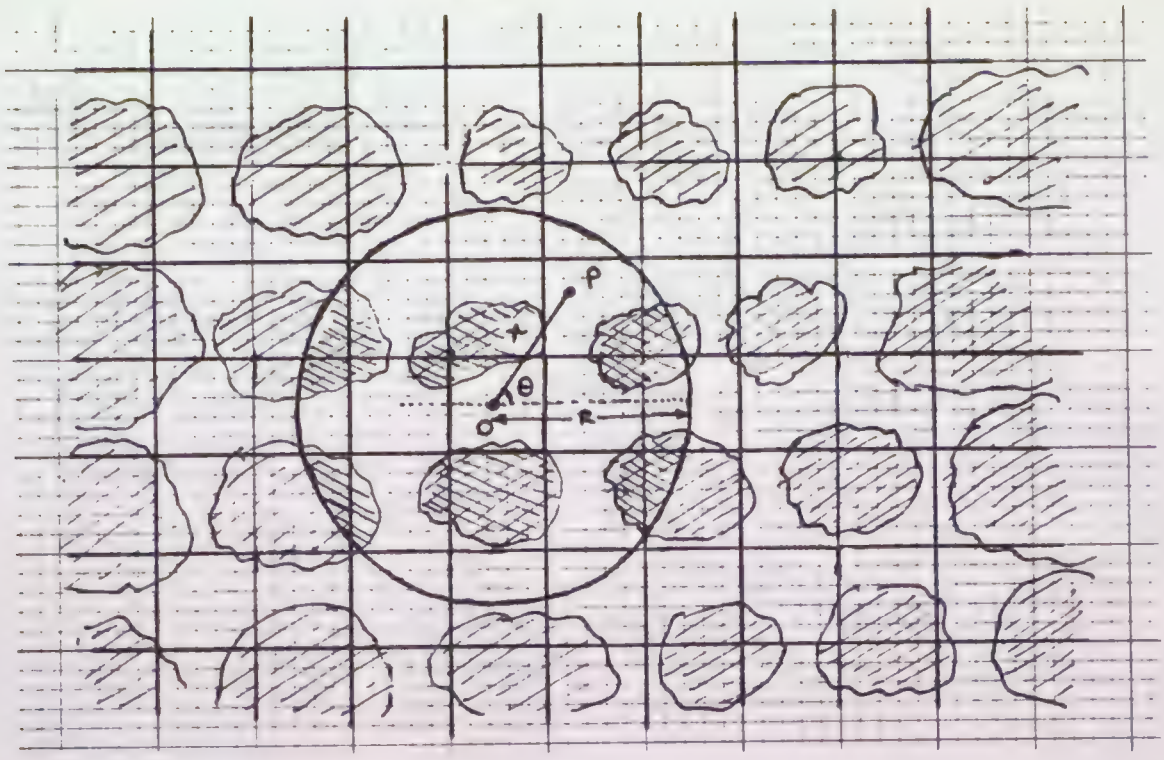

Pixels in reprojected image

Pixels in space-view image

Value to use in reprojected pixel, centre at "O" is

$$V = \int_0^R \int_0^{2\pi} F(r,\theta)\ v(r,\theta)\ d\theta\ r\,dr$$

where $v(r,\theta)$ is the value of the space-view pixel at point "P".

$F(r,\theta)$ is a weighting function:

e.g. $F(r,\theta) = 1/\pi R^2$

or $F(r,\theta) = \dfrac{\sin \pi r}{\pi r}$

or $F(r,\theta) = \dfrac{\sin \pi r}{\pi r}\left\{1 - \dfrac{r^2}{N^2}\right\}$

where 'N' is the number of pixels across integrating circle (above example, - N = 4)

Figure 5

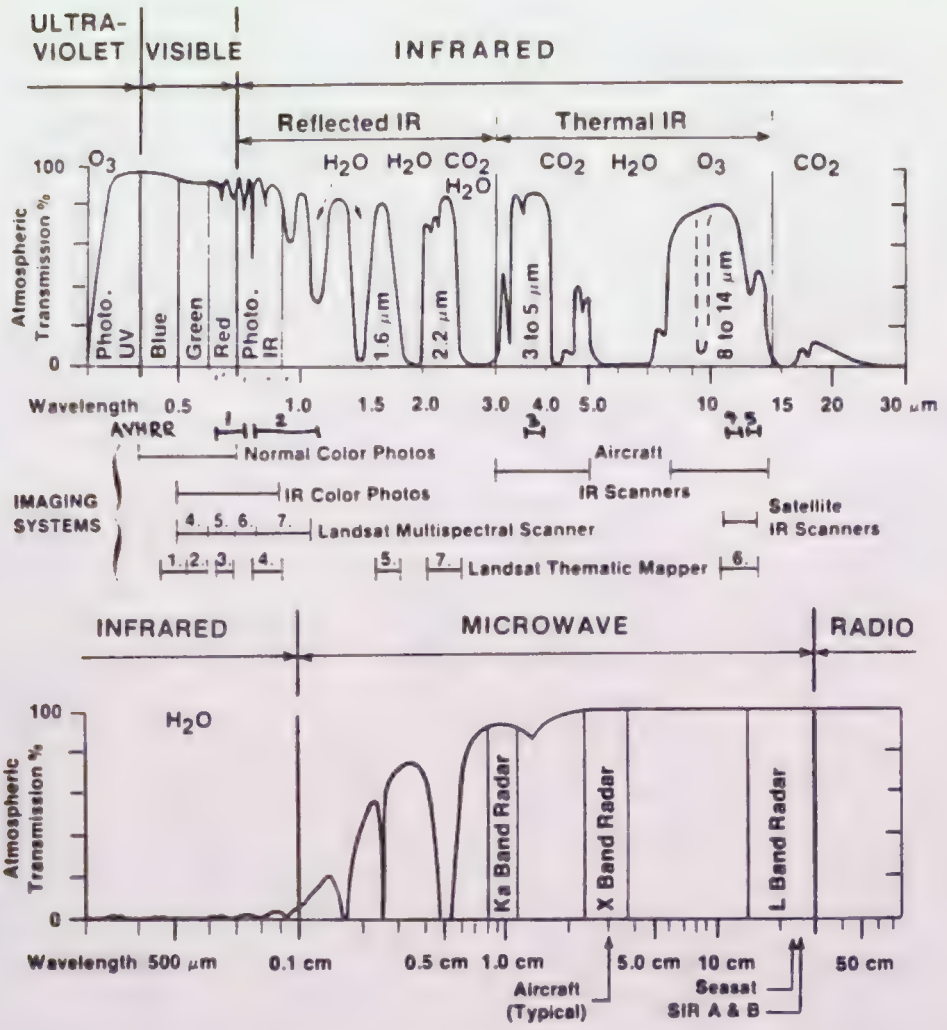

Expanded diagrams of the visible and infrared regions (upper) and the microwave region (lower) showing atmospheric windows. Wavelength bands of commonly used remote sensing systems are indicated. Gases responsible for atmospheric absorption are shown.

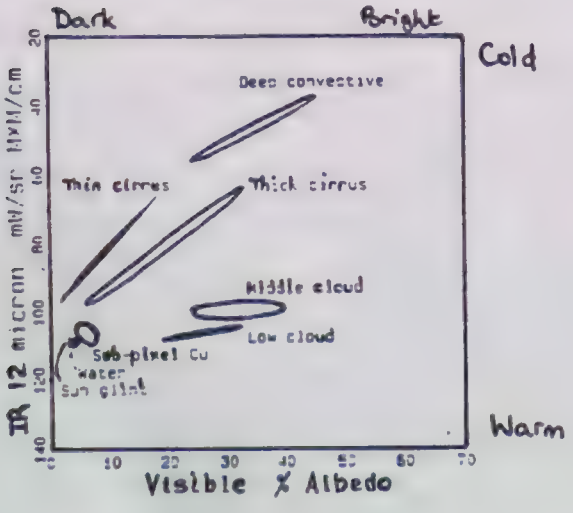

(From Fairman & Kither)

Figure 6

Identification of cloud types using two channels.

Figure 7a

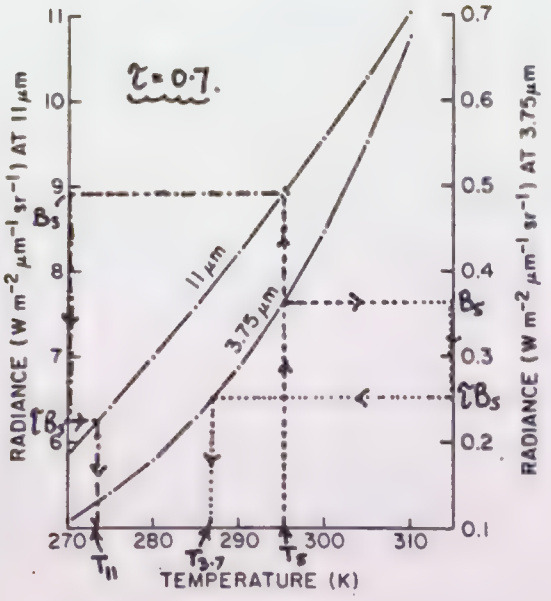

The effect of semi-transparent cloud on radiances.

Surface radiance B_s is reduced by semi-transparent cloud to τB_s.

Temperature corresponding to τB_s is higher for 3·7 μm than for 11 μm.

Figure 7b

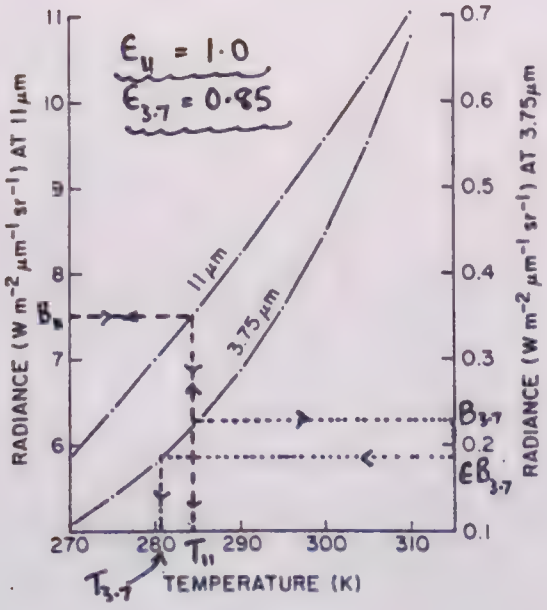

The effect of different emissivity on radiances.

Radiance received at satellite, B_{sat}, is

$$B_{sat} = \varepsilon B(T_s)$$

where ε is emissivity
B is black-body function
T_s is surface temperature.

For low cloud and fog;

$\varepsilon_{11\mu m} \approx 1{\cdot}0$

$\varepsilon_{3{\cdot}7\mu m} \simeq 0{\cdot}85$.

The temperature corresponding to $\varepsilon B(T_s)$ is higher for 11 μm than for 3·7 μm.

S.O. COURSE ADVANCED LECTURES 1987

SATELLITE METEOROLOGY

7. THE USE OF DATA FROM THE ERS-1 SATELLITE

D. Offiler Met.O.19b

7.1 INTRODUCTION

The European Space Agency (ESA) is planning to launch its first remote sensing satellite, ERS-1, early in 1990. Its main complement of instruments are various types of radar, operating at microwave frequencies (5-15 GHz), plus a passive infra-red instrument, the Along-Track Scanning Radiometer (ATSR), being built by the Rutherford Appleton Laboratory with Meteorological Office assistance. Table 7.1 summarises the instruments to be carried, their main purpose and expected accuracies. Primarily, the satellite mission is to sense several oceanographic parameters, both for experimental purposes and as a demonstration that such instruments could have a role to play in operational meteorology and oceanography on the global scale.

Main geophysical parameter	Range	Accuracy	Instrument
Wind field			
Speed	4-24ms^{-1}	±2ms^{-1} or 10% whichever is greater	Wind scatterometer and altimeter
Direction	0-360°	±20°	Wind scatterometer
Wave field			
Significant wave height	1-20m	±0.5m or 10% whichever is greater	Altimeter
Wave direction	0-360°	±15°	AMI Wave mode
Earth surface imaging	80km swath	30x30m resolution	SAR
Altitude			
Over ocean	745-825km	2m absolute ±10cm relative	Altimeter
Satellite range		±10cm relative	PRARE
Sea surface temperature	500km swath	±0.5K	ATSR/IR
Water vapour	15km spot	10%	ATSR/M

TABLE 7.1 ERS-1 main geophysical measurement objectives

Of these instruments, the one most applicable to meteorology is the Advanced Microwave Instrument (AMI) in its wind mode of operation. This is designed to sense the near-surface (equivalent 10m) wind vector over the oceans. This lecture will describe the principles of operation of this type of sensor, and the processing necessary to interpret its raw measurements into familiar geophysical units. Any form of instrument needs calibrating, and the AMI is no exception, so the plans to achieve this will also be outlined. Finally, the use to be made of the resulting data within the Meteorological Office will be mentioned.

7.2 THEORETICAL AND EXPERIMENTAL BACKGROUND

As soon as microwave radar became widely used in the 1940's, it was found that at low elevation angles, surrounding terrain (or at sea, waves) caused large, unwanted echoes. Ever since, designers and users of radar equipment have sought to reduce this noise (e.g. Harrold, 1974). Researchers investigating the effect found that the backscattered echo from the sea became larger with wind speed, so opening the possibility of remotely measuring the wind (e.g. Krishen, 1971, Jones and Schroeder, 1978). Radars designed to measure this type of echo are known as "scatterometers".

The backscattering is due principally to in-phase reflections from a rough surface; for incidence angles of more than about 20° from the vertical, this occurs when the Bragg condition is met:

$$\Lambda \sin \theta_i = n \lambda / 2 \qquad \ldots(7.1)$$

where Λ is the surface roughness wavelength, λ is the radar wavelength, θ_i the incidence angle and n=1,2,3... First order Bragg scattering (n=1), at microwave frequencies, arises from the small ripples (cats' paws) generated by the instantaneous surface wind stress. The level of backscatter from an extended target, such as the sea surface, is generally termed the Normalised Radar Cross-Section (NRCS), or σ°. For a given geometry and transmitted power, σ° is proportional to the power received back at the radar. In terms of other known or measureable radar parameters,

$$\sigma^{o} = \frac{P_R}{P_T} \cdot \frac{64\ \pi^3\ R^4}{\lambda^2\ L_s\ G_o^2\ (G/G_o)^2\ A} \qquad \ldots(7.2)$$

where P_T is the transmitted power and P_R the power received back at the radar. R is the slant range to the target of area A. λ is the radar wavelength, L_s includes atmospheric attenuation and other system losses, G_o is the peak antenna gain and G/G_o the relative antenna gain in the target direction. Equation 7.2 is often referred to as the Radar Equation. σ^o may be set in a linear form (as above) or in deciBels - i.e. $\sigma^o_{dB} = 10 \log_{10} \sigma^o_{lin}$

Experimental evidence from scatterometers operating over the ocean show that σ^o increases with surface wind speed (as measured by ships or buoys), decreases with incidence angle, and is also dependent on the radar beam angle relative to wind direction. Figure 7.1 is a plot of σ^o aircraft data against wind direction for various wind speeds. Direction 0° corresponds to looking upwind, 90° to crosswind and 180° to downwind.

Over the past three winters, ESA have coordinated a number of experiments to confirm these types of curves at 5.3GHz, the AMI operating frequency. Several aircraft scatterometers have been flown close to instrumented ships and buoys, in the North Sea, Atlantic and the Mediterranean. The σ^o data is then correlated with the surface wind, which has been adjusted to a common anemometer height of 10m (assuming neutral stability). An empirical model function has been fitted to this data (Long, 1986) of the form:

$$\sigma^o = a_0 \cdot U^{\gamma} (1 + a_1 \cos \phi + a_2 \cos 2\phi) \qquad \ldots(7.3)$$

where the coefficients a_0, a_1, a_2 and γ are dependent on incidence angle. This model relates the neutral stability wind speed at 10m, U, and the wind direction relative to the radar, ϕ, to the NRCS.

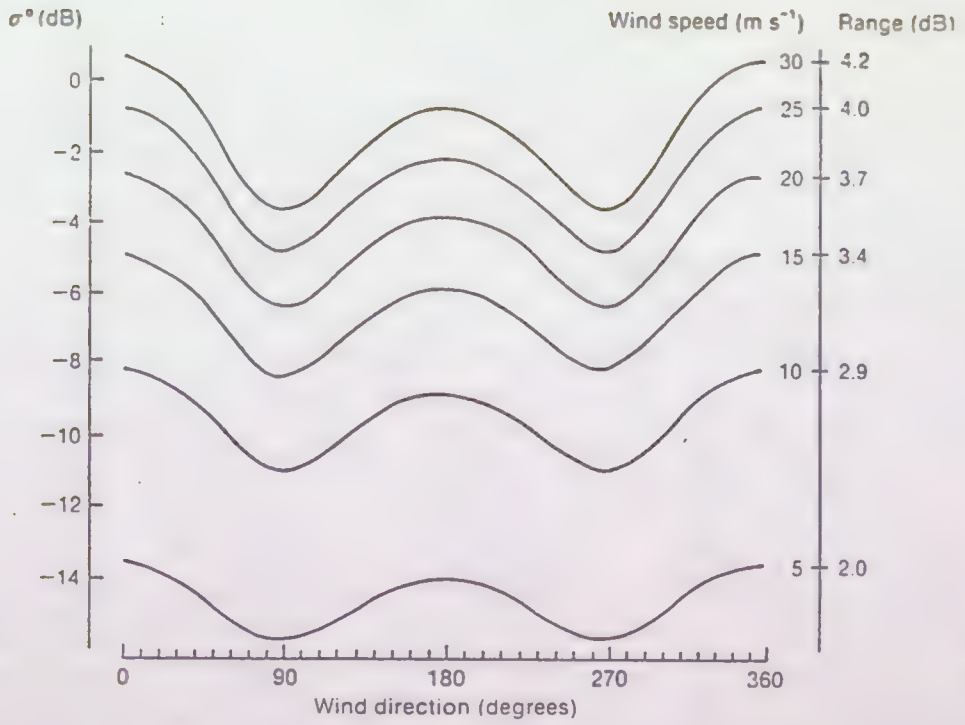

Figure 7.1. Measured backscatter, σ^o (in decibels) against relative wind direction for different wind speeds. Data for 13GHz, vertical polarisation.

It may also be the case that σ^o is a function of sea surface temperature, sea state and surface slicks (natural or man-made), but these parameters have yet to be demonstrated as having any significant effect on the accuracy of wind vector retrieval.

7.3 THE AMI SCATTEROMETER

Since σ^o shows a clear relationship with wind speed and direction, in principle, measuring σ^o at two or more different azimuth angles allows both wind speed and direction to be retrieved. However, the direction retrieved may not be unique; there may be "ambiguous" directions.

The first wind scatterometer to be flown on a satellite - the SEASAT-A Satellite Scatterometer (SASS) - was in 1978 and ably demonstrated the accuracy of this new form of measurement. The specification, as for the AMI, was for RMS accuracies of 2 ms^{-1} for

wind speed and 20° for direction; comparisons with JASIN conventional wind measurements showed that these figures were met if the rough wind direction was known, so as to select the best from the ambiguous set of SASS directions (Offiler, 1984).

The SASS instrument used two beams either side of the spacecraft; the ERS-1 AMI scatterometer uses a third, central beam to improve wind direction discrimination, but is only a single-sided instrument, so its coverage is less. Figure 7.2 shows the geometry of the ERS-1 scatterometer. The three antennae each produce a narrow beam of radar energy in the horizontal, but wide in the vertical, resulting in a narrow band of illumination of the sea surface across the 500km width of the swath. As the satellite travels forward, the centre, then rear beam will measure from the same part of the ocean as the fore beam. Hence each part of the swath, divided into 50km squares, will have three σ^0 measurements taken at different relative directions to the local surface wind vector.

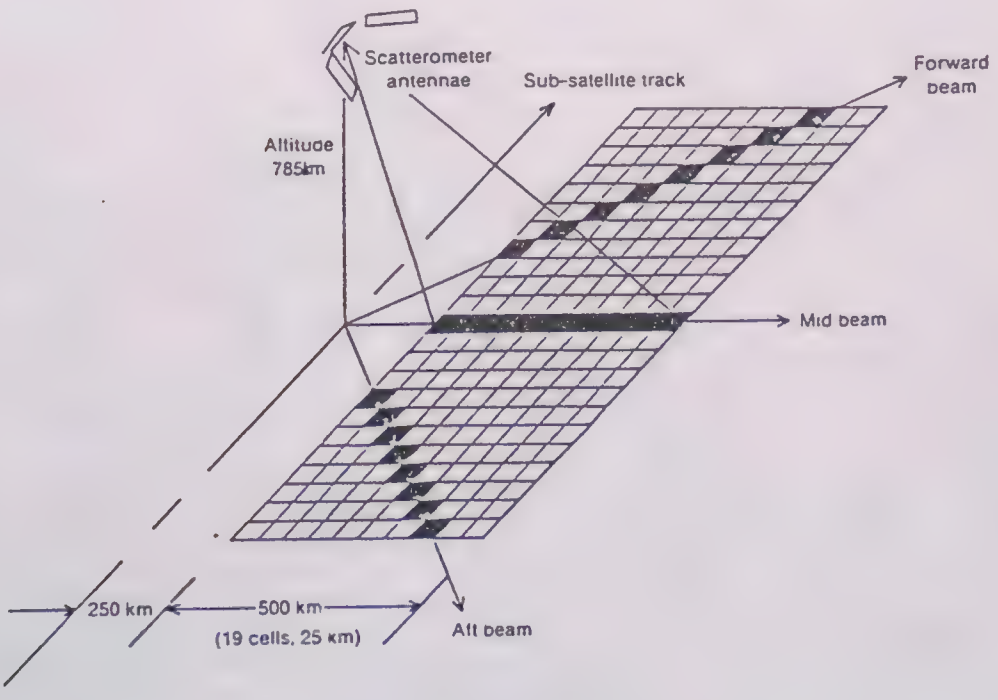

Figure 7.2. ERS-1 wind scatterometer geometry. For clarity, the 500km-wide swath is shown as 10 non-overlapping cells. In reality, there are 19 cells across the swath, on a 25km grid, each one being 50x50km in size.

Figure 7.3 shows the coverage to be expected of the scatterometer for the North Atlantic over 24 hours. These swaths are not static, but "move" westwards to fill in the large gaps on subsequent days. Even so, the coverage will not be complete, due to the relatively small swath width in relation to say, the AVHRR imager on the NOAA satellites. However, there will potentially be a wind available every 50km within the coverage area, globally, and ESA are committed to delivering this to operational users within three hours of measurement time. The raw instrument data are to be recorded on board and replayed to ESA ground stations each orbit, the principle station being at Kiruna in northern Sweden, where the wind vectors will be derived.

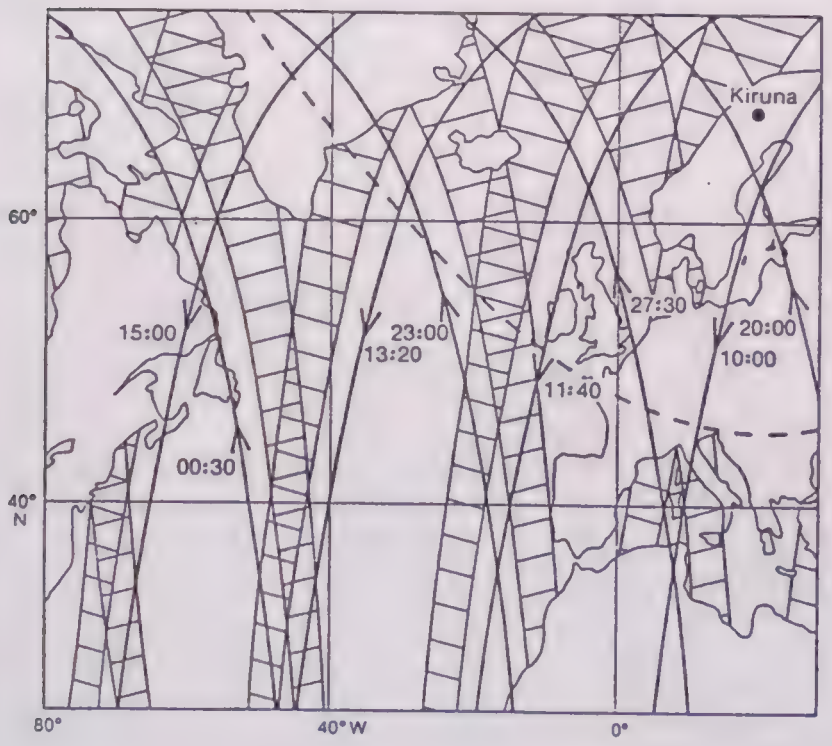

Figure 7.3. ERS-1 sub-satellite tracks and wind scatterometer coverage of the North Atlantic region over 1 day. The large gaps are partially filled on subsequent days; nominally this occurs on a three-day cycle. The dashed line shows the limits of reception for the Kiruna ground station in Sweden.

7.4 WIND VECTOR RETRIEVAL

7.4.1 Generation of ambiguous vectors

As already mentioned, the AMI scatterometer principally measures the power level of the backscatter at a given location at different azimuth angles. Since we know the geometry, such as range and incidence angles, Equation 7.2 can be used to calculate a triplet of σ^o's for each cell.

It ought to be possible to use the model function (Equation 7.3) to extract the two pieces of information required - wind speed and direction - using appropriate simultaneous equations. However, in practice this is not feasible; the three σ^o's will have a finite measurement error, and the function itself is highly non-linear. Indeed, the model, initially based on aircraft data, may not be applicable to all circumstances. The wind speed and direction must be extracted numerically, usually by minimising a function of the form:

$$R = \sum_{i=1}^{3} \left\{ \frac{\hat{\sigma}_i^o - \sigma^o (v, \phi_i, \theta_i)}{\hat{\sigma}_i^o \cdot Kp_i} \right\}^2 \qquad ...(7.4)$$

R is effectively the sum of squares of the residuals, comparing the measured σ^o's to those from the model function (using an estimate of wind speed and direction), weighted by the noise in each beam (Kp_i, related to the S/N ratio). The wind vector estimate is refined so as to minimise R. Starting at different first guess wind directions, the numerical "solution" can converge on up to four distinct, or ambiguous, wind vectors, although often there are only two obviously different ones - usually about 180° apart. One of these is the "correct" solution, in that it is the closest to the true wind direction and within the required RMS accuracies of $2ms^{-1}$ and 20°.

7.4.2 Ambiguity removal

Selecting which of the ambiguous set of solutions is the correct one, when the true wind is unknown (as is the case for an operational system), is termed ambiguity removal. This is merely assigning a probability of correctness to each solution and choosing the one with the highest probability. This may sound easy, but to do this with a consistent high skill (ideally one would want to choose correctly on 100% of cases) is a difficult task. A first stage is to see which extracted vector best fitted the model function, ranking them in increasing order of R and choosing the first rank. Simulations (Offiler, 1985), have indicated that this technique might be expected to have a skill rating of not more than 70%. (Compare this with SASS, which, with only two beams, could only manage a random 25% skill.)

Further processing may be done by objectively seeking areas of the swath where the first rank shows some consistency in direction, and selecting a different rank for nearby cells which do not at first agree with this general trend. This may yield a skill score of 90% or so in most cases, but areas which have been consistently ranked wrongly to start with will only be reinforced, so drastically reducing our skill in picking the right solution (Offiler, 1985).

Ideally, we would like some indication of the "true" direction, such as from ships or buoys, or even better, because of greater spatial coverage, the wind analysis from a numerical model. Unfortunately, while these may be available after a few hours, at the time the satellite winds are required, these independent data will not be ready in time. The best that we could have is a forecast field of say 6 or 12 hours ahead for the verification time of the satellite data. Winds from a forecast grid can be interpolated to each scatterometer data point and the solution with the nearest direction chosen. While this can result in high skill scores (over 95%), there is a major drawback; if a forecast is wrong in the positioning of a circulatory feature by 100-200km (a common occurrence), then there is an area of winds between the forecast centre and true centre which is 180° in error. Here, we will select exactly the wrong scatterometer solution. Worse, if fed back into the next analysis, these winds could reinforce the incorrect

forecast which is also being used as the assimilation background. Whilst there are probably enough conventional surface data to prevent this happening in the North Atlantic region, there could be a problem in the Southern oceans and Pacific where other data are sparse.

7.4.3 Example ERS-1 wind product

An example of a simulated ERS-1 swath of wind data is shown in Figure 7.4. The left hand side illustrates the data that might be available operationally; the AMI Rank 1 wind vectors covering a swath in the North Atlantic south of Greenland with the model 12-hour forecast field as a background. The right hand side shows the validation; the background is the model analysis for the same VT, and where the ERS-1 data is plotted are the occasions which were incorrectly ranked (the best rank is plotted).

In this example, the ambiguity removal has been done using the forecast field; the ranking errors are due to the incorrect forecast position of the low centre off the tip of Greenland. Cells to the south are ones where there were two very close ambiguities; errors in choosing wrongly here are not significant, as are winds at the centre of low and high pressure circulations.

7.5 CALIBRATION AND VALIDATION OF ERS-1 WINDS

7.5.1 Initial calibration

ESA intends that the first 3-6 months after launch will be reserved as a calibration phase. Initially, the correct operation of the space hardware and the ground systems, including processing software, will be checked. During the calibration phase, many collaborating laboratories, including the Meteorological Office will assist ESA to assess the accuracy of the satellite products against conventional measurements. To aid this special measurement programme, the MRF Hercules is planned to underfly the satellite, measuring the winds by flying at low level. Other institutes will deploy ships and special buoys across the swath, and this data will be used to calibrate

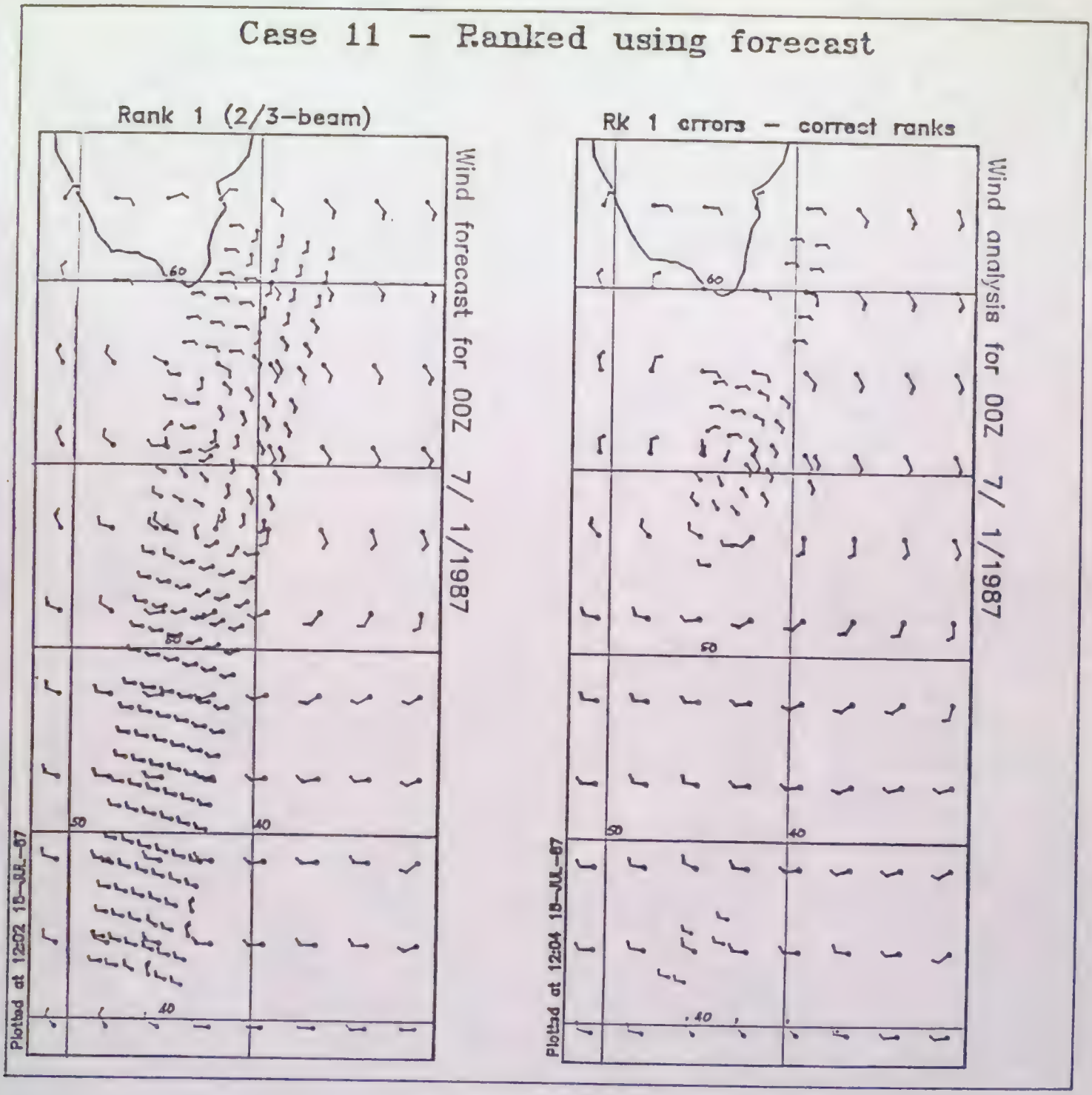

Figure 7.4. Example of simulated swath of ERS-1 winds and model forecast windfield (left) and its validation with associated analysis field (right). For clarity, only every third satellite and model wind is plotted.

the AMI winds by adjusting the initial coefficients in Equation 7.3 so as to minimise the wind retrieval RMS errors and to correct for any biases.

Additionally, all ship and buoy data received over the GTS (including data from buoys deployed by Met.0.16) will be used to compare with the satellite winds and waves, though since the quality of some of the VOF data can be suspect (and few are instrumented) there will need to be careful quality control.

7.5.2 Validation

After the calibration period, the model function (the coefficients in Equation 7.3) may need to be updated. Thereafter, validation, the process of keeping an objective eye on the quality of the satellite-derived data will be continuous, using a three-way comparison. This is illustrated in Figure 7.5;

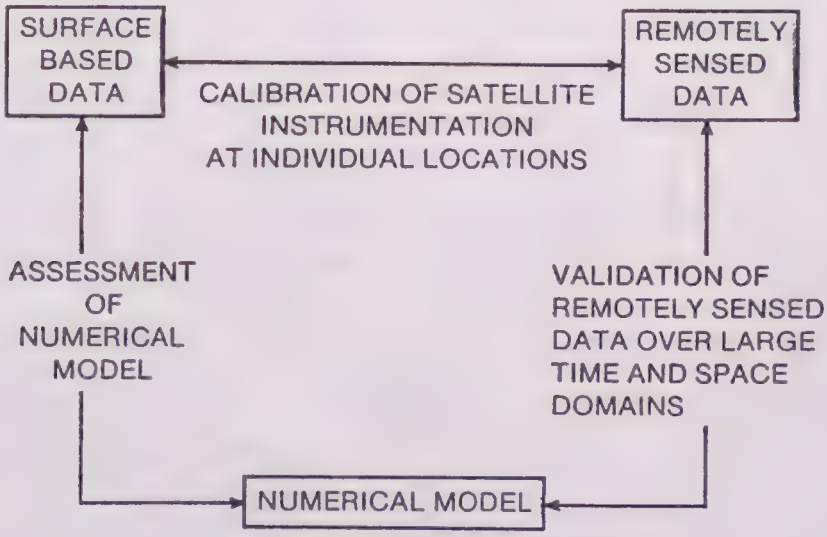

Figure 7.5. Three-way procedure to validate the ERS-1 data against conventional measurements and numerical models.

- the numerical model may be assessed against the surface data (and the surface data quality controlled against the model)

- the satellite data is directly compared with surface data where and when they coincide (not often, especially in the Pacific and Southern oceans)

- compare the satellite data with the model, particularly in areas where *in-situ* data is sparse.

Such an exercise is planned by Met.O.2b, and after the satellite wind and wave data have been shown to be of sufficient quality, they will be incorporated into the atmospheric and wave numerical models, and could also be of use in our storm warning and ship routing services.

7.6 THE MET. OFFICE - CURRENT INVOLVEMENT AND FUTURE USE OF ERS-1 DATA

The problems of extracting accurate wind data within the time constraints of an operational system, and the problems of ambiguity removal are the continuing subject of study within Met.O.19, on behalf of ESA. As part of the ERS-1 project, the United Kingdom is setting up a dedicated off-line ERS-1 Data Centre, to be constructed at RAE Farnborough. This will act as archive and product generation facility for both ESA and directly for UK needs. Here too, the Meteorological Office is involved in developing the algorithms to produce the best possible satellite winds for users not requiring them in real-time, and numerical model output will play a large part in both the derivation and validation of many products from ERS-1.

In order to fully utilise the data from ERS-1, ESA have issued an Announcement of Opportunity (AO) for scientists to use the data in operational meteorology, oceanography and for fundamental research. The Meteorological Office has responded positively to this AO, and expects to be a lead agency in assisting ESA to initially calibrate the wind and wave data after launch, then to validate and assimilate the information into its atmospheric and wave forecast models, as described above.

Simulated assimilation using SEASAT winds, currently being undertaken in the Dynamical Climatology Branch, suggests that such satellite data could have most impact when fully utilised as a global dataset. Met.O.2b are currently looking at ways to assimilate wave data into their wave model using SEASAT data, and Met.O.19 and Met.O.2b will shortly be collaborating on the detailed methods to be used to validate

the ERS-1 wind and waves in near-real time.

7.7 CONCLUSIONS

The wind and wave data from ERS-1 will not be unique; by the mid 1990's, there is expected to be two or three other satellites, operated by the United States, Canada and Japan which could have similar instruments. Indeed, the decision is to be taken soon whether a follow-on ERS-2 can be funded within Europe. Further into the decade, the Polar Platform, part of the US Space Station project is likely to carry similar microwave instruments as part of its fully operational payload. Although ERS-1 is strictly not operational, ESA intends that it can demonstrate this capability during its 2-3 year life. The Meteorological Office, together with other agencies, has taken that challenge, and intends to investigate the utility (or otherwise) of this new source of data, exploiting it fully, in numerical models and for storm warning and ship routing services.

REFERENCES

Harrold, TW	1974	Ground clutter observed in the Dee weather radar project. Met.Mag., 103, 140-141
Jones, WL & Schroeder, LC	1978	Radar backscatter from the ocean: dependence on surface friction velocity. Boundary Layer Met., 13, 133-149
Krishen, K	1971	Correlation of radar backscattering cross sections with ocean wave height and wind velocity. J. Geophys. Res., 76, 6528-6539
Long, AE	1986	Towards a C-band radar sea echo model for the ERS-1 scatterometer. Proc. Conf. on Spectral Signatures in Remote Sensing, Les Arcs, December 1985. ESA SP-247, 29-34.
Offiler, D	1984	A comparison of SEASAT scatterometer derived winds with JASIN surface winds. Int. J. Remote Sensing, 5, 365-378
Offiler, D	1985	ERS-1 surface wind ambiguity removal by means of objective processing and subjective human intervention. Final Report to ESA Contract No. 6154/85/NL/BI

ADVANCED LECTURES
SATELLITE METEOROLOGY
Lecture 8

SATELLITE ASPECTS OF THE FRONTIERS AND COST-73 PROJECTS

by

C. G. Collier

1. INTRODUCTION

The FRONTIERS* system is a computer-based system for merging radar and satellite data, and eventually other meteorological data, to produce precipitation nowcasts, ie detailed descriptions of the current distribution of precipitation plus forecasts for a few hours ahead, obtained by extrapolation. The System was designed and built by Logica Ltd to a Meteorological Office functional specification, and delivered in initial form in 1983 (Browning, 1979, Carpenter and Browning, 1984). Since then considerable effort has been put into bringing the system to operational status which was achieved by September 1986 in the Central Forecast Office at Bracknell.

During the last few years there has been considerable activity in Western Europe aimed at establishing national radar networks. In parallel with this work, several bilateral agreements to exchange weather radar data across national boundaries have been established. Effective international cooperation was stimulated by the European Economic Community (EEC) sponsored COST-72 Project** and this has led to the setting up of a continuation project for weather radar networking known as COST-73, Weather Radar Networking (Collier et al, 1987).

Both Frontiers and COST-73 have in common the aim of combining radar and satellite data to specify the probability of rainfall over extended areas.

*FRONTIERS - Forecasting Rain Optimized using New Techniques of Interactively Enhanced Radar and Satellite

** COST-72/73 - COoperation in Science and Technology Project No 72/73

In this paper we will discuss how satellite data are used in both projects. Techniques for estimating precipitation from satellite data are first reviewed in order to provide the context within which to explain why the approaches being pursued have been chosen. Although much of this paper will be concerned with using satellite data to estimate and forecast rainfall and to some extent low-level humidity, satellite data have a much wider use for short period forecasting, both from the point of view of imagery interpretation (see for example Purdom, 1986, Browning et al, 1987), and for providing sounding information for numerical models (see for example Isaacs et al, 1986, O'Lenic, 1986). Nevertheless, rainfall is a meteorological parameter which has a major impact upon many industries and day-to-day life in general (see for example Newsome, 1981, NWC, 1983) and therefore there is ample justification for devoting resources to its measurement from space.

2. SATELLITE-BASED TECHNIQUES FOR MEASURING PRECIPITATION

Most of the current satellite systems employ several different types of instrument. In general, however, they may be divided into systems using visible and infrared wavelengths, and those using microwave wavelengths, either passively (receiving microwaves generated at the earth's surface or within the atmosphere) or actively (receiving microwave output from the satellite system which is reflected or re-transmitted from the surface or the atmosphere to the satellite).

2.1 Visible and infrared data

Satellite photographs at visible frequencies allow estimates to be made of a variety of parameters for example the fraction of impervious area in a catchment, or the fraction of water surface or polluted area (see for example McGinnis et al, 1979). Flood inundation areas may also be analysed, provided the data resolution is

adequate (Ramamoorthi and Rao 1985). Indeed, it is also possible in some areas to infer likely underground water resources from such data (Salman, 1983).

Nevertheless visible and infra-red data have been most commonly used to make estimates of rainfall, snowfall and, to a much lesser extent, soil moisture. These estimates are made by relating the reflectivity of clouds or the earth's surface in the visible wavelengths, or the thermal infrared radiation emitted by a surface, to the values of independent measurements of the parameter. The relationship of the wavelength of maximum emitted radiance, λ max, and the absolute temperature, T, of the radiating surface is given by Wiens Displacement Law, which states that the product of absolute temperature and wavelength is constant for a blackbody (perfect emitter at all wavelengths);

$$\lambda_{max} T = W \qquad 1.$$

where w is Wien's displacement constant.

Infrared radiant emission is given by the Stefan - Boltzmann Law which relates the total radiant emittance from a blackbody to the fourth power of the absolute temperature;

$$W = \epsilon . \sigma . T^4 \qquad 2.$$

where W is the radiant power per unit area, ϵ is the emissivity of the surface, σ is the Stefan-Boltzmann constant, and T is the absolute temperature (°K). Water of all common natural surfaces is most like a blackbody, and emissivities may vary from 0 to less than 1.00 and depend on wavelength. The thermal inertia, P, is the resistance of a material to temperature change given by,

$$P = (k c \rho)^{1/2} \qquad 3$$

where K is the thermal conductivity, C is specific heat and ρ is the density.

The thermal infrared temperature that is measured from a satellite is modified by the atmosphere. The radiation measured when looking down vertically is partly made up of reflected radiation from the sky in the clear sky situation. If clouds are present then rapid changes in the radient emission from a surface can occur.

Two types of technique for estimating rainfall (snowfall has not been examined in any dpeth) have been developed, these being known as cloud indexing and life-history methods (for a comprehensive review see Barrett and Martin, 1981).

Cloud indexing was the first technique developed for rainfall estimation. A rainfall coefficient or cloud index was evaluated from features of the satellite cloud field defined by visible or infrared images, for example brightness or texture. These indices were then related, via regression equations, to raingauge observations of rainfall (Barrett, 1970, Follonsbee, 1973, Follonsbee and Oliver, 1975, Follonsbee, 1976, Fenner, 1982). These techniques were most successful for rainfall over periods of days or months, partly because satellite data from polar orbiter platforms are only available every 6 or 12 hours. Barrett et al (1986) describe the technique developed over a number of years at the University of Bristol. Regression techniques are used with both polar orbiting and geostationary satellite data, but the procedure involves a high level of subjective interpretation by an analysist. In general these techniques only function well for convective cloud, as opposed to frontal cloud. Figure 1 shows the derived relationship over southeast Australia between 90 minute rainfall totals and cloud top temperature. Pattern recognition techniques using textural or radiance features are also being assessed (Wu et al, 1985). Stout et al (1979) were able to estimate the rainfall produced by convective clouds from the sum of the area of the clouds and the rate of change of that area, that is,

Volumetric rain rate for a particular cloud,

$$R_v = a_o A_c + a_1 \frac{d\ Ac}{dt} \qquad 4$$

where Ac is the area of the cloud, dAc/dt is the rate of change of cloud area, and a_o and a_1 are empirical coefficients. This type of technique, known as a life-history procedure requires satellite images at frequent time intervals which can only be provided by geostationary satellites.

Variants on the Stout et al technique have been produced by Griffith et al (1976, 1978) (also described in Woodley et al, 1980), and Scofield and Oliver (1977a, b) (see also Scofield, 1984). In the latter technique precipitation is favoured by high cloud brightness (low cloud top temperature), and heavy rainfall is favoured by cold cloud top temperatures, growth and merging of clouds.

Improvements to deal more adequately with storms having warm tops have been proposed by Scofield (1981, 1982). More recently Neil (1984), Neil and Spagnol (1987) have suggested that the precipitation which falls in some time period can be approximated by a governing equation,

$$\Delta P = P_2 - P_1 \simeq \sum_{i=0}^{n} a_i \left[m\ \Delta\ \ln(rN) \right]^i \qquad 5$$

where a_i are empirical constants, m is the precipitable water content, r is the mean resolution factor for the cloud system being studied, and N is the number picture elements (pixels) which are part of the cold cloud area. Hence $\Delta \ln (rN)$ is the logarithm of the actual change in cloud area over time. It was found that a threshold cloud top temperature near the coldest tops should not be chosen, since cloud areas so defined were not always representative of cloud systems as a whole. Using data in the area of British Columbia, Canada the predictive graph shown in Figure 2 was derived. The addition of spectral and textural information from geostationary satellite data to the evolutionary data has been

investigated by Martin and Howland (1986), and found to produce useful improvements in the tropics.

Negri and Adler (1981) found that thunderstorm top ascent rates are correlated with maximum storm radar reflectivities, and the minimum blackbody temperature observed during the lifetime of a storm is correlated with the maximum volumetric storm rainfall. In general this technique only produces acceptable estimates of convective rainfall. However, Negri et al (1984) have concluded that the Griffith-Woodly technique is unnecessarily complicated for daily rainfall estimation. Doneaud et al (1985) have proposed a simple procedure in which the Area-Time-Integral (ATI) of cloud areas over the lifetime of a storm is related to the total rain volume. Initial investigations are encouraging, although again the technique is likely to work well only for convective rainfall.

Seasonal changes in snow cover can be monitored regularly from satellite visible and thermal infrared images (Rango et al, 1977, Dey et al, 1979, Rango and Martinec, 1979, Dey et al, 1983), although accurate classification of snow types and distribution requires the use of multispectral data as discussed in the next section. The use of these techniques in the USSR has been reviewed by Deleur (1980), and elsewhere by Rango and Itten (1976), Rango and Peterson (1980).

Measurement techniques based upon the use of visible and/or infrared images are limited to sensing the surface conditions of the snow (Martinec and Rango, 1981). As the snow melts it is very important for hydrologists to assess the potential run-off. Odegaard et al (1980) demonstrated the use of high resolution satellite data with in situ surface observations in hydrological studies of snow melt for hydroelectric generation. One problem in measuring the extent of snow cover from a satellite is the masking produced by clouds. However, it is possible to distinguish between clouds and snow cover by using a range of spectral bands as discussed in the next section.

2.2 Multispectral data

The use of single images, or sequences of images, of either visible or infrared data has been discussed in the previous section. However, procedures have not proved to be totally reliable as required for operational implementation. Improvements can be obtained by the combined use of data from several spectral bands.

Infrared sensors on satellites provide information on temperature, and thus indirectly on the heights of the tops of clouds. On the other hand visible sensors provide information on the depth of clouds, their geometry and composition. Combination of this information enables recognition of high cloud tops associated with deep clouds which are likely to produce significant rainfall. Early work on this type of technique was carried out by Lethbridge (1967), Dittberner and Von der Haar (1973), and Reynolds et al (1978). However problems arising from registration errors between visible and infrared images, instrument calibration, time difference between images, and illumination geometry caused the results of the early work to be less encouraging then workers had expected. Lovejoy and Austin (1979a) demonstrated that these problems could be overcome, and this technique is used in FRONTIERS and will be discussed further later in the paper.

Several investigations using models of convective processes aimed to tackle the problems from a physical rather than a statistical, point of view (Gruber, 1973; Wylie, 1979). These techniques are able to define rain areas. However, the estimation of rainfall amounts is more problematic, and ground-truth data such as that provided by radar may be needed for calibration of the satellite data when making estimates of rain amounts or reliable estimates of rain area. Tsonis and Isaac (1985) have proposed a scheme which uses radar data to define areas of rain/no rain for calibration and subsequently uses the satellite visible and infra-red data only to delineate

areas of rain; no quantitative estimates are produced however.

The latest generation of satellites provide data with high spatial and cloud top temperature resolution. Unfortunately these data are not adequate on their own to allow the automated analysis of different cloud types and the separation of these types into clouds producing precipitation, and those which are not.

Liljas (1982) has evolved a technique using data from three AVHRR spectral channels as follows:

Visible (VIS)	0.55 - 0.9 μm (micrometres)	(TIROS-N)
	0.58 - 0.68 μm	(NOAA-6, -7)
Near Infrared (NIR)	0.725 - 1.1 μm	
Infrared (IR)	10.5 - 11.5 μm	

The technique is similar to that proposed by Barratt and Grant (1978), and is based upon the assumption that different cloud types, land and water surfaces have different radiational properties in different parts of the electromagnetic spectrum. Signatures were derived of different cloud types within boxes in three-dimensional intensity space as shown in Figure 3. The technique has been assessed over southern Scandinavia with encouraging results, Figure 3b, c.

The problem of separating cloud and snow cover on visible and infrared images was mentioned in section 2.1. The thermatic Mapper on Landsats 4 and 5 provided data in seven wavelength bands as follows:

Band 1	0.45-0.52 μm
Band 2	0.52-0.60 μm
Band 3	0.63-0.69 μm
Band 4	0.76-0.90 μm
Band 5	1.55-1.75 μm
Band 6	10.40-12.50 μm
Band 7	2.08-2.3 μm

Bands 1 to 5 and 7 are in the visible, near-infrared and middle infrared wavelength regions and have a spatial resolution of 30m. Band 6, a thermal

infrared band, has a resolution of 120m. Band 5 may be used to distinguish between clouds and snow as the reflectance of snow decreases markedly at a wavelength of about 1.5 μ m, whereas the reflectance of clouds remains high.

2.3 Passive microwave techniques

The microwave radiation (roughly 10 to 0.1 cm wavelength) thermally emitted by an object is called its brightness temperature, T_B. The microwave radiation emitted from a blackbody is proportional to its physical temperature, T, but, as for infrared emission, most real surfaces or objects emit only a fraction of the radiation a blackbody would emit at the same physical temperature. This fraction is the emissivity ϵ, of the object given, for microwave wavelengths. The use of the microwave region of the electromagnetic spectrum to make measurements of precipitation has the advantage over visible and infrared techniques of detecting the precipitation itself with clouds being wholly or partly transparent.

One of the first instruments to be used meteorologically to measure the natural radiation in the microwave region was ESMR-5 (Electrically Scanning Microwave Radiometer) launched on Nimbus-5 in 1972. Simple comparisons of the ESMR-5 imagery operating at 19.33 GHz (1.55 cm wavelength) with imagery from visible and infrared wavelength radiometers, ground-based radars, and conventional meteorological observations established, over water, an association of areas of relatively warm brightness temperature with areas of rainfall (Theon, 1973, Wilheit et al, 1973, 1977). Curves of 19.35 GHz brightness temperatures and rainfall rate were published by Wilheit et al (1977) using a model based upon the concept of many optically thin layers bound on top by a variable freezing level.

In this work several problems were identified, notably that rainfall was rarely uniform over the whole field of view of the instrument and the

non-linearity of the relationship between rainfall rate and brightness temperature (Spencer et al, 1983). Improvements to the technique, including the use of both vertical and horizontal polarisation for measurements over land, have been proposed by Wilheit (1975). Nevertheless, measurements over the land are much more difficult due to variability of the emissivity and hence the background radiation measured by the satellite instrument.

In an attempt to overcome the problems of non-linearity mentioned above and ambiguities introduced between emissions due to rain and those due to non-precipitating cloud, Spencer (1986) proposed a technique based upon analysis of radiometric data gathered from the NIMBUS-7 SMMR at a frequency of 37 GHz (0.81 cm wavelength). This radiometer system provides dual polarized data at five different wavelengths (0.81 cm, 1.43 cm, 1.66 cm. 2.80 cm and 4.54 cm), and can be used to detect a wide range of snow and ice features as well as rainfall. Figure 4 shows how the difference between brightness temperatures from horizontal and vertical polarized radiation at 37 GHz is related to the mean brightness temperature and rainfall rate for convective rainfal over the USA.

Spencer (1986) suggests that 37 GHz can provide the best compromise for measuring rainfall over the oceans between an easily detectable precipitation signal (such as at 19.35 GHz) and cloud penetration ability. However, it was noted that the scattering signal at 37 GHz is not as strong as the emission signal of light precipitation at 19 GHz. Hence the 37 GHz technique may be better for observing heavy convective precipitation, and observations at 19 GHz may relate better to measurements of light precipitation.

2.4 Active (radar) microwave techniques

Measurements of the intensity of brightness of microwave energy generated in a radar mounted on a satellite and reflected or scattered from the

from the atmosphere or the earth's surface, may be made on receipt back at the satellite antenna. The amount of backscattered energy is related to the surface roughness, orientation, slope and the dielectric constant of the material from which the surface is composed. It also depends upon any rainfall intercepted by the radar beam, as short wavelengths are attenuated by heavy rainfall. Lee (1987) considers the potential accuracy of a satellite-borne radar for monthly rain measurements with and accuracy of 10-20%. He concludes that this accuracy cannot be attained at present.

Figure 5 shows the geometry of the Seasat Synthetic Aperture side looking Radar (SAR). This sensor used the motion of the satellite to synthesize a large aperture antenna, and operated at 1.275 GHz (23.5 cm). Hall and Martinec (1985) point out that the length of the electromagnetic wave with respect to the size of the terrain feature determines whether a surface appears rough or smooth at a particular wavelength. Smooth water surfaces are excellent specular reflectors, and because they are not normally viewed at right angles to the SAR, they specularly reflect all the microwave energy into space. However horizontal and vertical surfaces may appear to the SAR as corner reflectors and return a large part of the energy back to the antenna. In Figure 5 the image resolution in the across track direction, d_r, is given (Fu and Holt, 1982) by,

$$d_r = c\tau/2 \sin\theta \qquad (6)$$

where τ is the effective pulse width and c is the speed of light. The maximum resolution achieved by the Seasat SAR was 25 m x 25 m and the image area was 100 km by 4000 km. Seasat also carried a radar altimeter, operating at 13.56 GHz (2.2 cm wavelength) for measuring the roughness of the oceans.

Unfortunately Seasat only operated for 100 days, but this was long enough to indicate the potential of the data for measuring soil moisture (Ulaby et al, 1983, Brisco et al, 1983, see also Ulaby et al, 1986).

It has been suggested (Bernard et al, 1981) that active microwave techniques might be used with soil water balance models to estimate regional evaporation.

At present active microwave systems are not being flown on satellites, but several satellite launches are planned which will carry radars, for example the Tropical Rainfall Measuring Mission (TRRM) includes the proposal to fly 14 and 35 GHz active radars at an altitude of about 300 km (see Lee, 1987). Radar systems offer considerable potential. For example Atlas et al (1981) state that there is no doubt that "satellite active microwave systems could provide precision global distributions of rain rate given no constraints on the number of spacecraft, antenna size, and power". Problems of radar beam filling and the unwanted effects of radar echoes from the ground might be overcome by using a sufficiently large antenna. However a practical antenna size requires the use of short wavelengths which are attenuated by heavy rainfall. One possible solution, proposed by Atlas et al (see also Inomata et al, 1981) is to use two wavelengths, one attenuating and the other not. A further problem is that the signal averaging time needed to obtain a reliable estimate of the radar echo power implies either a very high radar pulse repetition frequency or a very slow scan.

The following possibilities were put forward by Atlas et al (1982):

a. use of a modified radar altimeter operating at 13.5 GHz (2.2 cm wavelength) used in conjunction with infrared images or a passive microwave radiometer; unfortunately this would be restricted to nadir measurements only.

b. use of a short wavelength scanning radar operating at two wavelengths (0.86 cm and 3 cm say); this would enable a narrow beamwidth to be obtained with a practical size antenna. Unfortunately

severe attenuation would occur in rainfall of only moderate intensity, limiting the accuracy which could be achieved.

c. use of a surface target attenuation radar using the scattering properties of the surface as a calibration for attenuation measurements. Unfortunately the scatting properties are influenced by soil moisture, and this problem would have to be overcome.

All of the above techniques are far from being operational at the present time.

2.5 Summary

Since several systems will provide measurements of the same parameters across a wide part of the electromagnetic spectrum, it is important to assess the relative merits and cost-effectiveness of each technique. By far the largest amount of effort has been put into the measurement of precipitation, in particular rainfall, and evaluations of the measurement techniques are now being carried out (for example see Johnstone et al, 1985). Table 1 presents a summary of the accuracy achieved, and that likely to be achieved using a range of techniques. Two points emerge from this table. Firstly that most of the assessments of the accuracy of rainfall totals have been made as integrations over areas greater than 10 km. However, some techniques are capable of measurements over areas as small as 50 km, or over areas approaching global scales. Secondly most of the studies have been concerned in the main with the measurement of convective rainfall rather than frontal rainfall.

TABLE 1

Summary of the performance of satellite rainfall estimation techniques (from Collier, 1985 partly based upon Lovejoy and Austin 1979b, 1980)

Technique	Area over which estimates are assessed (km^2)	Period of integration (hours)	Approximate percentage accuracy (%)	Sample references describing techniques (rainfall types)
Cloud indexing	10^5	24	122	Follonsbee and Oliver (1975) (convective/frontal)
Life-history	10^4	1	85	Griffith et al (1978)
	10^5	24	55	(convective)
	10^4	½	50	Wylie (1979) (convective)
	6×10^3	½	65	Stout et al (1979) (convective)
Bi-spectral	10^5	½ - 2	49	Lovejoy and Austin (1979 a, b) (convective/frontal)
Passive microwave	10^3	24	70	Lovejoy and Austin (1980) (convective/frontal) Wilheit et al (1973) Spencer et al (1983)
Active microwave	10^3	12	20 (when combined with bi-spectral technique)	The accuracy of this technique is unknown but Lovejoy (1981) suggests the figures given may be possible.

The first point is reinforced by the work of Augustine et al (1981), who found that the best correlations between satellite estimates of rainfall made using the Griffith/Woodley technique and raingauge/radar data were achieved for six hour periods over 9350 km^2 (the largest area considered), the worst correlations were found for half hour rainfall totals over areas of 55 km^2. The most accurate rainfall estimates in all rainfall types would appear to be obtained by the Lovejoy and Austin bi-spectral technique with an error of around 49% for rainfall totals of ½ to 1 hour over areas

of around 10^5 km^2. Other techniques (Griffith and Woodley, 1981), tuned to making measurements in convective rainfall, may attain this accuracy over areas of around 10^4 km^2. The accuracy of passive microwave techniques is uncertain as assessments have been rather limited, although an uncertainty in the region of ± 60% over 400 km^2 areas has been deduced. Active microwave techniques remain to be examined in practice. Estimates of likely performance have been made, but require experimental confirmation.

Rainfall amount is not measured with uniform accuracy. Some techniques for example Scofield (1982) are fine tuned to measure heavy convective rainfall likely to produce flash floods. However, any one technique cannot be expected, at present, to measure all rainfall amounts with the same accuracy. For example Wylie and Laitsch (1983) found that up to 30% of daily rainfall amounts at a point were correctly detected for rain amounts greater than 10 mm, yet only up to 15% of daily rainfall amounts were correctly detected for rain amounts greater than 25 mm. The procedure used was simple and more complex procedures are likely to improve on this performance; but nevertheless the difference between rainfall amounts is likely to remain.

Clearly the different satellite measurement techniques all have their advantages and disadvantages. It is unlikely for many years to come, even with the advent of active microwave techniques, that one satellite system for the measurement of rainfall will be universally accepted. The same is true for the determination of snow cover. Bellon and Austin (1986) concluded that at present satellite estimates of rainfall were better than raingauge estimates at locations where the nearest raingauge is further than 40 km. Therefore such techniques are limited to the data sparse regions of the world.

3. THE USE OF SATELLITE DATA IN FRONTIERS

3.1 Overview of Frontiers

The complementary nature of ground-based and space-based measurements, particularly when assessing rainfall amount has been recognised (Collier, 1985), and this principle is embodied in the FRONTIERS system. FRONTIERS operates on a half-hourly cycle synchronised with Meteosat's transmissions. The cycle is divided into three major stages, as shown in Figure 6 and outlined below (Conway, 1987).

In the radar analysis stage the operator aims to produce the best possible estimate of the intensity and areal extent of the rainfall within the area covered by the radars (figure 7). He does this by using data from other sources (conventional observations, Meteosat cloud-images, etc), and his understanding of the meteorological situation to help recognise and correct errors in the radar data.

In the second stage the operator extends the area of coverage beyond the radar area by attempting to deduce the extent (but not the intensity) of rainfall over the full FRONTIERS area from Meteosat cloud-images. The satellite-derived rainfall is merged with the quantitative radar rainfall map from the radar analysis stage to provide as complete a picture as possible of current rainfall in the FRONTIERS area.

The final stage is the production, by the linear extrapolation of recent movement, of a sequence of rainfall forecasts covering the next three hours. The operator divides the rainfall field from the second stage into a number of clusters to which he assigns independent velocities. FRONTIERS then computes the forecast by moving the clusters with their assigned velocities. This stage will not be discussed further in this paper.

3.2 Satellite analysis

Because the coverage provided by the UK weather radar network is insufficient, even for a three hour advection forecast for areas within radar coverage, Meteosat imagery is used to infer probable areas of precipitation outside the area for which good radar data are available. This depends upon rainfall type and is delineated by the Useable Data Boundary (UDB) (see Brown, 1987). To maximise the reliability of the operational system, only rain or no rain predictions are made at present. The method used is basically that described by Lovejoy and Austin (1979a) as this method was judged to be that most likely of success (see Table 1). The visible and infrared data are each divided into 16 classes and a table of "probabilities" of rain for each class produced by comparison with the radar data. Prior to correlation the forecaster can if necessary manually adjust the registration of the satellite imagery with respect to any coastline visible. Three tables are constructed: visible alone, infrared alone and visible + infrared, the latter being a two-dimensional table; an example is shown in Table 2. In order to apply the tables to the satellite data outside the UDB, it is necessary to select a critical probability which differentiates between rain and no rain. This is chosen dynamically, as the probability which predicts an areal extent of rain within the UDB which best matches the extent observed by radar.

The correlation technique often gives best results using the two-dimensional table because this contains information on cloud thickness and cloud-top temperature. Visible alone can be nearly as good but infrared alone is often inferior, particularly in frontal cases, where it tends to overestimate the extent of the precipitation ahead of the warm front.

An example of a visible + infrared correlation rainfall field is shown in Figure 8, constructed from the radar data in Figure 9. This agrees quite

well with the radar field although it predicts some spurious patches of precipitation to the east of the main precipitation band. It's most useful attribute is to extend the radar observed precipitation band to the north west and to the south. This was in accord with the 11 GMT synoptic observations, all stations in the northern half of Ireland were reporting rain, mainly moderate. Light rain was also being reported at several stations in the north west of France.

The correlation method cannot work in certain situations, for example when there is insufficient radar data to form a reliable correlation table because most of the precipitation is still outside the UDB. Universal correlation tables can then be used, which have been constructed from past experience. If neither technique produces a satisfactory result, both the visibile and infrared imagery can be sliced so that a contiguous range of brightnessesand temperatures represents the rainfall field. If most of the precipitation lies outside the UDB the forecaster must judge the result using available synoptic observations and conceptual models of the distribution of precipitation within the prevailing synoptic archetype.

The final step of the satellite analysis allows the forecaster to modify the satellite-derived rainfall field and merge it with the radar field. Because of the lower reliability of the satellite estimate, rainfall can be added to it or subtracted from it subjectively. The radar data is inviolate at this stage. Initially the combined rainfall field is displayed with the satellite estimate inserted beyond the maximum radar range of 210 Km. This often leads to gaps between satellite and radar fields so that the forecaster is allowed to bring the satellite estimate up to the UDB in any delineated area. If unrealistic gaps still persist the forecaster may judiciously merge the satellite field with the radar field inside the UDB. This is justifiable because the UDB is calculated assuming a

precipitation field of uniform depth and so cannot perfectly describe the actual limit of radar coverage. Clearly the satellite field should not be used close to the radars where the probability of detection by radar is high. Figure 10 shows the combined field resulting from the merger of the fields shown in Figures 8 and 9. The satellite estimate is displayed in white to distinguish it from the quantitative radar data. In this case the forecaster has deleted the leading edge of the satellite field to the west of Scotland to match the edge of the radar field and also to take account of the 11 GMT synoptic reports. The satellite estimate has been inserted within the UDB to produce a coherent field and makes a particularly significant contribution over the Irish Sea and to the west of Scotland.

3.3 Difficulties

The procedure described in the previous section enables the derivation of combined radar and satellite images, but does not provide estimates of surface precipitation beyond the UDB of the radar coverage. It is possible to employ the bispectral technique of Lovejoy and Austin to estimate rainfall amount using statistical analysis of the radar, IR, VIS values, but the technique does not derive rainfall amounts directly and really provides images of "calibrated" graded rainfall probabilities. Nevertheless it is possible to chose rainfall rates which optimise a defined skill score above the values likely to arise at random (Carpenter, unpublished report). The success of such a technique is however very uncertain.

A further problem is that the look-up tables are often rough when derived in real-time ie small and large VIS/IR counts are juxtaposed, and too many counts occur in the no rain class. It is also found that areas of no data sometimes appear in the middle of areas with data. Such gaps may be filled

by manual intervention or automatic interpolation, but it is often better to use a climatological look-up table providing suitably smoothed data.

4. THE USE OF SATELLITE DATA IN THE COST-73 PROJECT

In the COST-73 Project, the requirement is similar to that in FRONTIERS, namely to extend the coverage produced by a radar network, in this case the loosely coupled european radar network. A technique for estimating rainfall from satellite data is required needing no manual intervention and being capable of operation at night.

Consideration of section 2 of this paper indicates that no such technique is presently available. Nevertheless, the regular combination in polar stereographic coordinates of IR images and radar data is being undertaken (Collier et al, 1987). The procedure is simple, where radar data are available they are used, and where they are not medium (cloud top temperature < -15 to $-45°C$) and high level ($< -45°C$) cloud data are used. Examples are shown in Figure 11.

Experience with this simple procedure has highlighted the difficulties of using level sliced IR data to estimate rainfall. Figure 12 shows very heavy rainfall from thunderstorms along a squall line over eastern France. An area of light to moderate precipitation develops to the west of the main squall line associated with an area of medium level cloud. Similar rainfall intensities over western France are associated with low level cloud and over south east France with high level cloud as part of the thunderstorm rainfall. Note also the spiral pattern of the rainfall under the thunderstorm anvil of the large storm. Visible data relate much better to convective rainfall, but high level cirrus cloud and multi-level cloud decks often obscure rain-bearing cloud in frontal situations.

Whilst the radar data and conventional observations can identify those parts of cloud which are producing rain, there would not appear to be one, or

indeed a small number of, universal relationships which relate the different types of data. One aim of the COST-73 Project is to investigate how best to "calibrate" the satellite data using radar data. One approach, based upon Lovejoy and Austin's algorithm has been mentioned in the previous section of this paper, another technique might be adaption of the procedure investigated by Doneaud et al (1987) and considered below.

5. FUTURE DEVELOPMENTS

The measurement of precipitation from space is a challenging task which is to being persued in both the FRONTIERS and COST-73 Projects as elsewhere. Active radar devices are unlikely to provide for many years to come, the spatial and temporal coverage required for short period weather forecasting. The bispectral techniques seem to offer the best hope of developing an operationally viable system for estimating rainfall amount. However, unless highly sensitive instruments to measure moonlet scenes are developed for civil use, then the estimation of rainfall at night will remain very much more difficult than during the day.

The approaches which seem to offer the most chance of success are as follows. These approaches will have to involve compromises, and will result in techniques which may be pragmatic rather than scientifically robust.

5.1 Radar adjustment

Within the UDB of the radar coverage for either single radars or groups of radars in the same geographic location the VIS, IR and radar values are tabulated. The mean rainfall rate for stated VIS, IR and VIS/IR pairs are derived for each location. This procedure might be carried out for the total radar coverage area, but care must be taken to eliminate those areas of poor radar coverage caused by ground clutter and occultation effects. (blocking produced by hills or masts close to the radar sites).

Using VIS/IR pairs results in a relationship such as that derived by Bellon and Austin (1986), Figure 13, for convective rainfall. Average rainfall rates of less than 0.5mmh^{-1} that occur at VIS/IR pairs corresponding to warm temperatures and low visible counts are mainly a result of improper radar-satellite matching. Such problems arise from uncertainties in the satellite navigation, time differences between the radar and satellite data, or from mis-alignment between the satellite view of the cloud tops and the level of the radar observations. The rainfall rates of these pairs is set to zero to avoid the generation of spurious areas of small or trace rainfall amounts. This loss of rainfall of about 20% in the cases studied by Bellon and Austin has been allowed for by multiplying the data in Figure 13 by a factor of 1.2.

Similar procedures for VIS only and IR only were found by Bellon and Austin not to be as successful as using VIS/IR pairs. However, in principle, given more than one IR channel such as the 3.7μm and 11μm channels of the AVHRR instrument on the NOAA polar orbiting satellites, it may be possible to use the same type of technique. Such channels will become available on GOES NEXT and Meteosat 2nd Generation. Temperatures for these two channels are similar for land and sea, but the brightness temperature at 3.7μm is colder than that at 11μm for water cloud. Cirrus cloud appears to be warmer at 3.7μm than at 11μm. Differences in brightness temperatures between these two channels have been used successfully to identify regions of fog and low stratus(Allam, 1987). Comparison of these differences with radar data and the 11μm temperatures might remove some of the ambiguities in the IR/radar relationship which could be extended for use with geostationary satellite data during the interval between polar orbiting satellite passes. It remains to be seen to what extent this method is viable, but multi-spectral adjustment techniques in general must provide the best hope of a practical

rainfall estimation scheme. Statistical procedures involving the optimization of skill scores to derive rainfall amounts from the VIS/IR pairs seem to the author to be an unnecessary complication which may not provide a concomitant improvement in reliability or accuracy.

5.2 Area - Time - Integral techniques

Doneaud et al (1987) have demonstrated a technique for generating total rain volume estimates from satellite data. The technique does not estimate rain rates and has only been used for convective rainfall. Nevertheless, further research to extend the method as follows to statiform rainfall using radar data could prove profitable. Areas of the satellite IR image identified from radar as being above particular rainfall rates are recorded for the lifetime of a rainfall system or until it moves out of radar coverage. The total areas integrated over the system lifetime in the area of coverage are calculated, and related to the mean rainfall amounts in each area over the same period.

Beyond the area of radar coverage IR data are level-sliced to extract a range of cloud areas integrated over the same period as the radar analysis. Rainfall amounts are derived by comparison with the ATI/rainfall curve. Areas of cirrus cloud would have large values of ATI which hopefully would not appear on this calibration curve, but if the underlying rain cloud pattern was not evident at any time during the period rain estimates would not be possible. Cloud from which rain was falling would be likely to introduce texture to the images which level slicing might reveal. The presence of cirrus would also be inferred by the continuity of the area analysis during the period, and appropriate allowance made to construct a consistent sequence before integration. How successful and automatic this procedure will be remains to be seen. It is likely to work best for

convective rainfall, but could produce useful guidance where the effects of cirrus do not dominate continuously.

References

Allam, R. 1987 "The detection of fog from satellites". Preprints of Workshop on Satellite and Radar Interpretation, Reading, England, 20-24 July Eumetsat publ., pp495-507.

Atlas, D., Echerman, J., Meneghini, R. and Moore, R.K. 1982 "The outlook for precipitation measurements from space", Atmosphere-Ocean, 20(1), pp50-61

Augustine, J.A., Meitin, J.G., Griffith, C.G., and Woodley, W.L. 1981 "An objective evaluation of the Griffith/Woodley rain estimation technique", 4th Conf. on Hydromet., 7-9 Oct., Reno, Nevada, AMS, Boston, pp134-140.

Barrett, E.C. 1970 "The estimation of monthly rainfall from satellite data", Mon. Wea. Rev., 98, pp322-327.

Barrett, E.C. and Grant, C.K. 1978 "An appraisal of Landsat 2 cloud imagery and its implications for the design of future meteorological observing system", J Br Interplanet Soc 31, pp3-10.

Barrett, E.C. and Martin, D.W. 1981 The Use of Satellite Data in Rainfall Monitoring, Academic Press, London/New York/Toronto/Sydney/ San Francisco, 340 pp.

Barrett, E.C., D'Sousa, G. and Power, C.H. 1986 "Bristol techniques for the use of satellite data in rain cloud and rainfall monitoring", J. British Interpan. Soc., 39, pp517-526.

Bernard, R., Vauchin, M. and Vidal-Madjar, D. 1981 "Possible use of active microwave remote sensing data for prediction of regional evaporation by numerical simulation of soil water movement in the unsaturated zone", Water Res. Res., 17(6), pp1603-1610.

Bellon, A. and Austin, G.L. 1986 "On the relative accuracy of satellite and raingauge rainfall measurements over middle latitudes during daylight hours", J. Climate Appl. Met., 25, no 11, pp1712-1724

Brisco, B., Ulaby, F.T. and Dobson, M.C. 1983 "Spaceborne SAR data for land-cover classification and change detection", in IEEE Int. Geosci Remote Sensing Symp (IGARSS'83) Digest, San Francisco, 31 Aug-2 Sept (IEEE Cat No IEEE 83CH 1837-4).

Brown, R. 1987 "The use of imagery in the Frontiers percipitation nowcasting system", Preprints of Workshop on Satellite and Radar imagery interpretation, Reading, England, Eumetsat publ., 20-24 July, pp459-472.

Browning, K.A. 1979 "The Frontiers plan: a strategy for using radar and satellite imagery for very short-range precipitation forecasting", Met. Mag., 108, pp161-183.

Browning, K.A., Bader, M.J., Waters, A.J., Young, M.V. and Monk, G.A. 1987 "Application of satellite imagery in nowcasting and very short range forecasting", Met. Mag., 116, 1379, pp161-179.

Carpenter, K.M. and Browning, K.A. 1984 "FRONTIERS - progress with a system for nowcasting rain", Proc. Nowcasting II, Norrkoping, 3-7 Sept, ESA SP-208, pp427-432.

Collier, C.G. 1985 "Remote sensing for hydrological forecasting", in Facets of Hydrology Volume II, edited by J C Rodda, John Wiley & Sons Ltd., Chichester/New York, pp1-24.

Collier C.G., Fair, C.A. and Newsome, D.H.	1987	"Weather radar networking in western Europe - the COST-73 Project", submitted to Bull. Am. Met. Soc.,
Conway, B.J.	1987	"FRONTIERS: An operational system for nowcasting precipitation", Preprints IUGG Vancouver.
Delbeato, R. and Barrell, S.L.	1985	"Rain estimation in extratropical cyclones using GMS imagery", Mon. Wea. Rev., 113, pp747-755.
Deleur, M.S.	1980	Satellite Methods of studying Snow Cover, Leningrad (Bridrometeoizdat), 76pp in Russian.
Dey, B., Gregory, A.F. and Moore, H.	1979	"Application of satellite images for monitoring snowline in the Yukon and North west Territories", Polar Record, 19, no122, pp145-154.
Dey, B., Goswami, D.C. and Rango, A.	1983	"Utilization of satellite snow-cover observations for seasonal stream flow estiates in the Western Himalayas", Nordic Hydrology, 1983, pp257-266.
Dittberner, G.J. and Vonder Haar, T.H.	1973	"Large scale precipitation estimates using satellite data; application to the Indian Monsoon", Arch. Met. Geoph. Biokl., ser B, 21, pp317-334.

Doneaud, A.A., Miller, J.R., Johnson, L.R., Vonder Haar, T.H. and Laybe, P. 1985 "The area-time-integral technique to estimate convective rain volume over areas applied to satellite data - a preliminary investigation", Preprint Vol., 6th Conf on Hydromet, 29 Oct-1 Nov, pp238-245. Also in J. Climate App. Met., 26, pp156-169.

Fenner, J.H. 1982 "Using satellite imagery to estimate winter season rainfall in Europe", Preprints 9th Conf. Weather Forecasting and Analysis, Seattle, Washington, AMS, Boston, pp245-249.

Follonsbee, W.A. 1973 "Estimation of average daily rainfall from satellite cloud photographs", NOAA Tech Memo, NESS 44, Washington DC, 39pp.

1976 "Estimation of daily precipiation over China and the USSR using satellite imagery", NOAA Tech Memo NESS 81, Washington DC, 30pp.

Follonsbee, W.A. and Oliver, V.J. 1975 "A comparison of infrared imagery and video pictures in the estimation of daily rainfall from satellite data", NOAA Tech Memo NESS 62, Washington DC, 14pp.

Fu, L. and Holt, B. 1982 Seasat Views Oceans and Sea Ice with Synethetic-Aperture Radar, NASA Jet Propulsion Laboratory, JPL Publ. 81-120.

Gloersen, P. and Salomonson, V.V. 1975 "Satellites - new global observing techniques for ice and snow", J. Glaciol., 15, no73, pp373-389.

Griffith, C.G. and Woodley, W.L. 1981 "The estimation of convective precipitation from GOES imagery with the Griffith/Woodley technique" in Precipitation Measurements from Space Workshop Report, edited by D Atlas and O.W. Thiele, NASA Goddard Space Flight Center, ppD154-D158.

Griffith, C.G., Woodley, W.L., Browner, S., Teijeira, J., Maier, M., Martin, D.W., Stout, J. and Sikdar, D.N. 1976 "Rainfall estimation from geosynchronous satellite imagery during the daylight hours", NOAA Tech Rept., ERL 356-WPM07, Boulder, Colo, 106pp.

Griffith, C.G., Woodley, W.L., 1978 "Rain estimation from geosynchronous satellite imagery - visible and infrared studies", Mon. Wea. Rev., 106, pp1153-1171.

Gruber, A. 1973 "Estimating rainfall in regions of active convection", J. Appl. Met, 12, pp110-118.

Gurney, R.J. and Camillo, P.J. 1984 "Modelling daily evapotranspiration using remotely sensed data", J. Hydrology, 69, pp305-324

Hall, D.K. and Martinec, J. 1985 Remote Sensing of Ice and Snow, publ Chapman and Hall, London/ New York.

Inomata, H., Okamoto, K., Ajima, T., Masuko, H., Yohidada, S. and Gugono, M. 1981 "Remote Sensing of rainfall rates using airborne microwave rain-scatterometer/radiometer", Proc. 15th Int. Symp. on Remote Sensing of Environment, Ann Arbor, Michigan.

Isaacs, R.G., Hoffman, R.N. and Kaplan, L.D. 1986 "Satellite remote sensing of meteorological parameters for global numerical weather prediction", Rev. Geophysics., 24, no4, pp 701-743.

Johnstone, K.J., Hogg, W.D., Hanssen, A.J., Niitsoo, A. and Polavarapu, V.L. 1985 "An evaluation of some satellite rainfall estimation techniques", Preprints 6th Conf. on Hydromet, 29 Oct-1 Nov., AMS, Boston, pp233-237.

Lee, A.C.L. 1987 "Measurement of rain by satellite-borne radar", unpublished report, Met. Res. Sub-Comm. copy in Nat. Met. Lib., Bracknell.

Lethbridge, M. 1967 "Precipitation probability and satellite radiation data", Mon. Wea. Rev., 95, pp487-490.

Liljas, E. 1982 "Automated techniques for the analysis of satellite cloud imagery", in Nowcasting edited by K A Browning publ Academic Press, London/ New York, pp167-176.

Lovejoy, S. 1981 "Combining visible and infrared techniques techniques with LAMMR for daily rainfall estimates", Workshop Report Precipitation Measurements from Space, edited by D Atlas and O W Thiele, NASA, Goddard Space Flight Center, ppD184-D191.

Lovejoy, S. and Austin, G.L. 1979a "The delineation of rain areas from visible and IR satellite data for GATE and mid-latitudes", Atmosphere-Ocean, 17, pp77-92.

1979b "The sources of error in rain amount estimating schemes for GOES visible and IR satellite data", Mon. Wea. Rev., 107, pp1048-1054.

1980 "The estimation of rain from satellite-borne radiometers", Quart. J.R. Met. Soc., 106, pp255-276.

Martin, D.W. and Howland, M.R. 1986 "Grid history: a geostationary satellite technique for estimating daily rainfall in the tropics", J. Climate Appl. Met., 25, pp184-195.

Martinec, J. and Rango, A. 1981 "Areal distribution of snow water equivalent evaluated by snow cover monitoring", Water Resources Res., 17, no5, pp1480-1488.

McGinnis, D.R. Jr., Scofield, R.A., Schneider, S.R. and Berg, C.P. 1979 "Satellites as an aid to water resources managers", New York Am Soc. Civ Eng., Preprint 3485 pp.21.

Negri, A.J. and Adler, R.F. 1981 "Relation of satellite-based thunderstorm intensity to radar-estimated rainfall", J. Appl. Met., 20, pp288-300.

Negri, A.J., Adler, R.F. and Wetzel, P.J. 1984 "Rain estimation from satellites: an examination of the Griffith-Woodley technique", J. Climate Appl. Met., 23, pp102-116.

Neil, L. 1984 "Estimating precipitation areas over the eastern Pacific using GOES satellite data", Conf. on Satellite/Remote Sensing and Applications, Clearwater Beach, Florida, pp121-126.

Neil, L. and Spagnol, J. 1987 "Latest methods of inferring rainfall intensity and distribution from satellite data over the eastern Pacific", Preprints for Workshop on Satellite and Radar Imagery Interpretation, Reading, England, 20-24 July, Eumetsat publ, pp437-457.

Odegaard, H.A., Anderson, T. and Ostrem, G. 1980 "Applications of satellite data for snow mapping in Norway", NASSA CP 2116, pp93-106.

O'Lenic, L.A. 1986 "The effect of VISSR Atmospheric Sounder data on some LFM analysis and forecasts", Mon. Wea. Rev., 114, pp1832-1846.

Purdom, J.F.W. 1986 "Satellite contributions to convective scale weather analysis and forecasting", Preprints 11th Conf. Weather Forecasting and Analysis, Kansas City, Mo., 17-20 June, AMS, Boston, pp295-314.

Ramamoorthi, A.S. and Rao, P.S. 1985 "Inundation mapping of the Sahibi river flood of 1977", Int. J. Remote Sensing, 6, nos 3 and 4, pp443-445.

Rango, A. and Itten, K.I. 1976 "Satellite potentials in snowcover monitoring and run off prediction", Nordic Hydrology, 7, pp209-230.

Rango, A. and Martinec, J. 1979 "Application of a snowmelt-runoff model using Landsat data", Nordic Hydrology, 10, pp225-238.

Rango, A. and Peterson, R. (editors) 1980 Operational Application of Satellite Snowcover Observations, NASA Conf. Publ, 2116.

Rango, A., Salomonson, V.V. and Poster, J.L. 1977 "Seasonal streamflow estimation in the Himalayian region employing meteorological satellite snow cover observations", Water Resources Res., 13, pp109-112.

Reynolds, D.W., Vonder Haar, T.H. and Grant, L.O. 1978 "Meteorological satellites in support of weather modification", Bull Am Met Soc., 59, pp269-281

Salman, A.A.B. 1983 "Using Landsat imagery interpretation for underground water prospection around Qena Province, Egypt", Inst. J. Remote Sensing., 4, no2, pp179-189.

Scofield, R.A. 1981 "Analysis of rainfall from flash flood producing thunderstorms using GOES data", Proc IAMAP Symp Hamburg, 25-29 August, ESASP-175, June 1981, pp51-58.

1982 "A satellite technique for estimating rainfall from flash flood producing thunderstorms", Int. Symp on Hydromet, 13-17 June, Denver, Colo., edited by A I Johnson and R A Clark, Am Water Resources Ass, Bethesda, Maryland, pp121-128.

1984 "Satellite-based estimates of heavy precipitation", SPIE Vol 481, Recent Advances in Civil Space Remote Sensing, pp84-91.

Scofield, R.A. and Oliver, V.J. 1977a "A scheme for estimating convective rainfall from satellite imagery", NOAA Tech Memo NESS 86, Washington DC, pp47.

1977b "Using satellite imagery to estimate rainfall from two types of convective systems", Preprints 11th Tech Conf on Hurricans and Tropical Met, 13-16 Dec., Miami Beach, AMS, Boston, pp204-211.

Spencer, R.W. 1986 "A satellite passive 37-GHz scattering-based method for measuring oceanic rain rates", J Climate Appl. Met., 25, pp754-766.

Spencer, R.W., Hinton, B.B. and Olson, W.S. 1983 "Nimbus-7 37GHz radiances correlated with radar rain-rates over the Gulf of Mexico", J. Climate Appl. Met., 22, pp 2095-2099.

Stout, J.E., Martin, D.W. and Sikdar, D.N. 1979 "Estimating GATE rainfall with geosynchronous satellite images", Mon. Wea. Rev., 107, pp585-598

Theon, J. 1973 "A multi-spectral view of the Gulf of Mexico from Nimbus-5", Bull Am. Met. Soc., 54, pp934-937.

Tsonis, A.A. and Isaac, G.A. 1985 "On a new approach for instantaneous rain area delineation in the mid latitudes using GOES data", J Climate Appl. Met., 24, pp1208-1218.

Ulaby, F.T., Dobson, M.C. and Brunfeidt, D.R. 1983 "Improvements of moisture estimation accuracy of vegetation-covered soil by combined active/passive micro-wave remote sensing", J. IEEE Trans. Geosci. Remote Sensing., GE-21, pp300-307.

Ulaby, F.T., Moore, R.K. and Fung, A.K. Microwave Remote Sensing: Active and Passive Volume II: From Theory to Applications, Artech House Books.

Wilheit, T.H. 1975 "The electrically scanning microwave radiometer (ESMR) experiment". in Nimbus-6 User Guide, NASA Goddard Space Flight Center, pp87-108.

Wilheit, T.H., Theon, J., Shenk, W., and Allison, L. 1973 "Meteorological interpretation of the images from Nimbus 5 Electrically Scanned Microwave Radiometer", NASA X-651-73-189, Goddard Space Flight Center, pp21.

Wilheit, T.H., Chang, A.T.C., Rao, M.S.V., Rodgers, E.B. and Theon, J.S. 1977 "A satellite technique for quantitatively mapping rainfall rates over the oceans", J. Appl. Met., 16 pp551-560.

Woodley, W.L., Griffith, C.G., Griffin, J.S. and Stromatt, S.C. 1980 "The inference of GATE convective rainfall from SMS-1 imagery", J. Appl. Met., 19, pp388-408.

Wu, R., Weinman, J.A. and Chin, R.T. 1985 "Determination of rainfall rates from GOES satellite images by a pattern recognitition technique" J. Atm. Ocean Tech., 2, pp314-330.

Wylie, D.P. 1979 "An application of a geostationary satellite rain estimation technique to an extratropical area", J. Appl. Met., 18, pp1640-1648.

Wylie, D.P. and Laitsch, D. 1983 "The impacts of different satellite data on rain estimation schemes", J. Climate Appl. Met., 22, pp1270-1281.

FIGURE 1

Observed surface rainfall 90 min. totals (R) and cloud top temperature (CTT) over southeast Australia for cumuliform cloud or cloud in the convective sector of extratropical cyclones. The points are derived from several studies (adapted from Delbeato and Barrell, 1985).

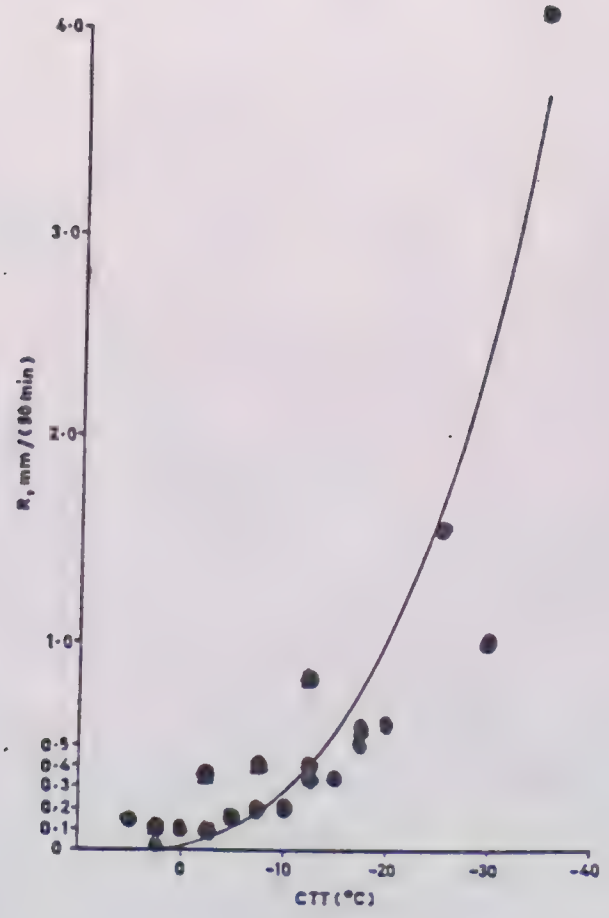

FIGURE 2

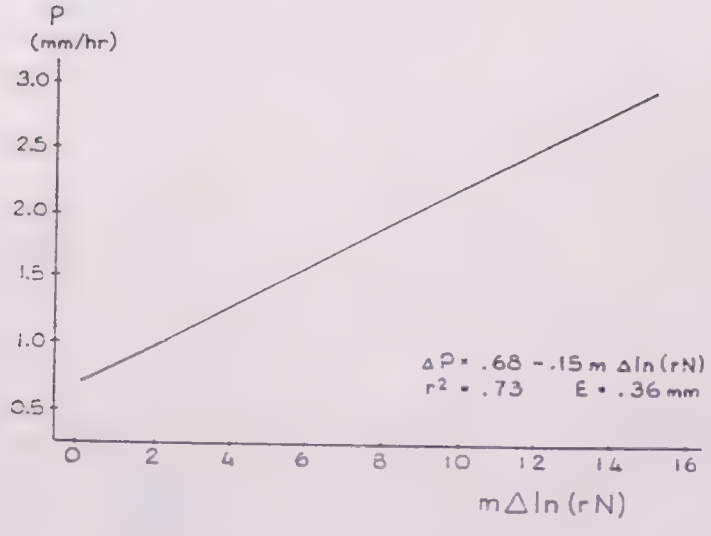

Prediction graph for precipitation intensity versus $m\Delta \ln(rN)$

FIGURE 3

Illustrating (a) a classification in a three-dimensional intensity space of cloud, fog, land, and water; (b) cloud analysed using this classification at 1500GMT 24 May 1975 over southern Scandinavia; and (c) the weather observed about 1½ hours after the satellite passage (after Liljas, 1982).

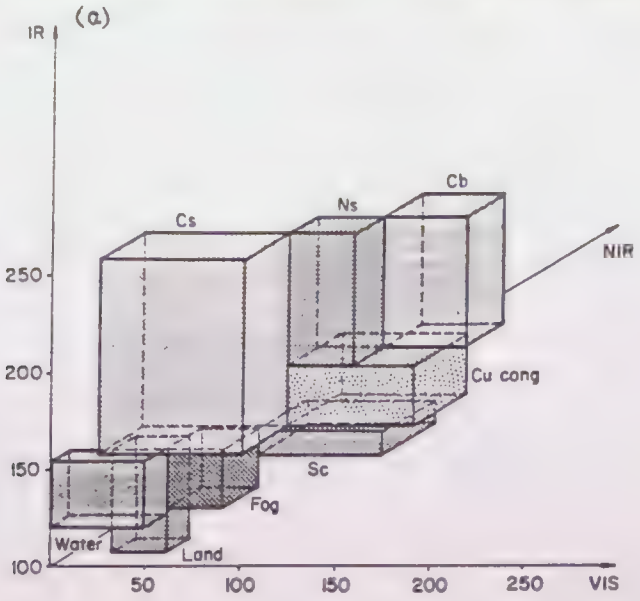

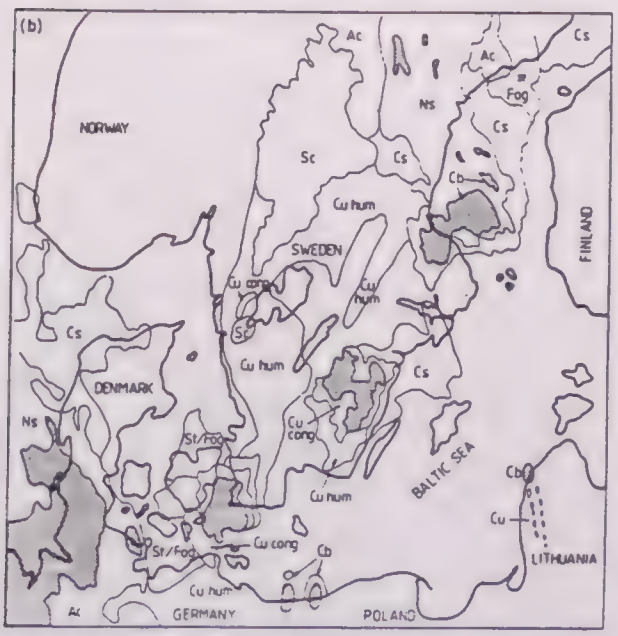

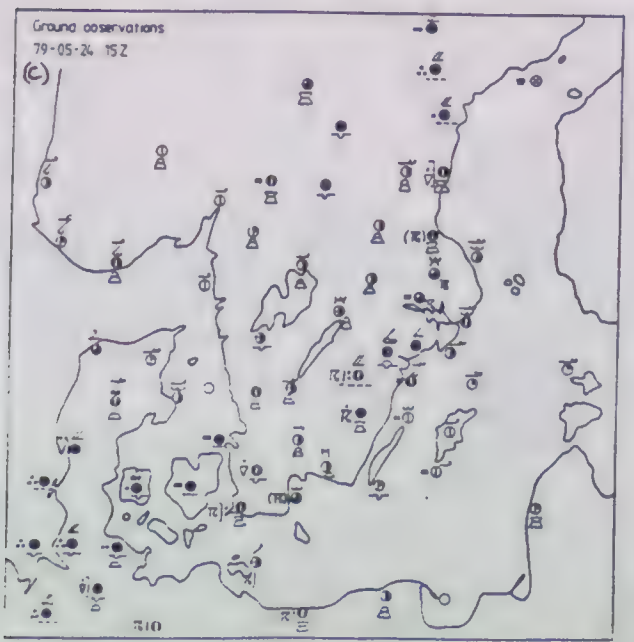

FIGURE 4

Bipolarization (horizontal/vertical) plot of rainfall rates with the observed relationship between radar rainfall rates and SMMR T_B during the summer over the United States (after Spencer, 1986).

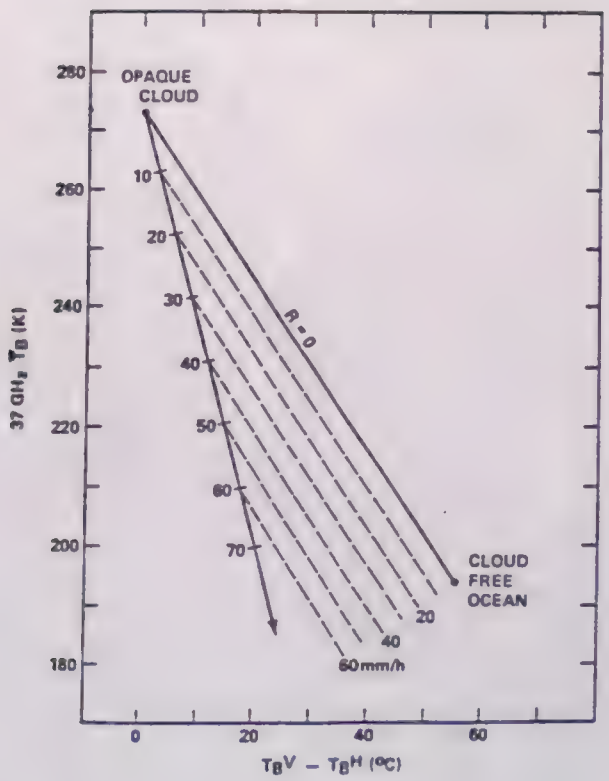

FIGURE 5
Geometry of Seasat SAR (adapted from Fu and Holt, 1982 by Hall and Martinec, 1985).

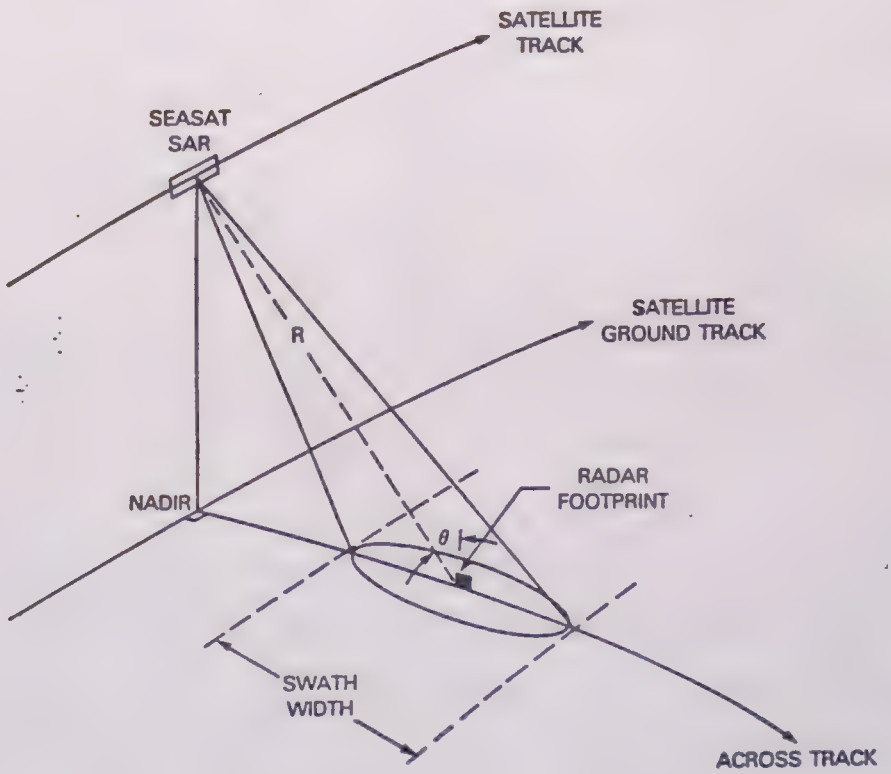

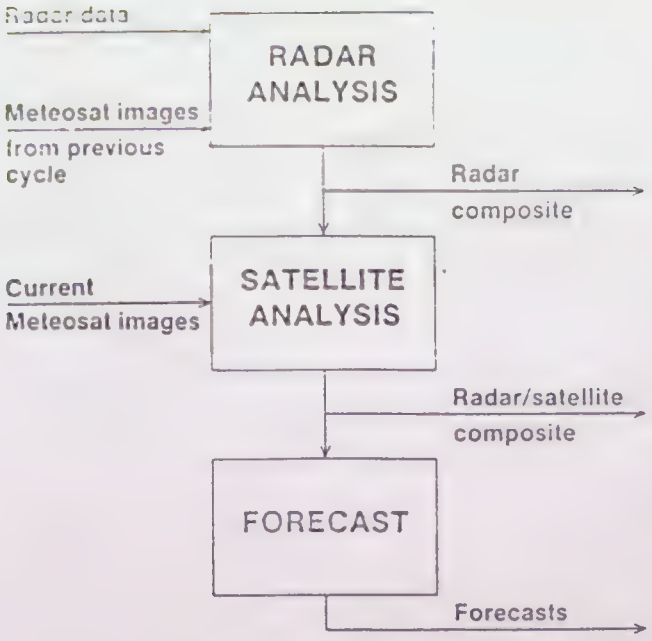

Figure 6 The main stages in the FRONTIERS 30-minute cycle. Meteosat images arrive later than the corresponding radar data so cloud pictures from the previous cycle are used to aid radar analysis in the first stage.

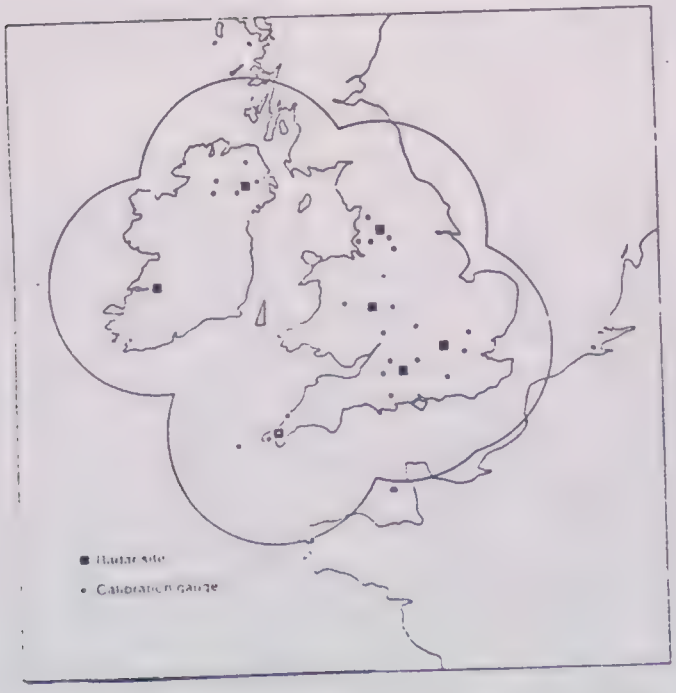

Figure 7. The radar network currently used by FRONTIERS, comprising six UK radars and Shannon in the Republic of Ireland. The circular arcs show the maximum range for detection of rain (about 210 km); the range for quantitative measurements is much smaller. FRONTIERS uses Meteosat images to extend coverage to the full area shown in the diagram.

FIGURE 8

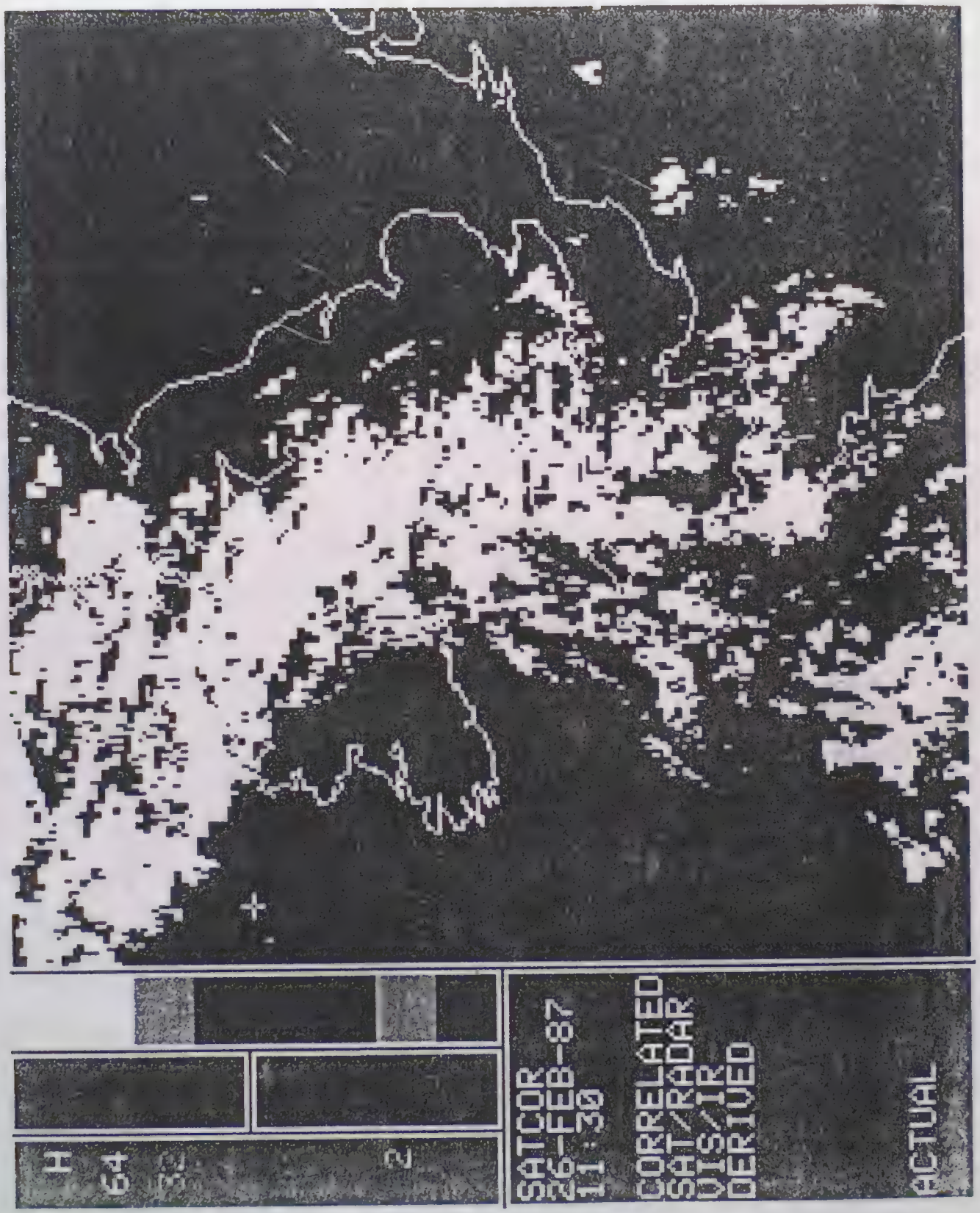
SATCOR
26-FEB-87
21:30
CORRELATED
SAT/RADAR
DIS/IR
DERIVED
ACTUAL
H
64

FIGURE 9

Radar composite and useable data boundary

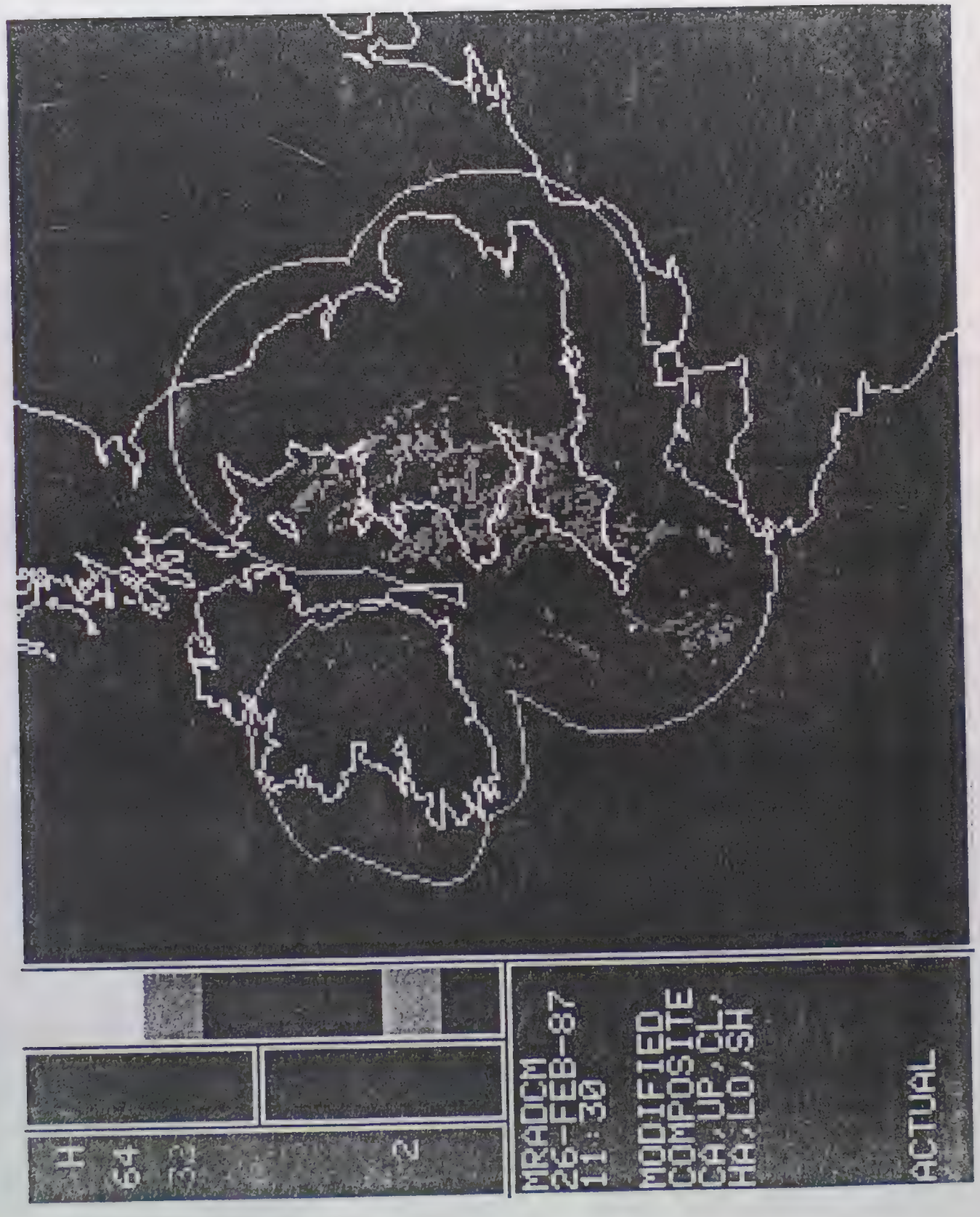

FIGURE 10

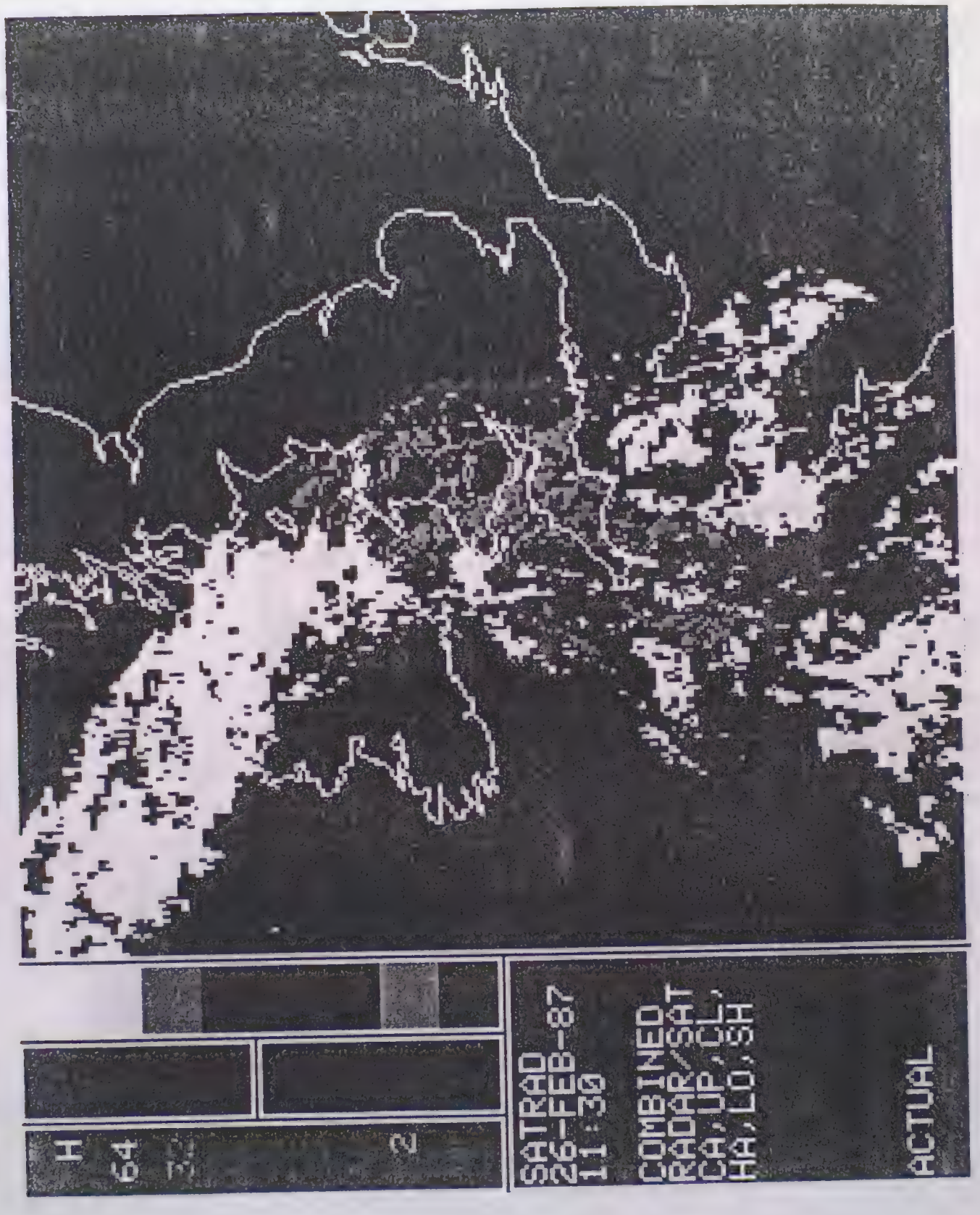

FRONTIERS combined radar and satellite-derived rainfall field for 11:30 GMT on 26 February 1987. A belt of frontal rain is seen crossing the UK. Rainfall intensities are shown in colour within the radar area (lowest is blue, <1mm/h; highest is yellow, 8-16 mm/h). Satellite-derived rainfall is shown in white and indicates only areal extent, not intensity. The Northern Ireland radar had not started supplying data to the network at the time of this case.

FIGURE 11

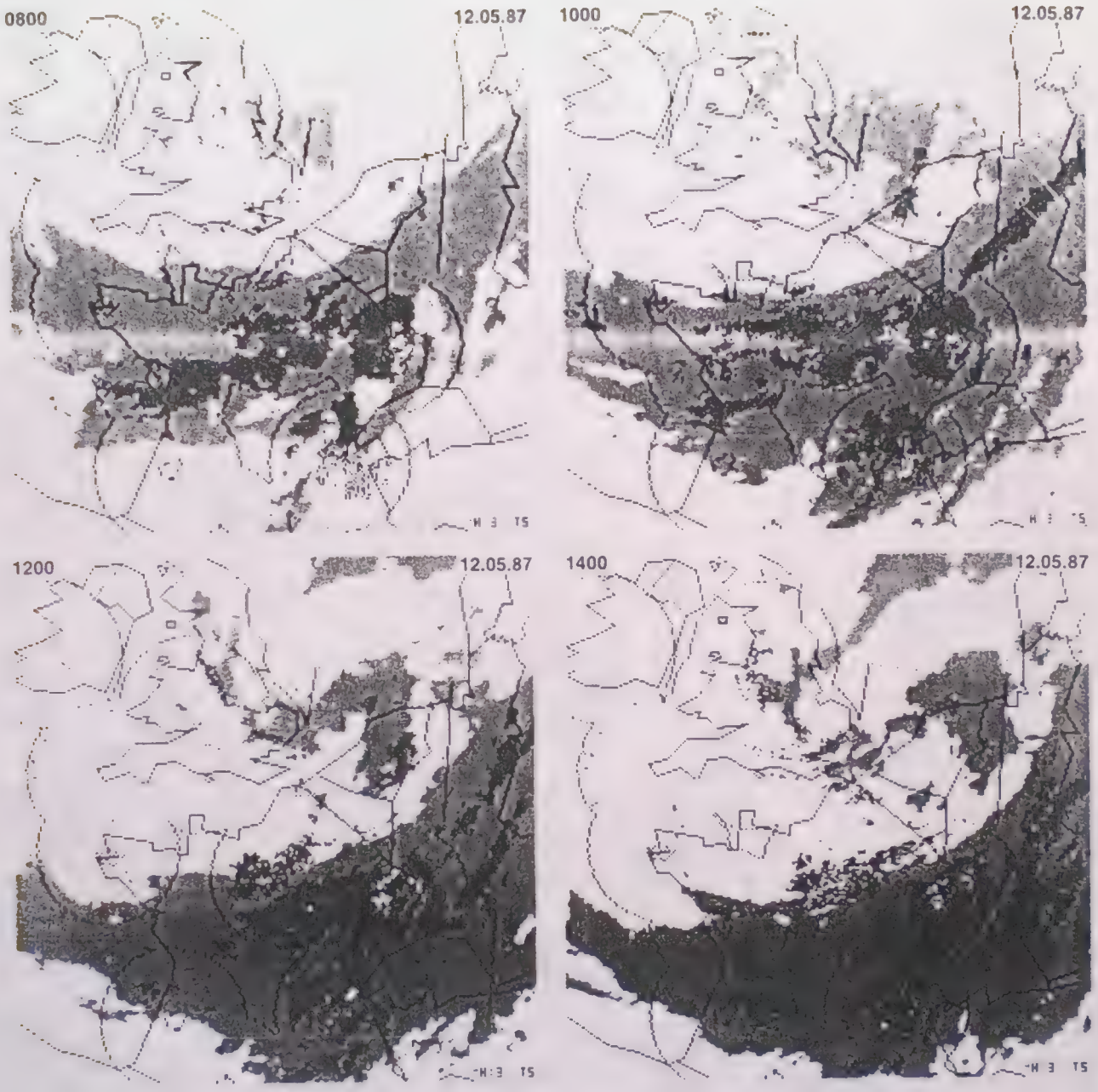

Examples of COST images, two hour intervals on 12 May 1987. The movement of a cold front towards the southeast and the development of showers over England and the Netherlands is illustrated. The data resolution is 5 km. Radar boundaries (circular and rectangular), coastlines and political boundaries are shown in black. The 1200 GMT image contains data from the UK, Ireland, France, Switzerland and the Netherlands. Key cloud: cyan $<-15°C$ to $-45°C$, blue $<-45°C$. Rianfall intensity: magenta 0.3 to 1 mmh^{-1}, green 1 to 3 mmh^{-1}, yellow 3 to 10 mmh^{-1}, red 10 to 30 mmh^{-1} and black >30 mmh^{-1}.

FIGURE 12.a

Key as for Figure 11.(a) no French radar data(b) with French radar data. See text for discussion.

FIGURE 126

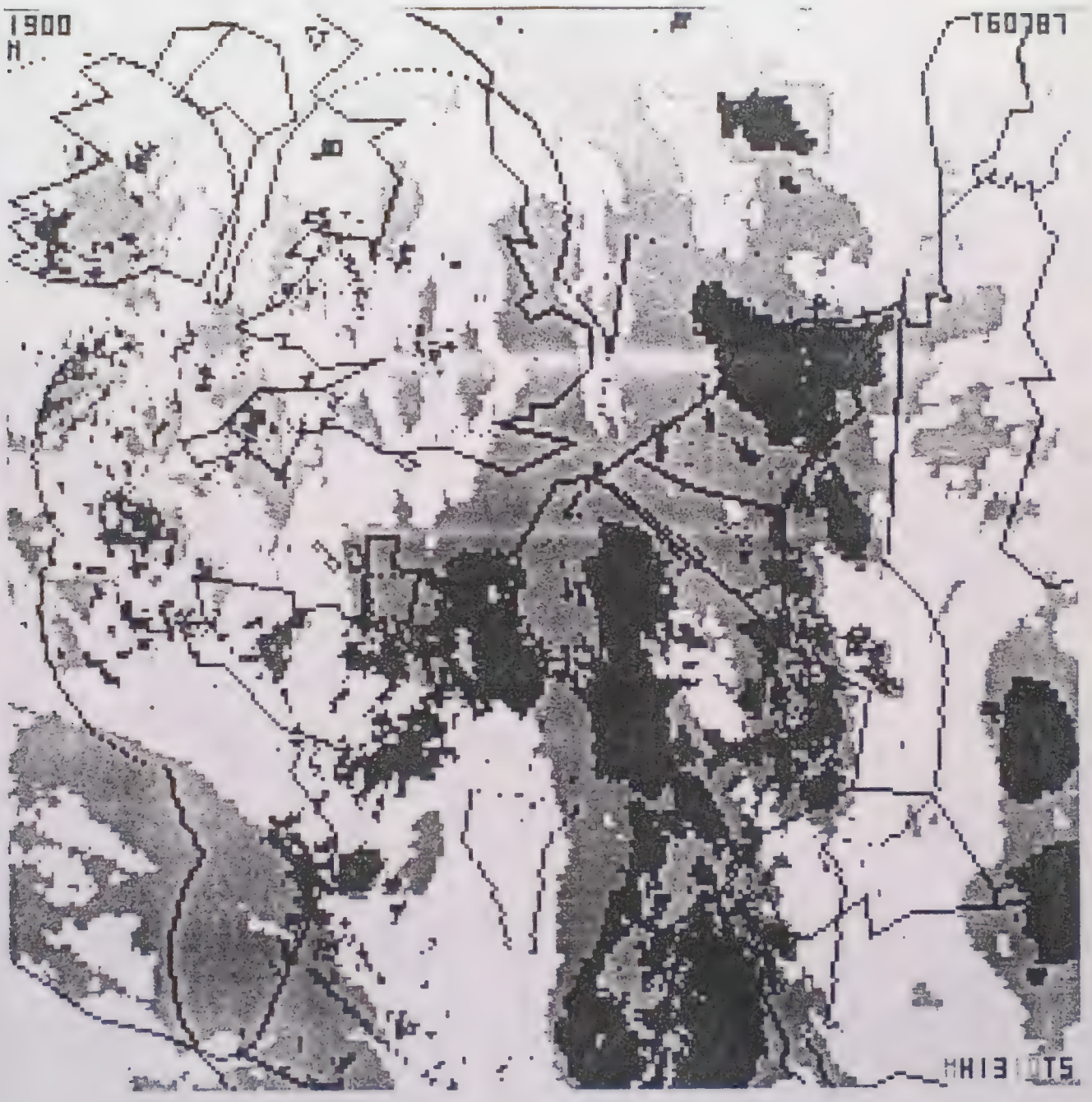

FIGURE 13

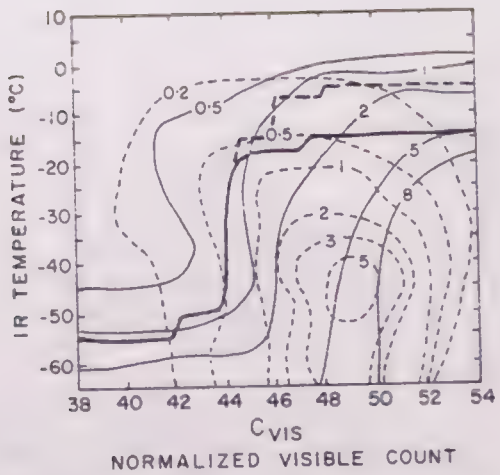

Rainfall rate in mm h^{-1} as a function of visible and IR temperatures derived from a comparison of four radar sequences of convective weather around the Montreal area (solid lines). The dashed lines are contours of percent rainfall contribution per VIS–IR pair. Each pair occupies an area in VIS–IR space of 5°C and two visible counts. The heavy line outlines the rain–no rain boundary in the binary decision scheme of Method 2. The visible data from the GOES-E satellite, which became operational in August 1981, need to be decremented by 10 counts before applying the above relationship.

John T. HOUGHTON,
Director General of the
British Meteorological Office,
Bracknell, UK.

The role of satellites in meteorology and the contribution of Europe to space meteorology

Twenty-five years of meteorological observation from space, together with the developments in computer technology, have brought about a revolution in the science and practice of meteorology. Europe's contribution to satellite observation has been through the geostationary satellite Meteosat and through the development of instrumentation for remote sensing of atmospheric parameters from polar orbiting satellites and through the development of space-based interrogation and location systems for remote platforms. For the future, Europe is developing ERS-1, a large remote sensing satellite to fly at the end of this decade, and is also discussing with the USA a co-operative programme for the Space Station which will include a substantial component of earth observation. European scientists are also deeply involved in international programmes concerned with the atmosphere and climate research.

It is just 25 years since weather pictures were transmitted from the first weather satellite — **Tiros I** — launched by the USA on April 1, 1960. At that time the potential of observations from space, even of the crude resolution and relatively poor coverage achieved by Tiros I was immediately obvious to the meteorological community. For the first time the detailed structure of complex weather systems could be seen at a glance, and the acquisition of meteorological observations covering the whole globe clearly became a real possibility.

A series of research satellites, the **Nimbus** series, of which the first was launched in 1964, began to exploit some of this potential. The realisation of an operational

system of meteorological satellites came with the launch by the US Environmental Science Services Administration (ESSA) of **ESSA I** in 1966. Observation of the earth from geostationary orbit began in the same year with NASA's **ATS-1,** although an operational geostationary system was not to be inaugurated until the first **GOES** (Geostationary Operational Environmental Satellite) was launched in 1975.

European scientists and laboratories had been involved to a considerable extent in the development of instruments for Nimbus satellites and in the interpretation of satellite data.

Europe's main contribution to the meteorological satellite observing system began with the launch of **Meteosat** into geostationary orbit on 23 November 1977. This was in time for it to be part of the observing system for the Global Weather Experiment — the largest internationally organised scientific experiment man has undertaken — which took place in 1979.

Since 1979, with the deployment of the **Tiros-N** polar orbiting satellite series, significant improvement has occurred in the performance of remote sounding instruments. Plans are being laid for a wider range of operational measurements to include ocean parameters as well as atmospheric ones.

Europe for its part is developing remote sensing satellites — the first, **ERS-1**, is to be launched around the end of this decade. The European Space Agency (ESA) is also discussing with the USA a cooperative programme with the Space Station which will include a substantial component of earth observations.

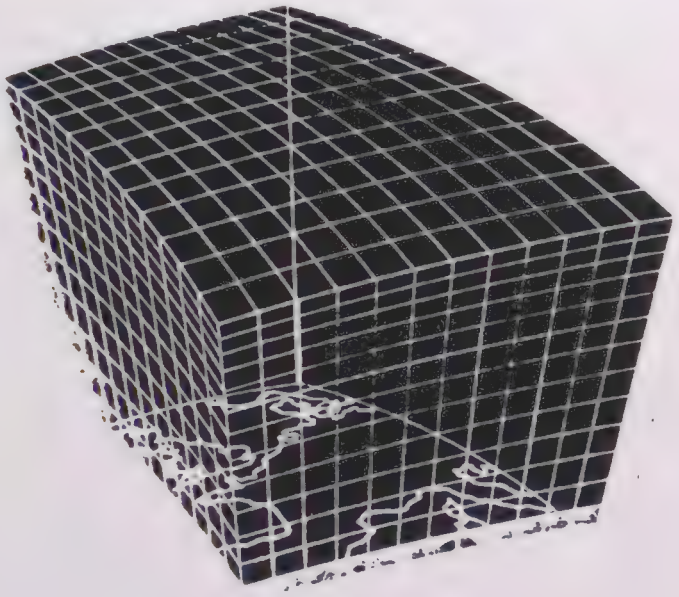

GLOBAL OBSERVATIONS FOR GLOBAL MODELS

During the past twenty years or so, the science and practice of meteorology has been revolutionised by the satellite and the computer Satellites enable global observations to be acquired rapidly and efficiently; powerful computers make it possible to integrate the equations of motion applied to the atmosphere's global circulation so as to produce forecasts of atmospheric movement and behaviour for up to a week or two ahead. Even for forecasts of three or four days ahead a global solution is necessary — atmospheric systems in one hemisphere can affect the circulation in the other hemisphere on relatively short time scales.

Typical global models, for instance those at the British Meteorological Office at Bracknell or the European Centre for Medium Range Forecasting (ECMWF) possess a horizontal grid of about 150 km and 15 levels in the vertical (**Fig. 1**). The total grid contains about 350,000 individual points. At each point the quantities which need to be specified are pressure (or geopotential height), temperature, components of the horizontal wind and humidity. Further, since boundary conditions need to be specified and all the major physical processes described, the data assimilation procedures and the model interpretations not only require the largest computers available but also require a great deal of sophisticated numerical analysis and physical insight.

Fig. 1 :
The grid of a global circulation model : 15 levels are shown in the vertical - approximate height in metres at these levels is on the right-hand side. (Courtesy of ECMWF).

The data available for assimilation into a global numerical model comes from a variety of observing systems (**Fig. 2**). The very large contribution made by satellites will immediately be clear. They contribute through remotely sensed observations of temperature, through observations of winds particularly in the tropics obtained by tracking cloud motions and through the interrogation and location of remote platforms using the satellite as a communications link.

For the Global Weather Experiment five geostationary satellites were deployed around the globe and a number of polar-orbiting satellites were also taking obser-

Fig. 2 : Data available for assimilation into the global model of the European Centre for Medium Range Weather Forecasting (ECMWF) near 12 noon on 4 june 1979.

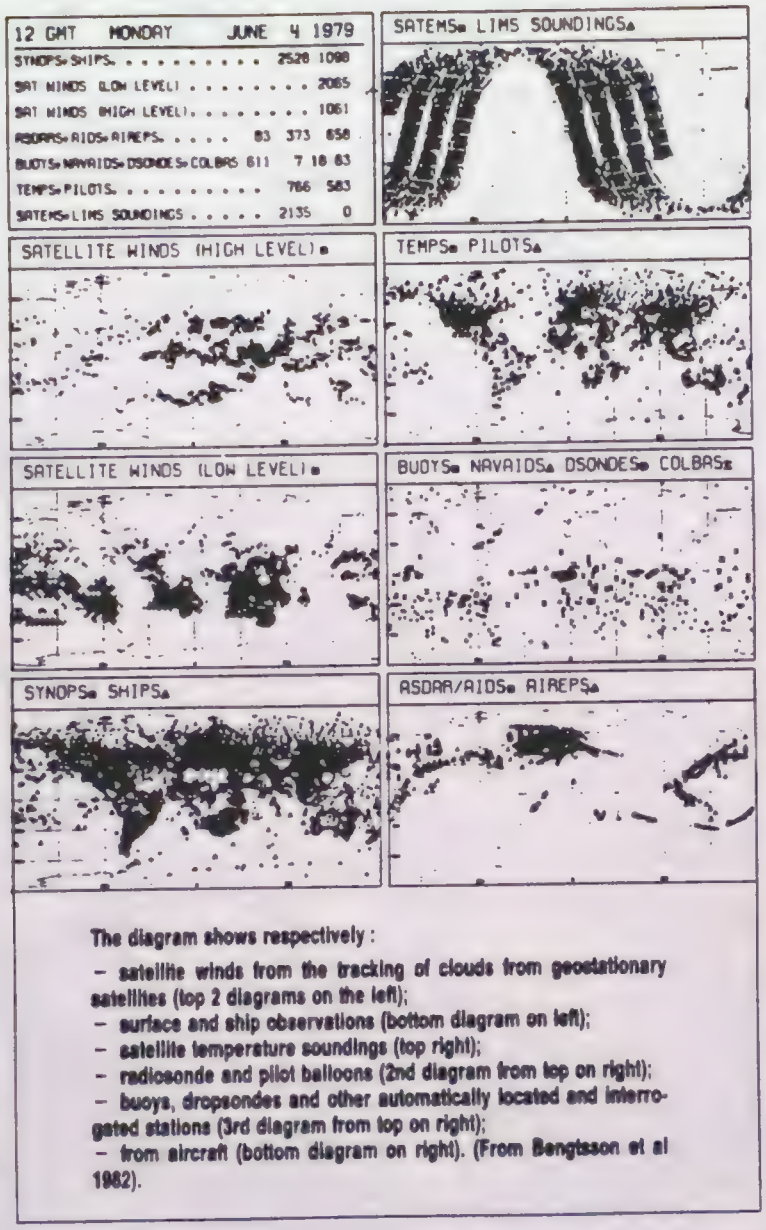

Fig. 3 (below) : Arrangement of 5 geostationary satellites and polar orbiting satellites for the Global Weather Experiment.

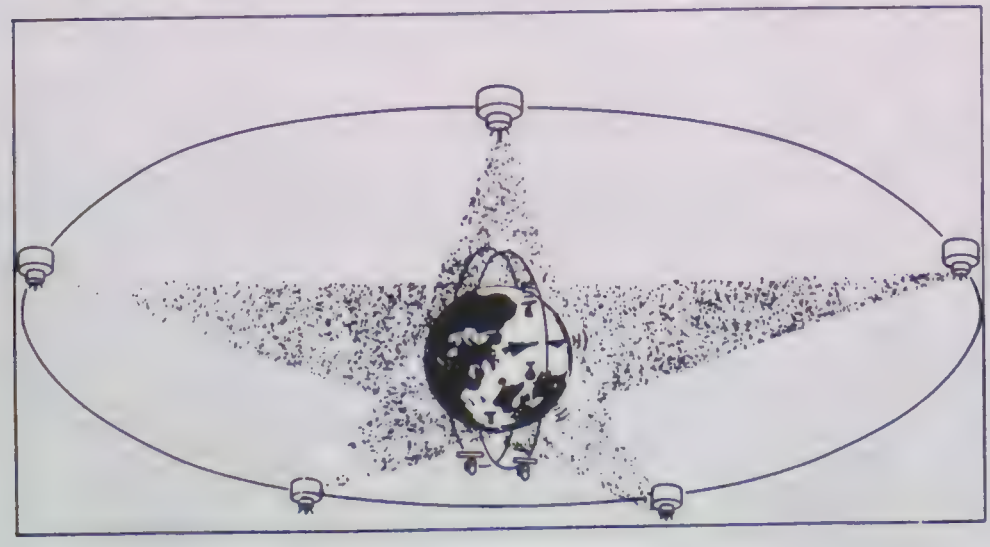

The diagram shows respectively :

- satellite winds from the tracking of clouds from geostationary satellites (top 2 diagrams on the left);
- surface and ship observations (bottom diagram on left);
- satellite temperature soundings (top right);
- radiosonde and pilot balloons (2nd diagram from top on right);
- buoys, dropsondes and other automatically located and interrogated stations (3rd diagram from top on right);
- from aircraft (bottom diagram on right). (From Bengtsson et al 1982).

vations (**Fig. 3**) Important characteristics of the data required for operational meteorology, which will be mentioned from time to time in this article, are that they should be of high quality, high accuracy and available at the right time. This latter means that data must be available within 3 hours of observation otherwise it cannot be assimilated into the operational forecasting model. This timescale of the availability of observations is of more importance than just for operational forecasting.

The process of assimilation of data into the global model creates an analysis of the atmospheric state which is the best description at that time given the assorted available data. These analyses become an important data base for climate research Since this process of assimilation and analysis will not be repeated except for very special occasions because of the effort and computer time involved, the need for making sure that all observations of importance are available and included cannot be emphasised too strongly. Satellite communications can clearly play a substantial role in ensuring that this is the case.

The employment of the satellite as a communications link was pioneered by French scientists through the **EOLE** experiment designed by the Centre Nationale d'Etudes Spatiales (CNES) which was carried out in the late 1960s. In this experiment, constant volume super-pressured balloons were flown and tracked to determine atmospheric circulation in the southern hemisphere. More recently, beginning in 1978, the CNES has been responsible for the **ARGOS** system mounted on the **Tiros** operational satellite series (**Fig. 12**), with which the location of up to several thousand platforms can be automatically de-

termined and data from the platforms received and distributed. Measurements with this technique from free floating buoys deployed in the southern oceans were a particularly important data source for the Global Weather Experiment.

Since 1979 development of the global meteorological observing system has continued through the World Weather Watch (WWW) programme of the World Meteorological Organisation (WMO). The aim of that programme is to achieve, on a continuous basis, observational coverage of the globe as good or better than that during the global experiment of 1979. Satellites clearly play a vital part in such a programme. The paragraphs which follow describe in more detail the various contributions from satellites. A much fuller description is available in Houghton, Taylor and Rodgers (1984).

METEOSAT

Meteosat is Europe's meteorological satellite in geostationary orbit nominally located at an altitude of nearly 36,000 km over the equator and the Greenwich meridian. It consists (**Fig. 4**) of a cylindrical body 2.1 m in diameter and a little over 3 m long, with a mass of about 300 kg at launch falling to about 250 kg as the hydrazine propellent used for spin and station keeping control is used up during the satellite's life. The whole satellite spins at 100 rpm about its axis which is aligned parallel to the earth's axis.

The principal instrument on board Meteosat is the multispectral radiometer (**Fig. 5**). Visible and infra-red radiances are received by the radiometer as its field of view is scanned over the earth's disc as the satellite spins, and as between each satellite rotation the telescope mirror is moved in small stages so as to view different lines across the earth. Full coverage of the earth's disc is thereby acquired during a period of 25 minutes.

Four spectral channels are included in the radiometer, two identical visible channels between 0.4 and 1.1 μm, one in the water-vapour band between 5.7 and 7.1 μm and one in the infrared window between 10.5 and 12.5 μm. The resolution of this visible channel at the sub-satellite point is 5 km for the infra-red channels and 2.5 km for the visible ones when both visible channels are employed. However, if the water-vapour infra-red channel is selected, only one visible channel (which then has a resolution of 5 km) can be transmitted.

Raw data is transmitted from the satellite to the Data Acquisition Telemetry and Tracking Station (DATTS) from where it goes to the Meteosat Ground Computer System and Control Centre (**Fig. 6**). There the data is collected and formatted into a variety of images. It is then retransmitted to the satellite ready for dissemination to user stations throughout Europe and countries outside Europe who are within sight of the spacecraft.

Data dissemination is either in analogue form for reception by relatively inexperienced ground stations (secondary data user stations) or in digital form for reception by more elaborate ground stations (primary data user stations). A data colection system is also included in Meteosat (**Fig. 6**) with which data from

Fig. 4 (below): The Meteosat satellite.

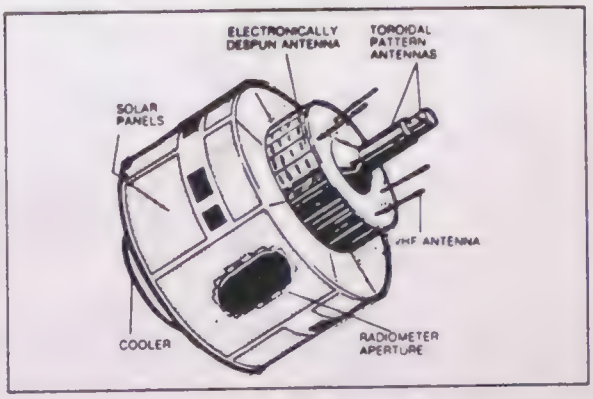

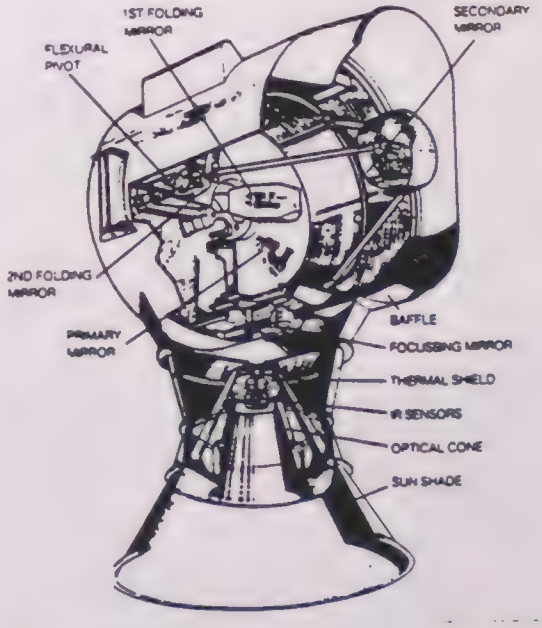

Fig. 5 (above): Layout of radiometer in Meteosat satellite.

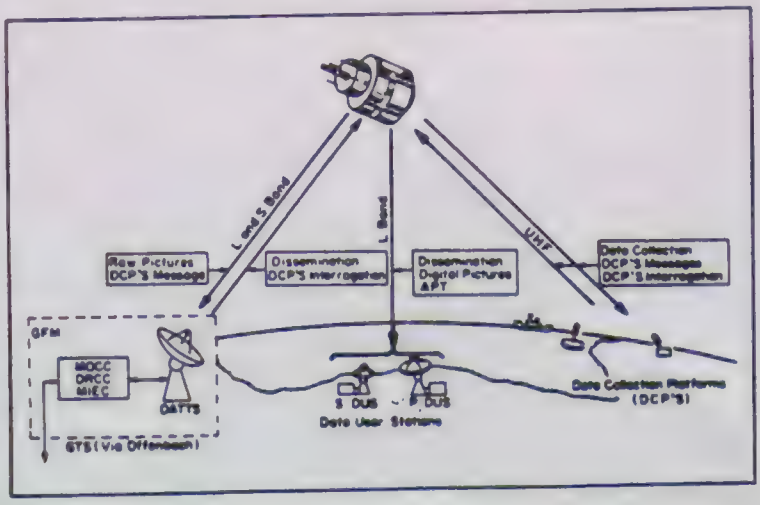

Fig. 6 (at left): Illustrating data dissemination system for Meteosat.

Fig. 7 a (above) :
Image including the British isles and Iceland from the AVHRR on Tiros N at about 1500 Z on 19 May 1979. The occluded front is a region of marked wind shear and exhibits wave structure most likely produced by barotropic instability. Behind the cold front, typical open-celled organisation of the convection in apparent with enhanced narrow bank of cloud prominent near the main frontal cloud mass. (Received and processed by the University of Dundee Electronics Laboratory).

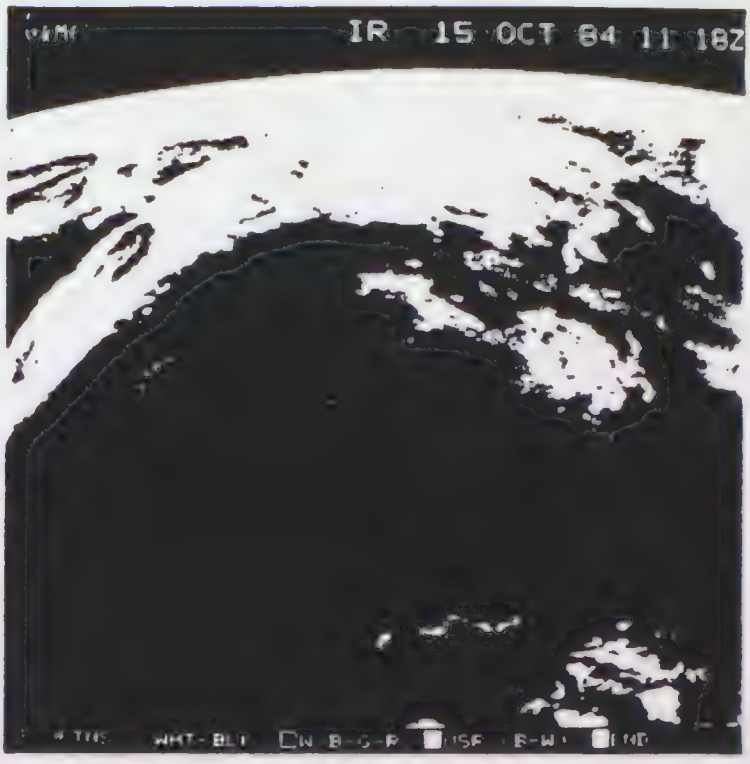

Fig. 8 (top right) :
Infra-red image from Meteosat.

Fig. 7 b (below) :
Synoptic situation at 1200 Z on 19 May 1979.

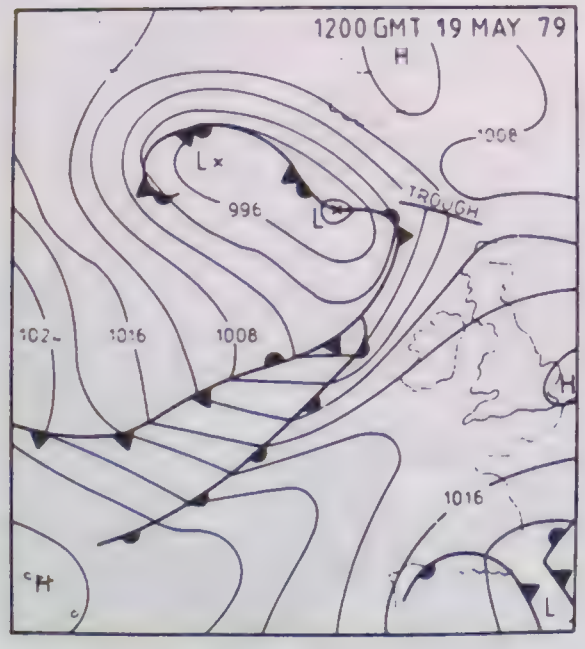

a large number of automatic data collection platforms deployed on the land or ocean surface can be received and distributed.

Images from Meteosat in the visible region show up very effectively the presence of cloud (**Fig. 7**). Since new images are available every half hour, the development and movement of weather systems and patterns can be followed from sequences of Meteosat images; the forecaster can learn by experience to interpret the variety of cloud signatures seen from space. Further information is available from the infra-red images (**Fig. 8**) from which the temperature of the cloud top or of the earth's surface can be inferred. Because temperature falls with altitude in the troposphere, the temperature of a cloud gives a good indication of the cloud's height although care needs to be taken with the interpretation of data from partially transparent clouds.

Regions of intense convection in the atmosphere are regions where there is thick cloud having tops at high altitude. They therefore show up on a Meteosat image as regions of high brightness in the visible (in meteorological parlance they possess high albedo) and of cold temperatures as measured in the infra-red. By comparing the characteristics of the image in such regions with surface measurements of rainfall intensity, experience can be acquired which can help in the identification of regions of precipitation from Meteosat imagery. Such work is being put to operational use in the FRONTIERS sytem at Bracknell in which images of radar data are integrated with satellite images to provide for the forecaster a more complete description of weather systems (European Space Agency 1985a).

Features of the circulation in the upper troposphere (about 5-10 km altitude) show up in an impressive way in Meteosat images of the water vapour channel (**Fig. 9**). In drier regions radiation emanates from lower

and therefore warmer altitudes than in wetter regions. Dry regions appear therefore of higher radiance (and therefore by convention are darker) in these images.

An important application of Meteosat image data is in the determination of winds at low latitudes. Because at low latitudes the atmospheric motion field cannot be inferred from the density field (in meteorological parlance, the geostrophic approximation does not apply) direct measurements of atmospheric motion are a vital input to the numerical models. By tracking clouds as seen on Meteosat images as a function of time (**Fig. 10**) winds may be measured commonly at two levels: at about 1 km altitude using small convective clouds, and near the top of the troposphere where cirrus clouds can be tracked. Care has to be taken with the choice of cloud — not all clouds move with the wind — and with the assignment of levels to the clouds. This latter is done by using the cloud temperature inferred from the infra-red channel — the problem of errors in this inference associated with partially transparent clouds has already been mentioned.

REMOTE SENSING OF ATMOSPHERIC TEMPERATURE

An image in the thermal infra-red part of the spectrum, as illustrated in **Fig. 8**, demonstrates clearly how the temperature of the earth's surface or of the upper surfaces of clouds may be determined for different parts of the image. The wavelength region 10-12 μm employed for such thermal imaging is one in which the atmosphere is largely transparent. If now the radiance is measured at wavelengths where the atmosphere absorbs, properties of the atmosphere itself — its temperature and composition — can be inferred.

For the infra-red part of the spectrum, the technique will be clear from an examination of **Fig. 11** where a portion of the emission spectrum of the earth plus atmosphere is shown. Temperatures can be assigned to any point on the spectrum from

Fig. 10 (below): Generation of winds from cloud tracks observed from Meteosat.

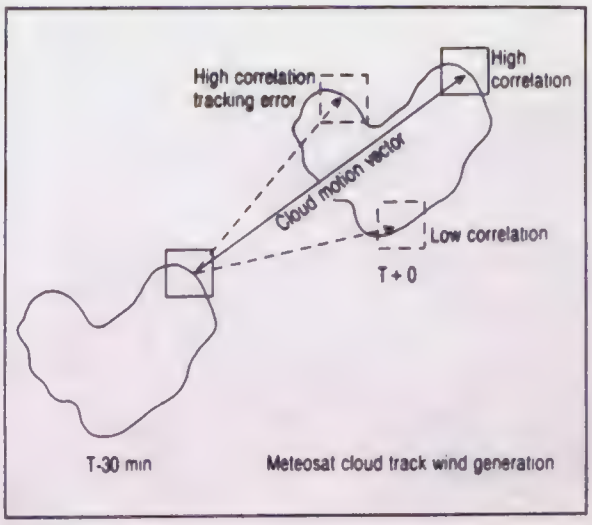

Fig. 9 (bottom left): Image from Meteosat in the 6.3 micron infra-red vapour channel.

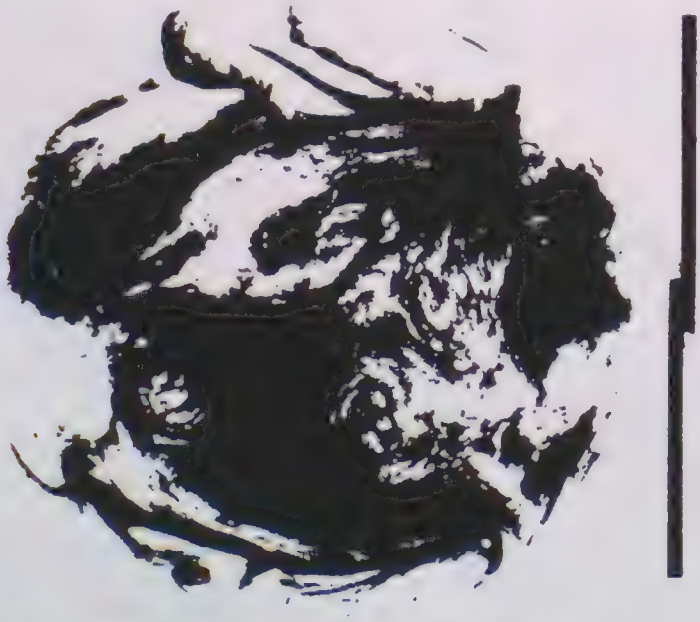

Fig. 11 (bottom right): Examples of thermal emission spectra recorded by IRIS D on Nimbus 4. Radiances of black bodies at several temperatures are superimposed. (a) Sahara; (b) Mediterranean; (c) Antartic; (all apodized) (From Hanel et al. 1971).

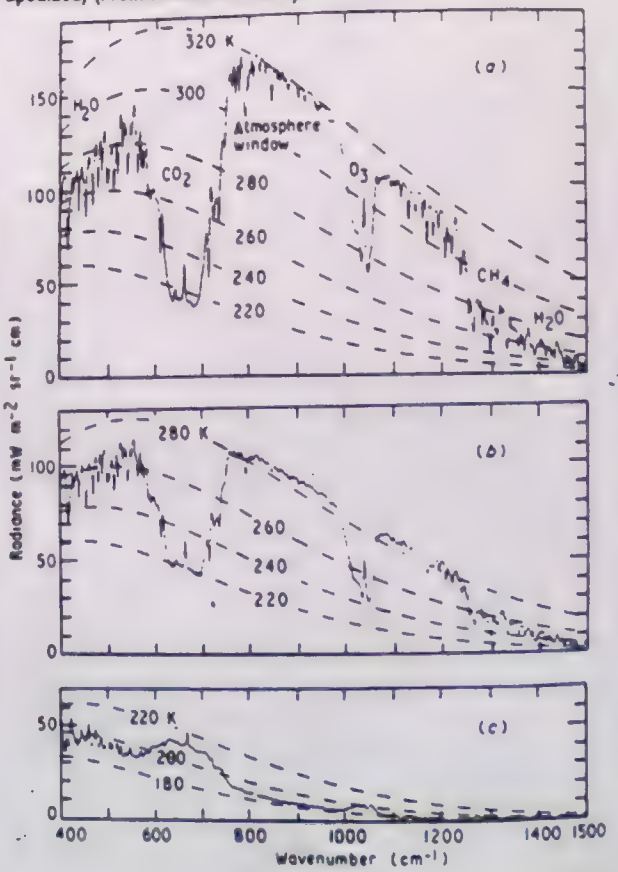

the emission curves of black body radiation which are plotted as dashed lines. In the atmospheric window region near 1000-800 cm^{-1} (10-12 μm) radiation originates near the surface — hot (320 K) over the Sahara and cold (180 K) over the Antarctic.

Near the centre of the carbon dioxide band at 667 cm^{-1} (15 μm) radiation originates in the stratosphere at approx. 220 K. Right in the middle of that band where CO_2 absorbs most strongly, radiation is originating from well into the stratosphere where the temperature has begun to increase with height. Between 800 and 700 cm^{-1} the radiance originates from different levels in the troposphere. The amount of CO_2 in the atmosphere being known in addition to detailed information about the CO_2 spectrum, it is possible from such satellite radiance data to infer the atmospheric temperature at different levels below the satellite. Similar temperature information may be obtained by measuring emission from atmospheric oxygen at wavelengths near 5 mm in the microwave part of the spectrum.

The horizontal resolution of satellite temperature soundings is, of course, very high compared with comparable measurements from the surface. In contrast, however, the vertical resolution is poor. At any given wavelength, radiation is sampled from a region of atmosphere 5-10 km in thickness. The measurements being made therefore approximate to the mean temperatures of different atmospheric slabs.

To be useful as input to forecasting models, the accuracy of such temperature measurements needs to be high; they need to be made within about IK. The achievement of this sort of accuracy makes tough demands on the instrumentation. High spectral resolution and high energy grasp as well as very careful calibration is required of the radiometers. To meet them, ingenious and novel techniques have been developed (Houghton, Taylor and Rodgers, 1984) and tried out on the Nimbus series of research satellites in the 1960s and 1970s before being employed operationally on the Tiros series. Three instruments for remote temperature sounding are currently being flown on the most recent National Oceanic and Atmospheric Administration (NOAA) operational series Tiros-N (**Fig. 12**). They are :

— the High Resolution Infra-Red Sounder (HIRS) : a twenty channel radiometer which includes channels in both the 4.3 μm and 15 μm spectral regions where carbon-dioxide emits;

— the Stratospheric Sounding Unit (SSU) : a three channel radiometer for sounding the stratosphere (10-50 km altitude) with spectral selection based on the pressure modulation technique and provided by the UK Meteorological Office;

— and the Microwave Sounding Unit (MSU) : a four channel radiometer observing emission from stratospheric oxygen near 0.5 mm in wavelength.

A new instrument being prepared for later satellites in the

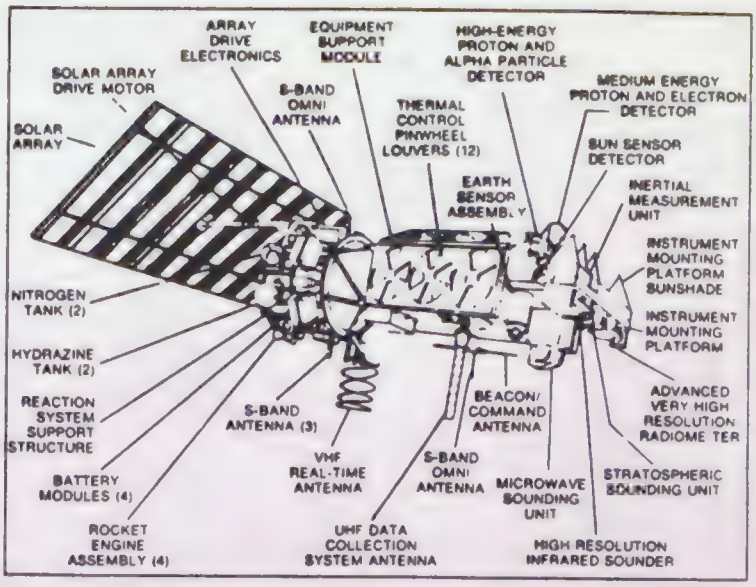

Fig. 12 (top right) : TIROS N spacecraft.

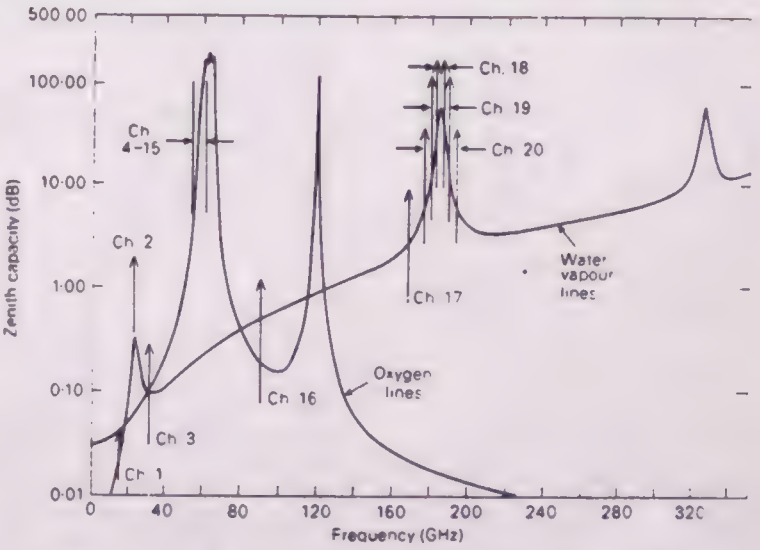

Fig. 13a (centre) : Location of spectral channels for the Advanced Microwave Sounding Unit.

Tiros-N series is the Advanced Microwave Sounding Unit (AMSU) which will exploit advances in microwave technology which have occurred in recent years. It consists of two separate instruments :

— the first, AMSU-A being provided by NOAA, possesses 15 channels for sounding temperature from the surface to 50 km altitude — the spectral locations of the channels and the associated weighting functions are shown in **Fig. 13**;

— the second part of the instrument, AMSU-B is being provided by the UK Meteorological Office and possesses 5 channels near 180 GHz in frequency ($\simeq$ 0 16 mm wavelength) for sounding the water-vapour distribution. this measurement is mentioned in more detail in the next section

The question might be asked as to why a number of different instruments operating in different spectral regions are required for sounding the atmosphere's temperature profile. The reason is concerned with the difficulty of converting a set of measurements of radiance into an accurate description of the temperature profile — a process known as temperature retrieval. Various factors complicate the retrieval process. For infra-red measurements the main problems arise because, also emitting infra-red radiation are clouds within the field of view of the radiometer — clouds which come in different shapes and sizes may be present at a variety of levels and are often partially transparent.

The advantage of the microwave part of the spectrum is that clouds, unless they are precipitating clouds, are substantially transparent to microwave radiation. However, the problems there are concerned with the varying emissivity of the surface and with the fact that a higher precision of radiance measurement is required to achieve the same accuracy in retrieved temperature.

Retrieval techniques for combining radiance measurements from a large number of spectral channels to achieve, with adequate quality control, the best possible temperature profile have not been easy to bring into operational use. During the last two or three years, however, the value of the incorporation of satellite temperature soundings into the data input to forecasting models has been well demonstrated. **Fig. 14** compares temperature profiles retrieved from satellite radiances with radiosonde measurements at coincident locations, showing rms differences of $\simeq$ 2 K between them. The aim is to reduce the errors in the satellite observations so that the rms differences compared with radiosondes approach IK — satellite observations of the mean temperature of atmospheric layers would then be as good as, if not better than, radiosonde measurements of the same quantities.

To achieve this improvement will require a lot of careful research into retrieval methods and quality control procedures. Pioneering work has been carried out at Madison, Wisconsin (Smith *et al.*, 1985); European groups in France (Chédin *et al.*, 1984) and the UK (Eyre et *al.*, 1985) are also very active. These groups play a substantial part in the international group which exchanges information about the exploitation of these satellite techniques (TOVS Study Conference 1985).

Because of the high horizontal resolution which is possible with satellite measurements, it is possible from the instruments on NOAA polar orbiting satellites to obtain images at different levels

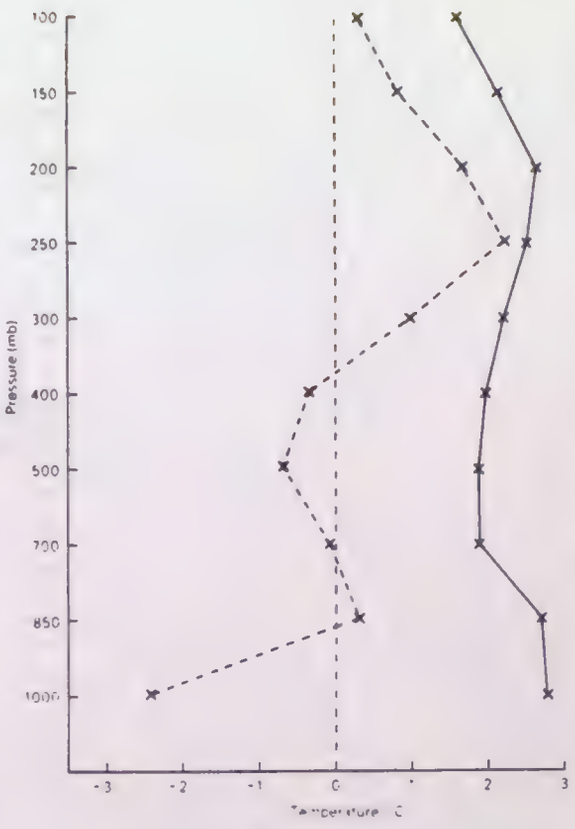

Fig. 14 (above) : Comparisons for October 1984 (bias dotted and standard deviation solid line) between temperatures obtained from satellite soundings from NOAA-7 and colocated radiosondes. (From Turner et al. 1985).

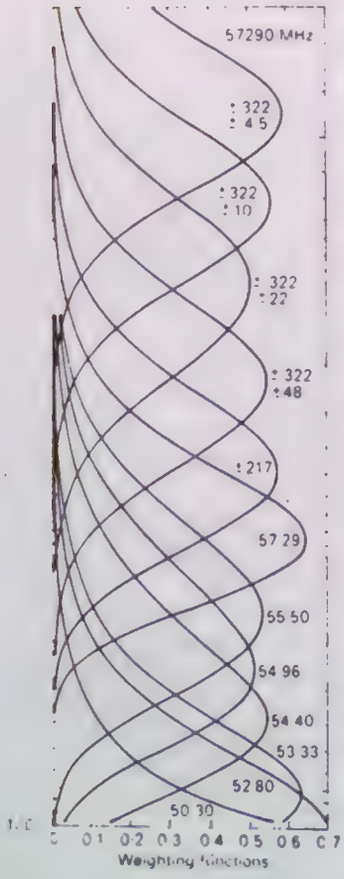

Fig. 13 b (bottom left) : Weighting functions (i.e. the region of atmosphere from which radiation originates) for the temperature sounding channels on the Advanced Microwave Sounding Unit.

Fig. 15 a (below) : 1 000-500 mb thickness and thermal winds analysed from locally received satellite temperature soundings from NOAA-7 for 12 November 1984. (Turner et al. 1985).

of the temperature field in which some of the smaller scale detail — for instance that associated with fronts — can be delineated. In **Fig. 15** an analysis of the 1000 — 500 mb thickness (another way of describing the mean temperature of the lowest 5 km or so of atmosphere) as retrieved from several orbits of radiance data from NOAA - 6 is compared with an analysis based on conventional data. The details of a substantial trough are much better described from the satellite data. Further, because the satellite data is available by direct transmission from the satellite as it goes over, it is available very soon indeed after observation

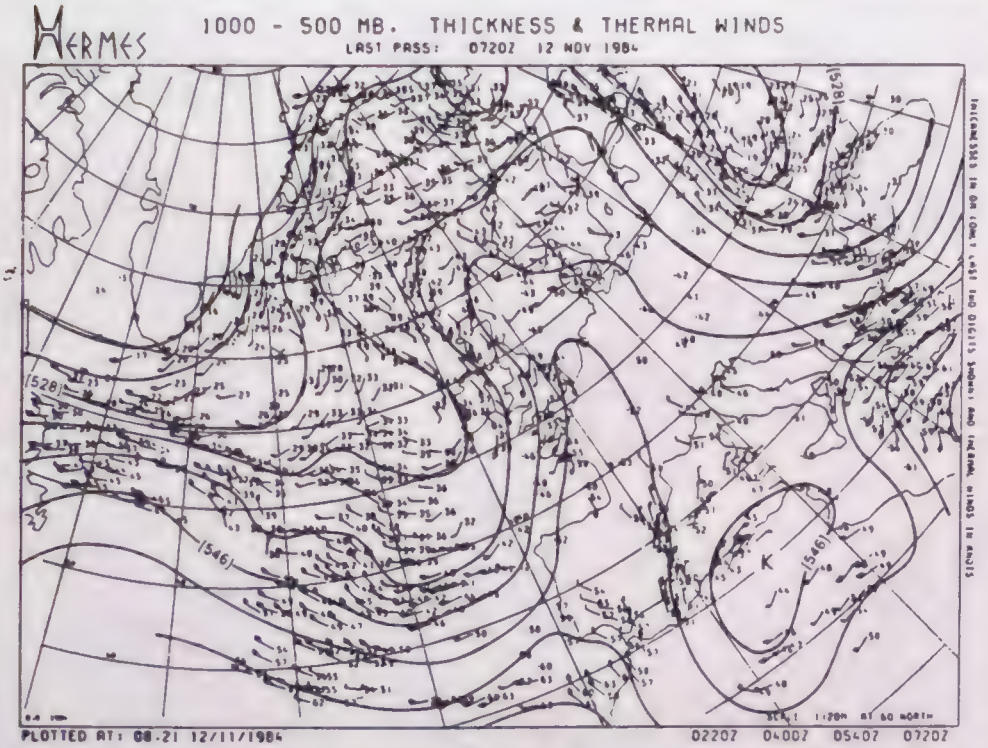

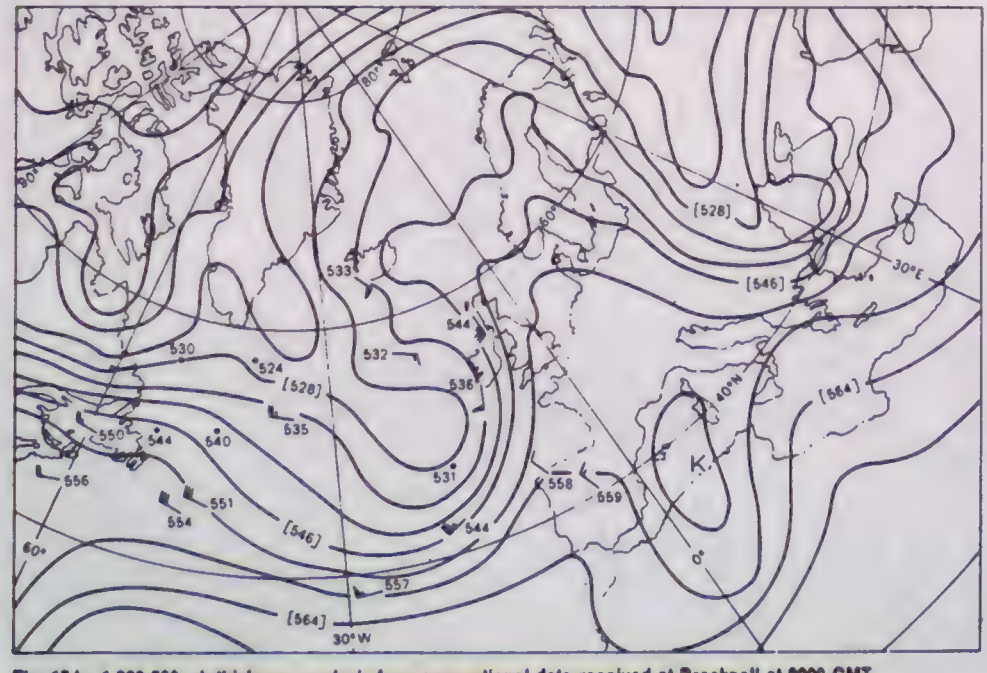

Fig. 15 b : 1 000-500 mb thickness analysis from conventional data received at Bracknell at 0000 GMT on 12 November 1984. (From Turner et al. 1985).

There would be considerable advantage if atmospheric temperature sounding data were available continuously rather than the twice a day which is available from a single polar orbiting satellite (four times a day if there are two polar orbiters) On NOAA's geostationary satellites the VISSR Atmospheric Sounder (**VAS**) provides an option for such measurements which has been employed extensively in following the development and behaviour of mesoscale systems (ESA 1985a). The possibility of mounting a radiometer with microwave channels on the second generation of the European geostationary satellite, Meteosat, is being seriously considered

Satellite observations of what is commonly called the middle atmosphere, between about 10 and 100 km in altitude, have revolutionised the study of the structure and dynamics of this region. Prior to satellites, a few rocket observations provided the only information available on a routine basis. The large scale dynamics of this region of the atmosphere is dominated by planetary waves generated in the troposphere and, under suitable conditions, propagated upwards. In winter they can reach very large amplitudes (up to about 100 K in temperature amplitude at about 45 km altitude has been observed) when they are known as stratospheric warmings. In **Fig. 16** is shown a cross-section of atmospheric temperature from the surface to 100 km altitude which has been derived solely from satellite data

In **Fig. 17** from SSU data, the structure of a particular planetary wave is illustrated showing

features analogous to waves breaking on a beach.

REMOTE SENSING OF ATMOSPHERIC COMPOSITION

In the section on Meteosat, reference has already been made to the observation of the distribution of water-vapour for which Meteosat possesses a channel. The technique of measurement is an extension to that described in the last section for atmospheric temperature determination. Given that the temperature structure is known, radiance observations at suitable wavelengths where different constituents emit enables the distribution of those constituents to be deduced.

Although Meteosat provides interesting data on water-vapour in the upper troposphere, of more importance is water-vapour at lower levels. Suitable wavelengths exist in the microwave region for the observation of water-vapour (**Fig. 13**). Some of these have already been exploited in satellite radiometers: a more comprehensive set to enable the details of the distribution of water-vapour in the vertical to be measured will be included in the AMSU-B instrument due to fly operationally around the end of the present decade.

Ozone is another important atmospheric constituent, which is mainly (though not completely) confined to the stratosphere. Sa-

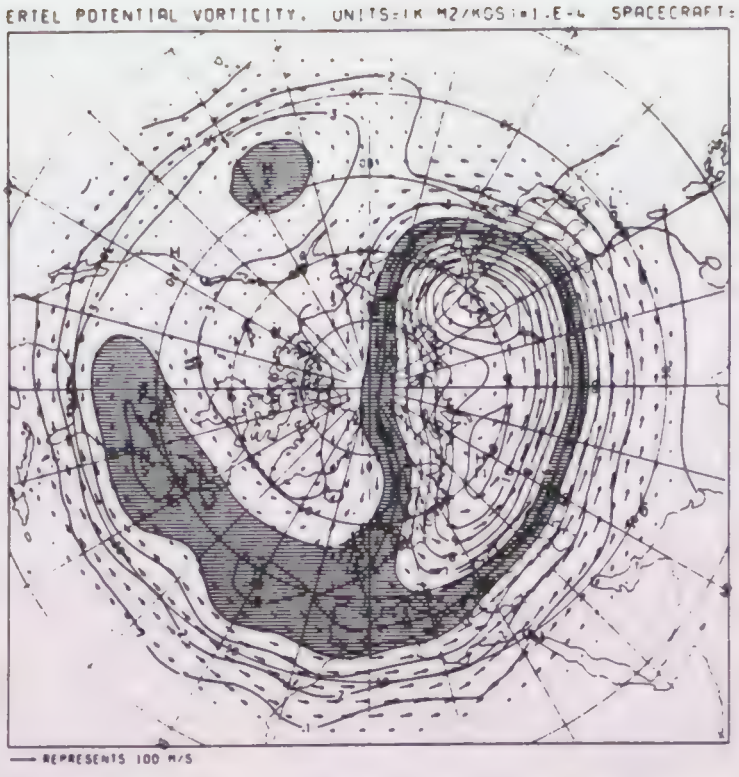

Fig. 16 (bottom left) : Temperature (K) cross-section of the atmosphere from 80° N to 80° S as deduced from radiance measurements from the selective chopper radiometer on Nimbus 5 and the pressure modulator radiometer on Nimbus 6 for 4 August 1975.

Fig. 17 (top) : ERTEL potential vorticity for the 850 K potential temperature surface (approximately 30 km altitude) for the 7 December 1981 from the SSU instrument on NOAA polar orbiting satellites. The structure of a « breaking » planetary wave is shown. (Clough et al. 1985).

Fig. 18 (centre right) : Temporal variations of the temperature at the 2 mb level from SCR and the ozone mass mixing ratio at the 1 mb level in a latitude band centred at 60 North from one year of Nimbus 4 data. (After Krueger et al. 1980).

Fig. 19 (bottom right) : Illustrating limb sounding.

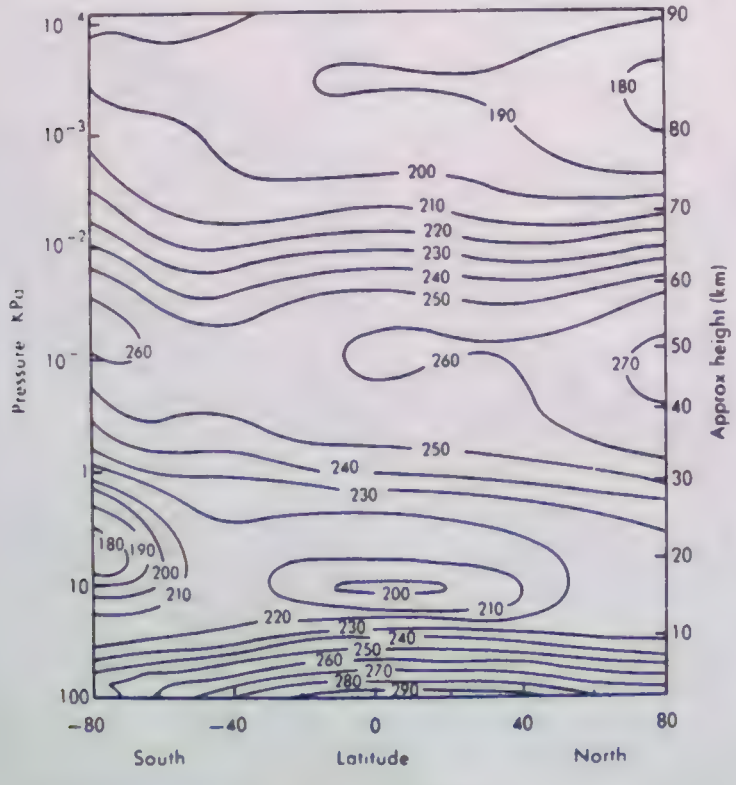

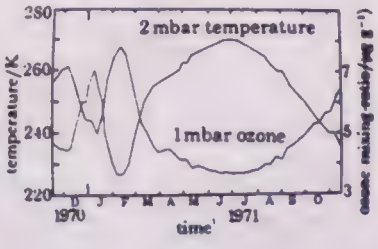

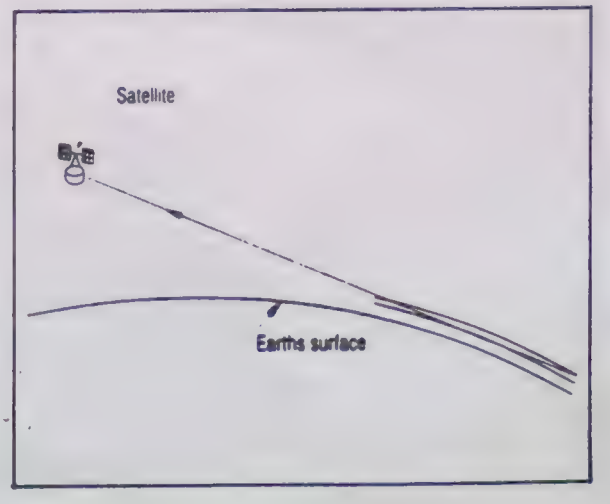

Fig. 20 (centre right): Number densities of NO and NO_2 versus altitude on 1 December 1983 measured by the Spacelab Grille Spectrometer. The near straight lines radiate constant volume mixing ratios from 10^{-6} to 10^{-5}. (From Laurent et al. 1985).

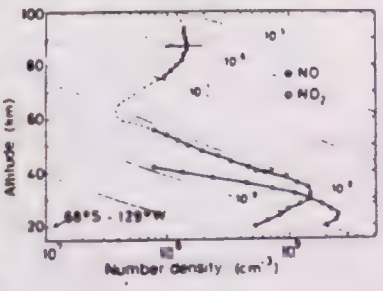

Fig. 22 (top right): Map of sea surface temperature near the British Isles taken by the AVHRR on NOAA - 6 on 26 August 1981. Different shades of grey are 2.5 K apart in temperature.

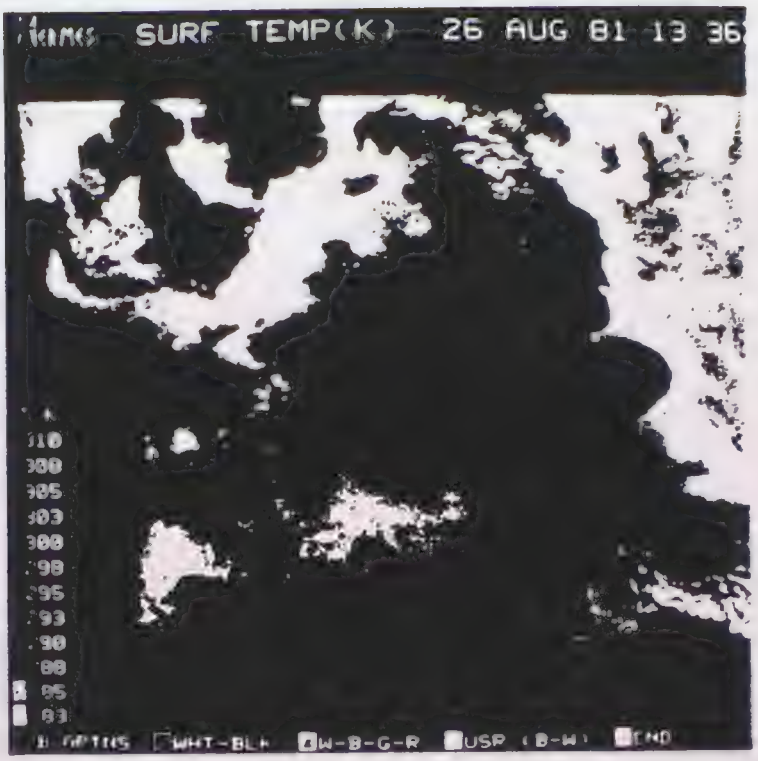

tellite observations of ozone have been made since around 1970 both with infra-red techniques and by measurements of radiation in the ultra-violet backscattered from the atmosphere in the region of the ozone absorption band. The distribution of ozone above about 25 km altitude, where it is largely controlled by photochemical processes, is strongly dependent on atmospheric temperature (**Fig. 18**). At lower levels in the stratosphere its distribution is controlled substantially by the atmospheric circulation — in fact, it is an important tracer of atmospheric motion.

Fig. 21 (below): Cross-section of methane distribution in the stratosphere around the 60° N circle of latitude during a period of stratospheric warming. Measurements are in ppm and were acquired by the Stratospheric and Mesospheric Sounder on Nimbus 7.

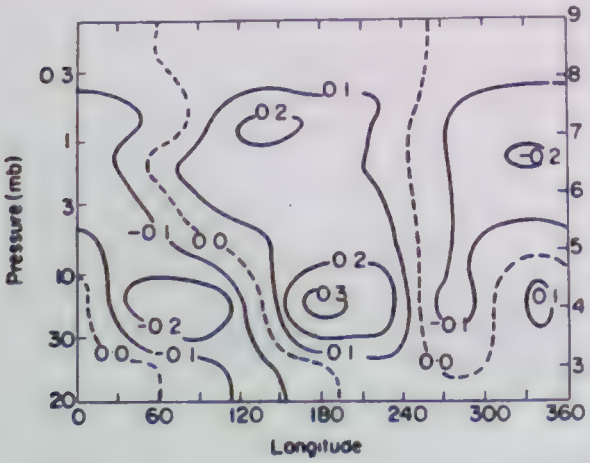

Recent attention has been given to the integrity of the ozone layer because of the possibility that it might be affected by man made pollutants (eg freons from aerosol cans). The chemistry of the interactions involved is highly complex and it is important to measure the distribution as a function of time of some of the minor constituents involved. Viewing from a satellite in appropriate infra-red spectral regions the emission or absorption by these constituent along an atmospheric limb path (**Fig. 19**) sufficient signal can be obtained to measure their concentration even though they may be present in only a few parts in 10^9. Instruments for measuring absorption spectra for that purpose have been mounted in the Space Shuttle by Belgian and French scientists leading to the acquisition of a number of vertical profiles of the distribution of molecules such as NO and NO_2 (Laurent *et al.*, 1985. **Fig. 20**). A Shuttle mounted limb sounder observing ozone and water-vapour spectra in the microwave region is also under preparation by German and Swiss scientists.

The global distribution of some constituents such as methane (**Fig. 21**) and nitrous oxide and the changes in their distribution with time has been observed through infra-red emission measurements from the Improved Stratospheric and Mesospheric Sounder built by UK scientists for the Nimbus 7 satellite. A major effort to acquire a wide range of data from the middle atmosphere will be made by NASA's Upper Atmosphere Research Satellite (UARS) — a mission in which European scientists are well involved — which is due to fly around the end of the decade

OTHER REMOTESENSING MEASUREMENTS

So far we have dealt largely with measurements in the free atmosphere. Since the exchange of heat and momentum with the earth's surface is of vital importance in determining the atmosphere's circulation, meteorologists also require detailed information about conditions at the atmosphere's lower boundary.

Probably the most important of surface measurements is that

of surface temperature especially over the ocean. The input of heat energy into the atmosphere is dominated by the latent heat input through evaporation which is a strong function of surface temperature. An infra-red radiometer mounted on a polar orbiting or geostationary satellite observing radiation from the surface in an atmospheric window region (**Fig. 11**) can easily provide the global coverage. The difficulty is to overcome the problems of partial cloud cover and correcting for atmospheric absorption sufficiently well for adequate accuracy to be achieved — sea surface temperature measured to better than about 0.5K is what the meteorologists and climatologists require.

Use of a narrow field of view has assisted in overcoming the cloud cover problem, the employment of several spectral channels has helped to overcome the problem of atmospheric absorption so that measurements approaching 1K in absolute accuracy are now available from satellite observations (**Fig. 22**). The Along Track Scanning Radiometer (ATSR) on ERS-1 (see next section and **Fig. 26**) includes an instrumental arrangement which enables the radiance of the ocean surface to be measured at different angles as well as in different spectral regions — its aim is to measure sea surface temperature to better than 0.5K.

Significant information regarding the properties of the surface can be acquired from observations at different microwave or centimetric wave lengths. Because of the very different emissivities of ice and water at 1.5 cm wavelength, images of the surface with the Electronically Scanned Microwave Radiometer (ESMR) have provided continuous observation of ice cover in both polar regions for more than a decade. Further, with this instrument, different types and ages of ice can be recognised. Emissivity of the land surface at these wavelengths depends strongly on soil moisture content although the effect can be masked by the many other characteristics of land which go towards determining the emissivity.

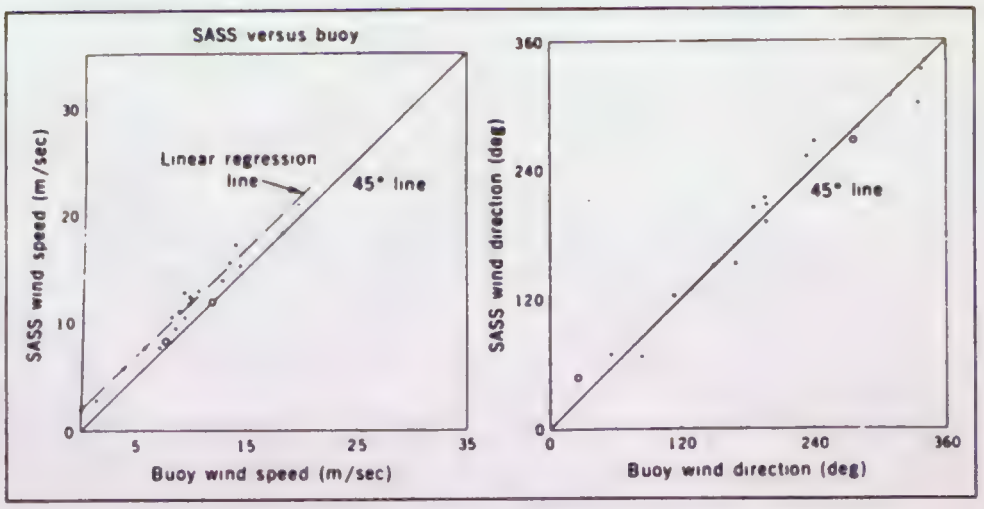

Fig. 23 (above): SASS wind vector comparisons with buoy reports during a study in the Gulf of Alaska. (From Jones et al. 1979)

OBSERVATIONS OF DIFFERENT WAVELENGTHS

The combination of images at different wavelengths can be of great importance in the interpretation of satellite data. For instance, low cloud or fog can be recognised in infra-red images by making use of the different spectral properties of the clouds and the land or ocean surface (Eyre *et al.*, 1984). The extent of snow cover and its variations has been determined by combining observations of different wavelengths from the Scanning Multichannel Microwave Radiometer (SMMR) on Nimbus 7 by Swiss scientists (Kunzi *et al.*, 1982). The natural extension of this sort of work is to combine observations in the microwave region with those at a number of visible and infra-red wavelengths. In this way monitoring of the land surface of the globe for reliable meteorological and climatological inputs will be possible — the International Satellite Land Surface Climatology Project (ISLSCP) has been formed with this end in view.

Precipitation, although an important component of the hydrological cycle, is very poorly measured when considered on the global scale — virtually no measurements, for instance, are available over the oceans. Since cloud droplets are little affected by microwave radiation, while droplets of precipitation size absorb quite strongly, information is, in principle, available from satellite-borne microwave radiometers. The difficulties are that typical rain cells are smaller than the resolution element of the ra-

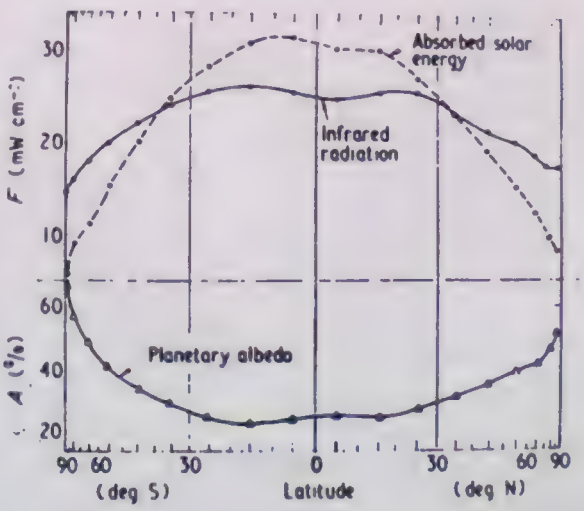

Fig. 24 (below): Components of the earth's radiation budget 1962-66. (From Vonder Haar and Suomi 1971).

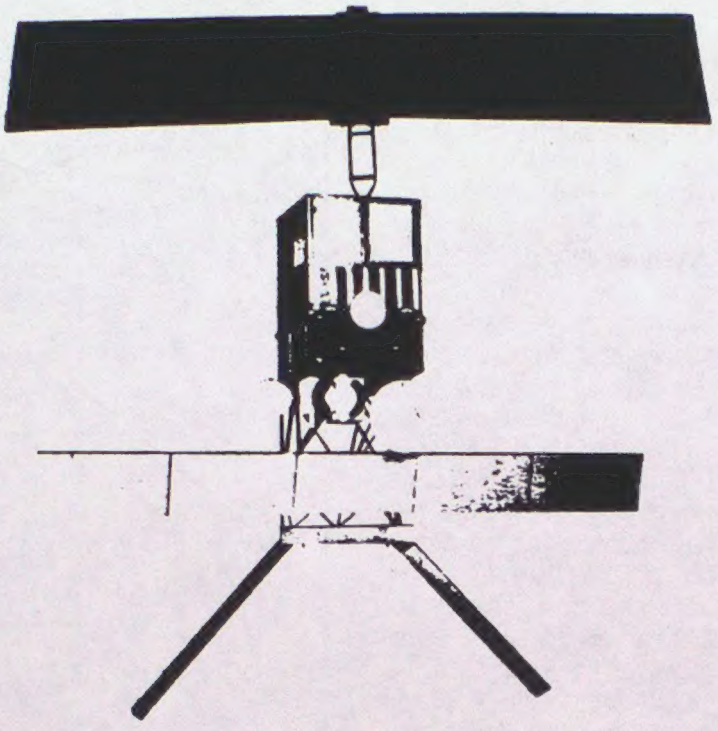

Fig. 25 : ERS-1 satellite

diometer and also that, because of the large variation of precipitation with time of day, it is important to make continuous measurements if the results are not to be affected by sampling problems.

Some progress has been made by correlating the visible and infra-red properties of cloud images with precipitation. An adequate solution to the problem of precipitation measurement will probably have to await the ability to mount much larger instruments on polar orbiting or geostationary satellites (see next section).

The NASA satellite **Seasat,** launched in 1978, demonstrated that radars could be successfully mounted in space to observe the earth's surface. The most important meteorological measurement from Seasat was that of surface wind — obtained by observing with a 2 cm radar the back-scattered signal from small capillary waves on the sea surface whose amplitude and direction is a function of the instantaneous wind (**Fig. 23**).

So far in this section we have been concerned with measurements of the earth's surface — the lower boundary for the meteorologist. Monitoring energy exchange across the upper boundary is also important. This needs to be done with accurate radiometers measuring the solar input, the solar radiation scattered away from the earth and the thermal radiation emitted by the earth-atmosphere system in the infra-red. Radiometers on early Nimbus satellites were able to make all these measurements somewhat crudely though with useful results (**Fig. 24**).

More careful measurements are currently being made from NASA and NOAA satellites in the Earth Radiation Budget Experiment (ERBE) whose purpose is to establish to what degree there are global or regional variations in components of the radiation budget from year to year. Associated with this is the International Satellite Cloud Climatology Project (ISCCP) which is taking data from polar orbiting and geostationary satellites, ensuring it is well calibrated, and using it to establish global and regional cloud climatologies over a five year period — data which will be of great value to the World Climate Research Programme (WCRP).

THE FUTURE OF SATELLITE METEOROLOGY

Of increased importance to the study of the atmosphere and its role in the total climate system is the furtherance of an understanding of ocean-atmosphere exchange. Through the World Climate Research Programme (see for instance Houghton 1984) and its component programmes, Tropical Ocean Global Atmosphere (TOGA) and the World Ocean Circulation Experiment (WOCE), a lot of emphasis will be placed during the next decade on observations of the oceans. A substantial contribution to this programme of ocean observation will be made by the first European Remote Sensing Satellite ERS-1 (**Fig. 25**) which will carry radar scatterometers for observing surface wind and surface waves and will also carry the ATSR for sea surface temperature measurement (**Fig. 26**) which has already been mentioned. The US and Japan are also planning to launch satellites for ocean observation during this period to aid in providing the coverage in space and time that is required.

A substantial advance in the possibilities for satellite observation of the earth will take place in the mid-1990s with the deployment of the US Space Station and the associated Polar Platform towards which Europe is planning to contribute substan-

tially (**Fig. 27**). A near polar orbit is required to achieve global coverage, so the Polar Platform is of particular interest to the meteorological and oceanographic communities. It opens up possibilities of mounting comparatively large instruments and of the exchange and maintenance of instruments in space. New and more accurate measurement possibilities thereby come into view, hopefully at a reasonable economic cost.

In the light of the new possibilities which are emerging, a lot of attention is being given on both sides of the Atlantic to the objectives and the content of a future programme of earth observation from space. The European Space Agency (1985b) has published a broad strategy for such a programme entitled *Looking Down, Looking Forward.*

The cornerstones of the proposed programme are :

— continuation and improvement of observations of the atmosphere;

— continuation and improvement of ocean and ice observations;

— optical and all-weather land observation;

— exploitation of precise measurement techniques for solid - earth research and applications;

— provision for payloads of opportunity.

Providing it turns out to be an economic solution; it is anticipated that the realisation of a considerable part of the proposed programme will come through exploitation of the Polar Platform.

So far as the atmospheric part of the programme is concerned, provision needs to be made to develop measurement capability in three areas. First, it is imperative that the capability of providing the basic information required for operational forecasting is maintained and improved. Secondly, substantial improvement needs to be made in observations related to components of the hydrological cycle. Thirdly, measurements are required with much better coverage and higher accuracy of the distribution of minor atmospheric constituents related to biogeochemical cycles. Each of these areas will be discussed briefly in turn.

For operational meteorology, McElroy and Schneider (1985) have put forward proposals for two platforms in sun synchronous near polar orbit at about 850 km altitude with equator crossing times at 0900Z and 1330Z respectively. A summary of the payload of operational instruments they propose for meteorological observations is given in **Table 1.** The specifications of the instruments listed in that table are based for the most part on instruments that have already flown in space or are in an advanced stage of preparation for flight on a future mission.

Other instruments they propose for operational payloads are directed to observations of the oceans or the land surface (eg the radar altimeter, ocean colour monitor, synthetic aperture radar and high resolution multispectral imager) and to monitoring the solar terrestial environment. The total mass of their proposed operational payload is around 3.000 kg and the power required between 3 and 4 kW.

For increased understanding of the hydrological cycle and its components, better measurements (i.e. with better accuracy, higher resolution and improved coverage) are required of the atmospheric water-vapour distribution, of precipitation, of soil moisture content and of evaporation. The challenges posed to the instrumentalist are considerable. Active and passive measurements in the microwave region will have to be exploited. The design of the large antennae required to achieve high spatial resolution presents some interesting problems.

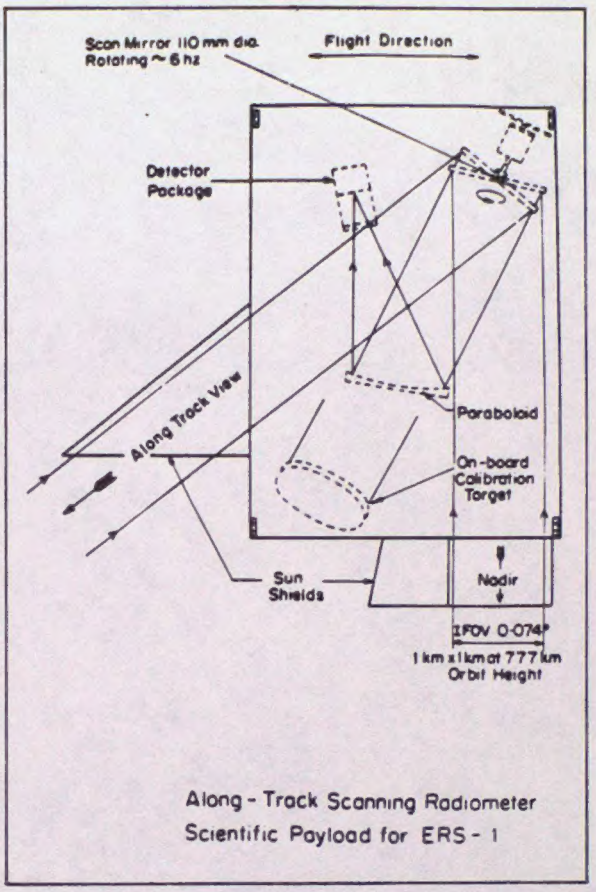

Fig. 26 (above) : Illustrating the Along Track Scanning Radiometer for sea surface temperature measurements from ERS-1.

The third area of the investiga-

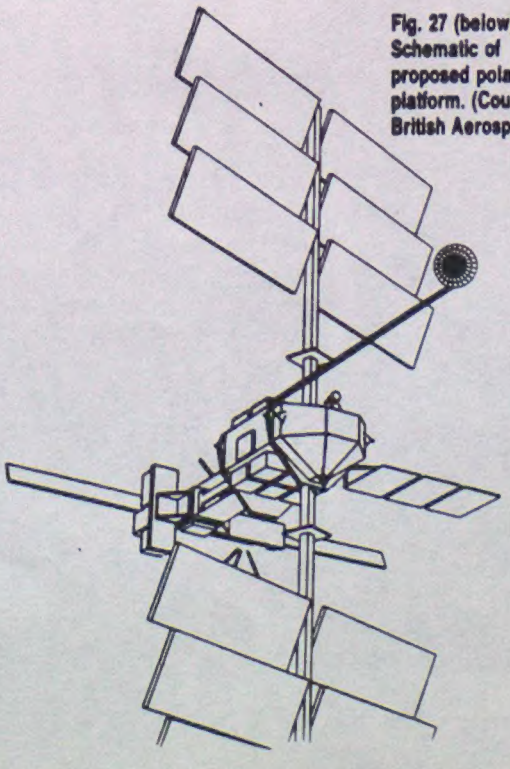

Fig. 27 (below) : Schematic of proposed polar platform. (Courtesy of British Aerospace).

TABLE 1

Instrument	Description	Purpose
Medium-Resolution Imaging Radiometer (MRIR)	10 spectral channels; 6 visible and near i.r., 4 thermal. i.r. ≃ 0.5 km horizontal resolution.	Cloud imaging, land surface properties, sea-surface temperature, mid-tropospheric water vapour.
High-Resolution Infra-Red Sounder (HIRS/3)	13 spectral channels in 15 μm and 4.3 μm CO_2 bands. ≃ 10 km horizontal resolution.	Surface temperature and atmospheric temperature profile up to 30 km altitude.
Advanced Microwave Sounding Unit (AMSU)	15 channels 23-89 GHz; 50 km horizontal resolution (AMSU-A); 5 channels 89 GHz-184 GHz; 15 km horizontal resolution, (AMSU-B).	Surface temperature and atmospheric temperature profile up to 50 km altitude (AMSU-A); water-vapour distribution (AMSU-B).
Passive Microwave Imaging Radiometers : — Advanced Microwave Radiometer (AMR); — Advanced Mechanical Scanned Radiometer (AMSR); — Special Sensor Microwave Imager (SSM/I).	Imaging radiometers at various frequencies between 5 and 90 GHz; horizontal resolution ≃ 20 km near 5 GHz, ≃ 2 km near 90 GHz.	Land and ocean surface properties, wind speed over oceans, precipitation, atmospheric water-vapour, ice cover.
Earth Radiation Budget Instrument (ERBI)	8 broad band channels in visible and thermal infra-red; field of view of some channels cover limb to limb.	Components of radiation budget at top of atmosphere.
Global Ozone Monitoring Radiometer (GOMR)	13 channels between 250 nm and 380 nm in ultra-violet; 170 km horizontal resolution — non-scanning.	Global ozone profiles.
Along Track Scanning Radiometer (ATSR)	3 infra-red channels, 3.17 μm, 11 μm and 12 μm, 1 km horizontal resolution — two separate viewing angles.	Sea surface temperature with high accuracy.
Radar Scatterometer (SCATT)	Radar at 14 GHz with 6 antennae; horizontal resolution 25 km.	Surface wind speed and direction.
Data Collection and Platform Location (DCPL)		Locating and interrogating buoys and remote observation platforms.

tion of biogeochemical cycles (e.g. the nitrogen, sulphur, chlorine cycles) through the measurements of minor constituents presents even greater challenges. So far such measurements have only been attempted from space in the stratosphere, which is almost completely free from cloud and where the spectral signatures of the different components do not overlap too much. To improve the stratospheric measurements and to make such measurements in the troposphere a lot of instrumental ingenuity will be required, in addition to overcoming technical problems such as that of building detectors and optics cooled to helium temperatures.

To achieve some of the goals I have presented, close international collaboration will be required — the programmes are too large for one nation or one group of nations to achieve on its own. Significant resources also need to be available not only for building and flying instrumentation which has already been proved, but also for ensuring a continuing instrumental development within Europe.

Preparation for the exploitation of new technology needs to be made. For instance, lidar technology will be important; lidars at suitable wavelengths have the potential to measure aerosol content in the stratosphere and in the lower atmosphere, to measure cloud properties and cloud heights, and, if sufficient power is available, also to measure atmospheric temperature structure, composition and the wind field. In this regard

the last cornerstone of the ESA programme is of importance, namely the provision of a suitable platform as soon as possible on which new instrumental ideas or concepts can be tried out in an economic and effective way.

Future developments on the scale envisaged cannot really be outlined without mentioning the importance of data utilisation. It goes without saying that there is no value in flying a space instrument if preparation is not made to use the data from it. Very large amounts of data — much more than even now we are used to — related to the atmosphere will flow from the programme which is being planned. The challenge of data control, management and exploitation is no less than that of instrument design. In fact they go together. It is important to view the platform, the instrument, the data plan and the application as an integrated system. An end-to-end view is required which will ensure a balanced use of resources in the component parts of the system.

It is further also important to see observation from space as one part, although perhaps the largest part, of the whole system of atmospheric observation which includes many other sources of data coming from surface-based instruments or from measurements made within the free atmosphere itself. Only by so doing will responsible use be made of the resources provided.

In this short article I hope I have succeeded in demonstrating the value of the great advances made in meteorological observation during the first twenty-five years of meteorological satellites. The next twenty-five years will, I am sure, be no less exciting. The demand for more accuracy, higher quality, and better coverage is as strong as ever, so therefore is the challenge to the instrumentalist, the data manager and the project organiser.

In addition, the meteorological enterprise, which is concerned with the acquisition of a much better understanding of the atmospheric environment and the climate, is one in which all mankind is involved and increasingly requires the closest of international collaboration. It is therefore enormously worthwhile.

John T. HOUGHTON

About the author, see biographical details in the Who's Who Section

References

Bengtsson, L., Kanamitsu, M., Kallberg, P. and Uppala, S., 1982. *FGGE 4 dimensional data assimilation at ECMWF.* Bulletin of American Meteorological Society. Vol. 63. N° 1.

Browning, K.A. (ed.) 1982. *Nowcasting.* Academic Press.

Chedin, A., Scott, N.A., Wahiche, C., Moulinier, P. Husson, N., and Rochard, G. 1985. *The 3I procedure applied to the retrieval of meteorological parameters from NOAA-7 and NOAA-8. (Proceedings of TOVS - Austria, etc. pp. 11-38).*

Clough, S.A., Grahame, N.S. and O'Neill, A. Quart J.R. Met Soc. (1985) 111 pp 335-358 *Potential vorticity in the stratosphere derived using data from satellites*

European Space Agency, 1985a. ESA Journal 9. N° 2.

European Space Agency, 1985b. *Looking Down. Looking Forward.* ESA SP-1073)

Eyre, J.R., Brownscombe, J.L., and Allam, R.J. 1984. *Detection of fog at night using AVHRR imaging.* Meteorological Magazine 113, pp. 266-271.

Eyre, J.R., Watts, P.D., Turner, J. and Lorence, A.C. 1985. *Research and development on TOVS retrievals in the UK.* The Proceedings of the 2nd International TOVS Study Conference, Austria, 1985. pp. 58-75. Published by CIMSS, Madison, Wisconsin, USA.

Hanel, R.A., Schlachman, B., Rogers, D. and Vanous, D. 1971. *Nimbus-4 Michelson Interferometer.* Applied Optics 10, 1376-1382.

Houghton, J.T., Taylor, F.W. and Rodgers, C.D. 1984. *Remote sounding of atmospheres.* CUP.

Houghton, J.T. (ed) 1984. *The Global Climate.* CUP.

Jones, W.L. *et al.* 1979 *Seasat scatterometer: results of the Gulf of Alaska Workshop.* Science 204, 1413-1415.

Krueger, A.J., Guenther, B., Fleig, A.J., Heath, D.F., Hilsenrath, E., McPeters, R. and Prabhahara, C. 1980. *Satellite ozone measurements.* Phil. Trans. R. Soc. London, A296, 191-204.

Kunzi, K.F., Paril, S., Rott, H. 1982. *Snow cover parameters retrieved from Nimbus-7 SMMR data.* IEEE Transactions on Geoscience & Remote Sensing. GE-20, pp. 452-467.

Laurent, J., Lemaitre, M.P., Besson, J., Girard, A., Lippens, C., Muller, C., Vercheval, J and Ackerman, M. 1985. *Middle atmospheric NO and NO_2 observed by the Spacelab grille spectrometer.* Nature. Vol. 315 126-127.

McElroy, J.H. and Schneider, S.R. 1985. *The Space Station Polar Platform: NOAA systems considerations and requirements.* NOAA Technical Report NESDIS 22.

Turner, J., Eyre, J.R., Jerrett, D., and McCallum E., 1985. *The HERMES System.* Meteorological Magazine 114, pp. 161-172.

TOVS Study Conference 1975 published by CIMSS, Madison, Wisconsin, USA.

Vonder Haar, T.H. and Suomi, V.E., 1971. *J. Atmos.* Sci., 28. 305-314.